Méthodes d'éléments finis pour le problème de changement de phase en milieux composites

Maimouna Mint Brahim

université de BORDEAUX

THÈSE PRÉSENTÉE
POUR OBTENIR LE GRADE DE

DOCTEUR DE L'UNIVERSITÉ DE BORDEAUX

ÉCOLE DOCTORALE SCIENCES PHYSIQUES ET DE L'INGÉNIEUR

SPÉCIALITÉ MÉCANIQUE

par Maïmouna MINT BRAHIM

Méthodes d'éléments finis pour le problème de changement de phase en milieux composites

---

soutenue le 30 Novembre 2016

Membres du jury :

Mejdi Azaiez, Professeur à l'Institut Polytechnique de Bordeaux. Directeur de thèse.
Belhachmi Zakaria, Professeur à l'université de Haute Alsace. Rapporteur.
Ionut Danaila, Professeur à l'université de Rouen. Rapporteur.
Faten Jelassi, Maître de conférence à l'université de technologie de Compiègne. Encadrante.
Elena Palomo Del Barrio, Professeur à l'université de Bordeaux. Co-directrice de thèse.
Cédric Le Bot, Maître de conférence à l'université de Bordeaux. Invité.
Gérard Vignoles, Professeur à l'université de Bordeaux. Président.

Acknowledgements

I would like first of all to express my gratitude to my supervisors, Faten Jelassi, Professor Mejdi Azaiez and Professor Elena Palomo Del Barrio. They have welcomed me in their team and were always ready to help me whenever I ran into a trouble spot or had a question about my research or writing. They have allowed me to work with freedom and have been there when I needed some guidance.

I am also thankful for Professor Faqer Ben Belgacem for helping me and for a collaborative work that is of great quality. I also which to thank Professor Christine Bernardi as well as Professor Jien Shen for giving me the opportunity to work with them.

I am especially grateful to Professor Ionut Danaila and Professor Zakaria Belhachmi, who kindly accepted to be the referees of this thesis. I appreciate deeply their interest in my work as well as their useful comments. I am also very grateful to Professor Gérard Vignoles , who agreed to be the committee chief, and to Cedric Lebot for accepting to be a committee member.

I am very thankful for all colleges and friends from the Institut de Mécanique et d'Ingénierie de Bordeaux where I spent three unforgettable years sharing very helpful and interesting conversations.

I also which to express my gratitude for the mathematical laboratory in Compiègne which have granted me the position of ATER for the last year.

Finally, my deepest thanks go to my parents and to all my family and my friends in Bordeaux and in Compiègne for their constant support, encouragement, and love.

"La patience est amère, mais ses fruits sont doux."

Jean-Jacques Rousseau

FINITE ELEMNT METHODS FOR THE PHASE CHANGE PROBLEM IN COMPOSITE MEDIA

Abstract

In this thesis we aim to develop a numerical tool that allow to solve the unsteady heat conduction problem in a composite media with a graphite foam matrix infiltrated with a phase change material such as salt, in the framework of latent heat thermal energy storage.

In chapter 1, we start by explaining the model that we are studying which is separated in three sub-parts : a heat conduction problem in the foam, a phase change problem in the pores of the foam which are filled with salt and a contact resistance condition at the interface between both materials which results in a jump in the temperature field.

In chapter 2, we study the steady heat conduction problem in a composite media with contact resistance. This allow to focus on the main difficulty here which is the treatment of the thermal contact resistance at the interface between the carbon foam and the salt. Two Finite element methods are proposed in order to solve this problem : a finite element method based on Lagrange $\mathcal{P}1$ and a hybrid dual finite element method using the lowest order Raviart-Thomas elements for the heat flux and $\mathcal{P}0$ for the temperature. The numerical analysis of both methods is conducted and numerical examples are given to assert the analytic results. The work presented in this chapter has been published in the *Journal of Scientific Computing* [10].

The phase change materials that we study here are mainly pure materials and as a consequence the change in phase occurs at a single point, the melting temperature. This introduces a jump in the liquid fraction and consequently in the enthalpy. This discontinuity represents an additional numerical difficulty that we propose to overcome by introducing a smoothing interval around the melting temperature. This is explained in chapter 3 where an analytical and numerical study shows that the error on the temperature behaves like ε outside of the mushy zone, where ϵ is the width of the smoothing interval. However, inside the error behaves like $\sqrt{\varepsilon}$ and we prove that this estimation is optimal due to the energy trapped in the mushy zone. This chapter has been published in *Communications in Mathematical Sciences* [58].

The next step is to determine a suitable time discretization scheme that allow to handle the non-linearity introduced by the phase change. For this purpose we present in chapter 4 four of the most used numerical schemes to solve the non-linear phase change

problem : the update source method, the enthalpy linearization method, the apparent heat capacity method and the Chernoff method. Various numerical tests are conducted in order to test and compare these methods for various types of problems. Results show that the enthalpy linearization is the most accurate at each time step while the apparent heat capacity gives better results after a given time. This indicates that if we are interested in the transitory states the first scheme is the best choice. However, if we are interested in the asymptotic thermal behavior of the material the second scheme is better. Results also show that the Chernoff scheme is the fastest in term of calculation time and gives comparable results to the one given by the first two methods.
Finally, in chapter 5 we use the Chernoff method combined with the hybrid-dual finite element method with $\mathcal{P}0$ and the lowest order Raviart-Thomas elements to solve the non-linear heat conduction problem in a realistic composite media with a phase change material. Numerical simulations are realised using 2D-cuts of X-ray images of two real graphite matrix foams infiltrated with a salt. The aim of these simulations is to determine if the studied composite materials could be assimilated to an equivalent homogeneous phase change material with equivalent thermo-physical properties. For all simulations conducted in this work we used the free finite element software FreeFem++ [41].

Key words : Finite element method, Mixed variational formulation, Hybrid-dual finite element method, numerical schemes for treatment of non-linearities, phase change materials, composite media, thermal contact resistance, homogenisation, FreeFem++.

MÉTHODES D'ÉLÉMENTS FINIS POUR LE PROBLÈME DE CHANGEMENT DE PHASE EN MILIEUX COMPOSITES

Résumé

Dans ces travaux de thèse on s'intéresse au développement d'un outil numérique pour résoudre le problème de conduction instationnaire avec changement de phase dans un milieu composite constitué d'une mousse de graphite infiltrée par un matériau à changement de phase tel que le sel, dans le contexte du stockage de l'énergie thermique solaire.
Au chapitre 1, on commence par présenter le modèle sur lequel on va travailler. Il est séparé en trois sous-parties : un problème de conduction de chaleur dans la mousse, un problème de changement de phase dans les pores remplis de sel et une condition de résistance thermique de contact entre les deux matériaux qui est traduite par une discontinuité du champ de température.
Au chapitre 2, on étudie le problème stationnaire de conduction thermique dans un milieu composite avec résistance de contact. Ceci permet de se focaliser sur la plus grande difficulté présente dans le problème qui est le traitement de la condition de saut à l'interface. Deux méthodes d'éléments finis sont proposées pour résoudre ce problème : une méthode basée sur les éléments finis Lagrange $\mathcal{P}1$ et une méthode hybride-duale utilisant les éléments finis Raviart-Thomas d'ordre 0 et $\mathcal{P}0$. L'analyse numérique des deux méthodes est effectuée et les résultats de tests numériques attestent des efficacités des deux méthodes [10].
Les matériaux à changement de phase qu'on étudie dans le cadre de cette thèse sont des matériaux pures, par conséquent le changement de phase s'effectue en une valeur de température fixe qui est la température de fusion. Ceci est modélisé par un saut dans la fonction fraction liquide et par conséquent dans la fonction enthalpie du matériau. Cette discontinuité représente une difficulté numérique supplémentaire qu'on propose de surmonter en introduisant un intervalle de régularisation autour de la température de fusion. Cette procédure est présentée dans le chapitre 3 où une étude analytique et numérique montre que l'erreur sur la température se comporte comme ε en dehors de la zone de mélange, où ε est la largeur de l'intervalle de régularisation. Cependant, à l'intérieur l'erreur se comporte comme $\sqrt{\varepsilon}$ et on montre que cette estimation est optimale. Cette diminution de vitesse de convergence est due à l'énergie qui reste bloquée dans la zone de mélange [58].
Dans le chapitre 4 on présente quatre des schémas les plus utilisés pour le traitement de

la non-linearité due au changement de phase: mise à jour du terme source, linéarisation de l'enthalpie, la capacité thermique apparente et le schéma de Chernoff. Différents tests numériques sont réalisés afin de tester et comparer ces quatre méthodes pour différents types de problèmes. Les résultats montrent que le schéma de linéarisation de l'enthalpie est le plus précis à chaque pas de temps tans dis que le schéma de la capacité thermique apparente donne de meilleurs résultats au bout d'un certain temps de calcul. Cela indique que si l'on s'intéresse aux états transitoires du matériaux le premier schéma est le meilleur choix. Cependant, si l'on s'intéresse au comportement thermique asymptotique du matériau le second schéma est plus adapté. Les résultats montrent également que le schéma de Chernoff est le plus rapide parmi les quatre schémas en terme de temps de calcul et donne des résultats comparables à ceux des deux plus précis.
Enfin, dans le chapitre 5 on utilise le schéma de Chernoff avec la méthode d'éléments finis hybride-duale Raviart-Thomas d'ordre 0 et $\mathcal{P}0$ pour résoudre le problème non-linéaire de conduction thermique dans un milieu composite réel avec matériau à changement de phase. Le but étant de déterminer si un matériau composite avec une distribution uniforme de pores est assimilable à un matériau à changement de phase homogènes avec des propriétés thermo-physiques équivalentes. Pour toutes les expériences numériques exposées dans ce manuscrit on a utilisé le logiciel libre d'éléments finis FreeFem++ [41].

Mots clés : Méthode d'éléments finis, Formulation variationnelle mixte, Méthode d'éléments finis hybride-duale, schémas numériques pour le traitement de non-linéarités, matériaux à changement de phase, domaines composites, résistance thermique de contact, homogénéisation, FreeFem++.

MÉTHODES D'ÉLÉMENTS FINIS POUR LE PROBLÈME DE CHANGEMENT DE PHASE EN MILIEUX COMPOSITES

Résumé détaillé

On s'intéresse au problème de conduction thermique, à l'échelle macroscopique, dans un milieu composite constitué d'une matrice en mousse de graphite remplie d'un matériau à changement de phase (MCP) pour les applications de stockage d'énergie solaire par chaleur latente. Dans certaines de ces applications, un fluide de transfert de chaleur est utilisé pour conduire celle-ci à partir du champ solaire dans le réservoir contenant le support composite. La température élevée du fluide de transfert conduit à un changement de phase dans le MCP, tandis que la matrice poreuse est utilisée en raison de sa conductivité thermique élevée afin d'accélérer le processus de changement de phase et par conséquent de réduire le temps de charge/décharge. Ainsi, afin de comprendre le transfert de chaleur dans ces milieux composites on doit étudier deux sous-problèmes différents: un problème de conduction thermique dans la matrice et un problème de conduction thermique avec changement de phase dans le MCP. De plus, une condition de résistance de contact à l'interface entre les deux matériaux est à prendre en compte. Cette résistance thermique à l'interface résulte du contact imparfait entre les deux matériaux.

Dans cette thèse, on s'intéresse à des matériaux purs où la chaleur latente est supposée être constante et les effets de surrefroidissement et de nucléations ne sont pas présents. Nous faisons également l'hypothèse que le transfert thermique est réalisé uniquement par conduction afin d'éviter des déplacements dans la partie liquide, les changements de densité sont supposés négligeables. La chaleur spécifique et la conductivité thermique sont supposées constantes par phase. Avec ces hypothèses, les équations qui modélisent le problème sont les suivantes

$$
\begin{cases}
\partial_t H(T) - \operatorname{div}(\kappa \nabla T) = g & in\ \Omega_S \cup \Omega_G, \\
[\kappa \partial_n T] = 0 & on\ \gamma, \\
R(\kappa \partial_n (T|_{\Omega_S})) = [T] & on\ \gamma, \\
T = T_D & on\ \Gamma_D. \\
\kappa \partial_n T = 0 & on\ \Gamma_N.
\end{cases}
$$

$\Omega_S = \cup_i \omega_i, \qquad \Omega_G = \Omega \setminus \overline{\Omega}_S, \qquad \gamma = \partial \Omega_S = \cup_i \partial \omega_i.$

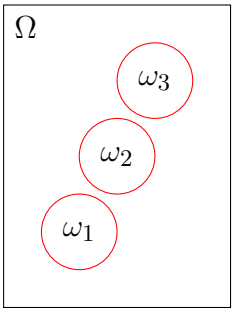

Ω_S représente les capsules de MCP, Ω_G la matrice et γ l'interface qui sépare les deux matériaux. L'enthalpie du matériau est notée H, T est la température, κ la conductivité thermique et R est la résistance thermique à l'interface γ.

Au chapitre 2, on étudie le problème stationnaire de conduction thermique dans un milieu composite avec résistance de contact. Ceci permet de se focaliser sur la plus grande difficulté présente dans le problème qui est le traitement de la condition de saut à l'interface γ. Deux méthodes d'éléments finis sont proposées pour résoudre ce problème : une première méthode de subdivision de domaines développée par Faten Jelassi et al. [48] utilisant les éléments finis Lagrange $\mathcal{P}1$ et une méthode hybride-duale utilisant les éléments finis Raviart-Thomas d'ordre 0 pour approcher le flux thermique et les éléments finis $\mathcal{P}0$ pour le champ de température. La deuxième méthode admet un avantage certain par rapport à la première puisque ça mise en œuvre ne dépend pas de la complexité de l'interface γ tandis que la première méthode est particulièrement difficile à mettre en place lorsque cette interface devient compliquée, ce qui est souvent le cas dans les applications qui nous intéressent. L'analyse numérique des deux méthodes pour différents types de géométries montrent leurs efficacités, en particulier une étude sur l'effet d'une singularité géométrique qui est due au chois du domaine Ω_S montre que la prise en compte de la résistance thermique de contact permet de découpler les effets de singularité dans les deux domaines Ω_S et Ω_G. Les résultats des différents tests numériques ont permis de corroborer les résultats analytiques. Le travail présenté dans ce chapitre a fait l'objet d'une publication dans *Journal of Scientific Computing* [10].

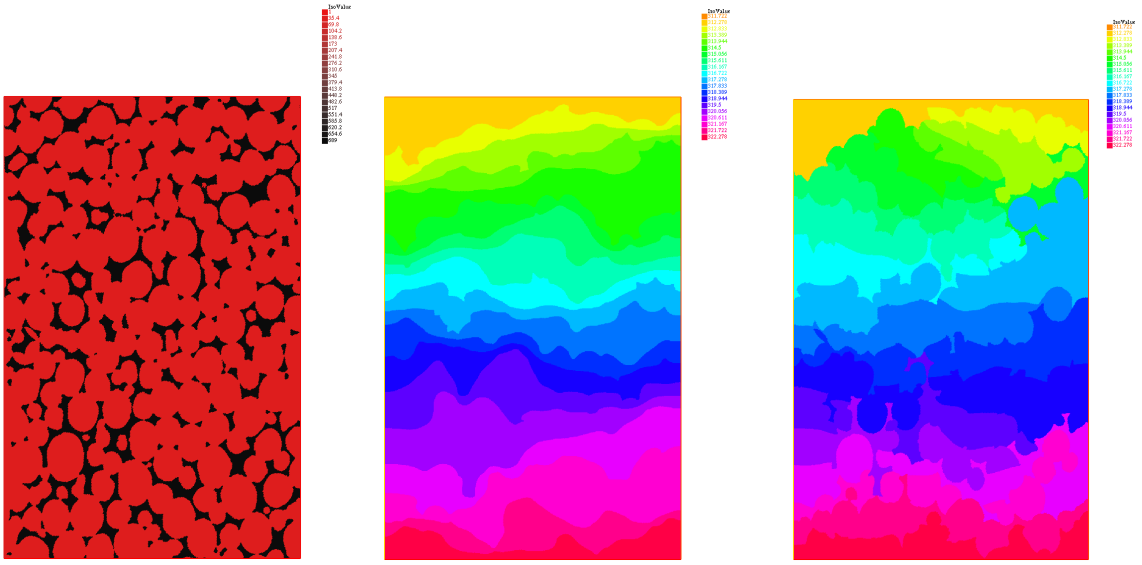

FIGURE 1: La conductivité thermique (à gauche), le champs de température pour $R = 0K/W$(centre) et $R = 0.5K/W$(à droite).

A titre d'exemple on donne les résultats d'un test numérique qui permet de mettre en évidence l'effet de la résistance thermique de contact sur la diffusion de la température au sein d'un matériau composite. La méthode hybride duale est utilisée pour résoudre le problème de conduction stationnaire avec un matériau composite constitué d'une mousse de carbone infiltrée par un sel et où l'échantillon est soumis à un gradient de température du haut vers le bas tandis que les parois latérales sont libres. Dans Figure 1, on représente à gauche la conductivité thermique du matériau, au centre le champ de température avec $R = 0K/W$ et à droite avec $R = 0.5K/W$. On constate que la diffusion de la température est freinée par la discontinuité à l'interface due à la résistance thermique. Cet exemple atteste également de l'efficacité de la méthode hybride duale dans le cas de géométries avec interface complexe.
Les matériaux à changement de phase qu'on étudie dans le cadre de cette thèse sont des matériaux pures, par conséquent le changement de phase s'effectue en une valeur de température fixe qui est la température de fusion. Ceci est modélisé par un saut dans la fonction fraction liquide et par conséquent dans la fonction enthalpie du matériau. Cette discontinuité représente une difficulté numérique supplémentaire qu'on propose de surmonter en introduisant un intervalle de régularisation autour de la température de fusion. Cette procédure est présentée dans le chapitre 3 où une étude analytique et numérique montre que l'erreur sur la température se comporte comme ε en dehors de la zone de mélange, où ε est la largeur de l'intervalle de régularisation. Cependant, à l'intérieur l'erreur se comporte comme $\sqrt{\varepsilon}$ et on montre que cette estimation est optimale. Cette diminution de vitesse de convergence est due à l'énergie qui reste bloquée dans la zone de mélange [58].

Dans le chapitre 4 on présente quatre des schémas les plus utilisés pour le traitement de la non-linéarité due au changement de phase: le schéma de mise à jour du terme source, le schéma de linéarisation de l'enthalpie, le schéma de la capacité thermique apparente et le schéma de Chernoff. Les résultats de convergence obtenus dans le chapitre précédent ont permis de tester et valider la mise en œuvre des différents schémas. Dans Figure 2 montrent les courbes de convergence, en fonction de ε, pour les fronts numériques de solidification (X_S) et de fusion (X_L) pour les schémas de linéarisation de l'enthalpie et de la capacité thermique apparente où on a une convergence d'ordre 1 dans les deux cas. Ces résultats ainsi que ceux de différents tests numériques présentés dans ce chapitre ont

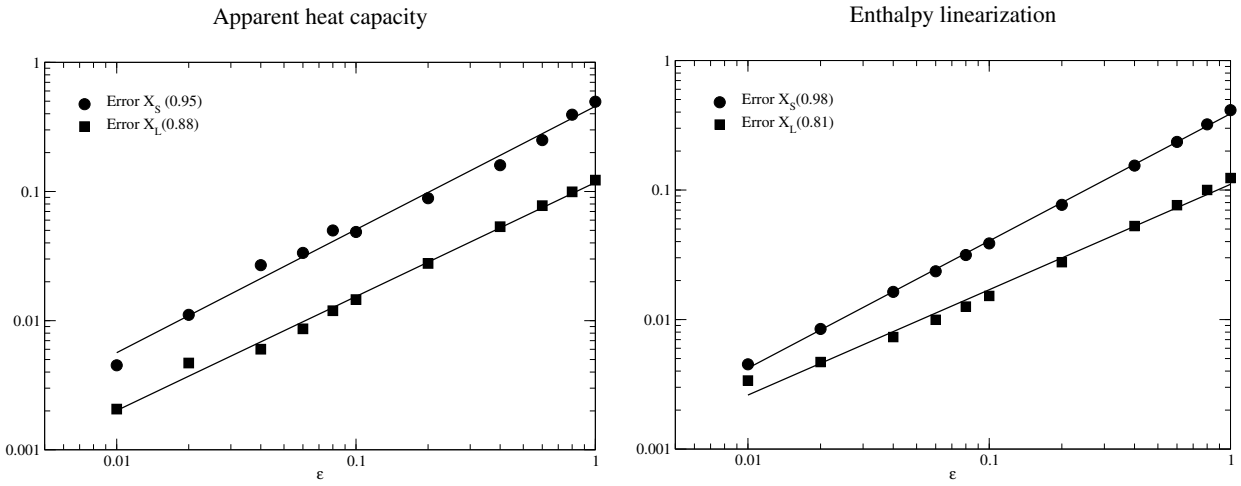

FIGURE 2: Courbes de convergence pour les fronts numériques pour le schéma de la capacité thermique apparente et le schéma de linéarisation de l'enthalpie.

permis de tester et comparer ces quatre méthodes pour différents types de problèmes. Les résultats montrent que le schéma de linéarisation de l'enthalpie est le plus précis à chaque pas de temps tans dis que le schéma de la capacité thermique apparente donne de meilleurs résultats au bout d'un certain temps de calcul. Cela indique que si l'on s'intéresse aux états transitoires du matériaux le premier schéma est le meilleur choix. Cependant, si l'on s'intéresse au comportement thermique asymptotique du matériau le second schéma est plus adapté. Les résultats montrent également que le schéma de Chernoff est le plus rapide parmi les quatre schémas en terme de temps de calcul et donne des résultats comparables à ceux des deux plus précis.

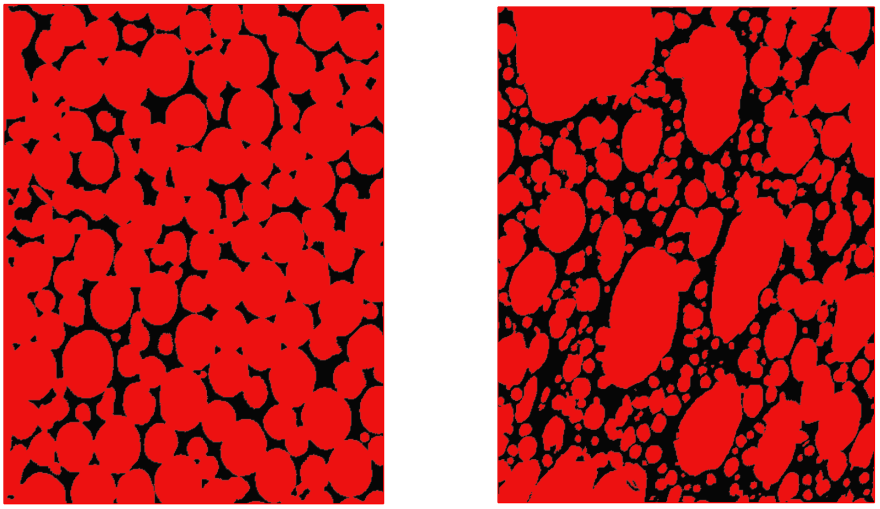

FIGURE 3: Images des échantillons des matériaux composites étudiés : $KL1\_250$ (à gauche) et $KD1$ (à droite).

Enfin, dans le chapitre 5 on utilise le schéma de Chernoff avec la méthode d'éléments finis hybride-duale Raviart-Thomas d'ordre 0 et $\mathcal{P}0$ pour résoudre le problème non-linéaire de conduction thermique dans un milieu composite réel avec matériau à changement de phase. La Figure 3 montre les deux matériaux composites étudiés, dans les deux cas on considère un matériau composite constitué d'une matrice de carbone (noir) infiltrée par un sel (rouge). On peut voir que le premier matériau présente des pores de même tailles et uniformément distribué tant dis que dans le deuxième matériau on peut voir en moyenne deux tailles de pores différentes. Les simulations réalisées dans ce chapitre ont permis de montrer qu'un matériau composite avec une distribution uniforme de pores (exemple: $KL1\_250$) est assimilable à un matériau à changement de phase homogènes avec des propriétés thermo-physiques équivalentes. Pour toutes les expériences numériques exposées dans ce manuscrit on a utilisé le logiciel libre d'éléments finis FreeFem++ [41].

Mots clés : Méthode d'éléments finis, Formulation variationnelle mixte, Méthode d'éléments finis hybride-duale, schémas numériques pour le traitement de non-linéarités, matériaux à changement de phase, domaines composites, résistance thermique de contact, homogénéisation, FreeFem++.

Table of Contents

Chapter 1

Context and problem formulation

Phase change materials (PCM)s are used in various industrial applications for storing energy due to their high thermal capacity. However, these materials usually have very low thermal conductivity. Several techniques involving mixing the PCM with other highly conductive materials allow to overcome this drawback. The resulting composite material have both high thermal conductivity and high thermal capacity. Depending on the technique, the shape of the interface between the different components of the composite material is more or less complex.

An important step to optimize the capacity of these thermal energy storage systems is to develop numerical tools that allow to accurately simulate the evolution of the thermal flow in the composite materials with PCM used in these systems. In order to accomplish this, great attention must be given to how handling the boundary conditions at the interface between the components of the composite material.

This chapter presents a general introduction to phase change materials and their use in latent heat thermal energy storage systems, the mathematical problem modeling the heat conduction with phase change in composite media used in these systems. In the last section we present the objectives of this thesis.

1.1 Context

The world's energy demand is expected to grow by 37% by 2040 according to the International Energy Agency (IEA)'s recently released *world energy outlook 2014* [87]. Most of this growth is expected to come from emerging economies of China, India and the Middle east where demand is driven by a strong economical growth.
In spite of renewable energy being one of the fastest-growing energy sources increasing by 2.5% per year, fossil fuels continue to supply nearly 80% of world energy use through 2040.
The industrial sector continues to account for the largest share of delivered energy consumption and is projected to consume more than half of global delivered energy in 2040. Based on current policies and regulations governing fossil fuel use, global energy-related carbon dioxide emissions are projected to rise to 45 billion metric tons in 2040, a 46% increase since 2010. Economic growth in developing nations, fueled by continuously relying on fossil fuels, accounts for most of the emissions increase [87].
An abundant renewable energy source is essential for reducing dependency on the fossil fuels and contributing to a cleaner environment. Solar energy is an essentially inexhaustible source potentially capable of meeting a significant portion of the world's future energy needs with a minimum of adverse environmental consequences [36].
For solar energy to become an important energy source, efficient, economical and reliable, solar thermal energy storage devices and methods have to be developed. The storage of energy is a present day challenge to the technologists. Energy storage not only reduces the mismatch between supply and demand but plays an important role in conserving the energy. It leads to saving of premium fuels which are limited and also contributes to a greener environment [76].

1.1.1 Thermal energy storage

Thermal energy storage (TES) technologies allow to store energy captured from the sun in order to release it at a later time for heating or cooling purposes or for power generation. For example in solar thermal power plants where most of the energy is produced during the day, the excess energy could be stored using a storage device, such as molten salt, to be released at night to generate steam and drive a turbine to produce electricity. On the other hand, a facility can use 'off-peak' electricity rates which are lower at night to produce ice, which could be incorporated into a building's cooling system to lower

demand for energy during the day.
TES can be achieved, depending on the storage mechanism, by three techniques: sensible heat storage, latent heat storage, and thermo-chemical heat storage [86]. In sensible heat storage, the amount of heat stored depends on the mass of the media (m), its specific heat (C_{ap}) and the temperature variation ($T_f - T_i$):

$$Q = \int_{T_i}^{T_f} mC_p dT \;=\; mC_{ap}(T_f - T_i)$$

As a result, sensible heat storage allow to store only relatively small quantities of thermal energy with larger volume materials and large temperature variation. In contrast to sensible heat storage, latent heat storage and thermo-chemical heat storage can store larger quantities of thermal energy with smaller temperature variation.
Thermo-chemical heat storage systems are based on the energy absorbed and released in breaking and reforming molecular bonds in a completely reversible chemical reaction [86]. An example of this is what happens when a solid material is heated and separated into two elements : a solid element and a gaseous element for heating purposes. Energy is released when the inverse reaction occurs i.e when the solid and gaseous elements are steered back together to react back to one solid element. The storage capacity of these systems depends on the amount of storage material, the endothermic heat of reaction (Δh_r) and the reaction fraction of the material (a_r):

$$Q = a_r m \Delta h_r.$$

In these systems, condensers are used to reduce the volume of the materials used in the reaction which makes these systems more complex. Even though these systems allow for the storage of high quantities of thermal energy, there are still a lot of unresolved issues at the laboratory level and their development is still at an early stage.
Latent heat storage systems are based on the energy released or absorbed when a material changes phase from solid to liquid or liquid to gas or vice versa [86]. The storage capacity of a latent heat system with a PCM depends on the mass of the material, its melting temperature (T_m), the specific heat in both phases (C_{sp} and C_{lp}), its liquid fraction (a_m) and its heat of fusion (Δh_m). For a PCM with an isothermal phase transition (ex: single

chemical components, eutectic alloys ...), the latent heat storage capacity is

$$\begin{aligned} Q &= \int_{T_i}^{T_f} m(1-a_m)C_{ps} + ma_m\Delta h_m + ma_m C_{pl}dT \\ &= \int_{T_i}^{T_m} mC_{ps}dT + m\Delta h_m + \int_{T_m}^{T_f} mC_{pl}dT \\ &= m[C_{ps}(T_m - T_i) + \Delta h_m + C_{pl}(T_f - T_m)]. \end{aligned}$$

Compared to the sensible and thermo-chemical storage systems, latent heat storage systems have higher storage density. Thus, these systems allow to minimize the volume of the storage materials and allow to reduce the size of the storage system. In addition, the thermal efficiency of these systems can be greatly increased since the temperature change of materials used can be smaller for the same energy requirement [96].

1.1.2 Phase change materials

In latent heat storage systems, PCMs are used as a storage device to solve the mismatch between energy demand and supply. They allow to store energy during the day and release it during the night. The latent heat is stored or released when the PCM changes phase from solid to liquid or liquid to solid. Unlike conventional (sensible) storage materials, PCM absorbs and release heat at a nearly constant temperature. They store 5–14 times more heat per unit volume than sensible storage materials such as water, masonry, or rock. However, these materials often have a very low thermal conductivity ($\sim 1W/mK$) that leads to low heat transfer and problem of oxidation on exposure to heat transport medium (air or heat transfer fluids like oils). To overcome this inconveniences several techniques have been developed [69].

A common technique suggests the use of foams with high thermal conductivity and high-porosity such as graphite foams. Infiltrating the foams with a PCM to provide TES in the form of latent heat has shown to be an efficient way to enhance the thermal conductivity of the storage material. Infiltrating the foam with PCM compensates for the relatively low conductivity of the PCM and allows for quick, even distribution of thermal energy into the PCM which leads to reduction in charging and discharging times when evaluated against other PCM storage options. The potential high storage density of this system will also allow for the possibility of a smaller TES system volume, thereby lowering the capital costs [57]. Figure 1.1 shows an example of graphite foam used in TES applications.

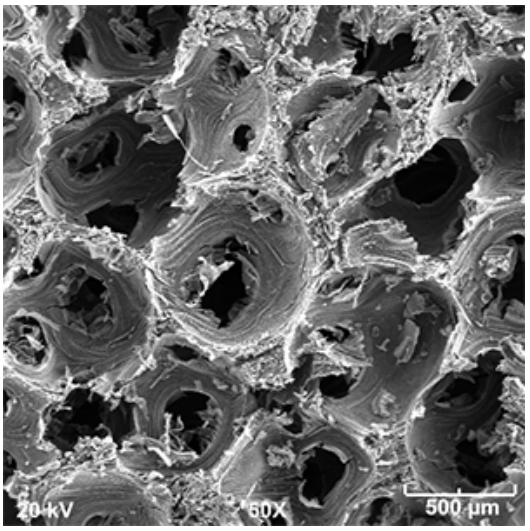

FIGURE 1.1: Microstructure of a highly thermal conductive carbon foam.

A crucial step into successful use of PCMs in latent heat storage systems, where the storage material's thermal conductivity is enhanced using an infiltration technique as the one described above, is to understand how the storage material behaves when it is subject to a thermal gradient. In what follows we explain the problem used to model the thermal behavior of the PCM, in the surrounding material and the exchanges at the interface separating both materials.

1.2 Problem formulation

We consider the problem of heat transfer, at the macroscopic scale, in a porous media consisting of a graphite foam matrix filled with a phase change material for latent heat storage applications. In these applications, a heat transfer fluid is used to conduct the heat from the solar field to the tank containing the composite media. The high temperature of the heat transfer fluid leads to a change in state of the PCM whilst a graphite foam matrix is used, as explained above, due to its high thermal conductivity to accelerate the phase change process and as a consequence reduce the charging/discharging times. Thus in order to understand the heat transfer in the composite media one needs to address two different sub-problems: a heat conduction problem in the graphite foam matrix and a heat conduction problem with phase change in the PCM. In addition, a contact resistance condition at the interface between the two components of the composite media, resulting from a difference in physical properties as well as the heat flow from one material to another, is to be taken into account.

In this section, we start by presenting the mathematical model for the heat conduction problem with phase change for a homogeneous PCM. Later we present the model for the heat conduction problem in the graphite foam matrix as well as the contact resistance condition at the interface between the graphite foam matrix and the PCM.

1.2.1 The phase change problem

There are several mechanisms at work when a solid melts or a liquid solidifies. Such a change of phase involves heat (and often also mass) transfer, possible supercooling, absorption or release of latent heat, changes in thermophysical properties, surface effects, etc [3]. In this section we give an overview of these phenomena and we give the formulation of the problem as well as the assumptions leading to this formulation.

1.2.1.1 An overview of the phenomena involved in a phase change process

Both solid and liquid phases are characterized by the presence of cohesive forces that keep atoms in close proximity. In a solid the molecules vibrate around fixed equilibrium positions, while in a liquid they are free to move between these positions. The macroscopic manifestation of this vibrational energy is what we call heat or thermal energy. Clearly atoms in the liquid phase are more energetic than those in the solid phase, all other quantities being equal. Thus before a solid can melt it must acquire a certain amount of energy to overcome the binding forces that maintain its solid structure. This energy is referred to as the latent heat of fusion of the material and represents the difference in enthalpy levels between liquid and solid states, all other things being equal. Of course, solidification of liquid requires the removal of this latent heat and the structuring of atoms into more stable lattice positions [3].

There are three possible modes of heat transfer in a material: conduction, convection and radiation. Conduction is the transfer of kinetic energy between atoms by any of a number of ways, including collision of neighboring atoms and the movement of electrons; there is no flow or mass transfer of the material. This is how heat is transferred in an opaque solid. In a liquid heat can also be transferred by a flow of particles, i.e. by convection. Radiation is the only mode of energy transfer that can occur in a vacuum (it requires no participating medium) [3].

The phase-transition region where solid and liquid coexist is called the interface. Its thickness may vary from a few Angstroms to a few centimeters, and its microstructure may be very complex, depending on several factors (the material itself, the rate of cooling, the temperature gradient in the liquid, the surface tension, etc.). In some cases, typically resulting from supercooling, or presence of multiple components (e.g. in binary alloys), the phase transition region may have apparent thickness and is referred to as a "mushy zone"; its microstructure may now appear to be dendritic or columnar. For other cases such as pure materials solidifying under ordinary freezing conditions at a fixed temperature, the interface appears (locally) planar and of negligible thickness. Thus, it may be thought of as a sharp front, a surface separating solid from liquid at the freezing temperature [3].

During the phase change, most thermophysical properties of a material (usually varying smoothly with temperature) undergo more or less sudden changes at the melting temperature. For example the heat capacity of aluminum changes by 11% at its melt temperature (of $659°C$), but that of silicon changes by only 0.3% (at $1083°C$). Such discontinuities in thermophysical properties complicate mathematical problems because they induce discontinuities in the coefficients of differential equations [3].

It is also possible to observe a variation in the density during the phase change. Typical density changes upon freezing or melting are in the range of 5% to 10% but can be as high as 30%. For most materials the solid is denser than the liquid, resulting in possible formation of voids in freezing or breaking of the container in melting. On the other hand water expands on freezing, resulting in broken pipes on cold days and ice floating instead of filling the bottom of the oceans. The density variation with temperature induces flow by natural convection in the presence of gravity, rapidly equalizing the temperature in the liquid and greatly affecting heat transfer [3].

1.2.1.2 Assumptions

In this thesis we are focusing on pure materials where the latent heat $\boldsymbol{L}$ is assumed to be constant and the effects of supercooling and nucleation difficulties are not present. We assume the change in phase to occur at a constant temperature $\boldsymbol{T_m}$ which is a very reasonable assumption for pure materials. We assume the heat transfer to be only made by conduction and in order to avoid the movement of the liquid part, the density changes during the phase change are ignored. We also assume the specific heat and the thermal conductivities to be phase-wise constant. With these assumptions the problem is called

the Stefan problem in reference to the work of Jozef Stefan in the 1890's on solid-liquid phase change.

1.2.1.3 Classical Formulation

The two-phase Stefan problem can be modeled using a heat conduction equation in each phase in addition to a jump condition at the interface called the Stefan condition. This condition is derived from the global energy balance in both phases [3]. Consider, for example, a semi-infinite slab $0 \leq x < \infty$, initially solid at a uniform temperature $\boldsymbol{T_0} \leq \boldsymbol{T_m}$ where $\boldsymbol{T_m}$ is the melting temperature of the material. At $x = 0$ the temperature is increased to a value greater than the melting temperature $\boldsymbol{T_1} > \boldsymbol{T_m}$. We assume that no internal heating sources are present in the material. An illustration is given in figure1.2. The mathematical formulation can be written as
in the liquid region:

$$\frac{\partial T_L}{\partial t} = \alpha_L \frac{\partial^2 T_L}{\partial x^2}, \qquad 0 < x < X(t), \quad t > 0 \tag{1.1}$$

in the solid region:

$$\frac{\partial T_S}{\partial t} = \alpha_S \frac{\partial^2 T_S}{\partial x^2}, \qquad X(t) < x, \quad t > 0 \tag{1.2}$$

interface temperature:

$$T(X(t),t) = T_m, \quad t > 0 \tag{1.3}$$

Stefan condition:

$$\rho L \frac{dX(t)}{dt} = -\kappa_L \frac{\partial T}{\partial x}(X(t),t) + \kappa_S \frac{\partial T}{\partial x}(X(t),t), \quad t > 0 \tag{1.4}$$

initial conditions:

$$T(x,0) = T_0 < T_m, \quad x > 0, X(0) = 0 \tag{1.5}$$

boundary conditions:

$$T(0,t) = T_1 > T_m, \quad lim_{x\to\infty} T(x,t) = T_0, \quad t > 0 \tag{1.6}$$

where T denotes the temperature, t is time, x is the spatial coordinate, and L , ρ , X, κ, and α are latent heat of fusion, density, interface location, conductivity, and diffusivity, respectively. Subscripts, L and S, refer to the liquid and the solid, respectively.

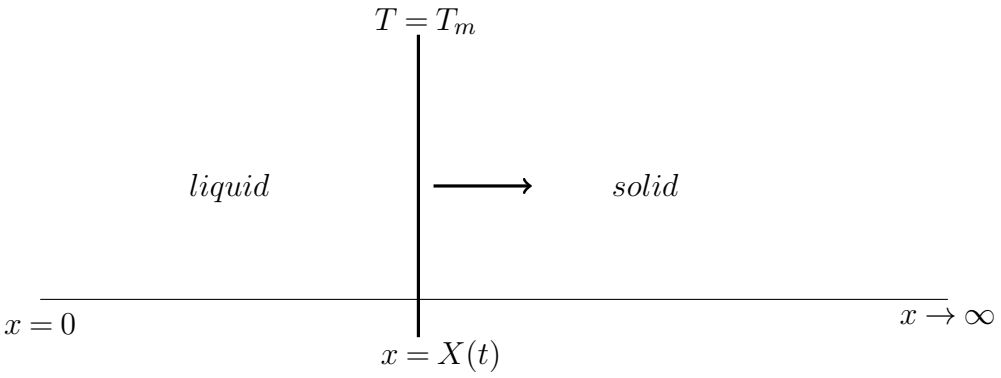

FIGURE 1.2: Domain with phases

This problem is referred to as the two-phase Stefan problem because both phases are active since the solid temperature is taken smaller then the melting temperature. For $T_S = T_m$ only the liquid phase is active and the problem is referred to as the one-phase Stefan problem.

The Stefan-type problems are moving boundary problems since the position of the interface separating the solid-region and the liquid-region is an unknown and is part of the solution to be found. This geometric non-linearity is the source of mathematical difficulties that moving boundary problems present [3].

In 1947, Rubinstein proved the local solvability, meaning there exists a time up to which a unique classical solution exists, of general 1-dimensional Stefan problems (see [81] for a historical survey of the mathematical development up to the mid 1960's). However, the well-posedness, meaning there exists a unique classical solution depending continuously on the data, without undue restrictions on the data was established only during the mid 1970's [17][3].

Classically formulated 1-dimensional Stefan problems may admit, under some restrictive conditions, exact solutions all of which are of similarity type. This is only the case if the following conditions are met : semi-infinite domain, constant phase-wise constant thermo-physical properties [3]. These exact solutions are often used to validate numerical methods as will be the case in the third chapter of this thesis.

Stefan-type problems can also be formulated classically in two or three dimensions but such formulations may admit no (classical) solution. Even one-dimensional problems with either internal sources or a variable fusion temperature may develop mushy regions rendering the above sharp-front classical formulation inappropriate [3]. Fortunately weak

or generalized (enthalpy) formulations, which are well-posed (and computable), came to the rescue in the early 1960's.

1.2.1.4 Enthalpy formulation

The enthalpy formulation is based on the concept of weak solutions. It was in the 1800's that David Hilbert introduced the idea of generalized solutions to PDE's, in the context of the classical Dirichlet problem for the Laplace equation, to weaken the continuity conditions for the solutions of PDE's and their derivatives up to the order of the PDE. These ideas where later developed in the 1930's an 1940's leading to the concepts of weak derivatives ans weak solutions within the frame work of Sobolev spaces. However, the development of a mathematical theory for Stefan problems started only fifty years after the original work of C. Neumann and Stefan due to there highly non-linear nature. The weak reformulation of the Stefan problem was first introduced in 1958 by S. Kamin and Oleinik [68] while enthalpy-based methods were already used in heat transfer and computing literature in the 1960's. The well-posedness of the weak solution of multidimensional Stefan problems was established in 1968 by Friedman [33](for more details on the historical background of this method see [3]).

The idea of the enthalpy approach is based on the fact that the energy conservation law, expressed in terms of enthalpy and temperature, together with the equation of state contain all the physical information needed to determine the evolution of the phases [3]. To explain how the method works we consider a time invariant unite volume V, ∂V its boundary and $-\vec{q}.\vec{n}$ is the heat flux into the volume V across its boundary ∂V and where $\vec{n}$ is the outgoing unit normal to ∂V. With the assumptions listed in section 1.2.1.2 in mind, we write the energy conservation over the volume V and over a random time interval $[t, t+\Delta t]$

$$\int_t^{t+\Delta t} \frac{\partial}{\partial t}\left(\int_V H \; dV\right)dt = \int_t^{t+\Delta t} \int_{\partial V} -\vec{q}.\vec{n} \; dS \; dt \tag{1.7}$$

where H is the energy(enthalpy) density per unite volume. We know that the heat flux is a vector pointing in the direction of heat flow and given by Fourier's law :

$$\vec{q} = -\kappa \vec{\nabla} T \tag{1.8}$$

where κ is the conductivity of the material, that we assume to be constant, and T the temperature. Using this definition of the flux equation (1.7) becomes

$$\int_t^{t+\Delta t} \frac{\partial}{\partial t}(\int_V H \; dV)dt = \int_t^{t+\Delta t} \int_{\partial V} \kappa \vec{\nabla} T.\vec{n} \; dS \; dt \tag{1.9}$$

Using the Divergence Theorem we obtain the general heat conduction equation

$$\partial t H - div(\kappa \nabla T) = 0 \tag{1.10}$$

The enthalpy H may be defined as the sum of sensible and latent heat

$$H(T) = \int_0^T \rho C dT + \rho f(T) L \tag{1.11}$$

where L is the latent heat of fusion and f is the liquid fraction and C is the specific heat. In the case of pure materials where the phase change occurs at a constant temperature T_m the liquid fraction is given by

$$f(T) = \begin{cases} 0, & T(x,t) < T_m \\ 1, & T(x,t) \geq T_m \end{cases} \tag{1.12}$$

Since we assume C to be phase-wise constant and ρ to be constant and not effected by the phase change, the enthalpy of the liquid and solid, for a pure material can be calculated from (1.11) as

$$H(T) = \begin{cases} \rho \int_{T_0}^{T} C_S dT, & T(x,t) < T_m \\ \rho(\int_{T_0}^{T_m} C_S dT + \int_{T_m}^{T} C_L dT + L), & T(x,t) \geq T_m \end{cases} \tag{1.13}$$

$$= \begin{cases} \rho C_S (T - T_0), & T(x,t) < T_m \\ \rho(C_S(T_m - T_0) + C_L(T - T_m) + L), & T(x,t) \geq T_m \end{cases} \tag{1.14}$$

where T_0 is the temperature of the material at the initial state.
Note that the main advantage of this formulation of the problem over the classical one is the fact that the position of the interface separating the liquid phase and the solid phase is not brought out explicitly as an unknown of the problem and is determined a-posteriori using the values of the temperature. This makes the enthalpy formulation more general than the classical formulation since the hypothesis of the phase change occurring at a constant temperature is no longer taken in consideration which allows for mushy regions.

As one can see in equation (1.13)-(4.11) the enthalpy exhibits a jump at the points where $T(x,t) = T_m$ which rises the questions of the meaning of the derivative $\partial_t H$ and in some cases this jump may also provoke some numerical instabilities. In order to overcome this difficulties we use a linearized expression of the enthalpy using a linearized expression for the liquid fraction.

Linearized enthalpy

Several expressions have been used in literature in order to approach the expression of the enthalpy given by equation (1.13) with a jump at the melting point T_m by an equivalent and smoothed one all of which are based on a linearized liquid fraction.
In [94] the liquid fraction defined by (1.12) is replaced by a smoothed function defined by

$$f(T) = \begin{cases} 0 & T < T_m - \epsilon \\ \frac{T - T_m + \epsilon}{2\epsilon} & T_m - \epsilon \leq T \leq T_m + \epsilon \\ 1 & T > T_m + \epsilon \end{cases} \tag{1.15}$$

where ϵ is half the size of the regularization interval.
In [48] the following expression is used

$$f(T) = \frac{1}{2} + \frac{1}{2} tanh(\frac{T - T_m + \epsilon}{2\epsilon}) \tag{1.16}$$

In [62] the liquid fraction is smoothed using an expression based on the normal distribution:

$$f(T) = exp(\frac{-(T - T_m)^2}{2\epsilon^2}) \tag{1.17}$$

Each of this expressions has its utility. In some of the numerical schemes that we use to solve the enthalpy problem, one needs to use the expression of the inverse of the enthalpy function. Using the first expression used in [94] will allow to determine the analytical expression of the inverse of the enthalpy. For this expression of the liquid fraction the linearized enthalpy is given by

$$H(T) = \begin{cases} \rho C_S T & T < T_m - \epsilon \\ \rho C_S (T_m - \epsilon) + \rho (C_\epsilon + \frac{L}{2\epsilon})(T - T_m + \epsilon) & T_m - \epsilon \leq T \leq T_m + \epsilon \\ \rho C_L T + \rho (C_S - C_L) T_m + \rho L & T > T_m + \epsilon \end{cases} \tag{1.18}$$

where

$$C_\epsilon = \frac{C_S + C_L}{2}$$

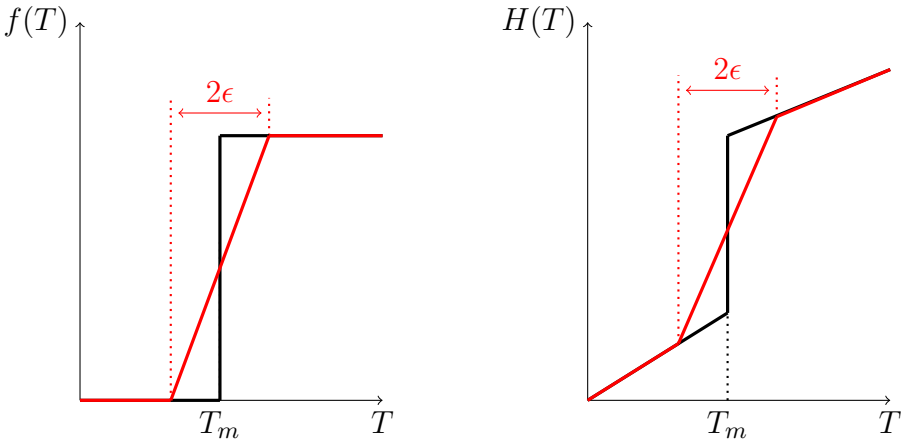

FIGURE 1.3: The liquid fraction for pure materials in black and linearized liquid fraction in red(left). The enthalpy for pure materials in black and linearized enthalpy in red(right).

1.2.1.5 Overview of numerical methods for the phase change problems

In early years, analytical methods were the only means available to provide a mathematical understanding of physical processes involving the moving boundary [45]. Unfortunately, analytical solutions of the Stefan problem exist only for very special cases which are mainly one-dimensional with infinite or semi-infinite region and simple initial and boundary conditions and constant thermal properties [20]. However, this is rarely the case for solidification and melting problems arising from practical applications. For example, in latent heat thermal energy storage the problem is rarely one dimensional and sometimes one has to deal with multiple fronts and extended mushy regions. Luckily, with the rise of high-speed digital computers, several numerical methods were developed in order to provide a broad understanding of the practical processes involving Stefan type problems [45]. All these methods can be classified into two main groups, the front tracking methods and the fixed grid methods [46].

The front tracking methods

The classically formulated Stefan problem is a numerically challenging problem due to its underlying geometrical nonlinearity : the regions in which the two heat conduction equations are valid change in time, and we have to compute the location of the interface

concurrently. The numerical methods used to solve the problem with the classical formulation are referred to as the front tracking methods since they aim to explicitly track the interface using the Stefan condition [3]. There are several approaches to accurately determine the location of the interface at each time step.
In [28] Douglas and Gallie presented a technique based on the idea of using a uniform spatial grid but a non-uniform time step such that the moving boundary coincides with a grid line in space at every time step. This techniques are referred to as the interface fitting methods or variable time step methods.
Another group of front tracking methods are deforming (dynamic) grid methods which are based on the idea of continuously deforming the space grid to always ensure that a line of specified node points lies on the phase change front. In this way, the Stefan heat balance condition, Eq. (1.4), can be easily satisfied and the movement of the front readily tracked [94].
For more details on these techniques the reader is referred to [3], [62], [45], [94], [27].
The major drawback of the front tracking techniques is in the way the front position is determined. In fact all the front tracking methods based on the classical formulation of the Stefan problem are based on the hypothesis that the phase change occurs at a single point which make these methods unsuitable to solve problems where the phase change occurs over an interval. Also, for these methods to provide good results one need to adapt the mesh around the interface location to insure that at all times there are grid points on the interface. This becomes very complex and time consuming when the problem is not one-dimensional and where there is a mushy region.

The fixed grid methods

The above mentioned drawbacks of front tracking methods can be overcome with the numerical methods based on the enthalpy formulation given by equation(1.10). In fact, in this formulation the Stefan condition at the interface is incorporated implicitly in the equations thus avoiding the difficulty of tracking the position of the interface over time. Following this, the position of the front is determined a posteriori using the temperature. In the following we will give an overview of the most significant among these methods.

The Apparent heat capacity

For this class of methods the main unknown is the temperature and the main idea is to

modify Equation 1.10 in order to have a heat transfer equation in the following form :

$$\rho C_{app}\frac{\partial T}{\partial t} - \nabla.(\kappa \nabla T) = 0$$

Where C_{app} is an equivalent heat capacity that is used to account for the latent heat effect. Comini and al. [25] determined C_{app} as the average local temperature gradient which in three dimensions is given by the following equation

$$C_{app} = \frac{1}{3}(\frac{\partial H/\partial T}{\partial x} + \frac{\partial H/\partial T}{\partial y} + \frac{\partial H/\partial T}{\partial z})$$

This expression has later been modified by Morgan and al. [59] and Lemon [55] to improve the convergence of the method. Another method that calculates C_{app} as the exact derivative of the enthalpy with respect to the temperature was proposed by Cleland and al. [24]. For cases where the change in phase occurs at constant temperature, these methods require a very small time step in order to ensure that every node undergoes the phase change. However this is no longer an issue for cases where the phase change occurs over an interval of time or in cases where a smoothing interval is introduced as in Equation 1.15. These methods are called space averaging [70] since they give an approximation of the apparent heat capacity with means of space derivatives of the temperature and/or the enthalpy. On the other hand, time averaging methods calculate the apparent heat capacity using the values of the enthalpy and the temperature at previous times steps. An example of such approximation is given by Morgan and al. [59].

The enthalpy linearization

Here the enthalpy is the main unknown, at each time step Equation 1.10 is solved and the temperature is calculated using the inverse of the enthalpy. This method was suggested by Atthey [9] and later Voller [94] gave an iterative version of this method where at each time step an iterative process is used to update the enthalpy using the corresponding value of the temperature solution to Equation 1.10. After this step the temperature is updated using the new value of the enthalpy. This loop is set to stop when the difference between two values of the enthalpy at two consecutive iterations becomes very small. This process insures that the enthalpy and temperature calculated verify the enthalpy equation at a each time step. Voller shows in [94] that the non-iterative enthalpy scheme performs exactly as an apparent heat capacity scheme. However, this method is well adapted to solve problems where the phase change occurs over an interval and where a

mushy zone appears between the two phases.

The source update method
The main idea of this method is to use the expression of the enthalpy and to pass the non-linear part as a source term in Equation 1.10. The main unknown becomes the temperature and the liquid fraction at the previous time step is used to solve the equation. An iterative procedure is used to update the liquid fraction using the temperature at each time step. This is explained in details in chapter 4. This method was first proposed by Voller [94]. A similar method was proposed by Rolph and Bathe [79] and Roose and Storrer [80] where a fictitious heat source is used to account for the latent heat effect.

1.2.2 Heat conduction in the Graphite foam matrix

In the Graphite foam matrix we have a pure conduction problem without phase change that is modeled by the following equation [20]

$$\rho c \frac{\partial T}{\partial t} = div(\kappa \nabla T) \tag{1.19}$$

where T is the temperature, ρ is the density, c the specific heat capacity and κ the thermal conductivity of the matrix.

1.2.3 Thermal boundary resistance

A temperature drop occurs when heat flows through an interface between two components of a composite media. This discontinuity in the temperature field is described using the thermal resistance which is known as interfacial thermal resistance and is the result of two phenomena. The first is the thermal resistance observed when two components are in contact as a result of poor mechanical and chemical bounds between the components. The second is when there is a discontiuity in the thermal property of the components of the material such as the thermal conductivity. The interfacial thermal resistance is defined as the ratio of temperature discontinuity $[T]$ at the interface to the heat rate flowing across the interface between two phases in contact, according to the equation [74]:

$$R = [T]/Q \tag{1.20}$$

using the definition of the thermal heat flux per unit area A given by :

$$Q/A = \kappa \partial_n(T) \tag{1.21}$$

where κ is the thermal conductivity, at the interface between the materials of the composite domain, hence we have

$$R = [T]/(\kappa \partial_n(T)) \tag{1.22}$$

In addition to the thermal boundary resistance condition on the interface we have the continuity of the heat flux at all times given by the following equation:

$$[\kappa \partial_n T] = 0 \tag{1.23}$$

1.2.4 The heat conduction problem with phase change in a composite media

Now we have all the elements to write the model for the heat conduction problem in a composite media with a graphite matrix foam infiltrated by a PCM such as salt for example. To be more specific consider a sample of this composite material filling a connected bounded domain Ω in $\mathbb{R}^d$, $d = 2$ *or* 3 with a Lipschitz-continuous boundary $\partial\Omega$ and we set:

$$\Omega_G = \Omega \setminus \overline{\Omega}_S, \qquad \gamma = \partial\Omega_S. \tag{1.24}$$

The indices S and G call to mind salt and graphite. We consider also that the boundary $\partial\Omega$ is the disjoint union of two parts, Γ_D and Γ_N. In this geometry, the differential system we intend to deal with is the unsteady heat conduction problem with phase change. The unknown is the temperature T of the medium that satisfies therefore

$$\begin{cases} \partial_t H(T) - \operatorname{div}(\kappa \nabla T) = g & in\ \Omega_S \cup \Omega_G, \\ [\kappa \partial_n T] = 0 & on\ \gamma, \\ R(\kappa \partial_n(T)|_{\Omega_S}) = [T] & on\ \gamma, \\ T = T_D & on\ \Gamma_D. \\ \kappa \partial_n T = 0 & on\ \Gamma_N. \end{cases} \tag{1.25}$$

Where $\boldsymbol{n}$ is the unit normal vector to $\partial\Omega$ exterior to Ω and also to γ exterior to Ω_S, $[\cdot]$ is the jump through γ, equal to the value on Ω_G minus the value on Ω_S. The temperature T, the conductivity κ, the density ρ and the specific heat capacity c are discontinuous through

γ. The parameter R represents the thermal resistance at the interface γ introduced in section 1.2.3. The heating data are the source g and the external temperature T_D.
$H(T)$ is the enthalpy function in the composite and is defined by

$$H(T) = \begin{cases} \rho_S c_S T_S + \rho_S L f(T) & \text{in } \Omega_S \\ \rho_G c_G T_G & \text{in } \Omega_G. \end{cases}$$

Note that only one equation is needed to model the conduction problem for both materials, this is made possible thanks to the enthalpy method presented in section 1.2.1.4 which allow for the phase change problem to be modeled by one equation for both phases and where the nonlinearity is taken into account in the expression of the enthalpy function.

1.3 Objective and outline of the thesis

The goal of this thesis is to develop a numerical tool that allow to solve the unsteady heat conduction problem in a composite media with a graphite foam matrix infiltrated with a phase change material such as salt, described by the system (1.25), in the framework of the latent heat thermal energy storage.

We started by studying the steady heat conduction problem in the composite media. Two Finite element methods are proposed in the first chapter in order to solve this problem: a Lagrange finite element method and the hybrid dual Raviart-Thomas finite element method. The reason behind choosing to focus on the simpler model of the steady heat conduction is because this allow to focus on the main theoretical and numerical difficulties, such as the well-posedness of the problem and also the a-priori error estimate of the methods, that we might encounter when we consider the whole unsteady conduction problem with phase change described by the system (1.25). The work presented in this chapter has been published in the *Journal of Scientific Computing* [10].

The phase change materials that we study here are manly pure materials and as consequence change phase at a single point the melting temperature. This introduces a jump in the liquid fraction and consequently in the enthalpy. This discontinuity represents an additional numerical difficulty that we propose to overcome by introducing a smoothing interval around the melting temperature. This is explained in chapter 3 where an analytical and numerical study gives how the errors on the moving boundary's position and on the temperature behave with respect to the width of the smoothing interval. This chapter has been published in *Communications in Mathematical Sciences* [58].

The next step is to determine a suitable time discretization scheme that allow to handle the non-linearity present in the model as consequence of the change in phase of the salt. For this purpose we present in the third chapter four of the most used numerical schemes to solve the non-linear phase change problem : the update source method, the enthalpy linearization method, the apparent heat capacity and the Chernoff method. In this chapter various numerical tests are conducted in order to test and compare these methods for various type of problems. The results show that the Chernoff scheme is faster and gives comparable results to the ones given by the enthalpy linearization and the apparent heat capacity.

Finally we use the Chernoff method combined with the Raviart-Thomas finite element method to solve the non-linear heat conduction problem in a composite media with a phase change material. The simulations are realised using 2D-cuts of X-ray images of two real graphite matrix foams infiltrated with a salt. The aim of these simulations is to

determine if the studied composite materials could be assimilated to an equivalent to a homogeneous phase change material.

Chapter 2

Finite element methods for the steady state heat conduction problem in composite media with contact resistance

In this chapter we consider the steady state heat conduction problem inside a composite medium. As explained in the previous chapter, the temperature field is discontinuous at the interface between the constitutive materials as a consequence of a contact resistance condition. These transmission conditions need to be handled carefully and efficiently. Our main concerns are accuracy and feasibility. Hybrid dual formulations are recommended here as the most popular mixed finite elements well adapted to account for the discontinuity of the temperature field. We therefore write the discretization of the steady state heat conduction problem by mixed finite elements and perform its numerical analysis. Of course, applying Lagrangian finite elements is possible in simple composite media but it turns out to be problematic for complex geometries. Nevertheless, we study the convergence of this finite element method to highlight some particularities related to the model under consideration and point out the effect of the contact resistance on the accuracy. Illustrative numerical experiments are finally provided to assess the theoretical findings.

2.1 Introduction

We study the thermal behavior of a composite media subject to a temperature gradient in the framework of latent heat thermal energy storage. The composite media consists in a graphite foam matrix with high thermal conductivity infiltrated with a phase change material such as salt. The unsteady heat conduction problem in the composite, presented in chapter 1, is described by the system of equations (1.25). After the time discretization scheme is applied to this system, one is left with a quasi-stationary problem that is modeled by a similar system of equations as (1.25) and where the first equation is replaced by

$$\lambda H(T) - \mathrm{div}(\kappa \nabla T) = g.$$

where λ is a parameter that depends on the time discretization scheme. For the backward Euler method, for example, λ is equal to the inverse of the time step. Since our aim in this chapter is to describe two finite element methods to solve this type of problems and the error analysis for these methods, we restrict our study to the steady state problem, where $H(T) = 0$ in the above equation, which already contains all the specific difficulties one may encounter either in the theoretical or in the numerical grounds. To present the steady state problem we recall the notations used in Chapter 1. We consider a connected bounded domain Ω in $\mathbb{R}^d$, $d = 2$ or 3, with a Lipschitz-continuous boundary $\partial\Omega$, ω_i a finite number of connected sub-domains, called "pores", such that each $\overline{\omega}_i$ is contained in Ω, and the intersection of $\overline{\omega}_i$ and $\overline{\omega}_j$ for $i \neq j$ is empty. We set:

$$\Omega_S = \cup_i \omega_i, \qquad \Omega_G = \Omega \setminus \overline{\Omega}_S, \qquad \gamma = \partial\Omega_S = \cup_i \partial\omega_i. \tag{2.1}$$

The indices S and G stand for salt and graphite. The boundary $\partial\Omega$ is the disjoint union of two parts, Γ_D and Γ_N, Γ_D and Γ_N are union of a finite number of connected components and Γ_D has a positive $(d-1)$-measure. In this geometry, the differential system we intend to deal with is the steady heat transfer boundary value problem. The unknown, the temperature T of the medium, satisfies therefore

$$\begin{cases} -\mathrm{div}(\kappa \nabla T) = g & in\ \Omega_S\ \Omega_G, \\ [\kappa \partial_n T] = 0 & on\ \gamma, \\ R(\kappa \partial_n (T)|_{\Omega_S}) = [T] & on\ \gamma, \\ T = T_D & on\ \Gamma_D. \\ \kappa \partial_n T = 0 & on\ \Gamma_N. \end{cases} \tag{2.2}$$

Where $\boldsymbol{n}$ is the unit normal vector to $\partial\Omega$ exterior to Ω and also to γ exterior to Ω_S. The symbol $[\cdot]$ is the jump through γ, equal to the value on Ω_G minus the value on Ω_S. Indeed, the temperature is likely discontinuous through γ. The parameter R represents the thermal resistance at the interface γ and κ is the thermal conductivity. The heating data are the source g and the external temperature T_D.

We consider here the finite element discretization of problem (2.2). The choice of the method to use is tightly dependent on the geometry of the composite medium. In simple configurations like the one depicted in Figure 2.1(left part), users may apply the Lagrangian finite element method after introducing substantial modifications. The continuity is actually prescribed in each component Ω_S and Ω_G while jumps are allowed across the interfaces. The construction of the finite element space is therefore expected to account for this fact : local continuity/global discontinuity. The implementation should be made so to manage these two levels and may be troublesome. The difficulties can possibly be controlled by some domain decomposition procedures. Nonetheless, it turns out to be a pain in the neck in complicated geometry as is the case for densely composite media. We provide an illustration in the right part of Figure 1. Programming such a method and finding suitable solvers become tedious.

An attractive alternative is offered by hybrid dual formulations as they bring about

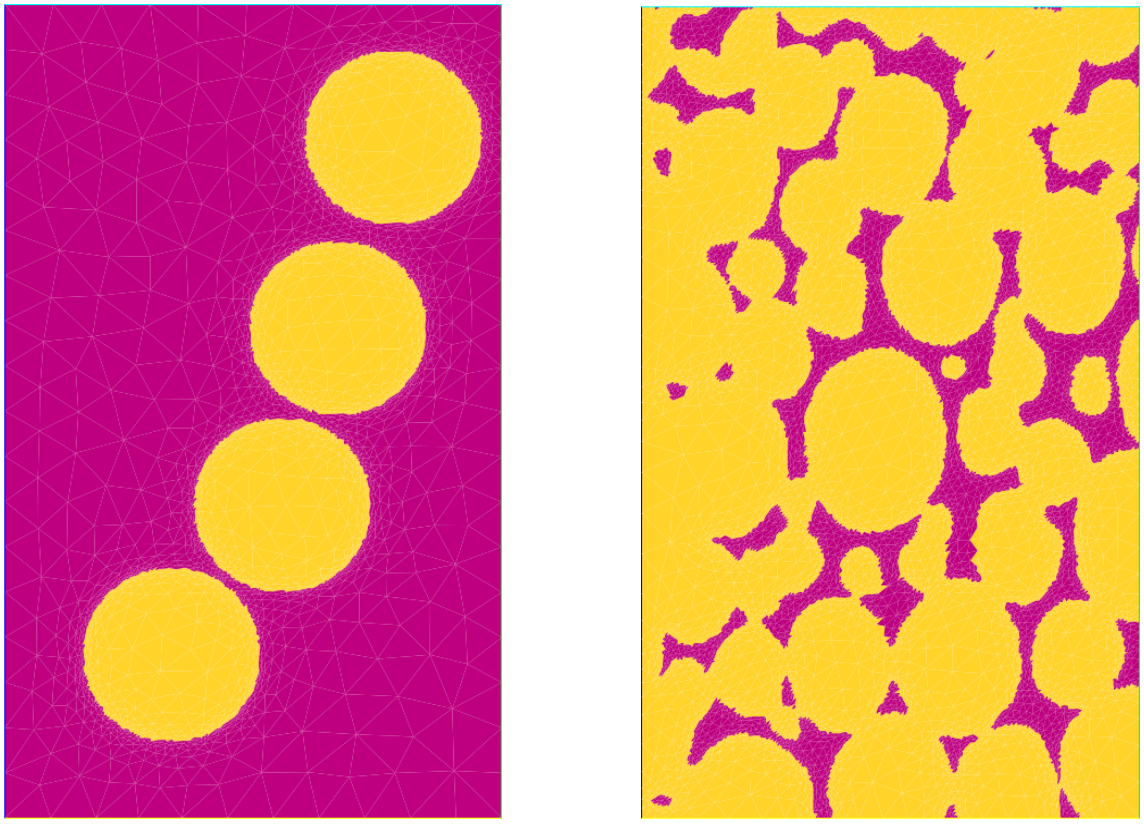

FIGURE 2.1: Two examples of composite media.

substantial advantages (see [77], [15]). The most important is that the construction of discrete spaces based on the mixed finite elements is natural and follows exactly the standard hybrid dual problem where the temperature field is continuous, i.e. $R = 0$. Conditions of contact resistance at the interfaces are naturally accounted for in the mixed variational formulation. Hybrid Dual Finite Element Software can easily be enriched to handle the problem we deal with here. The foundations of the finite elements library are not affected. Discontinuous Galerkin finite elements enjoy the similar properties as hybrid dual finite elements (see [7]). They can be used as well to solve problem (2.2). The cost is reduced to some suitable modifications to introduce on the variational problem. The structure of the finite elements should not be changed in softwares dedicated to elliptic problems.

The primary objective of this chapter is the description of both finite element methods and to conduct a numerical analysis for each of them. The outline of this chapter is as follows.

- In Section 2.2, we write the variational formulation of the problem and prove its well-posedness. The functional space fitting the problem is the broken Sobolev space. We consider also the hybrid dual variational model. The functional spaces currently used in the hybrid dual context allows jumps on the temperature field. They are not changed. We show how to take into account the interface conditions in the variational form. Before closing we conduct a brief discussion about the regularity of the solution and especially on the effect of the transmission conditions on the singularities born at the interfaces.

- Two finite element discretizations are proposed and analyzed for both variational problems in Sections 2.3 and 2.4, respectively. Using Aubin-Nitsche method together with a bootstrapping argument enables us to prove a local super-convergence result in the most interesting configurations.

- In Section 2.5, we present a few numerical experiments to assess the theoretical findings.

2.2 Variational formulations and well-posedness

The finite element method is not based on the strong form given by (2.2), but rather a minimization statement or, more generally, a weak formulation which allow to naturally account for the boundary conditions and allow for a more natural way to construct the

function spaces. This approach also give solid mathematical foundation and make the error analysis more systematic. We must thus develop and understand these formulations before proceeding with the finite element method. In order to write the weak formulation we need to give the functional framework in which we will work.

2.2.1 The Functional Framework

In this section we introduce the notation and review some useful results (without proofs) concerning the Sobolev spaces and the theory of distributions. For a more detailed introduction on to Sobolev spaces and the theory of distributions, we refer to [7, Chapter 3][56, Chapter 1].
We first denote by $L^2(\Omega)$ the space of real valued measurable functions which are square integrable on Ω with respect to the Lebesgue measure :

$$L^2(\Omega) = \{u : \Omega \mapsto \mathbb{R}, \quad \int_\Omega |u|^2 < \infty\}.$$

It is a Hilbert space with the scalar product defined by

$$(u, v)_{L^2(\Omega)} = \int_\Omega u(x)v(x)\ dx.$$

The associated norm is given by $\|u\|_{0,\Omega} = (u, u)^{1/2}_{L^2(\Omega)}$.
Given a multi-index for the derivative order $\alpha = (\alpha_1, ..., \alpha_n) \in \mathbb{N}^n$, we set :

$$D^\alpha v = \frac{\partial^{|\alpha|} v}{\partial x_1^{\alpha_1} ... \partial x_n^{\alpha_n}}, \quad \text{with } |\alpha| = \alpha_1 + ... + \alpha_n.$$

We introduce $\mathscr{D}(\Omega) = C_0^\infty(\Omega)$ as the space of infinitely differentiable functions with compact support. A distribution on Ω is a linear form m defined on $\mathscr{D}(\Omega)$, which is "continuous" in the following sense: for all sequence $(\varphi_n)_{n\in\mathbb{N}}$ converging to $\varphi \in \mathscr{D}(\Omega)$, we have : $m(\varphi_n) \mapsto m(\varphi)$, when $n \mapsto +\infty$.
We recall that the convergence in $\mathscr{D}(\Omega)$ is defined in the following way : $\varphi_n \mapsto \varphi$ in $\mathscr{D}(\Omega)$ if there exists a compact set $K, K \subset \Omega$, containing the support of φ and all the supports of the function φ_n, and if , for any $\alpha \in \mathbb{N}^n$, $D^\alpha \varphi_n$ converges uniformly on K to $D^\alpha \varphi$.
We denote by $\mathscr{D}'(\Omega)$ the set of distributions on Ω and by $< ., . >$ the duality bracket between the spaces $\mathscr{D}'(\Omega)$ and $\mathscr{D}(\Omega)$. If $m \in \mathscr{D}'(\Omega)$, we can define its derivative of any

order $\alpha \in \mathbb{N}^n$; it is the distribution, denoted by $D^\alpha m$, defined by :

$$\forall \varphi \in \mathscr{D}(\Omega),\ \ < D^\alpha m, \varphi >= (-1)^{|\alpha|} < m, D^\alpha \varphi > .$$

For any $s \geq 0$ we define the Sobolev space $H^s(\Omega)$ as follow

$$H^s(\Omega) = \{v \in L^2(\Omega) / \ \partial^\alpha(\Omega) \in L^2(\Omega)\ \forall \alpha = (\alpha_1, ..., \alpha_n) \in \mathbb{N}^n,\ |\alpha| = \alpha_1 + ... + \alpha_n \leq s\}$$

The partial derivative here are defined in the sense of distributions.
By extension, we can see that $H^0(\Omega) = L^2(\Omega)$.
For $s = 1$, $H^1(\Omega)$ is a Hilbert space with the scalar product defined by

$$(u, v)_1 = \int_\Omega u\ v + \sum_{i=1}^{n}\ \int_\Omega \partial_{x_i}\ \partial_{x_i} v = (u, v)_0 + \sum_{i=1}^{n} (\partial_{x_i} u, \partial_{x_i} v)$$

The associated norm is given by $\|u\|_{1,\Omega} = (u, u)_1^{1/2}$. We define a scalar product for $H^s(\Omega)$

$$(u, v)_s = \sum_{|\alpha| \leq m} (\partial^\alpha u, \partial^\alpha v)_0$$

and the associated norm

$$\|u\|_s = (u, u)_s^{1/2}$$

It is known that $H^s(\Omega)$ with the scalar product $(.,.)_s$ is a Hilbert space. We denote by $H_0^s(\Omega)$ the closure of $\mathscr{D}(\Omega)$ in $H^s(\Omega)$
We need to define the trace on $\partial\Omega$ for functions belonging to Sobolev spaces. We introduce the space $\mathscr{D}(\bar{\Omega})$ of restrictions in Ω of functions belonging to $\mathscr{D}(\mathbb{R}^n)$. Since we suppose Ω to be bounded with a Lipschitz-continuous boundary[37] we have that $\mathscr{D}(\bar{\Omega})$ is dense in $H^1(\Omega)$, which allows us to define, by density arguments, a trace operator.

Theorem 2.1. *There exists a continuous linear mapping $\gamma_0 : H^1(\Omega) \mapsto L^2(\partial\Omega)$, such that for all $v \in \mathscr{D}(\bar{\Omega})$, $\gamma_0(v) = v|\partial\Omega$. The kernel of this mapping is the space $H_0^1(\Omega)$ and its image, denoted by $H^{1/2}(\partial\Omega)$, is dense in $L^2(\partial\Omega)$. Conversely, any function $g \in H^{1/2}(\partial\Omega)$ can be extended to a function $v \in H^1(\Omega)$, but this extension is not unique (if v is an extension, the other ones are of the form $v + w$, where w is an arbitrary function in $H_0^1(\Omega)$). The space $H^{1/2}(\partial\Omega)$ is a Hilbert space with the norm defined by :*

$$\|g\|_{H^{1/2}(\partial\Omega)} = \inf_{v \in H^1(\Omega), \gamma_0(v) = g} \|v\|_{H^1(\Omega)}.$$

Now let us introduce the variational space

$$\mathbb{V} = \Big\{ v \in L^2(\Omega);\ \ v_G = v|_{\Omega_G} \in H^1(\Omega_G) \text{ and } v_S = v|_{\Omega_S} \in H^1(\Omega_S) \Big\}, \tag{2.3}$$

It is naturally endowed with the broken norm

$$\|v\|_{\mathbb{V}} = (\|v\|^2_{H^1(\Omega_G)} + \|v\|^2_{H^1(\Omega_S)})^{1/2}.$$

This norm determines a Hilbertian structure on $\mathbb{V}$. We will need the subspace

$$\mathbb{V}_0 = \Big\{ v \in \mathbb{V};\, v = 0 \text{ on } \Gamma_D \Big\}. \tag{2.4}$$

It is easily seen that $\mathbb{V}_0$ is closed in $\mathbb{V}$ and since every closed subspace in a Hilbert space is a Hilbert space we have that $\mathbb{V}_0$ is a Hilbert space.
In the subsequent, the restrictions of any function v in $\mathbb{V}$ to Ω_G and Ω_S are denoted by v_G and v_S, respectively.

We assume that the conductivity κ and the resistivity R belong to $L^\infty(\Omega)$ and $L^\infty(\gamma)$ respectively and are bounded away from zero,

$$\inf_{\boldsymbol{x}\in\Omega} \kappa(\boldsymbol{x}) > 0, \qquad \inf_{\tau\in\gamma} R(\tau) > 0.$$

We use sometimes the notation κ_S and κ_G for the restriction functions of κ to Ω_S and Ω_G, respectively. We also introduce the conductance $\alpha = R^{-1}$.
Now we have all the tools we need to write the variational formulation of the problem (2.2).

2.2.2 Variational formulation

Multiplying the first equation in (2.2) by a smooth function v on Ω_S, and after integrating by parts, we obtain that

$$\int_{\Omega_S} \kappa\,(\nabla T)(\boldsymbol{x}) \cdot (\nabla v)(\boldsymbol{x})\, d\boldsymbol{x} - \int_\gamma (\kappa\, \partial_n T)(\tau) v(\tau)\, d\tau = \int_{\Omega_S} g(\boldsymbol{x}) v(\boldsymbol{x})\, d\boldsymbol{x},$$

The normal $\boldsymbol{n}$ is exterior to Ω_S and τ denotes the tangential variable on γ. Similarly, multiplying the same equation by a smooth function v vanishing on Γ_D and integrate on

Ω_G results in

$$\int_{\Omega_G} \kappa\,(\nabla T)(\boldsymbol{x})\cdot(\nabla v)(\boldsymbol{x})\,d\boldsymbol{x} + \int_\gamma (\kappa\,\partial_n T)(\tau)v(\tau)\,d\tau = \int_{\Omega_G} g(\boldsymbol{x})v(\boldsymbol{x})\,d\boldsymbol{x}.$$

For any smooth function v in $\mathbb{V}_0$, we need to transform the integral term at the interface γ as follows

$$\begin{aligned}&\int_\gamma \Big(-\kappa_S(\partial_n T_S)(\tau)v_S(\tau) + \kappa_G(\partial_n T_G)(\tau)v_G(\tau)\Big)\,d\tau\\ &= \int_\gamma [\kappa\partial_n T](\tau)v_G(\tau)\,d\tau + \int_\gamma \kappa_S(\partial_n T_S)(\tau)[v](\tau)\,d\tau.\end{aligned}$$

Combining all this with the interface conditions (second and third equation in (2.2)), we derive that, for all function v in $\mathbb{V}_0$

$$\int_{\Omega_S\cup\Omega_G} \kappa\,(\nabla T)(\boldsymbol{x})\cdot(\nabla v)(\boldsymbol{x})\,d\boldsymbol{x} + \int_\gamma R^{-1}[T](\tau)[v](\tau)\,d\tau = \int_{\Omega_S\cup\Omega_G} g(\boldsymbol{x})v(\boldsymbol{x})\,d\boldsymbol{x}.$$

As a consequence, we are led to consider the variational problem:

Find T in $\mathbb{V}$ such that

$$T = T_D \qquad \text{on } \Gamma_D, \tag{2.5}$$

and

$$\forall v\in\mathbb{V}_0,\quad \int_{\Omega_S\cup\Omega_G} \kappa\,(\nabla T)(\boldsymbol{x})\cdot(\nabla v)(\boldsymbol{x})\,d\boldsymbol{x} + \int_\gamma \alpha[T](\tau)[v](\tau)\,d\tau = \int_{\Omega_S\cup\Omega_G} g(\boldsymbol{x})v(\boldsymbol{x})\,d\boldsymbol{x}. \tag{2.6}$$

The proof of the next proposition easily follows from the previous lines and from the density of $\mathscr{D}(\overline{\Omega}_S)\times\mathscr{D}(\overline{\Omega}_G)$ into $\mathbb{V}$, however it requires a further assumption which is not restrictive (sufficient conditions for it are given in [11]).

Proposition 2.2. *Assume that the partition of $\partial\Omega$ into Γ_D and Γ_N is sufficiently smooth for $\mathscr{D}(\overline{\Omega}_G\setminus\Gamma_D)$ to be dense in the space*

$$\Big\{v\in H^1(\Omega_G);\ v=0 \text{ on } \Gamma_D\Big\}.$$

Problems (2.2) and (2.5)–(2.6) are equivalent, in the sense that any function in $\mathbb{V}$ is a solution of (2.2) in the distribution sense if and only if it is a solution of (2.5)–(2.6).

Proof. Let T be a solution of problem (2.5)–(2.6). By taking v successively in $\mathscr{D}(\Omega_G)$, in $\mathscr{D}(\Omega_S)$, in $\mathscr{D}(\Omega)$ and finally in $\mathscr{D}(\Omega_G \cup \Omega_S)$ and using the same equations as previously, we derive that it is solution of (2.2) in the distribution sense. The converse property follows by the same arguments and by noting that the space

$$\Big\{v \in L^2(\Omega);\ \ v_G \in \mathscr{D}(\overline{\Omega}_G \setminus \Gamma_D) \text{ and } v_S \in \mathscr{D}(\overline{\Omega}_S)\Big\}, \tag{2.7}$$

is dense in $\mathbb{V}_0$. ■

In 1902, J. Hadamard formulated the concept of the well-posedness of problems for differential equations. A problem is called well-posed in the sense of Hadamard if there exists a unique solution to this problem that continuously depends on its data.
With this definition in mind, to establish the well-posedness of problem (2.5)–(2.6) we will need the following fundamental result[35].

Theorem 2.3. ***(Lax-Milgram Lemma)*** *We assume that a is a continuous and elliptic bilinear form on $\mathbb{V}$, i.e. there exist two constants M and $\alpha > 0$ such that*

$$|a(u,v)| \leq M\|u\|_{\mathbb{V}}\|v\|_{\mathbb{V}} \quad \forall u, v \in \mathbb{V}$$

and

$$a(u,v) \geq \alpha\|v\|_{\mathbb{V}}^2 \quad \forall v \in \mathbb{V}.$$

then, for $l \in \mathbb{V}'$, there exists a unique $u \in \mathbb{V}$ such that

$$a(u,v) = < l, v > \quad \forall v \in \mathbb{V}.$$

Moreover, the mapping $l \mapsto u$ is an isomorphism from $\mathbb{V}'$ onto $\mathbb{V}$.

Thus establishing the well-posedness of problem (2.5)–(2.6) requires to study the $\mathbb{V}$–ellipticity (or coerciveness) of the bilinear form

$$a(T,v) = \int_{\Omega_S \cup \Omega_G} \kappa\,(\nabla T)(\boldsymbol{x}) \cdot (\nabla v)(\boldsymbol{x})\, d\boldsymbol{x} + \int_{\gamma} \alpha[T](\tau)[v](\tau)\, d\tau. \tag{2.8}$$

Indeed, we have the following lemma.

Lemma 2.4. *The mapping: $v \mapsto a(v,v)^{1/2}$ is a norm on $\mathbb{V}_0$ equivalent to the norm $\|v\|_{\mathbb{V}}$.*

Proof. We first check out that $v \mapsto a(v,v)^{1/2}$ is a norm. Let then v be a function in $\mathbb{V}_0$ such that $a(v,v) = 0$. Thus, ∇v is zero on Ω_G and on Ω_S so that v is equal to a constant v_G on Ω_G, to a constant v_S on Ω_S. It follows from the boundary condition on Γ_D that v_G is zero. Moreover, since the jump $[v]$ vanishes on γ then v_S is equal to v_G, hence to zero. All this yields that v is zero.
Now, to show the equivalence with the norm $\|\cdot\|_{\mathbb{V}}$, observe that the continuity of the trace from $H^1(\Omega_G)$ and $H^1(\Omega_S)$ into $L^2(\gamma)$ yields that the norm $\|\cdot\|_{\mathbb{V}}$ is equivalent to the norm defined by

$$v \mapsto a(v,v)^{1/2} + (\|v\|^2_{L^2(\Omega_G)} + \|v\|^2_{L^2(\Omega_S)})^{1/2}.$$

The kernel of the first term is reduced to zero and, due to the compact embeddings of $H^1(\Omega_G)$ into $L^2(\Omega_G)$ and of $H^1(\Omega_S)$ into $L^2(\Omega_S)$, the second term is compact. We can see that the desired equivalence property is a direct consequence of the second property of the following Peeter–Tartar lemma 2.5 (see [35] for more details) with $A : v \mapsto Av = a(v,v)$ and $L : v \mapsto Lv = (v,v)^2_{\mathbb{V}}$ ■

Lemma 2.5. *(Peeter–Tartar) Let E_1, E_2 and E_3 be three Banach spaces, A an operator in $\mathscr{L}(E_1, E_2)$ and B a compact operator in $\mathscr{L}(E_1, E_3)$ such that*

$$\|u\|_{E_1} \cong \|Au\|_{E_2} + \|Bu\|_{E_3}, \quad \forall u \in E_1$$

Then the following properties hold :

1. *The dimension of $KerA = \{v \in X; Av = 0\}$ is finite; the mapping A is an isomorphism from $E_1/KerA \mapsto R(A)$(: the range space of A); $R(A)$ is a closed subspace of E_2.*

2. *There exists a constant C_0 such that, if F is a Banach space and $L \in \mathscr{L}(E_1; F)$ vanishes on $Ker(A)$, then*

$$\|Lu\|_F \leq C_0 \|L\|_{\mathscr{L}(E_1;F)} \|Au\|_{E_2} \quad \forall u \in E_1.$$

3. *If G is a Banach space and $M \in \mathscr{L}(E_1, G)$ satisfies*

$$Mu \neq 0, \quad \forall u \in KerA \backslash \{0\},$$

then,

$$\|u\|_{E_1} \cong \|Au\|_{E_2} + \|Mu\|_G \quad \forall u \in E_1.$$

Corollary 2.6. *For any data g in $L^2(\Omega)$ and T_D in $H^{1/2}(\Gamma_D)$, problem (2.5)–(2.6) has a unique solution T in $\mathbb{V}$. Moreover this solution satisfies*

$$\|T\|_{\mathbb{V}} \leq c\Big(\|g\|_{L^2(\Omega)} + \|T_D\|_{H^{1/2}(\Gamma_D)}\Big). \tag{2.9}$$

Proof. There exists a lifting $\overline{T}_D$ in $H^1(\Omega_G)$ of any extension of T_D in $H^{1/2}(\partial\Omega)$ which vanishes on γ and such that

$$\|\overline{T}_D\|_{H^1(\Omega_G)} \leq c\|T_D\|_{H^{1/2}(\Gamma_D)}.$$

Thus, writing the problem satisfied by $T_0 = T - \overline{T}_D$ and noting that it belongs to $\mathbb{V}_0$, we deduce by combining the Lax–Milgram lemma 2.3 with the ellipticity property proved in Lemma 2.4 that the problem has a unique solution. Moreover, the function $T = T_0 + \overline{T}_D$ satisfies (2.9). ∎

In spite of the discontinuity of the temperature solution T, the maximum principle holds true.

Proposition 2.7. *When g is equal to zero, for any data T_D in $H^{1/2}(\Gamma_D) \cap L^\infty(\Gamma_D)$, the solution T of problem (2.5)–(2.6) satisfies for a.e. $\boldsymbol{x}$ in Ω*

$$\min\Big\{0, \inf_{\tau\in\Gamma_D} T_D(\tau)\Big\} \leq T(\boldsymbol{x}) \leq \max\Big\{0, \sup_{\tau\in\Gamma_D} T_D(\tau)\Big\}. \tag{2.10}$$

Proof. Since the proofs of the two inequalities are fully identical, we only check out the second one. Set $M = \max\Big\{0, \sup_{\tau\in\Gamma_D} T_D(\tau)\Big\}$. Then, we observe that the function $T - M$ satisfies

$$\forall v \in \mathbb{V}_0, \quad \int_{\Omega_S\cup\Omega_G} \kappa\,(\nabla(T-M))(\boldsymbol{x})\cdot(\nabla v)(\boldsymbol{x})\,d\boldsymbol{x} + \int_\gamma \alpha[T-M](\tau)[v](\tau)\,d\tau = 0.$$

We choose v equal to $(T-M)_+ = \max\{T-M, 0\}$. Given that $T-M$ belongs to $\mathbb{V}$, then $(T-M)_+$ lies also in $\mathbb{V}$. Moreover, based on the definition of M this function belongs to $\mathbb{V}_0$. We have that

$$\int_{\Omega_S\cup\Omega_G} \kappa\,(\nabla(T-M)_+)^2\,d\boldsymbol{x} + \int_\gamma \alpha[T-M](\tau)[(T-M)_+](\tau)\,d\tau = 0. \tag{2.11}$$

Using the fact that $(r-s)(r_+ - s_+) \geq 0$ for all real numbers r, s, we derive that

$$\int_\gamma \alpha[(T-M)](\tau)[(T-M)_+](\tau)\,d\tau \geq 0. \tag{2.12}$$

As a result, both terms in the previous equation are zero. Thus, owing to Lemma 2.4, the function $(T-M)_+$ vanishes identically, hence the desired result. ■

2.2.3 Hybrid dual formulation

In the previous section we have presented a classical way to formulate problem (2.2) in a weak form [15]. Another less conventional way to write this problem is using a hybrid dual formulation where in addition to the temperature field as the unknown of the problem, the gradient of the temperature is introduced as a second unknown. The finite element methods based on this approach are known as the Mixed and hybrid finite element methods. These method allow to compute the temperature and the gradient temperature with equal accuracy which earned them an amount of popularity during the last few years[31].
To write the hybrid dual formulation for problem (2.2) we start by introducing the hybrid dual functional framework adapted to this problem. The flux conservation across the interface prompts us to consider the space

$$H(\mathrm{div};\Omega) = \Big\{ \boldsymbol{q} \in L^2(\Omega)^d;\ \mathrm{div}\,\boldsymbol{q} \in L^2(\Omega) \Big\}.$$

We recall from [35] the flowing theorem(Chap. I, Thm 2.5) :

Theorem 2.8. *The mapping* $: v \mapsto v.n|_{\partial\Omega}$ *defined on* $\mathscr{D}(\bar{\Omega})^d$ *can be extended by continuity to a linear and continuous mapping, from* $H(div;\Omega)$ *into* $H^{-1/2}(\partial\Omega)$.

Thus we have that the trace operator: $\boldsymbol{q} \mapsto \boldsymbol{q}\cdot\boldsymbol{n}$ is continuous from $H(\mathrm{div};\Omega)$ onto the space $H^{-1/2}(\partial\Omega)$.
From now on, we denote by $\langle\cdot,\cdot\rangle_{\partial\Omega}$ the duality pairing between $H^{-1/2}(\partial\Omega)$ and $H^{1/2}(\partial\Omega)$, and by $\langle\cdot,\cdot\rangle_{\Gamma_D}$ the duality pairing between the space $H^{1/2}(\Gamma_D)$ and its dual space.
To step further and to fully take into account the interface conditions we need to work in the space

$$\mathbb{X} = \Big\{ \boldsymbol{q} \in H(\mathrm{div};\Omega);\ \boldsymbol{q}\cdot\boldsymbol{n} = 0 \text{ on } \Gamma_N \text{ and } (\boldsymbol{q}\cdot\boldsymbol{n})|_\gamma \in L^2(\gamma) \Big\}. \tag{2.13}$$

It is a Hilbert space when equipped with the norm

$$\|\boldsymbol{q}\|_{\mathbb{X}} = \Big(\|\boldsymbol{q}\|^2_{L^2(\Omega)^d} + \|\mathrm{div}\,\boldsymbol{q}\|^2_{L^2(\Omega)} + \|\boldsymbol{q}\cdot\boldsymbol{n}\|^2_{L^2(\gamma)} \Big)^{1/2}. \tag{2.14}$$

To write the mixed formulation we introduce a second unknown(see [77], [15, Chap. I, §3 and §4]).

$$\boldsymbol{p} = \kappa \nabla T \tag{2.15}$$

An alternative to the variational problem (2.5)–(2.6) consists in considering the following hybrid dual problem:
Find $(T, \boldsymbol{p})$ *in* $L^2(\Omega) \times \mathbb{X}$ *such that*

$$\forall \boldsymbol{q} \in \mathbb{X}, \quad \int_\Omega \kappa^{-1}\, \boldsymbol{p}(\boldsymbol{x}) \cdot \boldsymbol{q}(\boldsymbol{x})\, d\boldsymbol{x} + \int_\gamma R(\boldsymbol{p}\cdot\boldsymbol{n})(\tau)(\boldsymbol{q}\cdot\boldsymbol{n})(\tau)\, d\tau + \int_\Omega (\operatorname{div} \boldsymbol{q})(\boldsymbol{x}) T(\boldsymbol{x})\, d\boldsymbol{x} = \langle T_D, \boldsymbol{q}\cdot\boldsymbol{n}\rangle_{\Gamma_D}, \tag{2.16}$$

$$\forall v \in L^2(\Omega), \quad \int_\Omega (\operatorname{div} \boldsymbol{p})(\boldsymbol{x}) v(\boldsymbol{x})\, d\boldsymbol{x} = -\int_\Omega g(\boldsymbol{x}) v(\boldsymbol{x})\, d\boldsymbol{x}. \tag{2.17}$$

The first equation is obtained when multiplying (2.15) by a test function $\boldsymbol{q} \in \mathbb{X}$ and integrating over Ω and by using a Green formula. The second equation is obtained by replacing $\kappa\nabla T$ by $\boldsymbol{p}$ in the first equation of (2.2) and by multiplying the resulting equation with a test function $v \in L^2(\Omega)$ and integrating over Ω.
This problem is of standard saddle point type, and it can be noted that no jump appears in its formulation. In order to establish its well-posedness we will use the following theorem see [35, Chap. I, Thm 4.1] or [15, Chap. II, Thm 1.1] for instance.

Theorem 2.9. *Let* X *and* M *be two Hilbert spaces,* $a(.,.)$ *a continuous bilinear form on* $X \times X$ *and* $b(.,.)$ *a continuous bilinear form on* $X \times M$*. Let us suppose that* a *is elliptic on* $Kerb$ *and* b *is such that*

$$\exists\ \beta > 0, \quad \sup_{\|p\|_X = 1} b(p, v) \geq \beta \|v\|_M \ \ \forall v \in M$$

then there exist a solution (u, p) *to*
Find $(p, u) \in X \times M$ *such that*

$$\begin{cases} a(p,q) + b(q,u) \ = \ L(q), & \forall q \in X, \\ b(p,v) \ = \ m(v), & \forall v \in M. \end{cases}$$

for all $(L, m) \in X' \times M'$.

Thus the to prove the well-posedness of problem (2.17) we need to prove the continuity and ellipticity of the bilinear form defined by:

$$(\boldsymbol{p},\boldsymbol{q}) \mapsto \int_\Omega \kappa^{-1}\,\boldsymbol{p}(\boldsymbol{x})\cdot\boldsymbol{q}(\boldsymbol{x})\,d\boldsymbol{x} + \int_\gamma R(\boldsymbol{p}\cdot\boldsymbol{n})(\tau)(\boldsymbol{q}\cdot\boldsymbol{n})(\tau)\,d\tau + \int_\Omega (\operatorname{div}\boldsymbol{q})(\boldsymbol{x})T(\boldsymbol{x})\,d\boldsymbol{x}$$

The kernel $\mathbb{K}$ defined by

$$\mathbb{K} = \Big\{\boldsymbol{q}\in\mathbb{X};\ \forall v\in L^2(\Omega),\ \int_\Omega (\operatorname{div}\boldsymbol{q})(\boldsymbol{x})v(\boldsymbol{x})\,d\boldsymbol{x} = 0\Big\} \tag{2.18}$$

is obviously characterized by

$$\mathbb{K} = \Big\{\boldsymbol{q}\in\mathbb{X};\ \operatorname{div}\boldsymbol{q} = 0 \text{ in } \Omega\Big\}. \tag{2.19}$$

Thanks to the definition (2.14) of the norm $\|\cdot\|_{\mathbb{X}}$, this yields the following result.

Lemma 2.10. *The bilinear form:*

$$m : (\boldsymbol{p},\boldsymbol{q}) \mapsto \int_\Omega \kappa^{-1}\,\boldsymbol{p}(\boldsymbol{x})\cdot\boldsymbol{q}(\boldsymbol{x})\,d\boldsymbol{x} + \int_\gamma R(\boldsymbol{p}\cdot\boldsymbol{n})(\tau)(\boldsymbol{q}\cdot\boldsymbol{n})(\tau)\,d\tau,$$

is elliptic on $\mathbb{K}$*, with ellipticity constant equal to* $\min\{\|\kappa^{-1}\|_{L^\infty(\Omega)}, \inf_{\tau\in\gamma} R(\tau)\}$.

The proof of this lemma is straightforward.

Proof.

$$\begin{aligned}
|m(\boldsymbol{q},\boldsymbol{q})| &= |\int_\Omega \kappa^{-1}\,\boldsymbol{q}(\boldsymbol{x})\cdot\boldsymbol{q}(\boldsymbol{x})\,d\boldsymbol{x} + \int_\gamma R(\boldsymbol{q}\cdot\boldsymbol{n})(\tau)(\boldsymbol{q}\cdot\boldsymbol{n})(\tau)\,d\tau| \\
&\geq |\int_\Omega \kappa^{-1}\,\boldsymbol{q}(\boldsymbol{x})\cdot\boldsymbol{q}(\boldsymbol{x})\,d\boldsymbol{x}| + |\int_\gamma R(\boldsymbol{q}\cdot\boldsymbol{n})(\tau)(\boldsymbol{q}\cdot\boldsymbol{n})(\tau)\,d\tau| \\
&\geq \|\kappa^{-1}\|_{L^\infty(\Omega)}\|\boldsymbol{q}\|^2_{L^2(\Omega)^d} + \inf_{\tau\in\gamma}(R(\tau))\|\boldsymbol{q}\cdot\boldsymbol{n}\|^2_{L^2(\gamma)} \\
&\geq min(\|\kappa^{-1}\|_{L^\infty(\Omega)} + \inf_{\tau\in\gamma}(R(\tau)))\|\boldsymbol{q}\|^2_X.
\end{aligned}$$

■

The next step is to investigate the properties of the following mixed bilinear form:

$$(\boldsymbol{q},v) \mapsto \int_\Omega (\operatorname{div}\boldsymbol{q})(\boldsymbol{x})v(\boldsymbol{x})\,d\boldsymbol{x}.$$

Lemma 2.11. *The following inf-sup condition holds for a positive constant β only depending on Ω*

$$\forall v \in L^2(\Omega), \quad \sup_{\boldsymbol{q}\in\mathbb{X}} \frac{\int_\Omega (\operatorname{div}\boldsymbol{q})(\boldsymbol{x})v(\boldsymbol{x})\,d\boldsymbol{x}}{\|\boldsymbol{q}\|_{\mathbb{X}}} \geq \beta \|v\|_{L^2(\Omega)}. \tag{2.20}$$

Proof. It is processed as in [78] after adding some modifications. For any v in $L^2(\Omega)$, we consider the solution w of the Laplace equation

$$\begin{cases} -\Delta w = -v & \text{in } \Omega, \\ w = 0 & \text{on } \Gamma_D, \\ \partial_n w = 0 & \text{on } \Gamma_N. \end{cases} \tag{2.21}$$

Obviously, this solution belongs to $H^1(\Omega)$. Then the function $\boldsymbol{q} = \nabla w$ satisfies $\operatorname{div}\boldsymbol{q} = v$ and

$$\left(\|\boldsymbol{q}\|^2_{L^2(\Omega)^d} + \|\operatorname{div}\boldsymbol{q}\|^2_{L^2(\Omega)}\right)^{1/2} \leq c\|v\|_{L^2(\Omega)}.$$

Moreover, $\boldsymbol{q}\cdot\boldsymbol{n} = \partial_n w$ vanishes on Γ_N. Owing to the elliptic regularity (see [38, Section 2.2.2]), w belongs to $H^2(\mathcal{O})$ for any smooth domain $\mathcal{O}$ such that $\overline{\mathcal{O}} \subset \Omega$. Since γ is strictly contained in Ω, there exists a neighborhood $\overline{\mathcal{O}}$ of γ in Ω such that

$$\|\boldsymbol{q}\cdot\boldsymbol{n}\|_{L^2(\gamma)} = \|\partial_n w\|_{L^2(\gamma)} \leq \|w\|_{H^2(\mathcal{O})} \leq c\|v\|_{L^2(\Omega)}.$$

Thus we have that

$$\|\boldsymbol{q}\|_{\mathbb{X}} \leq c\|v\|_{L^2(\Omega)}. \tag{2.22}$$

we know that

$$\int_\Omega (div\,\boldsymbol{q})(\boldsymbol{x})v(\boldsymbol{x})\ d\boldsymbol{x} = \int_\Omega v(\boldsymbol{x})^2 d\boldsymbol{x} = \|v\|^2_{L^2(\Omega)}$$

thus

$$\begin{aligned} \frac{\int_\Omega (div\,\boldsymbol{q})(\boldsymbol{x})v(\boldsymbol{x})\ d\boldsymbol{x}}{\|q\|_{\mathbb{X}}} &= \frac{\|v\|^2_{L^2(\Omega)}}{\|q\|_{\mathbb{X}}} \\ &\geq \beta \frac{\|v\|^2_{L^2(\Omega)}}{\|v\|_{L^2(\Omega)}} \quad \text{using (2.22)} \\ &= \beta\|v\|_{L^2(\Omega)} \end{aligned}$$

This concludes the proof. ∎

The well-posedness of problem (2.17) is now a consequence of Lemmas (2.10) and (2.11) and Theorem 2.9.

Theorem 2.12. *For any data g in $L^2(\Omega)$ and T_D in $H^{1/2}(\Gamma_D)$, problem (2.17) has a unique solution $(T, \boldsymbol{p})$ in $L^2(\Omega) \times \mathbb{X}$. Moreover this solution satisfies*

$$\|T\|_{L^2(\Omega)} + \|\boldsymbol{p}\|_{\mathbb{X}} \leq c \Big(\|g\|_{L^2(\Omega)} + \|T_D\|_{H^{1/2}(\Gamma_D)} \Big). \tag{2.23}$$

We conclude by comparing problem (2.17) with problem (2.2) (or equivalently with problem (2.5)–(2.6) thanks to Proposition (2.2)).

Proposition 2.13. *Assume that the partition of $\partial\Omega$ into Γ_D and Γ_N is sufficiently smooth for $\mathscr{D}(\Omega \cup \Gamma_D)$ to be dense in the space $\mathbb{X}$. Problems (2.2) and (2.17) are equivalent, in the sense that any function T in $\mathbb{V}$ is a solution of (2.2) in the distribution sense if and only if the pair $(T, \boldsymbol{p} = \kappa \nabla T)$ is the solution of problem (2.17).*

Proof. If $(T, \boldsymbol{p})$ stands for a solution of problem (2.17), we consider this problem with $\boldsymbol{q}$ in $\mathscr{D}(\Omega_G)^d \cup \mathscr{D}(\Omega_S)^d$ and v in $\mathscr{D}(\Omega)$. This yields

$$\kappa^{-1} \boldsymbol{p} = \nabla T \quad \text{in } \Omega_G \cup \Omega_S \qquad \text{and} \qquad \operatorname{div} \boldsymbol{p} = -g \quad \text{in } \Omega,$$

whence the equality $\boldsymbol{p} = \kappa \nabla T$ and also the first equation in (2.2). Since $\boldsymbol{p}$ belongs to $H(\operatorname{div}; \Omega)$, this also implies the second equation in (2.2). Taking $\boldsymbol{q}$ in $\mathscr{D}(\Omega)$ and integrating by parts in (2.17) leads to the third equation in (2.2). The fourth equation is obtained by taking $\boldsymbol{q}$ in $\mathscr{D}(\Omega_G \cup \Gamma_D)^d$ and the fifth one follows from the fact that $\boldsymbol{p}$ belongs to $\mathbb{X}$. Thus, T belongs to $\mathbb{V}$ and is a solution of (2.2). The converse property follows from the same arguments, together with the density assumption and the density of $\mathscr{D}(\Omega)$ into $L^2(\Omega)$. ■

2.2.4 Regularity and singularities

The investigation of the accuracy of any finite element method applied to problem (2.2) requires to know the regularity of the solution T. It is admitted that the regularity of the solution is tightly connected to the smoothness of the data and of the geometry. Let us have a first look at the case where the geometry is smooth. To avoid the well known effect of mixed boundary conditions, we suppose that the Neumann portion is empty, that is $\Gamma_N = \emptyset$. We focus on the case where the resistivity R is constant and the conductivity κ

is piecewise constant and takes two constant values κ_G and κ_S in Ω_G and Ω_S respectively. Similar results are valid for regular space varying κ and R.

Proposition 2.14. *Assume that the boundaries $\partial\Omega$ and γ are of class $\mathscr{C}^{1,1}$. Then T_S belongs to $H^2(\Omega_S)$. If in addition, the boundary datum T_D belongs to $H^{3/2}(\partial\Omega)$, then T_G also belongs to $H^2(\Omega_G)$.*

Before proceeding with the proof we give first the following theorem [38, Thm 2.2.2.5]

Theorem 2.15. *For every $f \in L_2(\Omega)$ there exists a unique $u \in H^2(\Omega)$ such that*

$$Au + \lambda u = f, \quad \text{in } \Omega$$

with the boundary condition $\gamma\partial u/\partial\nu_A = 0$, provided $\lambda > 0$. Where A is a second-order strongly elliptic real operator in Ω.

Now back to the proof of proposition 2.14.

Proof. Restricted to Ω_S, the temperature T is the solution of the Laplace equation with Neumann boundary condition

$$\begin{cases} -\kappa_S \Delta T_S = g & \text{in } \Omega_S \\ \kappa_S \partial_n T_S = \varphi & \text{on } \gamma, \end{cases}$$

where the function $\varphi = \alpha[T]$ belongs to $H^{1/2}(\gamma)$. The desired result follows from theorem 2.15 where in our case A is the Laplace operator. ■

Let us turn to the regularity on Ω_G. The temperature T is the solution of

$$\begin{cases} -\kappa_G \Delta T_G = g & \text{in } \Omega_G, \\ \kappa_G \, \partial_n T_G = \psi & \text{on } \gamma, \\ T_G = T_D & \text{on } \Gamma_D. \end{cases} \tag{2.24}$$

The function $\psi = \kappa_S \partial_n T_S$ is in $H^{1/2}(\gamma)$. Consequently, the solution T_G belongs to $H^2(\Omega_G)$.

Remark 2.16. If the data and the geometry are highly smooth, a bootstrapping argument enables us to check that the local temperature fields T_G and T_S are also highly regular notwithstanding the discontinuity of the global temperature T.

In the practice the geometry may not be so idealistic. We consider then more realistic cases where the geometry may have singular points or lines. Before giving the next result we need the following theorem (see [38, Thm 3.2.1.3]).

Theorem 2.17. *Let Ω be a convex, bounded and open subset of $\mathbb{R}^d$. Then for each $f \in L_2(\Omega)$ and for each $\lambda > 0$ there exists a unique $u \in H^2(\Omega)$ which is the solution of*

$$-\int_\Omega \nabla u \nabla v \; d\boldsymbol{x} + \lambda \int_\Omega uv \; d\boldsymbol{x} = \int_\Omega fv \; d\boldsymbol{x} \quad v \in H^1(\Omega).$$

Proposition 2.18. *Assume that any connected component ω_i of Ω_S is convex. Then the temperature T_S belongs to $H^2(\Omega_S)$. Moreover, if the boundary datum T_D belongs to $H^{3/2}(\partial\Omega)$, then the solution T_G belongs to $H^{1+r}(\Omega_G)$, for some r with $1/2 \leq r < 1$. The following stability holds*

$$\|T_S\|_{H^2(\Omega_S)} + \|T_G\|_{H^{1+r}(\Omega_G)} \leq c(\|g\|_{L^2(\Omega)} + \|T_D\|_{H^{3/2}(\partial\Omega)}). \tag{2.25}$$

Proof. The proof is conducted exactly as for the previous proposition. The conclusion can be achieved following Theorem 2.17. We refer to [49] for the case of a general Lipschitz boundary. ■

Remark 2.19. To have a deeper insight on this issue, let us have a close glance on the two-dimensional problem. We pay a particular attention to the case where the sub-domain Ω_S is polygonal. The limitation on the regularity of T_G is caused by the angular vertices of γ which create re-entrant corners for the domain Ω_G. Now, consider the corner $\mathbf{m}$ of a sector $\mathcal{V}$ included in Ω_G, with an aperture of the angle η in $]\pi, 2\pi[$: The temperature field T_G, solution of sub-problem (2.24) is expected to contain a singularity of type

$$S_G(\varrho, \theta) = \varrho^{\frac{\pi}{\eta}} \cos(\frac{\pi}{\eta}\theta)\varphi(\varrho).$$

The polar coordinates (ϱ, θ) are used with origin $\mathbf{m}$ and φ is a cut-off function around $\mathbf{m}$. Now, assume that $\mathcal{V}$ does not contain any other vertex. Then the singular function S_G belongs to any Sobolev space $H^s(\mathcal{V})$ provided that $s < 1 + \frac{\pi}{\eta}$ and can not be in $H^2(\mathcal{V})$. The questions now are : is such a singularity compatible with the interfaces conditions? Why S_G does not affect T_S through the flux conservation $[\kappa \partial_n T] = 0$? The answer is yes:

S_G is compatible with conditions along γ. The flux $\kappa\partial_n T_G = 0$ along both edges of the sector $\mathcal{V}$. The temperature T_S sees the singularity S_G through the condition

$$\kappa_S\, \partial_n T_S = \alpha[T], \qquad \text{on } \gamma.$$

This does not prevent $\kappa\partial_n T_S$ from belonging to $H^{1/2}(\gamma)$. Things happen as if the consequence of releasing the strong continuity on the temperature T, by the introduction of a resistivity of contact, is the cancellation of any effect of the singularity S_G on T_S. This will be addressed later on in the numerical section and a comparison will be conducted with the case of continuous temperature field for which the resistivity is zero, i.e. $R = 0$.

2.3 A Lagrange finite element discretization

Finite elements methods were proposed in a seminal work of Richard Courant[26], in 1943; unfortunately, the relevance of this article was not recognized at the time and the idea was forgotten. In the early 1950's the method was rediscovered by engineers, but the mathematical analysis of finite element approximations began much later, in the 1960's, the first important results being due to Milos Zlamal[97] in 1968. Since then finite element methods have been developed into one of the most general and powerful class of techniques for the numerical solution of partial differential equations and are widely used in engineering design and analysis[89].

In this section we describe the Lagrange finite elements method, for the approximation of the variational equation (2.6). This method is based on the Lagrange element, or nodal element, which was first defined with use of Lagrange interpolation polynomials in Courant's introduction of the finite element method[26]. We note however that we will only use this method in the case where the shape of the pores of the matrix, infiltrated with the phase change material, have a regular shape an example of this is presented in Figure 2.1(left). The sub-domain Ω_S is therefore the disjoint union of few connected components ω_i with reasonable boundaries. Handling local continuous/global discontinuous finite elements is therefore possible. At least, it can be managed without particular troubles in the numerical implementation grounds.

Experienced numerical practitioners may even build local meshes in Ω_S and Ω_G that do not match at the interface and use mortaring devices to glue corresponding finite element discretizations (see [12]). In spite of the high interest of such a mortar issue, we do not consider it here for conciseness.

Assume hence that Ω is a polygon ($d=2$) or a polyhedron ($d=3$). We also suppose that Ω_S is a union of polygons or polyhedra, so that the boundary γ is a polygonal curve or surface. The basic concept of the finite element method is the subdivision of the computational domain into a number of small, non-overlapping subdomains, the finite elements, over which functions are approximated by local functions, or in our case polynomials. Hence we start by defining a regular family of triangulations of Ω by triangles or tetrahedra $(\mathcal{T}_h)_h$ such that for each h:

- The boundary γ is the union of edges ($d=2$) or faces ($d=3$) of elements of $\mathcal{T}_h$.
- The union of all elements of $\mathcal{T}_h$ is equal to $\overline{\Omega}$.
- Each part Γ_D or Γ_N of the boundary $\partial\Omega$ is the union of edges ($d=2$) or faces ($d=3$) of elements of $\mathcal{T}_h$.
- The intersection of any two different elements of $\mathcal{T}_h$, if not empty, is a vertex or a whole edge or a whole face of both triangles or tetrahedra.
- The ratio of the diameter h_K of any element K of $\mathcal{T}_h$ to the diameter of its inscribed circle or sphere is smaller than a constant independent of h.

As usual, h stands for the maximum of the diameters h_K, $K\in\mathcal{T}_h$. In all that follows, c, c', ... are generic constants that can vary from line to line but are always independent of the parameter h.

Before defining the discrete space, let us introduce the local triangulations, for each mesh-size h,

$$\mathcal{T}_h^S=\Big\{K\in\mathcal{T}_h;\ \ K\subset\overline{\Omega}_S\Big\},\qquad \mathcal{T}_h^G=\Big\{K\in\mathcal{T}_h;\ \ K\subset\overline{\Omega}_G\Big\}.$$

The discrete spaces are then constructed as follows

$$\mathbb{V}_h=\Big\{v_h\in\mathbb{V};\forall K\in\mathcal{T}_h^S, v_h|_K\in\mathcal{P}_1(K)\ \text{ and }\ \forall K\in\mathcal{T}_h^G, v_h|_K\in\mathcal{P}_1(K)\Big\},$$

$$\mathbb{V}_{0h}=\mathbb{V}_h\cap\mathbb{V}_0$$

where $\mathcal{P}_1(K)$ stands for the space of affine functions on K. Extension to high-order discretizations is obvious.

The discrete problem is obtained from problem (2.5)–(2.6) by the Galerkin method. Denoting by i_h^D the Lagrange interpolation operator on Γ_D with values in the space of traces of elements in $\mathbb{V}_h$ and assuming the continuity of T_D, it reads

Find T_h in $\mathbb{V}_h$ such that

$$T_h=i_h^D T_D\qquad\text{on }\ \Gamma_D, \tag{2.26}$$

and

$$\forall v_h \in \mathbb{V}_{0h}, \quad \int_{\Omega_S \cup \Omega_G} \kappa\,(\nabla T_h)(\boldsymbol{x}) \cdot (\nabla v_h)(\boldsymbol{x})\, d\boldsymbol{x} + \int_\gamma \alpha [T_h](\tau)[v_h](\tau)\, d\tau = \int_{\Omega_S \cup \Omega_G} g(\boldsymbol{x}) v_h(\boldsymbol{x})\, d\boldsymbol{x}. \tag{2.27}$$

We can see that $\mathbb{V}_{0h}$ is imbedded in $\mathbb{V}_0$. Thus, this problem is well-posed thanks to the ellipticity property established in lemma 2.4 and the Lax–Milgram lemma 2.3 and we have the following result.

Proposition 2.20. *For any data g in $L^2(\Omega)$ and T_D continuous on $\overline{\Gamma}_D$, problem (2.26)–(2.27) has a unique solution T_h in $\mathbb{V}_h$. Moreover this solution satisfies*

$$\|T_h\|_{\mathbb{V}} \leq c\left(\|g\|_{L^2(\Omega)} + \|i_h^D T_D\|_{H^{\frac{1}{2}}(\Gamma_D)}\right). \tag{2.28}$$

2.3.1 Error analysis

First we can see that using the ellipticity property established in lemma 2.4, we derive straightforwardly the following version of Céa's lemma (see [23, Thm 2.4.1])

$$\|T - T_h\|_{\mathbb{V}} \leq c \inf_{S_h \in \mathbb{V}_h^D} \|T - S_h\|_{\mathbb{V}}, \tag{2.29}$$

where $\mathbb{V}_h^D$ stand for the affine space of functions in $\mathbb{V}_h$ equal to $i_h^D T_D$ on Γ_D. As a consequence, choosing S_h equal to the interpolate of T and using the following proposition (see [13, Chap. IX, Prop. 1.4]) yields the desired error estimate.

Theorem 2.21. *Assume that the solution T of problem (2.5)–(2.6) is such that*

$$T_S \in H^{s+1}(\Omega_S); \qquad T_G \in H^{r+1}(\Omega_G), \tag{2.30}$$

for real numbers s, r with $0 \leq s, r \leq 1$. Then, the following a priori error estimate holds between this solution and the solution T_h of problem (2.26)–(2.27)

$$\|T - T_h\|_{\mathbb{V}} \leq c\,(h^s \|T_S\|_{H^{s+1}(\Omega_S)} + h^r \|T_G\|_{H^{r+1}(\Omega_G)}). \tag{2.31}$$

Remark 2.22. Theorem 2.21 is worth some comments. Estimate 2.31 sounds artificial as it is. The effective form of the accuracy should be

$$\|T-T_h\|_{\mathbb{V}} \leq c\,h^{\min\{s,r\}}(\|T_S\|_{H^{s+1}(\Omega_S)}+\|T_G\|_{H^{r+1}(\Omega_G)}).$$

Céa's lemma, at the basis of that error estimate, fails to uncouple what happens in Ω_S and in Ω_G. In most of the real-life geometries the pores ω_i are convex. According to Proposition 2.18, the temperature field T enjoys more regularity within Ω_S than in Ω_G. Indeed, we have $s=1$ and $r\in]\frac{1}{2},1[$; thus T_S belongs to $H^2(\Omega_S)$ but T_G does not belong to $H^2(\Omega_G)$. Numericists and users may wonder whether a better accuracy within Ω_S may be derived.

2.3.2 Super-convergence for realistic geometries

We pursue an improved accuracy in the internal sub-domain Ω_S, when the components ω_i are convex. This is most often the case in the practice. The energy norm of the error decays actually like h rather than h^r with $r<1$, as predicted in Theorem 2.21.
We choose once again to develop the basic ideas in a simple context to avoid secondary technicalities that can be coped with following the specialized literature. We assume then that the conductivity is piecewise constant and takes the two constant values κ_S in Ω_S and κ_G in Ω_G. We consider also that $\Gamma_N=\emptyset$ for simplicity. The methodology we develop consists in using the combination of the duality argument and the regularity result, known as Aubin-Nitsche duality argument, then we call for a Gagliardo-Nirenberg inequality to obtain enhanced convergence rate at the interfaces and finally extend the result to Ω_S by a bootstrapping argument.

Proposition 2.23. *Assume g in $L^2(\Omega)$ and T_D in $H^{3/2}(\partial\Omega)$. Let all the connected components $\overline{\omega}_i$ of $\overline{\Omega}_S$ be convex. Then, the following a priori error estimate holds between the solution T of problem (2.5)–(2.6) and the solution T_h of problem (2.26)–(2.27)*

$$\|T-T_h\|_{L^2(\Omega)} \leq c\,h^{2r}\,(\|g\|_{L^2(\Omega)}+\|T_D\|_{H^{3/2}(\partial\Omega)}). \tag{2.32}$$

The real number r lies in $[1/2,1[$ and is defined in Proposition 2.18.

Proof. Observe first that by Theorem 2.21 we have

$$\|T-T_h\|_{\mathbb{V}} \leq ch^r(\|T_S\|_{H^2(\Omega_S)}+\|T_G\|_{H^{r+1}(\Omega_G)})$$

and owing to the stability (2.25) we have

$$\|T-T_h\|_{\mathbb{V}} \leq ch^r(\|g\|_{L^2(\Omega)}+\|T_D\|_{H^{3/2}(\Omega)}) \tag{2.33}$$

Next, to proceed with Aubin-Nitsche duality we start from the formula

$$\|T-T_h\|_{L^2(\Omega)} = \sup_{f\in L^2(\Omega)} \frac{\int_{\Omega_S\cup\Omega_G} f(\boldsymbol{x})(T-T_h)(\boldsymbol{x})\,d\boldsymbol{x}}{\|f\|_{L^2(\Omega)}}, \tag{2.34}$$

and, for each f in $L^2(\Omega)$, we solve the problem (we use here the notation 2.8 for brevity): Find w in $\mathbb{V}_0$ such that

$$\forall v\in\mathbb{V}_0, \quad a(v,w)=\int_{\Omega_S\cup\Omega_G} f(\boldsymbol{x})v(\boldsymbol{x})\,d\boldsymbol{x}.$$

Thus, we have obviously

$$\int_{\Omega_S\cup\Omega_G} f(\boldsymbol{x})(T-T_h)(\boldsymbol{x})\,d\boldsymbol{x} = a(T-T_h,w),$$

hence for any w_h in $\mathbb{V}_{0h}$ we have

$$\int_{\Omega_S\cup\Omega_G} f(\boldsymbol{x})(T-T_h)(\boldsymbol{x})\,d\boldsymbol{x} = a(T-T_h,w-w_h)+a(T,w_h)-a(T_h,w_h)$$

so that, by using problems (2.5)–(2.6) and (2.26)–(2.27) and the ellipticity property established in lemma 2.4, we have for any w_h in $\mathbb{V}_{0h}$,

$$\int_{\Omega_S\cup\Omega_G} f(\boldsymbol{x})(T-T_h)(\boldsymbol{x})\,d\boldsymbol{x} = a(T-T_h,w-w_h) \leq c\,\|T-T_h\|_{\mathbb{V}}\|w-w_h\|_{\mathbb{V}}. \tag{2.35}$$

Calling for Proposition 2.18 yields that w_S and w_G belong to $H^2(\Omega_S)$ and $H^{1+r}(\Omega_G)$, and satisfy

$$\|w_S\|_{H^2(\Omega_S)}+\|w_G\|_{H^{1+r}(\Omega_G)} \leq c\,\|f\|_{L^2(\Omega)}.$$

Choosing w_h equal to the Lagrange interpolate of w yields

$$\|w-w_h\|_{\mathbb{V}} \leq c\,h^r\,\|f\|_{L^2(\Omega)}. \tag{2.36}$$

Now we have all the elements to finish the proof.

$$\begin{aligned}\|T-T_h\|_{L^2(\Omega)} &\leq c \sup_{f\in L^2(\Omega)} \frac{\|T-T_h\|_{\mathbb{V}}\|w-w_h\|_{\mathbb{V}}}{\|f\|_{L^2(\Omega)}} \quad \text{using (2.34) and (2.35)}\\ &\leq c\;h^{2r}(\|g\|_{L^2(\Omega)}+\|T_D\|_{H^{3/2}(\Omega)}) \quad \text{using (2.36) and (2.33)}\end{aligned}$$

■

Now, the second step consists in deriving an error estimate on the L^2-norm of the jump of $[T - T_h]$ along the interface γ.

Lemma 2.24. *If assumptions of Proposition 2.23 are valid then the following estimate holds*

$$\|[T - T_h]\|_{L^2(\gamma)} \leq c h^{\frac{3}{2}r} \left(\|g\|_{L^2(\Omega)} + \|T_D\|_{H^{3/2}(\partial\Omega)}\right). \tag{2.37}$$

The proof uses the following trace theorem (see [14, Thm 1.6.6] for instance)

Theorem 2.25. *Suppose that Ω has a Lipschitz boundary, and that p is a real number in the range $1 \leq p \leq \infty$. Then there is a constant, C, such that*

$$\|v\|_{L^p(\partial\Omega)} \leq C \|v\|_{L^p(\Omega)}^{1-\frac{1}{p}} \|v\|_{W_p^1(\Omega)}^{\frac{1}{p}} \quad \forall v \in W_p^1(\Omega).$$

Where W_p^1 is the Sobolev space defined by

$$W_p^1 = \{u \in L^p(\Omega) : \ D^\alpha u \in L^p(\Omega) \ \forall \ |\alpha| \leq 1\}.$$

Now we proceed with the proof of lemma 2.24

Proof. It follows from the Theorem 2.25 that, for all v in $\mathbb{V}$,

$$\|v\|_{L^2(\gamma)} \leq c \|v\|_{L^2(\Omega_S)}^{\frac{1}{2}} \|v\|_{H^1(\Omega_S)}^{\frac{1}{2}}. \tag{2.38}$$

Of course, the same inequality holds with Ω_S replaced by Ω_G. Applying this inequality to $T - T_h$ yields

$$\|[T - T_h]\|_{L^2(\gamma)} \leq c \|T - T_h\|_{L^2(\Omega)}^{\frac{1}{2}} \|T - T_h\|_{\mathbb{V}}^{\frac{1}{2}}.$$

Using estimates (2.32) and (2.33) yields that

$$\|[T - T_h]\|_{L^2(\gamma)} \leq c h^{\frac{3}{2}r} (\|g\|_{L^2(\Omega)} + \|T_D\|_{H^{3/2}(\partial\Omega)}),$$

which is the desired result. ■

Remark 2.26. The same arguments as in the previous proof, see (2.38), also yield

$$\|T_S - T_h|_{\Omega_S}\|_{L^2(\gamma)} \leq c h^{\frac{3}{2}r} \left(\|g\|_{L^2(\Omega)} + \|T_D\|_{H^{3/2}(\partial\Omega)}\right). \tag{2.39}$$

Finally, we are in position to improve the error estimate in the sub-domain Ω_S.

Theorem 2.27. *If assumptions of Proposition 2.23 are valid then, the following a priori error estimate holds between the solution T of problem (2.5)–(2.6) and the solution T_h of problem (2.26)–(2.27)*

$$\|T - T_h\|_{H^1(\Omega_S)} \leq c h^{\min\{1,\frac{3}{2}r\}} \left(\|g\|_{L^2(\Omega)} + \|T_D\|_{H^{3/2}(\partial\Omega)}\right), \tag{2.40}$$

for the parameter r defined in Proposition 2.18.

Proof. Introduce first the notation $\mathbb{V}_{h,S} = \mathbb{V}_h|_{\Omega_S}$. Since T is the solution of problem (2.5)–(2.6) and T_h the solution of problem (2.26)–(2.27) we have

$$\forall v_h \in \mathbb{V}_h, \quad a(T - T_h, v_h) = a(T, v_h) - a(T_h, v_h) = 0.$$

Choosing v_h such that $v_h|_{\Omega_G} = 0$ and setting $w_h = v_h|_{\Omega_S} \in \mathbb{V}_{h,S}$ we obtain

$$\forall w_h \in \mathbb{V}_{h,S}, \quad \int_{\Omega_S} \kappa\,(\nabla(T - T_h))(\boldsymbol{x}) \cdot (\nabla w_h)(\boldsymbol{x})\, d\boldsymbol{x} + \int_\gamma \alpha[T - T_h](\tau) w_h(\tau)\, d\tau = 0. \tag{2.41}$$

Applying this equation with $w_h = S_h - T_h$, where S_h is in $\mathbb{V}_{h,S}$, yields

$$\begin{aligned}\int_{\Omega_S} \kappa\,(\nabla(T - T_h))^2(\boldsymbol{x})\, d\boldsymbol{x} = &\int_{\Omega_S} \kappa\,(\nabla(T - T_h))(\boldsymbol{x}) \cdot (\nabla(T - S_h))(\boldsymbol{x})\, d\boldsymbol{x} \\ &- \int_\gamma \alpha[T - T_h](\tau)(S_h - T_h)(\tau)\, d\tau, \quad \forall S_h \in \mathbb{V}\end{aligned}$$

whence, by using triangle inequalities and the trace theorem in the last term,

$$\|T - T_h\|^2_{H^1(\Omega_S)} \leq c\|T - S_h\|^2_{H^1(\Omega_S)} + c' \|[T - T_h]\|_{L^2(\gamma)} \Big(\|T - T_h\|_{L^2(\gamma)} + \|T - S_h\|_{L^2(\gamma)}\Big).$$

Observing that T_S belongs to $H^2(\Omega_S)$, see Proposition 2.18, applying Lemma 2.24 and Remark 2.26 and using the error estimate of the general theory of finite elements, we derive for appropriate constants c and c' depending on the data

$$\|T - T_h\|^2_{H^1(\Omega_S)} \leq c\ h^2 (\|g\|_{L^2(\Omega)} + \|T_D\|_{H^{3/2}(\partial\Omega)})^2 + c'\ h^{3r} (\|g\|_{L^2(\Omega)} + \|T_D\|_{H^{3/2}(\partial\Omega)})^2$$

hence

$$\|T - T_h\|_{H^1(\Omega_S)} \leq C\ h^{min(1,\frac{3}{2}r)}(\|g\|_{L^2(\Omega)} + \|T_D\|_{H^{3/2}(\partial\Omega)})$$

■

Remark 2.28. According to estimate (2.40) the optimal accuracy in the sub-domain Ω_S is guaranteed when $r > \frac{2}{3}$. The convergence speed is then of order $\mathcal{O}(h)$. The previous argument can be iterated to improve the result. Unfortunately, this bootstrap technique does not lead to the full optimal estimate for r close to $1/2$. So far the optimality is missing when the pores ω_i have acute angles ($\leq \pi/3$). Notice that the convergence rate of the error with respect to the energy norm in Ω_S is anyway better than $\mathcal{O}(h^{5/6})$. However, our feeling is that the optimality would be valid for any $r > 1/2$. The numerical discussion realized later on confirms this claim.

Remark 2.29. Although, we expose the procedure for enhancing the convergence rate in a particular geometry. It can be extended to a larger class of configurations provided that the convergence rate the global error with respect to the L^2-norm is higher than the rate with respect to the H^1-norm. Furthermore, the arguments exposed here may be applied locally as well. One may focus on a particular convex component ω_i instead of the whole Ω_S.

2.4 Hybrid dual Raviart–Thomas finite elements

For many interesting dense hybrid media as the one depicted in Figure 2.1, using Lagrange finite elements for the discretization of problem (2.2) compels practitioners to transform the finite elements Libraries which are the very foundation of most of existing Finite Element Computing Softwares. Users are reluctant to dive so deep in the programing layers (of the softwares). They prefer to work at the layers perceived as external layers. It is most often the level of the variational formulation writing. This is when the hybrid dual finite element method come to use, since in this method the jump in the temperature is accounted for in a natural way thanks to the element-wise continuous approximation functions used in this method.

Let us now introduce the finite element framework needed for the hybrid dual formulation. We recall by $(\mathcal{T}_h)_h$ the family of triangulations introduced in Section 2.3 and we denote by $\mathcal{E}_h$ the set of all edges ($d = 2$) or faces ($d = 3$) of elements of $\mathcal{T}_h$. Given an element $K \in (\mathcal{T}_h)_h$ we denote by $P_0(K)$ the space of constant functions on K. The discrete space

for the temperature is defined by

$$\mathbb{M}_h = \Big\{ v_h \in L^2(\Omega);\ \ \forall K \in \mathcal{T}_h,\, v_h|_K \in \mathcal{P}_0(K) \Big\}, \tag{2.42}$$

For the space aimed to approximate $\boldsymbol{p}$, we have decided to use the lowest order Raviart–Thomas element, introduced in [77], it is defined by

$$RT_0(K) = \boldsymbol{a} + \boldsymbol{x}b, \quad \boldsymbol{a} \in \mathbb{R}^d, b \in \mathbb{R}$$

The use of these elements to approximate $H(div;\Omega)$ is justified by the following proposition[15].

Proposition 2.30. *For any d-simplicial element K we have for $\boldsymbol{q} \in RT_0(K)$*

$$\begin{cases} div(\boldsymbol{q}) \in P_0(K), \\ \boldsymbol{q} \cdot \boldsymbol{n}|_{\partial K} \in R_0(\partial K). \end{cases}$$

Moreover, the divergence operator is surjective from $RT_0(K)$ onto $P_0(K)$.

where $R_0(\partial K)$ is the space of functions which are polynomials of degree 0 on each side or face of K. This also show the well-known $H(div;\Omega)$-conformity of this element.
Now we give the space used to approximate $H(div;\Omega)$:

$$\mathbb{X}_h = \Big\{ \boldsymbol{q}_h \in H(\mathrm{div};\Omega);\ \ \forall K \in \mathcal{T}_h,\, \boldsymbol{q}_h|_K \in RT_0(K) \Big\}, \qquad \mathbb{X}_h^0 = \mathbb{X}_h \cap \mathbb{X}, \tag{2.43}$$

With each e in ϵ_h, we associate the vector valued Raviart-Thomas basis function defined on each K that contains e by

$$\varphi_e(\boldsymbol{x}) = \frac{\boldsymbol{x} - \boldsymbol{a}}{d\,\mathrm{meas}(K)}, \tag{2.44}$$

where $\boldsymbol{a}$ is the vertex of K opposite to e, and equal to zero elsewhere. The degrees of freedom are the fluxes of vector filed φ_e for all the edges of the mesh[77] :

$$\int_b \varphi_e \cdot \boldsymbol{n}_e d\gamma = \delta_{e,f}, \quad \forall e, f \in \epsilon_h$$

A vector valued function $\boldsymbol{q} \in \mathbb{X}$ is a linear combination of the basis function φ_e :

$$\boldsymbol{q} = \sum_{e \in \epsilon_h} \boldsymbol{q}_e \varphi_e.$$

Remark 2.31. It is of course possible to use higher order elements. We work with the low cost finite element spaces defined above only for simplicity. It is also possible to use

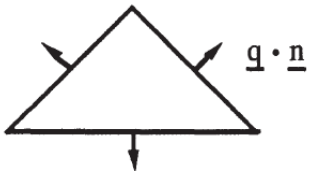

FIGURE 2.2: $2D$ RT_0 basis function

the so-called BDM_1 space (due to Brezzi, Douglas and Marini) instead of RT_0. Many extensions are possible and our feeling is that they do not arise any specific difficulty.

The discrete problem is now constructed from problem (2.17) by the Galerkin method, it reads
Find $(T_h, \boldsymbol{p}_h)$ *in* $\mathbb{M}_h \times \mathbb{X}_h^0$ *such that*

$$\begin{aligned} \forall \boldsymbol{q}_h \in \mathbb{X}_h^0, \quad & \int_\Omega \kappa^{-1}\, \boldsymbol{p}_h(\boldsymbol{x}) \cdot \boldsymbol{q}_h(\boldsymbol{x})\, d\boldsymbol{x} + \int_\gamma R(\boldsymbol{p}_h \cdot \boldsymbol{n})(\tau)(\boldsymbol{q}_h \cdot \boldsymbol{n})(\tau)\, d\tau \\ & \qquad + \int_\Omega (\operatorname{div} \boldsymbol{q}_h)(\boldsymbol{x}) T_h(\boldsymbol{x})\, d\boldsymbol{x} = \langle T_D, \boldsymbol{q}_h \cdot \boldsymbol{n} \rangle_{\Gamma_D}, \\ \forall v_h \in \mathbb{M}_h, \quad & \int_\Omega (\operatorname{div} \boldsymbol{p}_h)(\boldsymbol{x}) v_h(\boldsymbol{x})\, d\boldsymbol{x} = -\int_\Omega g(\boldsymbol{x}) v_h(\boldsymbol{x})\, d\boldsymbol{x}. \end{aligned} \tag{2.45}$$

Note that, due to the choice of $\mathbb{M}_h$ and $\mathbb{X}_h^0$, the discretization is fully conforming.

Proving the well-posedness of problem (2.17) relies on very similar arguments as for the continuous case and is based on Theorem 2.9. Let us introduce the kernel

$$\mathbb{K}_h = \Big\{ \boldsymbol{q}_h \in \mathbb{X}_h^0;\ \forall v_h \in \mathbb{M}_h,\ \int_\Omega (\operatorname{div} \boldsymbol{q}_h)(\boldsymbol{x}) v_h(\boldsymbol{x})\, d\boldsymbol{x} = 0 \Big\}. \tag{2.46}$$

Since, for each $\boldsymbol{q}_h$ in $\mathbb{X}_h^0$, the function $\operatorname{div} \boldsymbol{q}_h$ is constant on each element K of $\mathcal{T}_h$ thus $\operatorname{div} \boldsymbol{q}_h \in \mathbb{M}_h$, hence taking v_h equal to $\operatorname{div} \boldsymbol{q}_h$ we can see that $\mathbb{K}_h$ is characterized by

$$\mathbb{K}_h = \Big\{ \boldsymbol{q}_h \in \mathbb{X}_h^0,\ \ \operatorname{div} \boldsymbol{q}_h(\boldsymbol{x}) = 0 \Big\}.$$

and since $\mathbb{X}_h^0 \subset \mathbb{X}_h$ we have the following result.

Lemma 2.32. *The kernel* $\mathbb{K}_h$ *is imbedded in the kernel* $\mathbb{K}$.

Thus, the ellipticity property stated in Lemma 2.10 is still valid on $\mathbb{K}_h$. To proceed further, we introduce the so called Raviart–Thomas operator: for any $\boldsymbol{q}$ in $H(\operatorname{div}, \Omega)$,

$\Pi_h \boldsymbol{q}$ belongs to $\mathbb{X}_h$ and satisfies

$$\forall e \in \epsilon_h, \quad \int_e (\Pi_h \boldsymbol{q} \cdot \boldsymbol{n})(\tau)\, d\tau = \int_e (\boldsymbol{q} \cdot \boldsymbol{n})(\tau)\, d\tau. \tag{2.47}$$

It follows from the properties of the Raviart–Thomas element that the equations in (2.47) defines Π_h in a unique way, since on each edge $e \in \epsilon_h$, $\boldsymbol{q} \cdot \boldsymbol{n}$ is unique, see [13, Chap. VII, Lemma 3.19] for instance. We now state some properties of this operator.

Lemma 2.33. *The operator Π_h is continuous from $\mathbb{X}$ into $\mathbb{X}_h^0$. Moreover it satisfies*

$$\forall \boldsymbol{q} \in \mathbb{X}, \quad \|\Pi_h \boldsymbol{q}\|_{\mathbb{X}} \leq c \|\boldsymbol{q}\|_{\mathbb{X}}. \tag{2.48}$$

Proof. It follows from the definition (2.47) of the operator Π_h that it preserves the nullity of the normal component on Γ_N, hence maps $\mathbb{X}$ into $\mathbb{X}_h^0$. On the other hand, with each e in ϵ_h, we associate the bases functions of $\mathbb{X}_h$ φ_e defined on each K by equation (2.44). It is readily checked that

$$\Pi_h \boldsymbol{q} = \sum_{e \in \epsilon_h} \Big(\int_e (\boldsymbol{q} \cdot \boldsymbol{n})(\tau)\, d\tau \Big) \varphi_e,$$

We now proceed in three steps.
1) It follow from the previous formula and the continuity of the trace operator : $H(div;\Omega) \to H^{-1/2}(\partial\Omega)$ that

$$\|\Pi_h \boldsymbol{q}\|_{L^2(\Omega)} \leq C(\|\boldsymbol{q}\|_{L^2(\Omega)} + \|\operatorname{div} \boldsymbol{q}\|_{L^2(\Omega)}). \tag{2.49}$$

2) Since the divergence of each φ_e on any K that contains e is equal to $\frac{1}{\operatorname{meas}(K)}$, we have

$$\int_K (\operatorname{div} \Pi_h \boldsymbol{q})(\boldsymbol{x})\, d\boldsymbol{x} = \int_{\partial K} (\boldsymbol{q} \cdot \boldsymbol{n})(\tau)\, d\tau = \int_K (\operatorname{div} \boldsymbol{q})(\boldsymbol{x})\, d\boldsymbol{x}. \tag{2.50}$$

This leads to

$$\|\operatorname{div} \Pi_h \boldsymbol{q}\|_{L^2(\Omega)} \leq \|\operatorname{div} \boldsymbol{q}\|_{L^2(\Omega)}. \tag{2.51}$$

3) On the other hand, it is readily checked that, for each e contained in γ, there holds

$$\int_e (\Pi_h \boldsymbol{q} \cdot \boldsymbol{n})(\tau)\, d\tau = \int_e (\boldsymbol{q} \cdot \boldsymbol{n})(\tau)\, d\tau.$$

Hence, we obtain

$$\|\Pi_h \boldsymbol{q} \cdot \boldsymbol{n}\|_{L^2(\gamma)} \leq \|\boldsymbol{q} \cdot \boldsymbol{n}\|_{L^2(\gamma)}. \tag{2.52}$$

The desired result follows from (2.49), (2.50),(2.52) and the definition of the norm on $\mathbb{X}$ given by (2.14). ■

Fortunately, this technical proof leads to the inf-sup condition on the second form in problem (2.45).

Lemma 2.34. *The following inf-sup condition holds for a positive constant β_* independent of h*

$$\forall v_h \in \mathbb{M}_h, \quad \sup_{\boldsymbol{q}_h \in \mathbb{X}_h^0} \frac{\int_\Omega (\operatorname{div} \boldsymbol{q}_h)(\boldsymbol{x}) v_h(\boldsymbol{x})\, d\boldsymbol{x}}{\|\boldsymbol{q}_h\|_{\mathbb{X}}} \geq \beta_* \|v_h\|_{L^2(\Omega)}. \tag{2.53}$$

Proof. Let v_h be any function in $\mathbb{M}_h$. In the proof of Lemma (2.11), we have exhibited a function $\boldsymbol{q}$ in $\mathbb{X}$ such that $\operatorname{div} \boldsymbol{q} = v_h$ and

$$\|\boldsymbol{q}\|_{\mathbb{X}} \leq c \|v_h\|_{L^2(\Omega)}.$$

We have

$$\int_\Omega (\operatorname{div} \Pi_h \boldsymbol{q})(\boldsymbol{x}) v_h(\boldsymbol{x})\, d\boldsymbol{x} = \sum_{K \in \mathcal{T}_h} v_h|_K \int_K (\operatorname{div} \Pi_h \boldsymbol{q})(\boldsymbol{x})\, d\boldsymbol{x},$$

whence from (2.50)

$$\int_\Omega (\operatorname{div} \Pi_h \boldsymbol{q})(\boldsymbol{x}) v_h(\boldsymbol{x})\, d\boldsymbol{x} = \sum_{K \in \mathcal{T}_h} v_h|_K \int_K (\operatorname{div} \boldsymbol{q})(\boldsymbol{x})\, d\boldsymbol{x} = \|v_h\|^2_{L^2(\Omega)}.$$

hence

$$\frac{\int_\Omega (\operatorname{div} \Pi_h \boldsymbol{q})(\boldsymbol{x}) v_h(\boldsymbol{x})\, d\boldsymbol{x}}{\|q\|_{\mathbb{X}}} = \frac{\|v_h\|^2_{L^2(\Omega)}}{\|q\|_{\mathbb{X}}}$$

On the other hand, it follows from Lemma 2.33 that

$$\|\Pi_h \boldsymbol{q}\|_{\mathbb{X}} \leq c \|\boldsymbol{q}\|_{\mathbb{X}} \leq c' \|v_h\|_{L^2(\Omega)}.$$

hence we have

$$\begin{aligned} \frac{\int_\Omega (\operatorname{div} \Pi_h \boldsymbol{q})(\boldsymbol{x}) v_h(\boldsymbol{x})\, d\boldsymbol{x}}{\|q\|_{\mathbb{X}}} &\geq \frac{\|v_h\|^2_{L^2(\Omega)}}{c' \|v_h\|_{L^2(\Omega)}} \\ &= \frac{1}{c'} \|v_h\|_{L^2(\Omega)} \end{aligned}$$

Which yields the desired condition. ■

The well-posedness of the discrete problem (2.45) is now a direct consequence of Lemmas 2.10 (combined with Lemma 2.32) and 2.34 and Theorem 2.9.

Theorem 2.35. *For any data g in $L^2(\Omega)$ and T_D in $H^{\frac{1}{2}}(\Gamma_D)$, problem (2.45) has a unique solution $(T_h, \boldsymbol{p}_h)$ in $\mathbb{M}_h \times \mathbb{X}_h^0$. Moreover this solution satisfies*

$$\|T_h\|_{L^2(\Omega)} + \|\boldsymbol{p}_h\|_{\mathbb{X}} \leq c\Big(\|g\|_{L^2(\Omega)} + \|T_D\|_{H^{\frac{1}{2}}(\Gamma_D)}\Big). \tag{2.54}$$

We are also in a position to derive an a priori error estimate between the continuous and discrete solutions. We begin with the following version of the Strang's lemma.

Lemma 2.36. *The following bound holds between the solution $(T, \boldsymbol{p})$ of problem (2.17) and the solution $(T_h, \boldsymbol{p}_h)$ of problem (2.45)*

$$\begin{aligned} &\|\boldsymbol{p} - \boldsymbol{p}_h\|_{\mathbb{X}} \leq c\,\|\boldsymbol{p} - \Pi_h \boldsymbol{p}\|_{\mathbb{X}}, \\ &\|T - T_h\|_{L^2(\Omega)} \leq c\Big(\|\boldsymbol{p} - \Pi_h \boldsymbol{p}\|_{\mathbb{X}} + \inf_{S_h \in \mathbb{M}_h} \|T - S_h\|_{L^2(\Omega)}\Big). \end{aligned} \tag{2.55}$$

Proof. We prove successively the two estimates.
1) We first observe from (2.50) that $\Pi_h \boldsymbol{p} - \boldsymbol{p}_h$ belongs to the kernel $\mathbb{K}_h$. Then, we derive from Lemmas 2.10 and 2.32 that

$$\|\Pi_h \boldsymbol{p} - \boldsymbol{p}_h\|_{\mathbb{X}}^2 \leq c\left(\int_\Omega \kappa^{-1}\,(\Pi_h \boldsymbol{p} - \boldsymbol{p}_h)^2(\boldsymbol{x})\,d\boldsymbol{x} + \int_\gamma R\Big((\Pi_h \boldsymbol{p} - \boldsymbol{p}_h)\cdot \boldsymbol{n}\Big)^2(\tau)\,d\tau\right).$$

By using first problem (2.45) and second problem (2.17), this yields

$$\begin{aligned} \|\Pi_h \boldsymbol{p} - \boldsymbol{p}_h\|_{\mathbb{X}}^2 &\leq c\left(\int_\Omega \kappa^{-1}\,\Pi_h \boldsymbol{p}(\boldsymbol{x}) \cdot (\Pi_h \boldsymbol{p} - \boldsymbol{p}_h)(\boldsymbol{x})\,d\boldsymbol{x}\right. \\ &\quad \left. + \int_\gamma R(\Pi_h \boldsymbol{p}\cdot \boldsymbol{n})(\tau)\Big((\Pi_h \boldsymbol{p} - \boldsymbol{p}_h)\cdot \boldsymbol{n}\Big)(\tau)\,d\tau - \langle T_D, \Pi_h \boldsymbol{p} - \boldsymbol{p}_h\rangle_{\Gamma_D}\right) \\ &\leq c\left(\int_\Omega \kappa^{-1}\,(\Pi_h \boldsymbol{p} - \boldsymbol{p})(\boldsymbol{x}) \cdot (\Pi_h \boldsymbol{p} - \boldsymbol{p}_h)(\boldsymbol{x})\,d\boldsymbol{x}\right. \\ &\quad \left. + \int_\gamma R\Big((\Pi_h \boldsymbol{p} - \boldsymbol{p})\cdot \boldsymbol{n}\Big)(\tau)\Big((\Pi_h \boldsymbol{p} - \boldsymbol{p}_h)\cdot \boldsymbol{n}\Big)(\tau)\,d\tau\right) \\ &\leq c\left(\|\Pi_h \boldsymbol{p} - \boldsymbol{p}\|^2_{L^2(\Omega)^2} + \|\Pi_h \boldsymbol{p} - \boldsymbol{p}\|^2_{L^2(\gamma)}\right) \\ &\leq c\,\|\Pi_h \boldsymbol{p} - \boldsymbol{p}\|_{\mathbb{X}}. \end{aligned} \tag{2.56}$$

and we conclude the bound for $\|\boldsymbol{p}-\boldsymbol{p}_h\|_{\mathbb{X}}$ thanks to a triangle inequality.

$$\begin{aligned}\|\boldsymbol{p}-\boldsymbol{p}_h\|_{\mathbb{X}} &= \|\boldsymbol{p}-\Pi_h\boldsymbol{p}+\Pi_h\boldsymbol{p}-\boldsymbol{p}_h\|_{\mathbb{X}}\\ &\le \|\boldsymbol{p}-\Pi_h\boldsymbol{p}\|_{\mathbb{X}}+\|\Pi_h\boldsymbol{p}-\boldsymbol{p}_h\|_{\mathbb{X}}\\ &\le c\,\|\boldsymbol{p}-\Pi_h\boldsymbol{p}\|_{\mathbb{X}} \quad \textit{using (2.56)}.\end{aligned}$$

2) To prove the second estimate, we apply the inf-sup condition (2.53): For any S_h in $\mathbb{M}_h$,

$$\|T_h-S_h\|_{L^2(\Omega)} \le \beta_*^{-1} \sup_{\boldsymbol{q}_h\in\mathbb{X}_h^0} \frac{\int_\Omega (\operatorname{div}\boldsymbol{q}_h)(\boldsymbol{x})(T_h-S_h)(\boldsymbol{x})(\boldsymbol{x})\,d\boldsymbol{x}}{\|\boldsymbol{q}_h\|_{\mathbb{X}}}.$$

By using problems (2.45) and (2.17), we obtain

$$\begin{aligned}&\int_\Omega (\operatorname{div}\boldsymbol{q}_h)(\boldsymbol{x})(T_h-S_h)(\boldsymbol{x})(\boldsymbol{x})\,d\boldsymbol{x}\\ &= \langle T_D,\boldsymbol{q}_h\cdot\boldsymbol{n}\rangle_{\Gamma_D} - \int_\Omega \kappa^{-1}\,\boldsymbol{p}_h(\boldsymbol{x})\cdot\boldsymbol{q}_h(\boldsymbol{x})\,d\boldsymbol{x}\\ &- \int_\gamma R(\boldsymbol{p}_h\cdot\boldsymbol{n})(\tau)(\boldsymbol{q}_h\cdot\boldsymbol{n})(\tau)\,d\tau - \int_\Omega (\operatorname{div}\boldsymbol{q}_h)(\boldsymbol{x})S_h(\boldsymbol{x})(\boldsymbol{x})\,d\boldsymbol{x}\\ &= \int_\Omega \kappa^{-1}\,(\boldsymbol{p}-\boldsymbol{p}_h)(\boldsymbol{x})\cdot\boldsymbol{q}_h(\boldsymbol{x})\,d\boldsymbol{x}\\ &+ \int_\gamma R\Big((\boldsymbol{p}-\boldsymbol{p}_h)\cdot\boldsymbol{n}\Big)(\tau)(\boldsymbol{q}_h\cdot\boldsymbol{n})(\tau)\,d\tau + \int_\Omega (\operatorname{div}\boldsymbol{q}_h)(\boldsymbol{x})(T-S_h)(\boldsymbol{x})(\boldsymbol{x})\,d\boldsymbol{x}.\end{aligned}$$

All this gives

$$\|T_h-S_h\|_{L^2(\Omega)} \le c\Big(\|\boldsymbol{p}-\boldsymbol{p}_h\|_{\mathbb{X}}+\|T-S_h\|_{L^2(\Omega)}\Big),$$

and we conclude by using a triangle inequality.

$$\begin{aligned}\|T-T_h\|_{L^2(\Omega)} &= \|T-S_h+S_h-T_h\|_{L^2(\Omega)}\\ &\le \|T-S_h\|_{L^2(\Omega)}+\|S_h-T_h\|_{L^2(\Omega)}\\ &\le \|T-S_h\|_{L^2(\Omega)}+c\Big(\|\boldsymbol{p}-\boldsymbol{p}_h\|_{\mathbb{X}}+\|T-S_h\|_{L^2(\Omega)}\Big)\\ &\le c\Big(\|\boldsymbol{p}-\Pi_h\boldsymbol{p}\|_{\mathbb{X}}+\inf_{S_h\in\mathbb{M}_h}\|T-S_h\|_{L^2(\Omega)}\Big). \quad \textit{using first estimate in (2.55)}\end{aligned}$$

■

Evaluating the distance of T to $\mathbb{M}_h$ relies on fully standard arguments, see [13, Chap. IX, Th. 2.1] for instance. On the other hand, we deduce from Lemma 2.33 that, for all $\boldsymbol{q}_h$ in $\mathbb{X}_h^0$,

$$\|\boldsymbol{p}-\Pi_h\boldsymbol{p}\|_{\mathbb{X}} \le \|\boldsymbol{p}-\boldsymbol{q}_h\|_{\mathbb{X}}+\|\Pi_h(\boldsymbol{p}-\boldsymbol{q}_h)\|_{\mathbb{X}} \le c\,\|\boldsymbol{p}-\boldsymbol{q}_h\|_{\mathbb{X}},$$

and we take $\boldsymbol{q}_h$ equal to the interpolate of $\boldsymbol{p}$ by piecewise affine functions, see [13, Chap. IX, Prop. 1.4].

We are in position to provide the error estimate. We need first to complete the notation. We define the space

$$\mathbb{X}^{s,r} = \Big\{ \boldsymbol{q} \in \mathbb{X}; \quad (\boldsymbol{q}, \operatorname{div} \boldsymbol{q})|_{\Omega_S} \in H^s(\Omega_S)^{d+1}; \\ (\boldsymbol{q}, \operatorname{div} \boldsymbol{q})|_{\Omega_G} \in H^r(\Omega_G)^{d+1}; \quad (\boldsymbol{q} \cdot \boldsymbol{n})|_\gamma \in H^{\min\{s,r\}}(\gamma) \Big\}.$$

The following result is a direct consequence of Lemma 2.36.

Theorem 2.37. *Assume that the solution $(T, \boldsymbol{p})$ of problem (2.17) is such that*

$$\boldsymbol{p} \in \mathbb{X}^{s,r}, \qquad T \in H^s(\Omega_S) \times H^r(\Omega_G),$$

for real numbers s, r such that $0 \leq s, r \leq 1$. Then, the following a priori error estimate holds between this solution and the solution $(T_h, \boldsymbol{p}_h)$ of problem (2.45)

$$\|\boldsymbol{p} - \boldsymbol{p}_h\|_{\mathbb{X}} + \|T - T_h\|_{L^2(\Omega)} \leq c h^{\min\{s,r\}} \left(\|\boldsymbol{p}\|_{\mathbb{X}^{s,r}} + \|T_S\|_{H^s(\Omega_S)} + \|T_G\|_{H^r(\Omega_G)} \right). \quad (2.57)$$

Remark 2.38. Estimate (2.57) is fully optimal and proves the convergence of the discretization. Likely, super-convergence results as in Theorem 2.27 could be obtained on the field $\boldsymbol{p}$. Unfortunately we did not succeed in doing so. Nevertheless the numerical experiments we run show that this super-convergence takes place.

2.5 Numerical experiments

In this section we present two numerical tests for solving problem (2.2) that were conducted in order to evaluate the ability of the Lagrange finite elements to produce accurate results for some simple geometries and compare this to the results obtained using the Hybrid Dual Finite Element method using Raviart-Thomas lowest order elements presented in the previous section. These numerical tests aim also to asses the a-priori error estimates results demonstrated in Section 2.3 and in particular the super-convergence provided in Theorem 2.27. In all examples, we underline the pertinence of the convergence rate proved here. A third numerical test is made using an 2D-cut from an X-ray image of a real graphite foam matrix infiltrated with a salt using the Raviart-Thomas finite element

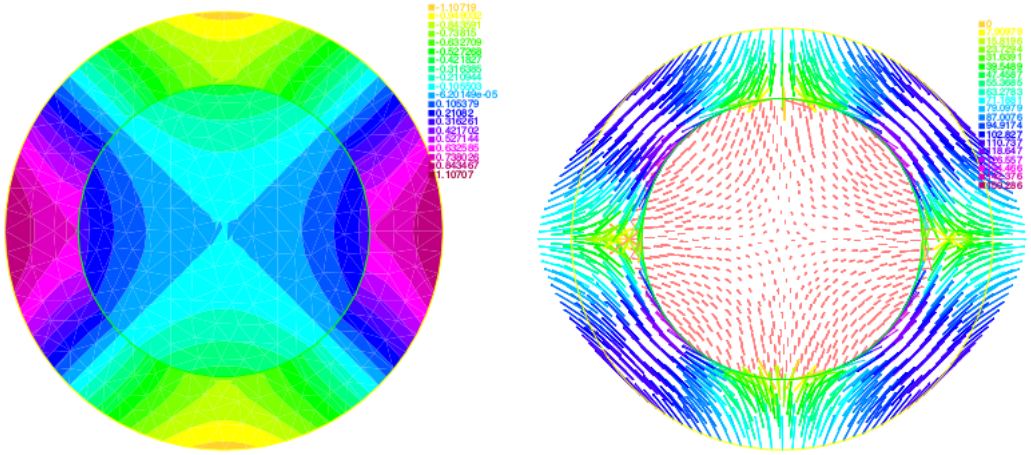

FIGURE 2.3: Temperature field T. Heat vector field $\boldsymbol{p}$.

method. We note that the Lagrange finite element method is implemented using a domain decomposition method given in [48] which prevent from having to change the data structure of the finite element. The computational study is conducted by means of the code `FreeFem++` developed by F. Hecht and his team (see [41], [43], [42]).

2.5.1 An explicit solution

In this first example we have chosen the domain as well as the boundary conditions in a way that allow to explicitly determine the exact solution of problem (2.2). Thus Ω is taken to be the disc centered at the origin with radius 1.5. The sub-domain Ω_S coincides with the unit circle and the sub-domain Ω_G is then the annulus with double radius $(1, 1.5)$. The exact solution T is given by

$$\begin{aligned} T_S(x_1, x_2) &= a(x_1^2 - x_2^2), \\ T_G(x_1, x_2) &= (x_1^2 - x_2^2)\left(b + \frac{c}{(x_1^2 + x_2^2)^2}\right). \end{aligned} \tag{2.58}$$

The conductivities are chosen so that $(\kappa_S, \kappa_G) = (1, 100)$ and the contact resistivity is fixed to $R = 0.5$. The coefficients a, b, c are computed owing to the interface conditions so as the Dirichlet datum enforced on the whole boundary $\partial\Omega$ which is provided by

$$T_D(x_1, x_2) = \frac{4}{9}(x_1^2 - x_2^2).$$

The temperature T and the heat vector field $\boldsymbol{p} = \kappa \nabla T$ are represented in Figure 2. Next, we compute the discrete solutions T_h by Lagrangian finite element method and $(T_h, \boldsymbol{p}_h)$ by hybrid dual finite element method, for various meshes. The gap with the exact $(T, \boldsymbol{p})$ is evaluated in the L^2-norm. In the Lagrange computations, the vector field $\boldsymbol{p}_h$ is not an independent unknown. It is indeed derived by computing the gradient of T_h and is then piecewise constant. Figure 3 provides the errors for both methods in logarithmic scales. To check out the convergence rates for each method we need the slopes of the linear regressions of the error curves. In the Lagrange method, we found the slopes $(1.92, 0.99)$ for the temperature T and the heat vector field $\boldsymbol{p}$. Those in the dual hybrid method are given by $(1.19, 1.04)$. Given that the effective smoothness of the exact temperature is higher than $H^2(\Omega_S) \times H^2(\Omega_G)$, the convergence speed is hence limited only by the degree of the finite elements we use. This is in agreement with the theoretical predictions in Theorem 3.2, Proposition 3.4 and Theorem 4.7.

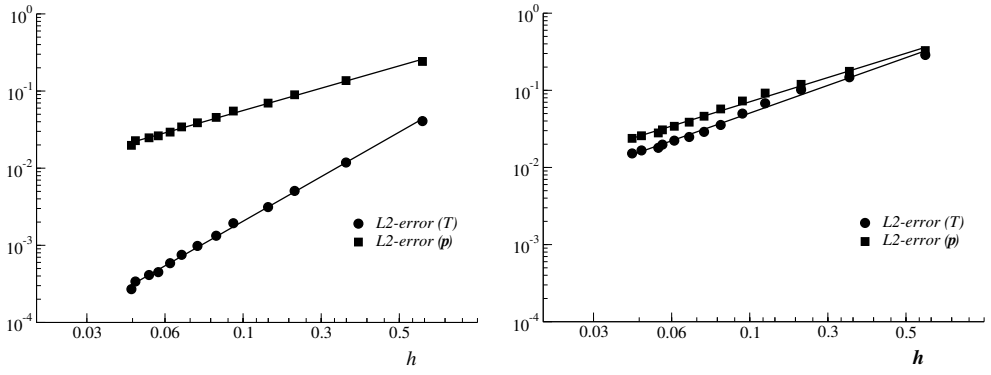

FIGURE 2.4: Convergence curves. Lagrange FEM (left) and hybrid dual FEM (right)

2.5.2 A singular solution

In the second experiment we pursue an approximation of a singular solution. The domain Ω is a disc centered at the origin with radius 0.5. The internal sub-domain Ω_S is a triangle. The geometry can be seen in Figure 4. The circular boundary $\partial\Omega$ is subjected to the following Dirichlet condition (here also $\Gamma_N = \emptyset$)

$$T_D(x_1, x_2) = 2e^{2(x_1 - x_2)} \cos(\frac{\pi}{2}(x_1 + x_2)).$$

The thermal parameters are unchanged compared with the first test, that is $\kappa_G = 100, \kappa_S = 1$ and $R = 0.5$. The isolines of the solution are represented in Figure 4.

Following the theoretical discussion in Section 3.2, only Ω_G is expected to suffer from the singularities born at the vicinity of the vertices of Ω_S. The convergence rate (in Ω_G) is lower than one for the heat vector field $\boldsymbol{p}$. It is expected to be equal to $4/7$ or may be to $2/3$ if the singularity created by the right angle is more intensive than the two others. A careful examination of the heat vector field plot provided in Figure 4 seems to corroborate this fact. The stress intensity factor at the right angle is substantially higher than for the two acute angles.
The accuracy in the convex set Ω_S should not slow down and the decreasing rate is excepted to be linear here again.

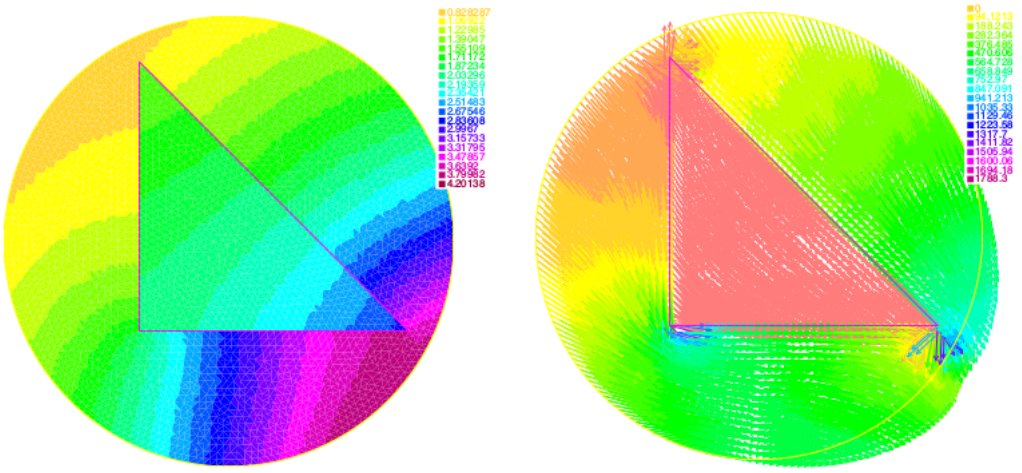

FIGURE 2.5: Singular temperature T. Singular heat vector field $\boldsymbol{p} = \kappa \nabla T$.

Now, to check out these claims, we compute a reference finite element solution $(T_h, \boldsymbol{p}_h)$ using a high resolution mesh and assimilate it to the exact $(T, \boldsymbol{p})$. Then, we run numerical simulations using meshes with moderate sizes. The slopes of linear regressions of the convergence curves are $(1.93, 0.97)$ for $(T, \boldsymbol{p})$ in the internal sub-domain Ω_S and $(1.52, 0.70)$ in the sub-domain Ω_G. The convergence in Ω_S seems to be of order one for $\boldsymbol{p}$ and of a second order for T. The lower order convergence observed in Ω_G is an illustration of the effectiveness of the angular singularity which is responsible of the slowing down of the convergence speed. These trends are almost in perfect agreement with the theoretical findings concerning the convergence for $\boldsymbol{p}$. Concerning the special behavior of the error on T in the hybrid method, we fall short in the proof of the observed convergence rate. This is still an open question.

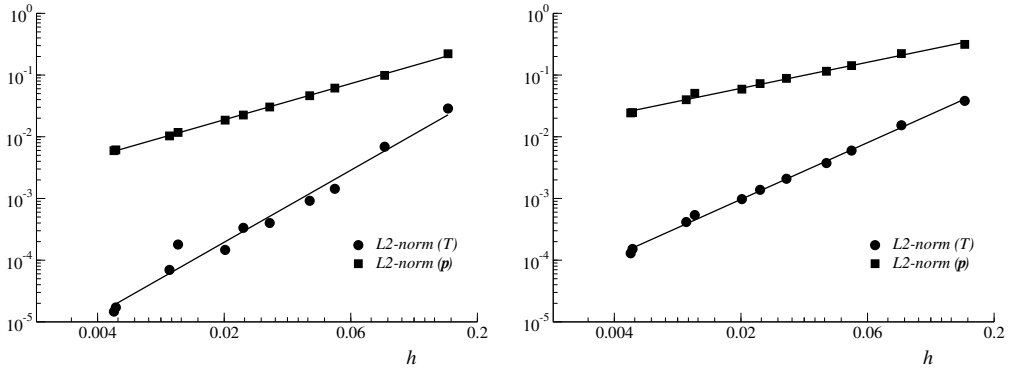

FIGURE 2.6: Accuracy curves for the Lagrange FEM in Ω_S (left) and in Ω_G (right).

Switching to the hybrid dual solutions, the convergence rates are all expected to be linear except for the heat field $\boldsymbol{p}$ in the external sub-domain Ω_G. The slope for the linear regression of the accuracy curve for $\boldsymbol{p}|_{\Omega_G}$ is close to 0.64. The convergence rates evaluated in Ω_S give $(0.96, 1.01)$ for $(T, \boldsymbol{p})$.

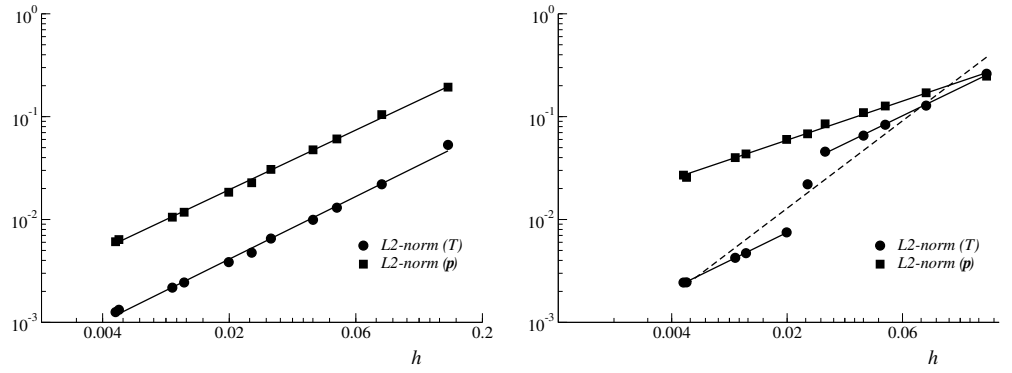

FIGURE 2.7: Accuracy curves for the hybrid dual FEM in Ω_S (left) and in Ω_G (right).

Finally, the curve for the L^2-error on T in Ω_G seems a little bit strange. The apparent slope of the linear regression (dashed line) is 1.41 and it does not seem pertinent. However a closer look to that curve shows that it has separate components, the slope of each is not far form one as we have 0.90 a for the first component and 0.91 for the last one. We unfortunately have no explanation of this break off in the convergence curve. None of the observations made here on the super-convergence in the sub-domain Ω_S, is mathematically proved. Nevertheless, they are in a perfect accordance with the common feeling.

2.5.3 A realistic geometry

We conclude with an example of a realistic geometry depicted in Figure 2.1, right part. As indicated earlier running computations can be reasonably achieved for the hybrid dual method. The composite medium we consider is a small sample with a rectangular shape. The width is equal to 0.003222 while the length is 0.005382. Almost a fraction four fifths of the media is made of salt which corresponds to the yellow part of the domain in Figure 1. The remaining one fifth fraction is composed of graphite and is colored in red. The sample is differentially heated along horizontal walls. The temperature is then fixed to $T_D = 587$ along the upper wall. It is given by $T_D = 577$ along the lower wall. Both vertical walls are adiabatic. The conductivities are chosen to be $\kappa_S = 1$ and $\kappa_G = 500$. They are close to the real conductivities of the graphite and to the sodium chloride. We realized two simulations. In one the resistance is given by $R = 5 \times 10^{-4}$ and in the other it is equals $R = 5 \times 10^{-2}$. The temperature fields are depicted in Figure 7. For larger resistance the diffusion process of the heat from the upper wall towards the lower wall is somehow slowed down, especially in the right side of the sample. Indeed, the heat has to flow across more interfaces there than in the left side of the sample. These computations bring to light the efficiency of the discretization that we propose.

2.6 Conclusion

Hybrid dual finite elements and alike methods sound well fit for the numerical simulation of the heat diffusion in composite media with contact resistance. The reason why we undertook this work is the feasibility and implementation facility. Using hybrid dual finite elements enables users to build their simulations on existing data structures in softwares. The intervention of programmers is limited to the definition of the variational problem to solve. Things are obviously different for Lagrangian finite elements especially for complex geometry such as the one considered in the third example in numerical section. Indeed, the finite element structure in scientific computing codes has to be revisited and drastically modified to account for the local continuity/global discontinuity. The numerical analysis conducted here shows the reliability of the mixed Raviart-Thomas/piecewise constant finite elements $RT_0/\mathcal{P}_0$ to provide accurate discrete solutions to problem (2.2).

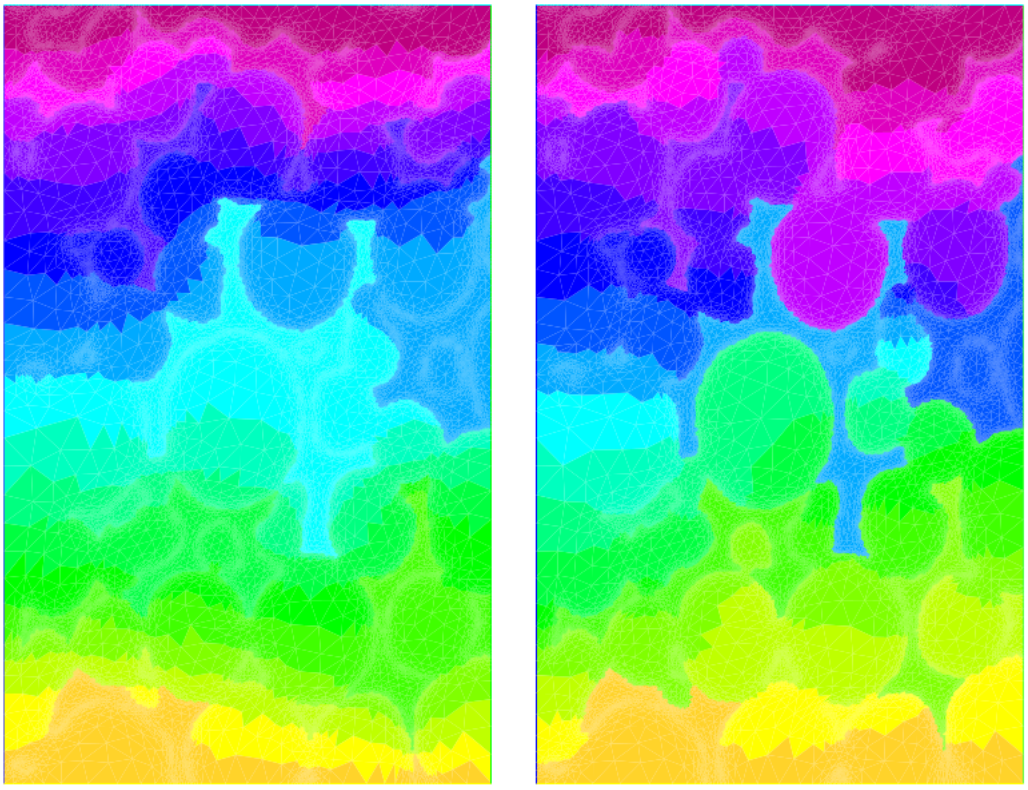

FIGURE 2.8: Two simulations for a realistic domain.

Chapter 3

Two Phases Stefan Problem with Smoothed Enthalpy

Abstract

The enthalpy regularization is a preliminary step in many numerical methods for the simulation of phase change problems. It consists in smoothing the discontinuity (of the enthalpy) caused by the latent heat of fusion and yields a thickening of the free boundary. The phase change occurs in a curved strip, i.e. the mushy zone, where solid and liquid phases are present simultaneously. The width ϵ of this (mushy) region is most often considered as the parameter to control the regularization effect. The purpose we have in mind is a rigorous study of the effect of the process of enthalpy smoothing. The melting Stefan problem we consider is set in a semi-infinite slab, heated at the extreme-point. After proving the existence of an auto-similar temperature, solution of the regularized problem, we focus on the convergence issue as $\epsilon \to 0$. Estimates found in the literature predict an accuracy like $\sqrt{\epsilon}$. We show that the thermal energy trapped in the mushy zone decays exactly like $\sqrt{\epsilon}$, which indicates that the global convergence rate of $\sqrt{\epsilon}$ cannot be improved. However, outside the mushy region, we derive a bound for the gap between the smoothed and exact temperature fields that decreases like ϵ. We also present some numerical computations to validate our results.

3.1 Introduction

Two-phase Stefan problem is a basic model for melting (or solidification) of phase change materials. The unknowns are the temperature field and the location of the melting front delimiting the liquid and solid phases. The front, also called interphase or the free boundary, is dynamic and the moving velocity is given by the Stefan conditions which express the energy conservation and involve the latent heat of fusion absorbed during the melting process. Mathematically, the resulting problem is non-linear, with an enthalpy jump along the liquid-solid interface. In spite of these complications, Stefan problem is widely used because of the availability of an analytical form of the exact solution in some standard geometries (see [4, 91]). It is also a benchmark for testing and assessing mathematical and numerical methods developed for phase transition problems (cf. [4, 40] and references therein).

The discontinuity of enthalpy is a source of difficulty for computation. Many numerical methods, especially those based on the enthalpy derivatives such as implicit time schemes with Newton type algorithms, start by embedding the original problem into a collection of regularized problems (see [4, 29, 39, 54]). The enthalpy function becomes continuous and (piecewise) differentiable. As a result, the sharp front disappears and we have instead a mushy zone where solid and liquid phases are present simultaneously. We are interested in, first, the analysis of the smoothed version of Stefan problem, then we deal with the convergence of the regularized solution with respect to the width ϵ of the mushy zone. We recall that this question has been addressed in the specialized literature where convergence results are established [66, 50]. They predict that the gap between the smoothed and the exact solutions decays like $\sqrt{\epsilon}$, in the energy norm. We aim at investigating the distribution of the error to have a better insight of the accuracy inherent to the regularizing process. In particular, we zoom in the mushy zone to show that it is responsible of 'slowing down' of the convergence to $\sqrt{\epsilon}$. Outside the mushy zone, we derive an order ϵ convergence rate. This sharp analysis is conducted for phase change problem in a semi-infinite slab. The substantial advantages of such a choice is the availability of analytical form of the (exact and smoothed) temperature fields, owing to Neumann similarity.

The outline of the paper is as follows. In Section 3.2, we set up the two phase Stefan problem modeling a melting process in a semi-infinite slab. We describe how the enthalpy is smoothed to become a single valued function. In Section 3.3, we prove the existence of a Neumann auto-similar solution to the heat equation when arbitrary regularization is applied. Mathematical tools used here come from the theory of ordinary

differential equation, easier than variational methods especially in unbounded domains. Using the Cauchy-Lipschitz theorem, we are able to derive useful qualitative features of the smoothed temperature and enthalpy fields. These properties are helpful in the convergence analysis conducted in Section 3.4 for piecewise linear enthalpy smoothing. We begin by showing that the mushy zone, of width ϵ, comes close to the free boundary with an accuracy of ϵ. Then, we prove that the thermal energy trapped in that mushy zone behaves exactly like $c\sqrt{\epsilon}$. This is an indication why the global convergence rate given in [50] can not be improved. We also provide a bound of order ϵ on the gap between regularized and exact temperature field outside the mushy region. We emphasize that the key of the study is the availability of analytical solutions to the regularized problems we deal with. Numerical experiments using SCILAB are presented at the end to validate the theoretical predictions.

Notations — Let $I \subset \mathbb{R}$ be an open interval. We denote by $L^2(I)$ the space of measurable and square integrable functions on X. The space $\mathscr{C}(I)$ contains the continuous functions on I and $\mathscr{C}^1(I)$ is for these space of functions that are continuously differentiable. To alleviate the presentation we use the symbols φ and ψ $(= 1 - \varphi)$ for the error and complementary error functions which were usually denoted by the symbols (erf) and (erfc) in the literature (see [1]).

3.2 Enthalpy smoothing

The two phase Stefan problem can be expressed as a heat conduction problem in a semi-infinite slab geometrically represented by $I = (0, \infty)$. We set $Q = I \times]0, \infty[$. The generic point in I is denoted by x and the generic time is t. The slab is initially solid at the temperature $T(\cdot, 0) = 0$. It is then gradually melted by imposing the temperature $T(0, \cdot)$ to a fixed value T_1, larger than the melting temperature T_m. We have $T_1 > T_m > 0$. We therefore introduce the enthalpy function,

$$E(\theta) = \lambda\theta + Lf(\theta),$$

where $f(\theta)$ is the fraction of liquid phase at the temperature θ. There is a range of the possible values of f at the fusion temperature T_m. Hence, f is multi-valued and is defined

by

$$f(\theta) = \begin{cases} 0 & \theta < T_m \\ [0,1] & \theta = T_m \\ 1 & \theta > T_m \end{cases} .$$

We have set

$$\lambda = (\rho C)\kappa^{-1}, \qquad L = (\rho L_a)\kappa^{-1},$$

where L_a is the latent heat of fusion, the density ρ, the specific heat capacity C and the conductivity κ are supposed to have the same values in the solid and liquid phases. This choice is made only by the desire to simplify the presentation. The overall results we develop here extend as well to account for different options, at the cost of more technical calculations.

The temperature distribution is a solution of the following enthalpy problem: *find* (T, H) *with* $H \in E(T)$ *and*

$$\begin{aligned} \partial_t H - \partial_{xx} T = 0 \qquad & \text{in } Q, \\ T(0,\cdot) = T_1, \quad T(\infty,\cdot) = 0 \qquad & \text{on } (0,\infty), \\ T(\cdot,0) = 0 \qquad & \text{on } I. \end{aligned} \tag{3.1}$$

The notation $T(\infty,\cdot)$ should be taken in the sense of the limit $x \to \infty$. This is the two phase Stefan problem that can be formulated as a free boundary problem. Considering $X(t)$ as the melted depth of the solid phase which is a function of time; the Stefan problem consists of finding (T, X) such that

$$\begin{aligned} \lambda\partial_t T - \partial_{xx} T = 0 \qquad & \text{in } (0, X(t)) \times (0,\infty), \\ \lambda\partial_t T - \partial_{xx} T = 0 \qquad & \text{in } (X(t),\infty) \times (0,\infty), \\ X(0) = 0, \quad T(X(t),t) = T_m, \quad L(\partial_t X)(t) = [\partial_x T](X(t),t), \qquad & \text{in } (0,\infty), \\ T(0,\cdot) = T_1, \quad T(\infty,\cdot) = 0 \qquad & \text{on } (0,\infty), \\ T(\cdot,0) = 0 \qquad & \text{on } I. \end{aligned} \tag{3.2}$$

The unknowns are the temperature field T and the moving interface position $X(\cdot)$. This problem has been solved analytically (cf., for instance, [95, 82, 40]). The auto-similar Neumann solution is given by

$$T(x,t) = u(\frac{x}{\sqrt{t}}), \qquad X(t) = \alpha\sqrt{t}.$$

Plugging these expression into problem (3.2), we come up with some differential equations. Solving them provides the solution

$$\begin{aligned} u(\zeta) &= A\phi(\omega\zeta) + T_1, \qquad \forall \zeta \in [0, \alpha[, \\ u(\zeta) &= D\psi(\omega\zeta), \qquad \forall \zeta \in]\alpha, \infty[, \end{aligned} \tag{3.3}$$

where the symbols ω, A, D are

$$\omega = \frac{\sqrt{\lambda}}{2}, \qquad A = -\frac{T_1 - T_m}{\phi(\omega\alpha)}, \qquad D = \frac{T_m}{\psi(\omega\alpha)}.$$

The coefficient $\alpha > 0$, determining the melting front, is the unique positive solution of the following transcendental equation

$$\frac{T_1 - T_m}{\phi(\omega\alpha)} - \frac{T_m}{\psi(\omega\alpha)} - \left(\frac{\sqrt{\pi}L}{4\omega}\right)\alpha e^{(\omega\alpha)^2} = 0. \tag{3.4}$$

The multi-valued enthalpy function is usually smoothed for numerical and computational feasibility. The regularized value problem can be handled by means of standard functional tools for non linear partial differential equations, and its numerical approximation is easier than for differential inclusions (see [8]). Indeed, regularization is highly recommended when an implicit time scheme and a Newton method is used for the enthalpy.

Smoothing the enthalpy consists in replacing f by a single-valued smoothed function f_ε. We are therefore in the case of non-isothermal phase change (see, eg [44]). The function f_ε we select here is piecewise linear, as commonly used in the literature:

$$f_\epsilon(\theta) = \begin{cases} 0 & \theta < (T_m)^- \\ \dfrac{1}{2\varepsilon}(\theta - (T_m)^-) & \theta \in [(T_m)^-, (T_m)^+] \\ 1 & \theta > (T_m)_+ \end{cases}, \tag{3.5}$$

where we have set $(T_m)^\pm = T_m \pm \varepsilon$. When close to zero, the parameter $\epsilon > 0$ controls the approximation of f by f_ε. The resulting enthalpy function is therefore

$$E_\epsilon(\theta) = \lambda\theta + Lf_\epsilon(\theta) = \begin{cases} \lambda\theta & \theta < (T_m)^- \\ \lambda_\varepsilon\theta + L_\varepsilon & \theta \in [(T_m)^-, (T_m)^+] \\ \lambda\theta + L & \theta > (T_m)^+ \end{cases},$$

where we have set

$$\lambda_\varepsilon = (\lambda + \frac{L}{2\epsilon}), \qquad L_\varepsilon = -\frac{L}{2\epsilon}(T_m)^-.$$

The mushy zone is then defined by the range $(T_m)^- \leq \theta \leq (T_m)_+$.

Remark 3.1. Many examples of smoothing enthalpy functions f_ε may be found in the literature and may be classified into two categories according to whether they agree with f away from T_m. In our case, we have that $f_\varepsilon = f$ in $\mathbb{R}\backslash](T_m)^-, (T_m)^+[$. Here we provide some examples that do not coincide with f (away from T_m),

$$f_\epsilon(\theta) = \frac{1}{2}\left(1 + \frac{\theta - T_m}{\sqrt{(\theta - T_m)^2 + \epsilon^2}}\right), \qquad f_\epsilon(\theta) = \frac{1}{2}\left(1 + \tanh\frac{\theta - T_m}{\epsilon}\right). \tag{3.6}$$

Below, we plot, in the left panel, the exact fraction function f (dashed line) with $T_m = 0$ and the piecewise linear smoothed function f_ε (solid line). In the right panel, both examples in (3.6) are represented, the first with a dashed line and the second with a solid line.

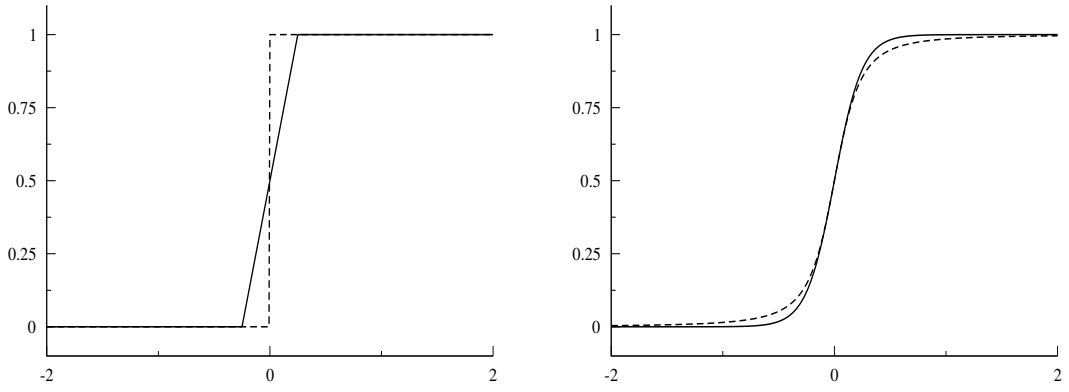

FIGURE 3.1: Examples of the liquid fraction functions f and f_ε.

The regularized boundary value problem is hence transformed into the following non-linear heat equation consisting in: *finding* $(T_\varepsilon, H_\varepsilon)$ *such that* $H_\varepsilon = E_\varepsilon(T_\varepsilon)$ *and solution*

$$\begin{aligned} \partial_t H_\epsilon - T_\epsilon'' &= 0 && \text{in } Q, \\ T_\epsilon(0,\cdot) = T_1, \qquad T_\epsilon(\infty,\cdot) &= 0 && \text{on } (0,\infty), \\ T_\epsilon(\cdot,0) &= 0 && \text{on } I. \end{aligned} \tag{3.7}$$

According to the auto-similarity of the solution for the melting Stefan problem given previously, one may ask whether the smoothed enthalpy problem has also an auto-similar solution. Basically, we aim to bring a positive answer to this question by establishing the existence of an auto-similar temperature field solution of this smoothed enthalpy problem.

Although we are specifically interested on the piecewise linear smoothing of the enthalpy function, we address the issue of existence in the general frame of regularizing functions.

We need some additional assumptions. Suppose that E_ε is continuous and piecewise continuously differentiable. The function E'_ε has a finite number of jumps and T_1 is not among the discontinuity points of it. Moreover, we assume that

$$\lambda \leq E'_\varepsilon(\cdot) \leq \mu_\varepsilon = \frac{\mu}{\varepsilon}, \qquad \text{a.e. in } \mathbb{R}. \tag{3.8}$$

This means in particular that the liquid fraction function f_ε is non-decreasing and has a bounded derivative.

3.3 Auto-similarity

For the sake of simplicity, we shall omit the index ε from the notations in this section. We denote $J_\xi = [0,\xi[$. To look for an auto-similar solution for the smoothed enthalpy equation, we write T and H (i.e., T_ε and H_ε) under the following form,

$$T(x,t) = u(\frac{x}{\sqrt{t}}), \qquad H(x,t) = e(\frac{x}{\sqrt{t}}) = E(u)(\frac{x}{\sqrt{t}}).$$

Notice that E is actually E_ε which is a continuous single-valued function. Moreover, we wrote u instead of u_ε. Substituting in (3.7), making necessary calculations and after introducing the new variable ξ (for $\frac{x}{\sqrt{t}}$) we arrive at the following reduced boundary value problem

$$\begin{aligned} -\frac{1}{2}\xi e'(\xi) - u''(\xi) = 0 \qquad \forall \xi \in J_\infty, \\ u(0) = T_1, \qquad u(\infty) = 0. \end{aligned} \tag{3.9}$$

for all $\gamma \in \mathbb{R}$, we define (u_γ, e_γ), with $e_\gamma = E(u_\gamma)$, as the solution of the ordinary differential equation

$$\begin{aligned} -\frac{1}{2}\xi e'_\gamma(\xi) - u''_\gamma(\xi) = 0 \qquad \forall \xi \in J_\infty, \\ u_\gamma(0) = T_1, \qquad u'_\gamma(0) = \gamma. \end{aligned} \tag{3.10}$$

Then, we consider the algebraic problem : find γ such that

$$u_\gamma(\infty) = 0. \tag{3.11}$$

If this equation is solved for some γ_*, then u_{γ_*} is solution of (3.9).

The main task of this section is to prove that this problem has only one solution.

3.3.1 The differential equation

We focus here on the problem (3.10). We start by rewriting the differential equation in the principal unknown u_γ,

$$\begin{aligned} -\frac{1}{2}\xi\, E'(u_\gamma)u'_\gamma - u''_\gamma = 0 \qquad & \text{in } J_\infty, \\ u_\gamma(0) = T_1, \qquad u'_\gamma(0) = \gamma. & \end{aligned} \tag{3.12}$$

Various obstacles have to be surmounted for a satisfactory existence and uniqueness result. The first one is the discontinuity of E'. We have thus to cope with the question of determining accurately $E'(u_\gamma)$. The other is that, even if E' is continuous, and hence the function $E'(u_\gamma)$ makes sense, one may possibly use the Cauchy-Peano existence theorem (see [64]), but the uniqueness is not ensured and this may be troublesome. To bypass these complications, we integrate this equation to obtain that

$$\begin{aligned} -\frac{1}{2}\xi\, E(u_\gamma) + \frac{1}{2}\int_0^\xi E(u_\gamma)(\zeta)\, d\zeta - u'_\gamma = 0 \qquad & \text{in } J_\infty, \\ u_\gamma(0) = T_1, \qquad u'_\gamma(0) = \gamma. & \end{aligned}$$

Checking the equivalence between this differential equation and the equation (3.12) is straightforward. If now we introduce the new unknown w_γ for the integral term, then we get the following differential system

$$\begin{aligned} u'_\gamma &= -\frac{1}{2}\xi\, E(u_\gamma) + w_\gamma, && \text{in } J_\infty, \\ w'_\gamma &= \frac{1}{2}E(u_\gamma), && \text{in } J_\infty, \\ u_\gamma(0) &= T_1, \qquad w_\gamma(0) = \gamma. & & \end{aligned} \tag{3.13}$$

That $(\xi, u) \mapsto \xi E(u)$ is Lipschitz continuous on any bounded interval J_{ξ_*} allows us to apply the Cauchy-Lipschitz theorem. As a result we have a unique maximum solution which is global.

Lemma 3.2. *The differential system* (3.13) *has a unique solution* $(u_\gamma, w_\gamma) \in \mathscr{C}^1(J_\infty, \mathbb{R}^2)$.

The well-known Gronwall lemma results in the continuous dependence of the solution upon the initial conditions. The proof of the following can be found in [64].

Corollary 3.3. *Forall $\xi_* > 0$, there exists a constant $C = C(\xi_*) > 0$ such that the following bound holds*

$$\|u_\gamma - u_{\gamma_*}\|_{\mathscr{C}(J_{\xi_*},\mathbb{R})} + \|w_\gamma - w_{\gamma_*}\|_{\mathscr{C}(J_{\xi_*},\mathbb{R})} \leq C|\gamma - \gamma_*|.$$

3.3.2 Shooting problem

The objective here is to use the shooting method to solve (3.11). Denoting $d_\gamma = u'_\gamma$, we can rewrite equation (3.11) in an equivalent form

$$\int_0^\infty d_\gamma(\zeta)\, d\zeta = -T_1. \tag{3.14}$$

We shall first show that the integral term depends continuously upon γ, and then use the classical intermediate value theorem.

Proposition 3.4. *The following function is continuous on $\mathbb{R}$,*

$$S : \gamma \mapsto \int_0^\infty d_\gamma(\zeta)\, d\zeta. \tag{3.15}$$

The proof of this proposition requires an intermediary result on the behavior of d_γ at the vicinity of $+\infty$.

Lemma 3.5. *There holds that*

$$|d_\gamma(\xi)| \leq |\gamma| e^{-\frac{\lambda}{4}\xi^2}, \qquad \forall \xi \in J_\infty.$$

Moreover, if $\gamma > 0$ then $d_\gamma < 0$.

Proof. Let us first assume that the function $E'(u_\gamma)$ is defined almost everywhere. This means that

$$\Xi = \Big\{ \xi \in J_\infty;\ \ E' \text{ is discontinuous at } u_\gamma(\xi) \Big\} \tag{3.16}$$

is a negligible set. Considering the first equation in (3.13), it is easily seen that

$$d'_\gamma = -\frac{1}{2}\xi E'(u_\gamma) d_\gamma = \varphi'(\xi) d_\gamma, \qquad \text{in } J_\infty,$$

with $\varphi' = -\frac{1}{2}\xi E'(u_\gamma)$. Integrating this equation yields that

$$d_\gamma(\xi) = \gamma e^{\varphi(\xi)}, \qquad \forall \xi \in J_\infty. \tag{3.17}$$

Now, using the assumption (3.8) on E' yields the desired result.

It remains to show that the (Lebesgue-) measure of the set Ξ defined in (3.16) cannot be positive. In fact, it is a discrete set and all its points are isolated. We shall prove this statement by contradiction.
Ξ is obviously a closed set and let $\Xi'(\subset \Xi)$ denote the set of its limit points. If the statement is false, then Ξ has at least one limit point and the set Ξ' is not empty. According to [83, Chapter 2, Exercice 6], $\Xi' \subset J_\infty$ is a closed set and has therefore a minimum value we denote by $\xi_\flat$. We set $T_\flat = u_\gamma(\xi_\flat)$; it is a jumping point for the function E'. Then, there exists a sequence $(\xi_n)_{n\geq 0}$ converging towards $\xi_\flat$ and $u_\gamma(\xi_n) = T_\flat$. This yields in particular that $d_\gamma(0) = u'_\gamma(\xi_\flat) = 0$. Next, as $E'(u_\gamma)$ is defined a.e in $J_{\xi_\flat}$, we deduce that the expression (3.17) is valid for d_γ at least in $J_{\xi_\flat}$. Passing to the limit of d_γ at $\xi_\flat$ shows that it is positive and cannot be zero, unless we have that $\lim_{\xi\to\xi_\flat} \varphi(\xi) = +\infty$ which cannot be true. Hence, Ξ is negligible. The proof is complete. ■

Proof. Proposition 3.4 Using Corollary 3.3 and referring once again to the first equation in (3.13), the map $\gamma \mapsto d_\gamma$ is a continuous (and even Lipschitz-continuous) mapping from $\mathbb{R}$ into $\mathscr{C}(J_{\xi_*}, \mathbb{R})$, forall $\xi_* > 0$. As a result,

$$\lim_{\gamma\to\gamma_*} \int_0^{\xi_*} |d_\gamma - d_{\gamma_*}|(\zeta)\, d\zeta = 0.$$

To obtain the desired result, we use the bound of Lemma 3.5. Indeed, we have that

$$\int_{\xi_*}^{\infty} |d_\gamma - d_{\gamma_*}|(\zeta)\, d\zeta \leq \frac{1}{\omega}\psi(\omega\xi_*)\,(|\gamma| + |\gamma_*|),$$

where $\omega = \frac{1}{2}\sqrt{\lambda}$. Finally, the triangular inequality gives that

$$|S(\gamma) - S(\gamma_*)| = \left|\int_0^{\infty} (d_\gamma - d_{\gamma_*})(\zeta)\, d\zeta\right| \leq \int_0^{\xi_*} |d_\gamma - d_{\gamma_*}|(\zeta)\, d\zeta + \frac{1}{\omega}\psi(\omega\xi_*)\,(|\gamma| + |\gamma_*|).$$

The term in ψ can be made arbitrary small, provided that ξ_* is chosen large enough. Moreover, the integral term tends towards zero as $\gamma \to \gamma_*$, which implies that the function S is continuous. The proof is complete. ■

Remark 3.6. According to (3.17), forall $\gamma < 0$ we have $d_\gamma < 0$. As a result the solution u_γ is decreasing, and we have

$$T_1 + \frac{\gamma}{\omega}\psi(\omega\xi) \leq u_\gamma(\xi) \leq T_1, \qquad \forall \xi \in J_\infty.$$

The function u_γ has therefore a limit when $\xi \to +\infty$. Notice that, if $\gamma > 0$, then $d_\gamma \geq 0$, u_γ is increasing and (3.14) cannot be satisfied.

Proposition 3.7. *Problem* (3.14) *has at least one solution* γ *which is negative. The corresponding function* u_γ *is then decreasing.*

Proof. Following Remark 3.6, any solution γ is necessarily negative. We look for a solution γ in $]-\infty, 0]$. Proceeding like in the proof of Lemma 3.5, we can derive

$$\gamma\sqrt{\frac{\pi}{\lambda}} \leq \int_0^\infty d_\gamma(\xi)\, d\xi \leq \gamma\sqrt{\frac{\pi}{\mu}} \leq 0$$

As a result, the 'shooting' function S is continuous from $]-\infty, 0]$ into $]-\infty, 0]$. By the intermediate values theorem, it takes at least once the negative value $(-T_1)$. The fact that u_γ is decreasing is ensued from the negativity of $d_\gamma = u'_\gamma$ according to (3.17). The proof is complete. ■

3.3.3 Uniqueness

The uniqueness may be reached by establishing the monotonicity of the function (3.15). To this end, consider γ and γ_* be two real-numbers with $\gamma < \gamma_* \leq 0$. We intend to show that $u_\gamma(\infty) > u_{\gamma_*}(\infty)$. To proceed, we denote

$$g = \frac{u_\gamma - u_{\gamma_*}}{\gamma - \gamma_*}, \qquad k = \frac{w_\gamma - w_{\gamma_*}}{\gamma - \gamma_*}, \qquad F = \frac{E(u_\gamma) - E(u_{\gamma_*})}{u_\gamma - u_{\gamma_*}}.$$

Both functions g and k are continuously-differentiable on J_∞ while F is measurable with

$$0 < \lambda \leq F(\xi) \leq \mu, \qquad \forall \xi \in J_\infty.$$

It is easily checked that (g,k) is the unique solution of the linear system

$$\begin{aligned} g' &= -\frac{1}{2}\xi F g + k, \qquad \text{in } J_\infty, \\ k' &= \frac{1}{2} F g, \qquad\qquad\quad \text{in } J_\infty, \\ g(0) &= 0, \qquad k(0) = 1. \end{aligned} \tag{3.18}$$

Notice that according to Remark 3.6, the limit of u_γ (and of u_{γ_*}) at infinity exists and is finite. As a result, the limit $g(\infty)$ exists and is finite.

The next lemma, which indicates that $g(\infty) > 0$, yields the desired result.

Lemma 3.8. *We have that*

$$g(\xi) > 0, \qquad k(\xi) > 1, \qquad \forall \xi \in J_\infty.$$

Moreover, the following holds

$$\lim_{\xi \to +\infty} g(\xi) > 0$$

and the function (3.15) *is increasing.*

Proof. We start by noticing that $g'(0) = 1$. Hence, g is increasing at the vicinity of $\xi = 0$, and $g(\xi) > 0$ in some interval $]0, \xi_0[$, with $\xi_0 > 0$. Next, we prove by contradiction that $\xi_0 = +\infty$.

Assume that $\xi_0 < +\infty$ and $g(\xi_0) = 0$. This yields $g'(\xi_0) \leq 0$. from the first equation of (3.18), we obtain that $k(\xi_0) \leq 0$. This cannot be true since we derive from the second equation of (3.18) that $k'(\xi) > 0$ in $]0, \xi_0[$. Hence $k(\xi_0) > k(0) = 1$. By contradiction, we have $g > 0$ in $]0, +\infty[$. Thus $k' > 0$ and k is increasing, which shows that $k > 1$ in $]0, +\infty[$. The proof is complete.

■

Combining the above results, we have proved the main result of this section showing existence and uniqueness together with the 'uniform' stability of the solution.

Theorem 3.9. *Problem* (3.9) *has an unique solution* $(e_\varepsilon, u_\varepsilon)$. *The temperature field* T *is decreasing, and there holds that*

$$\|e_\varepsilon\|_{L^2(J_\infty)} + \|u'_\varepsilon\|_{L^2(J_\infty)} \leq C|T_1|,$$

where the constant C does not depend on ε. Moreover, the solution u_ε is decreasing in J_∞, from T_1 towards 0.

3.4 Convergence

In this section, we carry out the convergence analysis for the piecewise linear smoothing enthalpy problem. The issue has been tackled in [50] (see also [66]), where variational techniques are used in bounded domains. The smoothed temperature T_ε is proved to approximate the exact T, solution to the Stefan problem. The convergence rates with respect to L^2-norm and H^1-norm are of order $\sqrt{\varepsilon}$. Our purpose is to find out what exactly happen locally in the slab. Is the accuracy of $\sqrt{\varepsilon}$ uniformly distributed (in the slab) or is it only concentrated in the mushy zone? How does the temperature field T_ε (or equivalently of u_ε) behave in the solid and liquid regions? To answer these questions, we zoom in the mushy zone and undertake a detailed analysis based on the analytic form of the solution to the smoothed enthalpy problem.

According to Theorem 3.9, the auto-similar temperature u_ε decreases in the slab from T_1 towards zero. This suggests that the enthalpy form changes twice. Different ions are related to the events: $u_\varepsilon \geq (T_m)^+$, $(T_m)^- \leq u_\varepsilon \leq (T_m)^+$ and $u_\varepsilon \leq (T_m)^-$. Then, there exist two real-numbers $0 < a_\varepsilon < b_\varepsilon$ such that $u_\varepsilon(a_\varepsilon) = (T_m)^+$ and $u_\varepsilon(b_\varepsilon) = (T_m)^-$. The interfaces $X_\varepsilon(t) = a_\varepsilon\sqrt{t}$ and $Y_\varepsilon(t) = b_\varepsilon\sqrt{t}$ enclose the mushy zone that separates the solid and liquid phases. They are expected to come close to each other and to eventually coincide with the sharp interface $X(t) = \alpha\sqrt{t}$, at the limit $\epsilon \to 0$. This will be the central point of the analysis. Splitting the whole interval into three subintervals $J^f = (0, a_\varepsilon)$, $J^\varepsilon = (a_\varepsilon, b_\varepsilon)$ and $J^s = (b_\varepsilon, +\infty)$, and solving the smoothed problem in the three subintervals gives the following solution u_ε,

$$u_\varepsilon(\zeta) = \begin{cases} A_\varepsilon\phi(\omega\zeta) + T_1, & \forall \zeta \in J^f, \\ B_\varepsilon\phi(\omega_\varepsilon\zeta) + C_\varepsilon & \forall \zeta \in J^\varepsilon, \\ D_\varepsilon\psi(\omega\zeta) & \forall \zeta \in J^s, \end{cases}$$

where $\omega_\varepsilon = \frac{\sqrt{\lambda_\varepsilon}}{2}$. Recall that J^f and J^s are the liquid and solid zones respectively while J^ϵ is the mushy zone.

All the constants are dependent upon ε. For simplicity we choose henceforth to drop off the index ε in some places and put it back only when necessary.

Using the fact that $u_\varepsilon(a_\varepsilon) = (T_m)^+$ and $u_\varepsilon(b_\varepsilon) = (T_m)^-$, we derive

$$A = -\frac{T_1 - (T_m)^+}{\phi(\omega a_\varepsilon)}, \qquad D = \frac{(T_m)^-}{\psi(\omega b_\varepsilon)}. \tag{3.19}$$

The continuity of u_ε at both points a_ε and b_ε results in

$$B = \frac{2\varepsilon}{\phi(\omega_\varepsilon a_\varepsilon) - \phi(\omega_\varepsilon b_\varepsilon)}, \qquad C = (T_m)^+ - B\phi(\omega_\varepsilon a_\varepsilon). \tag{3.20}$$

To fully solve the problem, we need to enforce the flux conservation at points a_ε and b_ε which leads to

$$\begin{aligned} A\omega\, e^{-(\omega a_\varepsilon)^2} &= B\omega_\varepsilon\, e^{-(\omega_\varepsilon a_\varepsilon)^2}, \\ -D\omega\, e^{-(\omega b_\varepsilon)^2} &= B\omega_\varepsilon\, e^{-(\omega_\varepsilon b_\varepsilon)^2}. \end{aligned} \tag{3.21}$$

Plugging in (3.21), the coefficients A, D as given in (3.19) and B as in (3.20), results in a non-linear algebraic system of two equations for two unknowns a_ε and b_ε. A direct consequence of the foregoing analysis is that this system has a unique solution $(a_\varepsilon, b_\varepsilon)$ with $b_\varepsilon > a_\varepsilon > 0$.

Next we would like to show that the sequences $(a_\varepsilon)_{\varepsilon>0}$ and $(b_\varepsilon)_{\varepsilon>0}$ converge and share the same limit α, the solution of the transcendental equation (3.4). We aim also to exhibit an accurate convergence rate.

Lemma 3.10. *The sequences $(a_\varepsilon)_{\varepsilon>0}$ and $(b_\varepsilon)_{\varepsilon>0}$ are uniformly bounded away from zero, i.e., there exist two constants α_L and α_R with $0 < \alpha_L < \alpha_R < \infty$ such that*

$$\alpha_L \le a_\varepsilon < b_\varepsilon \le \alpha_R, \qquad \forall \varepsilon < \min(T_m, T_1 - T_m).$$

Proof. These results are consequences of the uniform bound on $\|u'_\varepsilon\|_{L^2(J_\infty)}$ of Theorem 3.9. Indeed, if for instance a_ε goes to zero, it can be checked that $\|u'_\varepsilon\|_{L^2(J^f)}$ will blow up for small ε. ■

Lemma 3.11. *There holds that*

$$(b_\varepsilon - a_\varepsilon) \le K\varepsilon,$$

for some positive constant K.

Proof. We derive from (3.21) that

$$e^{-\omega_\varepsilon^2(b_\varepsilon^2 - a_\varepsilon^2)} = -\frac{D}{A} e^{-\omega^2(b_\varepsilon^2 - a_\varepsilon^2)}.$$

Using the expressions of A and D as in (3.19), we obtain

$$e^{\frac{L}{8}\frac{(b_\varepsilon^2-a_\varepsilon^2)}{\varepsilon}} = \frac{T_1-(T_m)^+}{(T_m)^-}\frac{\psi(\omega b_\varepsilon)}{\phi(\omega a_\varepsilon)}. \tag{3.22}$$

Now, Lemma 3.10 implies that the term on the righthand side is uniformly bounded in ϵ. As a result, we have that

$$(b_\varepsilon^2 - a_\varepsilon^2) \leq K\varepsilon,$$

for some constant $K > 0$. The lemma is then a consequence of the boundedness of a_ε and b_ε. ■

The next step is to show that $(a_\varepsilon)_{\varepsilon>0}$ and $(b_\varepsilon)_{\varepsilon>0}$ are convergent. We prove that each of them has α as the only accumulative point. By Bolzano-Weierstrass theorem, the boundedness of $(a_\varepsilon)_{\varepsilon>0}$ and $(b_\varepsilon)_{\varepsilon>0}$ yields that each sequence has at least an accumulative point. There exist then two convergent subsequences we still call $(a_\varepsilon)_{\varepsilon>0}$ and $(b_\varepsilon)_{\varepsilon>0}$, with a slight abuse of notation. According to Lemma 3.11, both sequences share the same limit which we denote by a. The last step is to prove that the only possible value for a is α, the solution of (3.4).

Lemma 3.12. *The (whole) sequences $(a_\varepsilon)_{\varepsilon>0}$ and $(b_\varepsilon)_{\varepsilon>0}$ converge toward α, the solution of the transcendent equation (3.4).*

Proof. Let $(a_\varepsilon)_{\varepsilon>0}$ and $(b_\varepsilon)_{\varepsilon>0}$ be convergent subsequences with the limit $a > 0$. Using equalities (3.19) results in

$$-A\omega\, e^{-(\omega a_\varepsilon)^2} - D\omega\, e^{-(\omega b_\varepsilon)^2} = -B\omega_\varepsilon(e^{-(\omega_\varepsilon a_\varepsilon)^2} - e^{-(\omega_\varepsilon b_\varepsilon)^2}).$$

Replacing B as in (3.20) leads to

$$-A\omega\, e^{-(\omega a_\varepsilon)^2} - D\omega\, e^{-(\omega b_\varepsilon)^2} = 2\epsilon\omega_\varepsilon\frac{e^{-(\omega_\varepsilon a_\varepsilon)^2} - e^{-(\omega_\varepsilon b_\varepsilon)^2}}{\phi(\omega_\varepsilon b_\varepsilon) - \phi(\omega_\varepsilon a_\varepsilon)}. \tag{3.23}$$

The term on the righthand side can be bounded above and below as ([1])

$$2\epsilon\omega_\varepsilon(\sqrt{\pi}\omega_\varepsilon a_\varepsilon) \leq 2\epsilon\omega_\varepsilon\frac{e^{-(\omega_\varepsilon a_\varepsilon)^2} - e^{-(\omega_\varepsilon b_\varepsilon)^2}}{\phi(\omega_\varepsilon b_\varepsilon) - \phi(\omega_\varepsilon a_\varepsilon)} \leq 2\epsilon\omega_\varepsilon(\sqrt{\pi}\omega_\varepsilon b_\varepsilon). \tag{3.25}$$

[1] We use the double inequality

$$\sqrt{\pi}x(\phi(y)-\phi(x)) \leq e^{-x^2} - e^{-y^2} \leq \sqrt{\pi}y(\phi(y)-\phi(x)), \qquad 0 \leq x \leq y. \tag{3.24}$$

Passing to the limit ($\varepsilon \to 0$) shows that the three sequences have the common limit $\frac{1}{4}\sqrt{\pi}La$.

Resuming equation (3.23) and after going to the limit we get that a is solution of the same equation (3.4) as α, which implies $a = \alpha$. The proof is complete. ■

Next, we establish the convergence rate of $(a_\varepsilon)_{\varepsilon>0}$ and of $(b_\varepsilon)_{\varepsilon>0}$ towards α.

Proposition 3.13. *There exists a constant K such that*

$$|a_\varepsilon - \alpha| + |b_\varepsilon - \alpha| \leq K\varepsilon.$$

Proof. Let us introduce the function

$$G(\varrho) = \frac{T_1 - T_m}{\phi(\omega\varrho)} - \frac{T_m}{\psi(\omega\varrho)} - \left(\frac{\sqrt{\pi}L}{4\omega}\right)\varrho e^{(\omega\varrho)^2}$$

It is smooth and decreasing in $]0,\infty[$. Moreover, α is the unique root of G in $]0,\infty[$, that is

$$G(\alpha) = 0. \tag{3.26}$$

On the other hand, let us consider the following perturbed function

$$G_\varepsilon(\varrho) = \frac{T_1 - (T_m)^+}{\phi(\omega\varrho)} - \frac{(T_m)^-}{\psi(\omega\varrho)} - \left(\frac{\sqrt{\pi}L}{4\omega}\right)\varrho e^{(\omega\varrho)^2}.$$

According to (3.23), the point a_ε may be seen as solution of

$$G_\varepsilon(a_\varepsilon) = r_\varepsilon, \tag{3.27}$$

where

$$\begin{aligned} r_\varepsilon = \left[2\epsilon\frac{\omega_\varepsilon}{\omega}\frac{e^{-(\omega_\varepsilon a_\varepsilon)^2} - e^{-(\omega_\varepsilon b_\varepsilon)^2}}{\phi(\omega_\varepsilon b_\varepsilon) - \phi(\omega_\varepsilon a_\varepsilon)} - \left(\frac{\sqrt{\pi}L}{4\omega}\right)a_\varepsilon\right]e^{(\omega a_\varepsilon)^2} \\ + \left[\frac{e^{-(\omega b_\varepsilon)^2}}{\psi(\omega b_\varepsilon)} - \frac{e^{-(\omega a_\varepsilon)^2}}{\psi(\omega a_\varepsilon)}\right](T_m)^- e^{(\omega a_\varepsilon)^2}. \end{aligned} \tag{3.28}$$

Let $[\alpha_L, \alpha_R]$ be contained in $]0,\infty[$, we can derive immediately from

$$G_\varepsilon(\varrho) - G(\varrho) = \epsilon\left(-\frac{1}{\phi(\omega\varrho)} + \frac{1}{\psi(\omega\varrho)}\right).$$

that

$$\sup_{\varrho\in[\alpha_L,\alpha_R]} |G_\varepsilon(\varrho)-G(\varrho)| \le K\varepsilon.$$

We can show (cf. Appendix) that

$$|r_\varepsilon| \le K\varepsilon. \tag{3.29}$$

Now, we derive from (3.27) and (3.26) that

$$G(\alpha)-G(a_\varepsilon) = (G_\varepsilon(a_\varepsilon)-G(a_\varepsilon))-r_\varepsilon.$$

This implies that

$$|G(\alpha)-G(a_\varepsilon)| \le |G_\varepsilon(a_\varepsilon)-G(a_\varepsilon)|+|r_\varepsilon| \le K\varepsilon.$$

Calling for the mean value theorem we derive that $|\alpha-a_\varepsilon| \le K\varepsilon$. Of course, the constant K depends on $\min_{\varrho\in[\alpha_L,\alpha_R]}|G'(\varrho)|>0$. The proof is complete. ■

The first and major consequence of this result is the optimal convergence of u_ε towards u outside the mushy region. To state the accuracy result, let us set $(a_\varepsilon)^- = \min(a,a_\varepsilon)$ and $(b_\varepsilon)^+ = \max(\alpha,b_\varepsilon)$.

Corollary 3.14. *The following estimate holds*

$$\|u-u_\varepsilon\|_{L^\infty(0,(a_\varepsilon)^-)} + \|u-u_\varepsilon\|_{L^\infty((b_\varepsilon)^+,\infty)} \le K\varepsilon.$$

Proof. Since

$$\|u-u_\varepsilon\|_{L^\infty(0,(a_\varepsilon)^-)} \le |A_\varepsilon - A| = \left|\frac{T_1-(T_m)^+}{\phi(\omega a_\varepsilon)} - \frac{T_1-T_m}{\phi(\omega\alpha)}\right|,$$
$$\|u-u_\varepsilon\|_{L^\infty((b_\varepsilon)^+,\infty)} \le |D_\varepsilon - D| = \left|\frac{(T_m)^-}{\psi(\omega b_\varepsilon)} - \frac{T_m}{\psi(\omega\alpha)}\right|.$$

The desired results then follow from Proposition 3.13. The proof is complete. ■

Corollary 3.14 provides the convergence rate of u_ε towards u, away from the mushy portion of the slab. Next, to assess the behavior of u_ε within the mushy zone we need to sharpen the estimate of Lemma 3.10.

Lemma 3.15. *We have that*

$$\lim_{\varepsilon\to 0}\frac{b_\varepsilon-a_\varepsilon}{\varepsilon} = \rho > 0.$$

Proof. We prove first that $C = \inf_{\varepsilon>0} \frac{b_\varepsilon - a_\varepsilon}{\varepsilon} > 0$. We proceed by contradiction. Assume that $C = 0$. Then, $\frac{b_\varepsilon - a_\varepsilon}{\varepsilon}$ converges towards zero (modulo a subsequence). Passing to the limit in (3.22), we derive that

$$\frac{T_1 - T_m}{T_m} \frac{\psi(\omega\alpha)}{\phi(\omega\alpha)} = 1.$$

This yields that

$$\phi(\omega\alpha) = \frac{T_1 - T_m}{T_1}, \qquad \psi(\omega\alpha) = \frac{T_m}{T_1}.$$

Replacing in (3.4) gives that $\alpha = 0$. This cannot occur since $T_m < T_1$. Now, we claim that $\frac{b_\varepsilon - a_\varepsilon}{\varepsilon}$ has only one accumulation point. This is because, if we take (3.22) to the limit, we have

$$\lim_{\varepsilon\to 0} \frac{b_\varepsilon - a_\varepsilon}{\varepsilon} = \frac{4}{L\alpha} \ln\left[(\frac{T_1}{T_m} - 1)(\frac{1}{\phi(\omega\alpha)} - 1) \right] > 0.$$

The proof is complete. ■

Proposition 3.16. *There exists a constant such that*

$$\|u_\varepsilon\|_{L^2(a_\varepsilon,b_\varepsilon)} = \mathcal{O}(\sqrt{\varepsilon}), \qquad \|u'_\varepsilon\|_{L^2(a_\varepsilon,b_\varepsilon)} = \mathcal{O}(\sqrt{\varepsilon}).$$

Proof. We start from the double bound

$$(T_m)^- \le u_\varepsilon(\zeta) \le (T_m)^+, \qquad \forall \zeta \in (a_\varepsilon, b_\varepsilon).$$

After integration we obtain

$$(T_m)^- \sqrt{b_\varepsilon - a_\varepsilon} \le \|u_\varepsilon\|_{L^2(a_\varepsilon,b_\varepsilon)} \le (T_m)^+ \sqrt{b_\varepsilon - a_\varepsilon}.$$

Invoking Lemma 3.15 gives the first estimate.

Next, we integrate

$$u'_\varepsilon(\zeta) = B_\varepsilon \omega_\varepsilon e^{-(\omega_\varepsilon \zeta)^2}$$

to get

$$\|u'_\varepsilon\|^2_{L^2(a_\varepsilon,b_\varepsilon)} = (2\sqrt{2}\omega_\varepsilon \varepsilon^2) \frac{\phi(\sqrt{2}\omega_\varepsilon b_\varepsilon) - \phi(\sqrt{2}\omega_\varepsilon a_\varepsilon)}{(\phi(\omega_\varepsilon b_\varepsilon) - \phi(\omega_\varepsilon a_\varepsilon))^2}.$$

Applying twice the double inequality (3.24) and carrying out some calculations will lead to

$$\|u'_\varepsilon\|_{L^2(a_\varepsilon,b_\varepsilon)} = \mathcal{O}(\varepsilon\sqrt{\omega_\varepsilon}) = \mathcal{O}(\sqrt{\varepsilon}).$$

The proof is complete. ■

Remark 3.17. One can get more information about the solution u_ε within the mushy zone. In fact, one can check readily that

$$\lim_{\varepsilon\to 0}\frac{\|u_\varepsilon\|_{L^2(a_\varepsilon,b_\varepsilon)}}{\sqrt{\varepsilon}}=T_m\rho,\qquad \lim_{\varepsilon\to 0}\frac{\|u'_\varepsilon\|_{L^2(a_\varepsilon,b_\varepsilon)}}{\sqrt{\pi\varepsilon}}=\frac{L\alpha}{4}\ cotanh\ (\frac{L\alpha}{8}\rho).$$

Here, ρ is the limit provided in *Lemma 3.15*.

3.5 Numerical results

To compute α, one has to solve numerically the transcendental equation (3.23), and to obtain $(a_\varepsilon,b_\varepsilon)$, one has to solve the algebraic system (3.22) and (3.23). Equation (3.23) may be rewritten in such a form that $\omega\alpha$ depends only on two dimensionless numbers: Stefan numbers St_F and St_S. They are provided as the ratio of the sensible and the latent heats in the liquid and in the solid phases,

$$St_L=\frac{\lambda}{L}(T_1-T_m)=\frac{C}{La}(T_1-T_m),\qquad St_S=\frac{\lambda}{L}T_m=\frac{C}{La}T_m.$$

Numerical examples are performed using SCILAB to assess the theoretical findings in the previous sections about the gaps $(a_\varepsilon-\alpha)$ and $(b_\varepsilon-\alpha)$. Nonlinear equations are solved by Newton's algorithm.

Example one — In the first test, we fix the parameters with $\lambda=10$ and $L=250$ with $T_0=-2$, $T_1=10$ and $T_m=0$. Stefan numbers are therefore given by $St_L=0.4$ and $St_S=0.08$. Initially the slab is frozen at the temperature $T_0=-2$. A melting process starts at the origin $x=0$, because the temperature at that point is brought to $T_1=10$, above the melting level $T_0=0$. The auto-similar solutions u and u_ε are represented in Figure 3.2, with $\varepsilon=0.5$ and $\varepsilon=0.1$. Recall that $T_{(\varepsilon)}(x,t)=u_{(\varepsilon)}(\frac{x}{\sqrt{t}})$. The vertical lines indicate the location of α (solid line) and the positions of a_ε and b_ε (dashed lines). The regularized solution is close to the exact one, and becomes closer for smaller ε. Moreover, results recorded in Table 3.1 illustrate the order one decaying of the error, with respect ϵ. Observe also that the exact α lays within the mushy zone, and for smaller ε the mushy zone shrinks around the melting front.

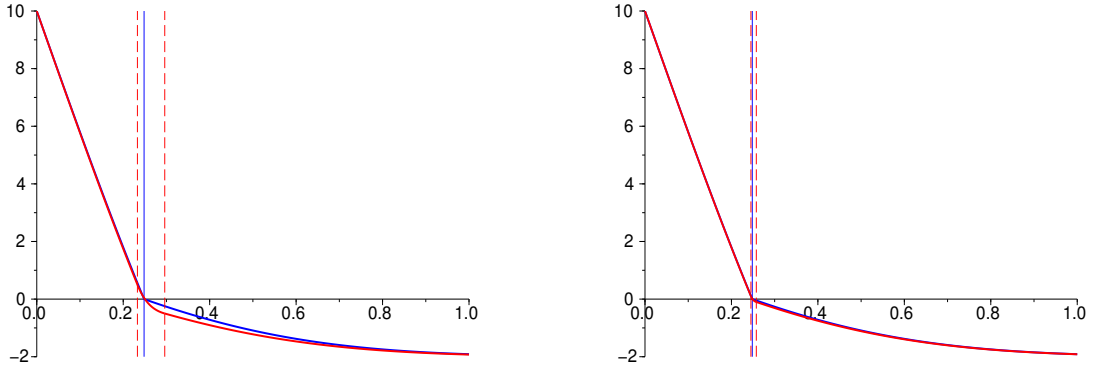

FIGURE 3.2: Auto-similar functions u and u_ε with $\varepsilon = 0.5$ (left) and $\varepsilon = 0.1$ (right). $T_{(\varepsilon)}(x,t) = u_{(\varepsilon)}(\frac{x}{\sqrt{t}})$.

$\varepsilon =$	1	0.1	0.01
$(a_\varepsilon - \alpha)$	-1.21×10^{-1}	-1.26×10^{-2}	-1.27×10^{-3}
$(b_\varepsilon - \alpha)$	4.10×10^{-1}	3.74×10^{-2}	3.72×10^{-3}

TABLE 3.1: Errors on the position of the melting front coefficient α.

Example two — We keep all the parameters unchanged except setting now $\lambda = 250$. This means that the specific heat capacity C of the slab is higher, and the ratio of sensible/latent heat is increased. Stefan numbers are given by $St_F = 10$ and $St_S = 2$. The exact and regularized auto-similar representations of the temperature, u and u_ε, are depicted in Figure 3.3, for $\varepsilon = 0.5$ and $\varepsilon = 0.1$. Gaps between them are small, especially for $\varepsilon = 0.1$. In, Figure 3.4, the convergence history is plotted, confirming the order one convergence rate of the melting font location with respect to ε.

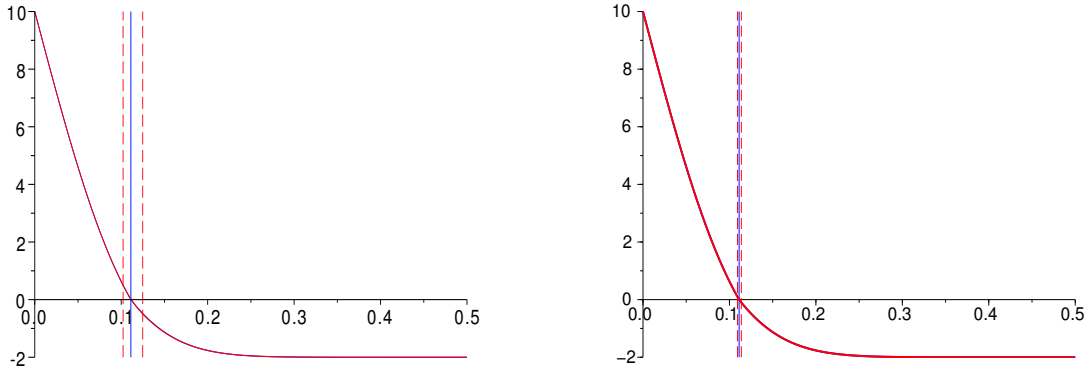

FIGURE 3.3: Functions u and u_ε with $\varepsilon = 0.5$ (left) and $\varepsilon = 0.1$ (right).

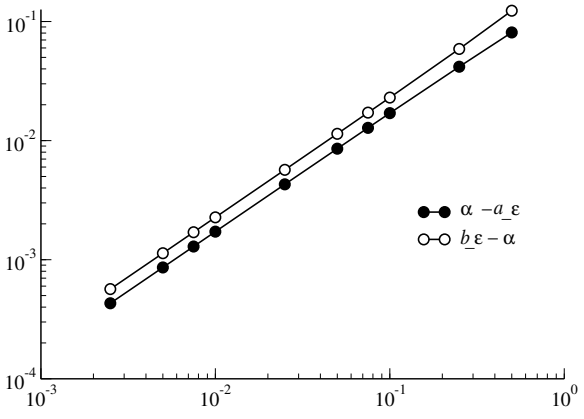

FIGURE 3.4: Convergence curves of the melting front coefficient α.

3.6 Conclusion

We considered the melting free-boundary Stefan problem set in a semi-infinite slab. The effects of the smoothing procedure applied to the enthalpy equation, in phase transition models, are investigated semi-analytically. We obtained detailed estimates of order $\sqrt{\epsilon}$ (ϵ being the width of the mushy zone) within the mushy zone and of order ϵ outside of the mushy zone.

A direct consequence is that the (global) estimate obtained in [50] is optimal and cannot be improved. The limitation is due to the energy trapped within that mushy region. A careful investigation outside this zone shows that the regularized enthalpy and temperature converge towards their exact counterparts like ε. We emphasize that the analysis developed here may be conducted as well for many other non-linear models where a closed form for the solution is available (see [91, 92]).

3.7 Appendix

We sketch below the proof of (3.29) which is necessary for the proof of Proposition 3.13.

The residual r_ε is composed of two contributions $(r_\varepsilon)_1$ and $(r_\varepsilon)_2$ in (3.28). Using the double inequality (3.25), we find

$$\left[\frac{2\sqrt{\pi}}{\omega}\epsilon(\omega_\varepsilon)^2-\left(\frac{\sqrt{\pi}L}{4\omega}\right)\right]a_\varepsilon e^{(\omega a_\varepsilon)^2}\leq(r_\varepsilon)_1\leq\left[\frac{2\sqrt{\pi}}{\omega}\epsilon(\omega_\varepsilon)^2 b_\varepsilon-\left(\frac{\sqrt{\pi}L}{4\omega}\right)a_\varepsilon\right]e^{(\omega a_\varepsilon)^2}.$$

Recalling that

$$(\omega_\varepsilon)^2=\frac{\lambda_\varepsilon}{4}=\frac{\lambda}{4}+\frac{L}{8\epsilon}=\omega^2+\frac{L}{8\epsilon},$$

from which we derive

$$[2\sqrt{\pi}\omega\epsilon]a_\varepsilon e^{(\omega a_\varepsilon)^2}\leq(r_\varepsilon)_1\leq\left[2\sqrt{\pi}\omega\epsilon a_\varepsilon+\left(\frac{\sqrt{\pi}L}{4\omega}\right)(b_\varepsilon-a_\varepsilon)\right]e^{(\omega a_\varepsilon)^2}.$$

The boundedness of the sequence $(a_\varepsilon)_\varepsilon$ together with the bound obtained in Lemma 3.11 yields the desired estimate on $(r_\varepsilon)_1$.
Bound for $(r_\varepsilon)_2$ can be obtained by applying the mean value theorem to the inverse of

the scaled complementary error function

$$\rho \mapsto \frac{e^{-\rho^2}}{\psi(\rho)},$$

and another use of Lemma 3.11.

Chapter 4

Numerical schemes for the unsteady heat transfer problem with nonlinear phase change in a composite media

In this chapter we study the unsteady heat conduction problem with phase change in a composite media consisting of a graphite matrix foam infiltrated by a phase change material in latent heat thermal energy storage context. This problem is modelled by the energy balance equation in both domains in which a nonlinear part, in the PCM domain, describes the phase change phenomena for a homogeneous material. From a numerical point of view, the main difficulty is in the treatment of this non-linear part of the equation. In this chapter we will be focusing on the phase change problem in the PCM domain, at first, to compare four different numerical schemes since these schemes are specially designed to simulate the solution of these type of problems. The PCMs considered in this chapter are such that the phase change occurs at a one melting point : the melting temperature. This is described by a jump in the liquid fraction and consequently in the enthalpy as a function of the temperature. In order to overcome this difficulty we introduce a smoothed expression of the liquid fraction function.
We present some of the most commonly used numerical schemes to solve the phase change problem. An exact solution is given for the special case of melting a 1D rod of a solid PCM to compare the different numerical approaches.

4.1 Introduction

In latent heat thermal energy storage systems, phase change materials are very commonly used thanks to their high capacity to store or release energy during a phase change process, from liquid to solid or from solid to liquid. However, these materials usually have very low thermal conductivity ($\sim 1W/m$), one technique that allow to overcome this inconvenience is to use these PCMs embedded in highly conductive structure such as a graphite foam matrix [69]. The resulting composite material have both high thermal capacity and high thermal conductivity. This mix however present some flaws that are described by a jump in the temperature field across the interface between both materials [90].

4.2 Problem formulation

We recall the heat conduction problem in a composite media with a graphite matrix foam infiltrated by a PCM such as salt for example described by the following set of equations (see chapter 1)

$$\begin{cases} \partial_t H(T) - \operatorname{div}(\kappa \nabla T) = 0 & in\ \Omega_S \cup \Omega_G, \\ [\kappa \partial_n T] = 0 & on\ \gamma, \\ R(\kappa \partial_n (T|_{\Omega_S})) = [T] & on\ \gamma, \\ T = T_D & on\ \Gamma_D. \\ \kappa \partial_n T = 0 & on\ \Gamma_N. \end{cases} \tag{4.1}$$

where the subscripts S and G designate salt and graphite. We have

$$\Omega_G = \Omega \setminus \overline{\Omega}_S, \qquad \gamma = \partial \Omega_S. \tag{4.2}$$

We consider also that

$$\partial \Omega = \Gamma_D \cup \Gamma_N$$

The unknown is the temperature T of the medium, $\boldsymbol{n}$ is the unit normal vector to $\partial\Omega$ exterior to Ω and also to γ exterior to Ω_S, $[\cdot]$ is the jump through γ, equal to the value on Ω_G minus the value on Ω_S. The temperature T, the conductivity κ, the density ρ and the specific heat capacity c are discontinuous through γ. The parameter R represents

the thermal resistance at the interface γ introduced in section 1.2.3. T_D is the external temperature. The enthalpy H in Ω is defined by :

$$H(T) = \begin{cases} (\rho c)_S T + \rho L_a f(T) & in \quad \Omega_S \\ (\rho c)_G T & in \quad \Omega_G \end{cases} \tag{4.3}$$

Looking at this equation we notice that the main difficulty for solving problem (4.1) comes from the nonlinear part in Ω_S modeling the phase change which results in the enthalpy H being a non-linear function of the temperature T. Hence, the key to finding an accurate solution to this problem depends strongly on finding the best numerical scheme to solve this nonlinearity.

There are two classes of numerical methods present in literature specially designed to solve this problem : the front tracking methods([28],[62],[27],[3],[45] and [94]) and the fixed grid methods ([25],[59],[55],[24],[70],[9],[80] and [94]). The front tracking methods are mainly used to solve the Stephan problem with the classical formulation where the unknowns of the problem are both the temperature and the position of the interface between the two phases and the fixed grid methods are used when we consider solving the Stephan problem with the enthalpy formulation where the unknowns are the enthalpy and the temperature in each phase and the position of the interface is calculated a posteriori as a function of the temperature.

The problem that we study here is based on the enthalpy formulation of the Stephan problem, therefore only the numerical schemes that are used in case of a fixed grid approximation are considered here.

In what follows we will be focusing on the problem in domain Ω_S and we will present four of the most used numerical schemes in literature to solve the Stefan problem with the enthalpy formulation.

For all schemes we use the first order Euler backward method for time discretization by choosing a time step Δt and at step n of the time loop. We introduce H^n and T^n an approximation of the temperature $T(t_n)$ and the enthalpy $H(t_n)$ at time $t_n = n\Delta t$ and we fix $T^0 = T_0$.

The principle of the following time schemes is to approach the solution of the global nonlinear problem by solving a set of linear problems which are solved using the lowest order Raviart-Thomas finite element method presented in the previous chapter.

The source update method

First presented in [94] the main idea of the source update method is to reformulate the

following equation

$$\partial_t H(T) - div(\kappa \nabla T) = 0 \quad in \quad \Omega_S \tag{4.4}$$

in order to pass the nonlinear part as a source term by making it dependent on the value of the temperature at the previous time step. To explain how this is done we consider this equation which could be rewritten using (4.3)

$$\rho C \frac{\partial T}{\partial t} - div(\kappa \nabla T) = -\rho L_a \frac{\partial f(T)}{\partial t} \tag{4.5}$$

with the first order Euler backward method for time discretization we obtain :

$$\rho C \frac{T^{n+1}}{\Delta t} - div(\kappa \nabla T^{n+1}) = \rho C \frac{T^n}{\Delta t} - \rho L_a \frac{f^{n+1} - f^n}{\Delta t} \tag{4.6}$$

where f^{n+1} is the liquid fraction at time step $t_{n+1} = (n+1)\Delta t$. We can see that the nonlinear part is secluded into a source term.
The iterative linearization loop(k) within a time step is as follows : first all fields are initialized to their values at the previous time step, second we solve the equation

$$\rho C \frac{{T_k}^{n+1}}{\Delta t} - div(\kappa \nabla {T_k}^{n+1}) = \rho C \frac{T^n}{\Delta t} - \rho L_a \frac{f_{k-1}^{n+1} - f^n}{\Delta t} \tag{4.7}$$

using the known values at the previous time step : T^n and f^n and the known value of the liquid fraction at the previous iteration of the linearization loop at the current time step : f_{k-1}^{n+1}. The third step of the scheme consists on correcting the value of the liquid fraction f_{k-1}^{n+1} using the value of the temperature field ${T_k}^{n+1}$ calculated in the previous step of the linearization loop and the value of the liquid fraction f_{k-1}^{n+1} at the previous iteration of the linearization loop. The correction formula is established as follows :
at melting temperature ($T^{n+1} = T_m$) we have :

$$\rho C \frac{T_m}{\Delta t} - div(\kappa \nabla {T_k}^{n+1}) = \rho C \frac{T^n}{\Delta t} - \rho L_a \frac{{f_k}^{n+1} - f^n}{\Delta t} \tag{4.8}$$

by subtracting equation (4.8) to equation (4.7) we obtain :

$$\rho C \frac{{T_k}^{n+1} - T_m}{\Delta t} = \rho L_a \frac{{f_k}^{n+1} - f_{k-1}^{n+1}}{\Delta t} \tag{4.9}$$

which gives the expression used to correct the liquid fraction at each iteration of the linearization process.

$${f_k}^{n+1} = f_{k-1}^{n+1} + \lambda \frac{{T_k}^{n+1} - T_m}{\rho L_a} \tag{4.10}$$

where λ is a relaxation factor. The second and third step of the linearization loop are curried until the difference between the values of the liquid fraction at two successive iterations of the linearization loop falls under a fixed small value.

The enthalpy linearization

The enthalpy linearization scheme was proposed by R. Voller in [94]. We consider Equation 4.4 using the first order Euler backward method for the time discretization we obtain:

$$\frac{H^{n+1} - H^n}{\Delta t} - div(\kappa \nabla T^{n+1}) = 0 \tag{4.11}$$

with a Taylor development series of the enthalpy as a function of the temperature we obtain

$$H_k{}^{n+1} = H_{k-1}^{n+1} + \frac{dH}{dT}|_{H_{k-1}^{n+1}}[T_k{}^{n+1} - T_{k-1}^{n+1}] \tag{4.12}$$

We define the apparent heat capacity C^A given by the equation :

$$C^A = \frac{dH}{dT} \tag{4.13}$$

for a smoothed liquid fraction given by

$$f(T) = \begin{cases} 0 & T < T_m - \epsilon \\ \frac{T - T_m + \epsilon}{2\epsilon} & T_m - \epsilon \leq T \leq T_m + \epsilon \\ 1 & T > T_m + \epsilon \end{cases} \tag{4.14}$$

The enthalpy function is defined by Equation 1.18 in chapter 1. For simplicity, we consider here the case $C_L = C_S$

$$H(T) = \begin{cases} (\rho C)T + \rho L_a & \text{for} \quad T > T_m + \epsilon \\ (\rho C)T + \rho L_a (T - T_m + \epsilon)/2\epsilon & \text{for} \quad T_m - \epsilon \leq T \leq T_m + \epsilon \\ (\rho C)T & \text{for} \quad T < T_m - \epsilon \end{cases} \tag{4.15}$$

we have

$$C^A(T) = \begin{cases} (\rho C) & \text{for} \quad T > T_m + \epsilon \\ (\rho C) + \rho L_a / 2\epsilon & \text{for} \quad T_m - \epsilon \leq T \leq T_m + \epsilon \\ (\rho C) & \text{for} \quad T < T_m - \epsilon \end{cases} \tag{4.16}$$

and we give the temperature as the inverse of the enthalpy function

$$T = \begin{cases} \frac{H-\rho L_a}{(\rho C)} & \text{for} \quad T > T_m + \epsilon \\ \frac{H-\rho L_a \frac{\epsilon - T_m}{2\epsilon}}{(\rho C)+\frac{\rho L_a}{2\epsilon}} & \text{for} \quad T_m - \epsilon \leq T \leq T_m + \epsilon \\ \frac{H}{(\rho C)} & \text{for} \quad H < (\rho C)(T_m - \epsilon) \end{cases} \tag{4.17}$$

Combining equations (4.11), (4.12) and (4.13) we obtain :

$$\frac{C^A(H_{k-1}^{n+1})}{\Delta t}(T_k^{n+1} - T_{k-1}^{n+1}) - div(\kappa \nabla T_k^{n+1}) = \frac{H^n - H_{k-1}^{n+1}}{\Delta t} \tag{4.18}$$

The enthalpy linearization scheme works as follows : first all the fields are set to their values at the previous time step, second a prediction is made for the value C^A with equation (4.13) using the known temperature and enthalpy fields at the previous iteration of the linearization loop, third we solve equation (4.18), forth the enthalpy field is corrected using equation (4.12) and using the temperature field obtained at the previous step of the linearization process and the temperature field is updated using the inverse function of the enthalpy given by (4.17) to ensure the compatibility between the two fields. The previous steps are carried out to convergence which is obtained when the norm of the difference between the enthalpy field at the current iteration and the enthalpy field at the previous iteration falls under a fixed small value.

The linearization loop in this scheme ensures that at each time iteration the temperature and enthalpy fields are the solution of equation (4.18) which is very important when one is interested in the transitory state to determine the exact real time it took the material to change from one state to another. But when one is only interested in calculating the temperature field of the steady state at the convergence of the time loop the linearization process could slow down the convergence process. The following numerical scheme uses the same logic that the enthalpy linearization scheme without a linearization loop which leads to a very fast convergence to the solution of the steady state equation.

The Chernoff scheme

We consider Equation 4.4 and using the first order Euler backward method for the time discretization we obtain :

$$\frac{H^{n+1} - H^n}{\Delta t} - div(\kappa \nabla T^{n+1}) = 0 \tag{4.19}$$

We rewrite the enthalpy using a new function β as follows

$$H = \beta^{-1}(T) \tag{4.20}$$

β is defined as $T = \beta(H)$ [84] using this definition we can express the derivative of the enthalpy with respect to time as a function of the temperature and β

$$\frac{\partial H}{\partial t} = \frac{1}{\beta'(T)} \frac{\partial T}{\partial t} \tag{4.21}$$

And we define :

$$H^{n+1} = H^n + \gamma(T^{n+1} - \beta(H^n)) \tag{4.22}$$

where γ is a factor corresponding to $\frac{1}{\beta'(T)}$, with equations (4.19) and (4.22) we obtain :

$$\frac{\gamma}{\Delta t}(T^{n+1} - \beta(H^n)) - div(\kappa \nabla T^{n+1}) = 0 \tag{4.23}$$

The Chernoff numerical scheme for solving equation (4.4) is as follows : first we choose an initial guess for the enthalpy $H^0 = H_0$ at time step $t = 0$ and a value for the factor γ which is chosen as $\gamma \leq \frac{1}{max\beta(T)}$ to ensure the stability of the scheme (see [5] for more details), the second step consists on solving equation (4.23) and the third step consists on updating the enthalpy using equation (4.22) and for consistency the temperature field is corrected using the update enthalpy field and using the definition of the function β that is defined as the inverse of the enthalpy function. As an example for an enthalpy defined by equation (4.15) β is defined by equation (4.17). The two last steps are executed only once in a time iteration. With only solving the linear problem once this method is faster than the previous two methods : the source update method and the enthalpy linearization method.

Like the Chernoff scheme the next numerical scheme does not uses a linearization process in a time step but is more efficient because it uses the exact derivative of the function H with respect to the temperature at each time whereas the Chernoff scheme uses an approximated value : the factor λ.

The apparent heat capacity

The apparent heat capacity scheme proposed by R. Voller [94] is one of the most widely used enthalpy schemes. We consider Equation 4.4 and we start by differentiating the enthalpy with respect to the temperature as follows :

$$\frac{\partial H}{\partial t} = \frac{dH}{dT} \frac{\partial T}{\partial t} = C^A \frac{\partial T}{\partial t} \tag{4.24}$$

We can see that the nonlinearity is now taken in consideration in the expression of C^A which is the apparent heat capacity.
Using equation (4.24) Equation 4.4 becomes :

$$C^A \frac{\partial T}{\partial t} - div(\kappa \nabla T) = 0 \tag{4.25}$$

With the first order Euler backward method for the time discretization we obtain :

$$\frac{C^A}{\Delta t} T^{n+1} - div(\kappa \nabla T^{n+1}) = \frac{C^A}{\Delta t} T^n \tag{4.26}$$

The apparent heat capacity scheme is as follows : first step consist on initializing all fields to their values at the previous time step, second step consist in calculating an approximation of the value of C^A, third we solve equation (4.26) using an approximation for C^A, fourth step consist on correcting the enthalpy at the current iteration using a formula similar to the one used with the enthalpy linearization scheme, the formula is obtained with a Taylor development series of the enthalpy as a function of the temperature:

$$H^{n+1} = H^n + C^A[T^{n+1} - T^n] \tag{4.27}$$

the temperature field is corrected using the update enthalpy value at the current time iteration and using the function inverse of the enthalpy to ensure the compatibility between the temperature field and the enthalpy field. This process is performed only once in each time step which means that the temperature and enthalpy fields at each iteration do not necessary verify Equation 4.4 before convergence of the time loop but at the convergence of time loop the fields calculated are the solution of the steady state equation.
The expression of the derivative of the enthalpy with respect to temperature called the apparent heat capacity and given by equation (4.24) could lead to some numerical problems such as the appearance of plates in the phase front position, although this could be avoided if an appropriate time step is chosen depending on the length of the smoothing gap. An other option is to use the following expression first proposed by Morgan and al. in [60] :

$$(C^A)^n = (H^n - H^{n-1})/(T^n - T^{n-1}) \tag{4.28}$$

All this previous expressions used for calculating the apparent heat capacity present a discontinuity since C^A is defined as the derivative of the enthalpy $H(T)$ with respect to the temperature. This could provoke some numerical instabilities in the linearization interval of size 2ϵ. A remedial is given in [63] where the apparent heat capacity is defined

as the derivative of a normal distribution of parameter 2ϵ

$$(C^A)^n = exp[-2\epsilon^2(T^n - T_m)^2] \tag{4.29}$$

by using this expression for the apparent heat capacity we have no longer problems as consequence of the discontinuity. The following graph shows a plot of the apparent heat capacity as a function of the temperature using the expression given by (4.28) in the left side and the plot when using the expression given by (4.29) in the right side.

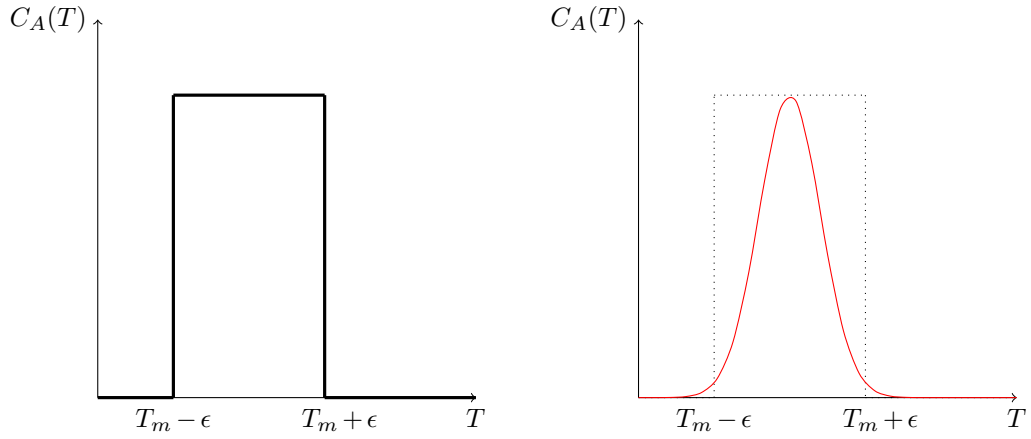

FIGURE 4.1: The apparent heat capacity for pure materials (left) and the smoothed apparent heat capacity(right) as functions of the temperature.

In the following section we conduct numerical experiments in order to test and compare the accuracy of the above presented numerical schemes.

4.3 Numerical Tests

In this section, we present the results of three numerical experiments. The first test is the melting of a material in a semi-infinite domain. In this case we are dealing with the classical Stefan problem where an analytical solution has been established by Carslaw and Jaeger in [21, p. 124]. The aim of this first test is to validate the implementation of the different numerical schemes by comparing the numerical solutions with the analytical one. After comparing their accuracy we have chosen the best three numerical schemes to use in the following tests. For the second test case we address the 2D-problem of the inward-freezing of a pipe presented in [94] and where a radial analytic solution is given. The aim of the second test is to demonstrate the accuracy of the selected numerical schemes for

a 2D-problem. At last we present a numerical test where we consider solving the phase change problem in a composite media described by equation (4.1) where the domain and thermo-physical properties of the components of the composite are taken from real experiments[16]. In this case we don't have an analytic solution thus we compare the temperature fields given by each numerical scheme with the temperature field obtained with a Newton method. The fastest between the most accurate schemes will be later used for applications with real geometries where the shape of the composite media is very complex and therefore a large number of degrees of freedom is needed to have a good numerical representation of the material hence the need for very fast numerical schemes.

4.3.1 Melting of a semi-infinite slab

In literature, there are very few cases where an analytical solution of the classical Stefan problem has been established. The test that we describe here, is very often used in publications to validate numerical methods used for solving Stefan type problems.
We consider the problem of melting a pure material in a semi-infinite media. The material is initially at a solid state at temperature $T_0 = -2°C$ bellow the melting temperature $T_m = 0°C$. We impose Neumann boundary conditions on both upper and lower walls and a liquid temperature $T_1 = 10°C$ at the right wall where $x = 0$ in such away that the melting process will began from the left side to the right side of the domain. In order to avoid having any error resulting from approximating the solution in the case of a semi-infinite domain on a finite domain we introduce the following Dirichlet boundary condition at the right end of the wall

$$T(x = l, t) = T_{analytic}(x = l, t)$$

where $T_{analytic}$ is the analytic solution in the case of a semi-infinite domain. The thermo-physical properties are taken as follows : $C = 10\ J/kg/K$, $L = 250\ J/kg$, $\rho = 1\ kg/m^3$ and $\kappa = 1\ W/mK$.
This Stefan problem has been presented in Chapter 3 where an analytic solution of similarity type is determined as follows

$$T_L(x,t) = T_1 + (T_m - T_1)\frac{erf(\omega\frac{x}{\sqrt{t}})}{erf(\omega\xi)} \tag{4.30}$$

$$T_S(x,t) = T_0 + (T_m - T_0)\frac{erfc(\omega\frac{x}{\sqrt{xt}})}{erfc(\omega\xi)} \tag{4.31}$$

where ξ is solution of the following transcendantal equation

$$\frac{St_L}{erf(\omega\xi)e^{\omega^2\xi^2}} - \frac{St_S}{erfc(\omega\xi)e^{\omega^2\xi^2}} = \sqrt{\pi}\omega\xi \tag{4.32}$$

where $\omega = \frac{1}{2}\sqrt{\frac{\rho C}{\kappa}}$ and

$$St_L = (T_1 - T_m)\frac{\frac{\rho C}{\kappa}}{L_a} \tag{4.33}$$

is the Stefan number in the liquid phase and

$$St_S = (T_m - T0)\frac{\frac{\rho C}{\kappa}}{L_a}$$

the Stefan number in the solid phase. The analytic front position is

$$X(t) = \xi\sqrt{t} \tag{4.34}$$

As explained in Chapter 1 the PCM considered here is supposed to have a change of phase at a constant temperature, the melting temperature T_m where in this case the liquid fraction function is given by

$$f(T) = \begin{cases} 0, & T(x,t) < T_m \\ 1, & T(x,t) \geq T_m \end{cases} \tag{4.35}$$

As one can see this function is discontinuous and might introduce additional difficulty to the numerical resolution. Thus we chose to use the following regularized form

$$f(T) = \begin{cases} 0 & T < T_m - \epsilon \\ \frac{T - T_m + \epsilon}{2\epsilon} & T_m - \epsilon \leq T \leq T_m + \epsilon \\ 1 & T > T_m + \epsilon \end{cases} \tag{4.36}$$

where a smoothing interval of length 2ε is introduced around the melting temperature. It has been proven in Chapter 3 that for ε very small the regularized solution converges to the exact one. More precisely if we denote the position of the liquid front X_L and the position of the solid front X_S we can define

$$ErrorX_L = \frac{|X_L - X_{analytic}|}{X_{analytic}} \tag{4.37}$$

and

$$ErrorX_S = \frac{|X_S - X_{analytic}|}{X_{analytic}} \tag{4.38}$$

as the errors between the positions of the numerical fronts obtained when solving the problem with the smoothed liquid fraction and the analytic front position given by (4.34). Than it has been proven that both errors decrease as ε. The main goal of the first set of simulations is to try to reproduce these analytic results using the numerical schemes introduced in section 4.2. This is also a great way to compare the accuracy of these schemes since only the best ones will be able to reproduce the analytic results.

For space discretization we use the hybrid-dual finite element method presented in chapter 2, where Lagrange P0 finite elements are used to approach the temperature field and the lowest order Raviart-Thomas finite elements are used to approach the thermal heat flux. The problem was solved using all four numerical schemes with several values of ε, these values are chosen greater than 0.01. This choice is motivated by results of simulations conducted using smaller values for ε (< 0.01). They showed that for ε smaller than 0.01 the errors on the numerical fronts start to increase as a consequence of the error introduced by the hybrid-dual finite element method.
The time step $dt = 10^{-4}$ and the mesh size $h = 2 \times 10^{-5}$ are chosen small enough to ensure that every node of the mesh undergoes the phase change. For every value of ε the simulation is set to stop after 150 time iterations or if the problem has reached the steady state which is determined when the variations in the temperature field from one time step to the next falls under a given tolerance fixed at 10^{-8}.
Table 4.3 shows the values of both $Error_L$ and $Error_S$ between the numerical front position and the analytic front position defined by (4.37) and (4.38) for every time scheme and for several values of ε.

Figure 4.2 shows these errors as functions of ε for the Chenroff scheme and the update source method. We can see that for the first method the errors stagnate from $\varepsilon \leq 0.1$, this is due to the fact that this scheme does not rely on the exact expressions of the derivative of the enthalpy with respect to the temperature defined by Equation 4.21 and rather uses the coefficient γ introduced in the previous section to approximate its values. As for the update source scheme the errors stagnate around $\varepsilon = 0.5$ which shows that this scheme is much less accurate than the Chernoff scheme. As for the apparent heat capacity and the enthalpy linearization we were able to find some very accurate results shown in Figure 4.3.

	AHC		*EntL*		*Chernoff*		*USM*	
ε	$Err\ X_S$	$Err\ X_L$	$Err\ X_S$	$Err\ X_L$	$Err\ X_S$	$Err\ X_L$	$Err\ X_S$	$Err\ X_L$
1	0.495	0.12	0.413	0.123	0.425	0.125	0.234	0.294
0.8	0.393	0.09	0.321	0.100	0.343	0.106	0.234	0.294
0.6	0.249	0.077	0.235	0.076	0.27	0.08	0.058	0.118
0.4	0.159	0.053	0.154	0.052	0.203	0.073	0.058	0.118
0.2	0.088	0.027	0.076	0.027	0.146	0.061	0.058	0.118
0.1	0.048	0.014	0.038	0.015	0.116	0.057	0.058	0.118
0.08	0.049	0.011	0.031	0.012	0.114	0.057	0.058	0.118
0.06	0.033	0.008	0.023	0.009	0.108	0.056	0.058	0.118
0.04	0.026	0.006	0.016	0.007	0.106	0.056	0.058	0.118
0.02	0.011	0.004	0.008	0.004	0.101	0.056	0.058	0.118
0.01	0.004	0.002	0.004	0.003	0.101	0.056	0.058	0.118

TABLE 4.1: Relative errors on the melting front position for several values of ε.

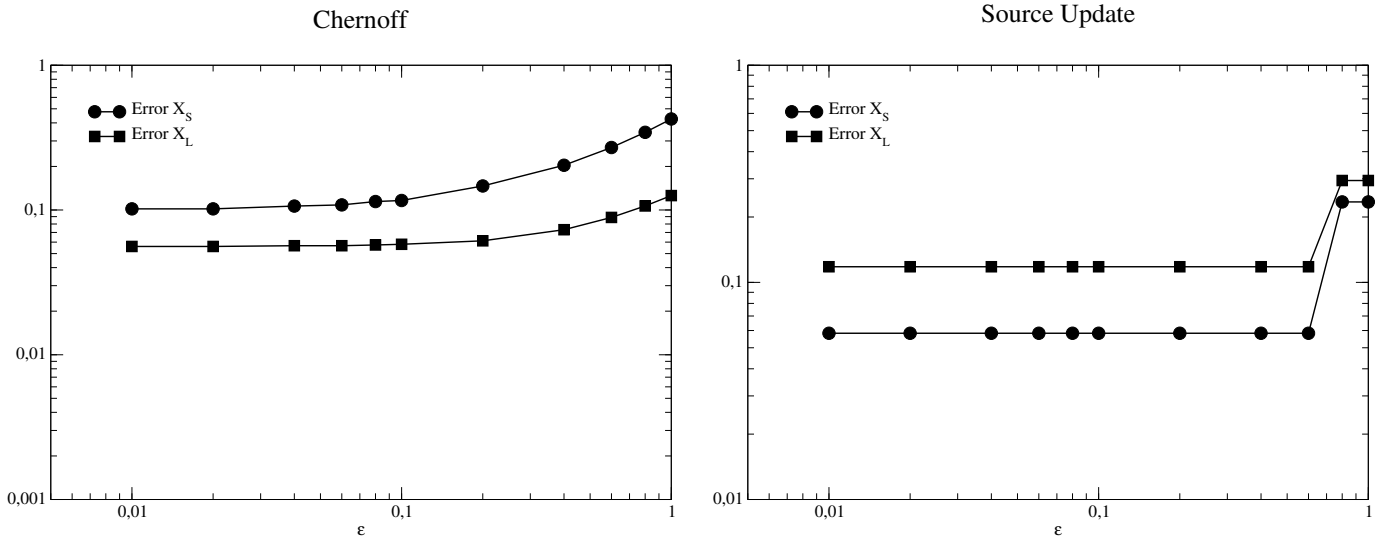

FIGURE 4.2: The errors on the fronts positions as functions of ε for Chernoff and source update method.

Indeed for the first scheme we found that $Error_L$ and $Error_S$ are close to order one of decay (0.91 and 0.88 respectively) and for the second scheme we have (0.98 and 0.81). This shows that these two schemes are the best when it comes to solving this type of problems with a smoothed liquid fraction of the type (4.14). We can also see that the apparent heat capacity is slightly more accurate than the enthalpy scheme especially for locating the solid front. This is a direct result of the choice for the maximum number of iteration for the time loop which was chosen large enough in order to have a comparable

behaviour as stated in [94]. In fact the apparent heat capacity scheme is expected to give comparable results to the ones given by the enthalpy linearization scheme after a few time steps.

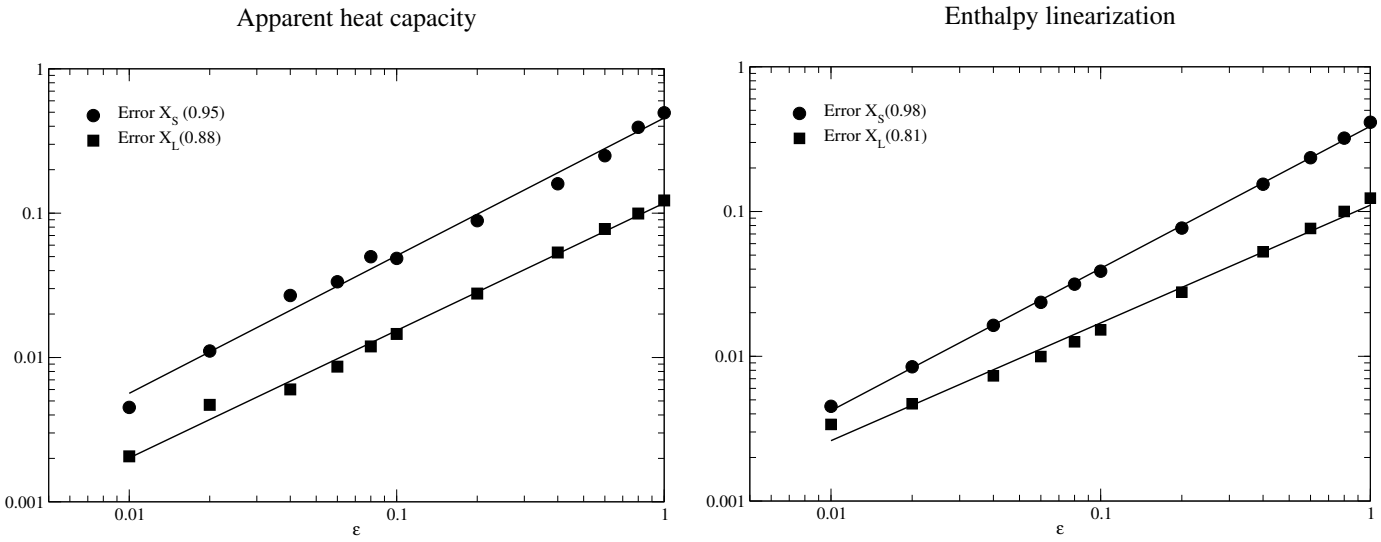

FIGURE 4.3: The errors on the fronts positions as functions of ε for the apparent heat capacity and the enthalpy linearization.

As an example we plot in Figure 4.4 the solid front position (in blue) and the liquid front position (in red) both as functions of time obtained by solving the problem using the enthalpy linearization scheme and for different values of ε. In each case we plot in black the analytic front position calculated using Equation 4.34 where ξ is determined by solving Equation 4.32 using the fsolve function in Scilab[85] which finds the zero of a system of nonlinear functions using a modification of the Powell hybrid method. With the thermo-physical values given above we have $\xi = 0.248$.

We observe that the liquid front is closer to the analytic front compared to the solid one. This is due to the values of the Stefan numbers, indeed with the thermo-physical values chosen for this test we have the following value for the Stefan numbers $\text{Stefan}_S = 0.08$ and $\text{Stefan}_L = 0.4$. The liquid Stefan number is much greater than the solid one which leads to the liquid phase moving faster than the solid phase.

We can see as well that for every value of ε the analytic front is located between the solid front and the liquid front. We observe also that the gap between the solid and liquid fronts and the analytic front vanishes as ε decreases which is the expected behaviour.

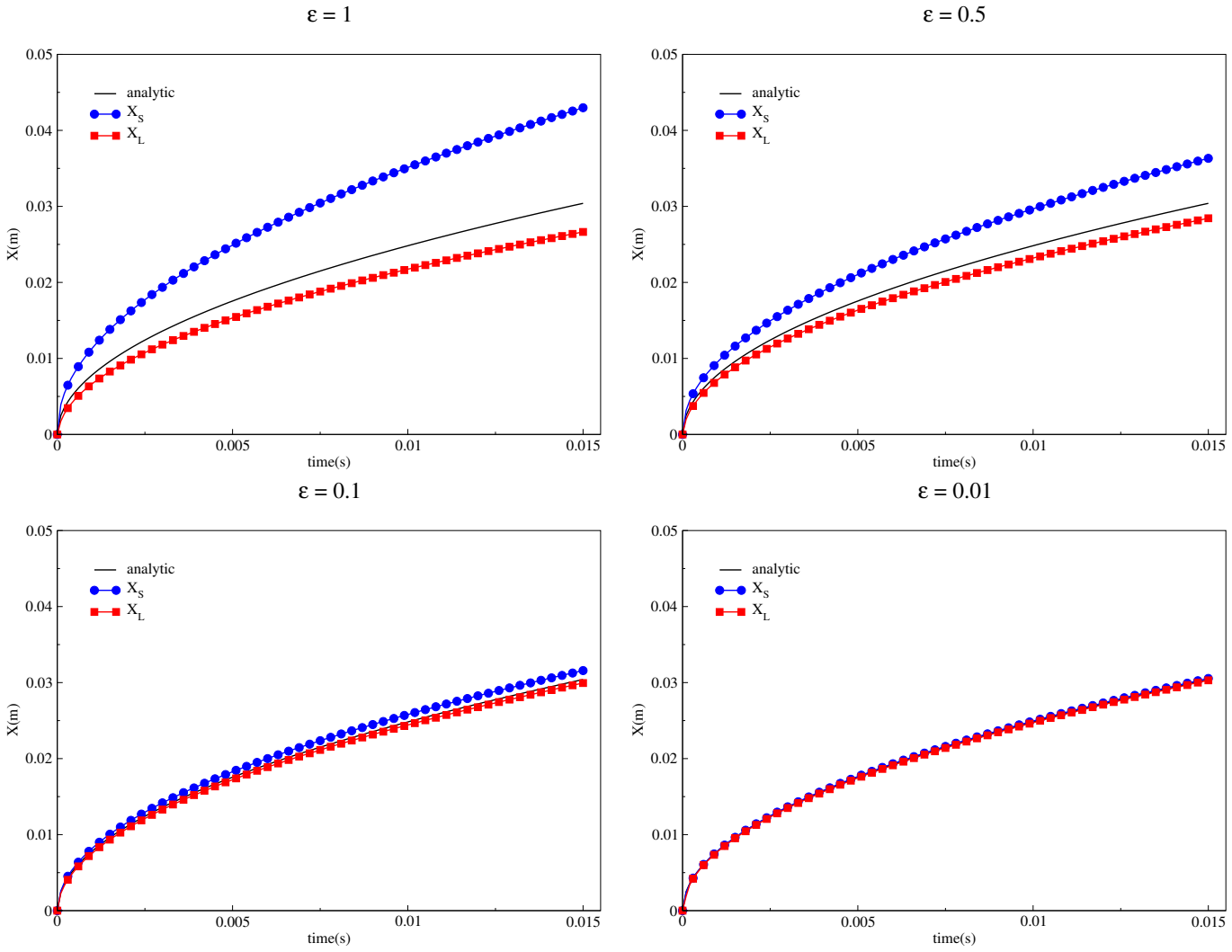

FIGURE 4.4: The liquid front in blue, the solid front in red and the analytical front position in black for Stefan = 0.4.

The previous results showed that the source update method is the least accurate method therefore in the remaining of this chapter we will be focusing on the other three schemes: Chernoff, the apparent heat capacity and the enthalpy linearization.

The Stefan number is of great importance in thermal energy storage applications since it gives the ratio of specific to latent heat storage [88]. Hence the importance of developing numerical schemes that allow to have very precise results for all values of the Stefan number. With this goal in mind we aimed to compare the accuracy of the numerical schemes by running tests for various values of the liquid Stefan number given by Equation 4.33

which from now on will be referred to as the Stefan number. The choice of investigating the effect of changing the liquid Stefan number as oppose to the solid one is due to the nature of the considered problem. Indeed in this section we are tackling the problem of melting a phase change material and in this case it is more interesting to look at what happens when changing the liquid Stefan number.
For this purpose we solved the previously described melting problem with the same initial and boundary conditions. For convenience reasons we set $C = 1$ and all the other thermophysical values are kept unchanged. However since we want to test the performance of the numerical schemes for different values of the Stefan number we have taken several values for the latent heat of fusion given in Table 4.2 with the corresponding values for the Stefan number and the auto-similarity variable ξ solution of the transcendantal Equation 4.32.

$L\ (J/kg)$	1000	100	10	1
Stefan	0.01	0.1	1	10
ξ	0.139	0.426	1.099	1.757

TABLE 4.2: Values of the Latent heat of fusion taken for this test and the corresponding values for the Stefan number and ξ..

The regularization parameter $\varepsilon = 10^{-4}$ is taken small enough such that $X_L = X_S$. The time step is $dt = 10^{-4}$ and all simulations are set to stop after 1000 time iterations. In Figure 4.5 we plot the evolution over time of the analytic front position and the numerical ones calculated with Chernoff, the apparent heat capacity and the enthalpy linearization schemes. The temperature fields as functions of space and at $time = 0.1\ s$ are presented in Figure 4.6. These graphs show that the Chernoff scheme slightly over estimates the analytic position of the melting front for Stefan$= 0.01$ and gives very good results for larger Stefan number. A similar observation is made for the temperature fields where a small gap between the numerical and the analytic value is visible for Stefan$= 0.01$ and vanishes as the Stefan number increases. We make similar observations for the front positions and the temperature fields obtained with the apparent heat capacity and the enthalpy linearization schemes where small gaps are observed between the analytic and numerical values for Stefan $= 0.01$. Moreover we can see that for the last two numerical schemes the errors made on the estimation of the front position and the temperature field seems to be close to the error made with the Chernoff schemes while being slightly

smaller.

To look at this last observation more in depth we give in Table 4.3 the analytic front position at different times and for several values of the Stefan number. First we notice that almost always the apparent heat capacity and the enthalpy linearization schemes give the same results. It is obvious that in fact for all three numerical schemes the error made on the position of the liquid front decreases as the Stefan number increases. It is also clear that the error made with the apparent heat capacity and the enthalpy linearization is always smaller while being very close to the error made with the Chernoff scheme.

time(s)	$X_{analytic}$	Err_{EntL}	Err_{AHC}	$Err_{Chernoff}$	
0.01	0.0139977	0.0474612	0.0474612	0.682487	
0.025	0.0221323	0.0360985	0.0360985	0.397562	
0.05	0.0312998	0.0344265	0.0344265	0.26162	**Stefan=0.01**
0.075	0.0383342	0.0261096	0.0261096	0.211613	
0.1	0.0442646	0.0160172	0.0160172	0.176667	
0.01	0.0426558	0.0205841	0.0205841	0.187293	
0.025	0.0674448	0.0115367	0.0115367	0.116973	
0.05	0.0953813	0.0121519	0.0121519	0.0867065	**Stefan=0.1**
0.075	0.116818	0.0108048	0.0108048	0.0640691	
0.1	0.13489	0.00494696	0.00494696	0.057665	
0.01	0.109945	0.00556167	0.0379011	0.0702406	
0.025	0.173838	0.00290313	0.00221018	0.0438097	
0.05	0.245844	0.00207748	0.00207748	0.0310028	**Stefan=1**
0.075	0.301096	0.00216482	0.00216482	0.0257822	
0.1	0.347676	0.00290313	0.00290313	0.0207997	
0.01	0.175766	0.00372727	0.0087845	0.0290134	
0.025	0.277911	0.00207798	0.00207798	0.0212688	
0.05	0.393025	0.00260864	0.00260864	0.0139169	**Stefan=10**
0.075	0.481356	0.00281636	0.000969727	0.0120495	
0.1	0.555822	0.000478748	0.000478748	0.00847492	

TABLE 4.3: Relative errors on the melting front position for several Stefan numbers.

A similar observation is made for the temperature field. In Table 4.4 we give the values of the analytic temperature for different values of the space variable $\boldsymbol{x}$ and the relative errors made with all three numerical schemes and $time = 0.1\ s$. It is obvious that in this case as well the error on the temperature decreases as the Stefan number increases.

In conclusion we have shown that Chernoff, apparent heat capacity and enthalpy linearization all give very accurate estimations for the temperature field and the front position and

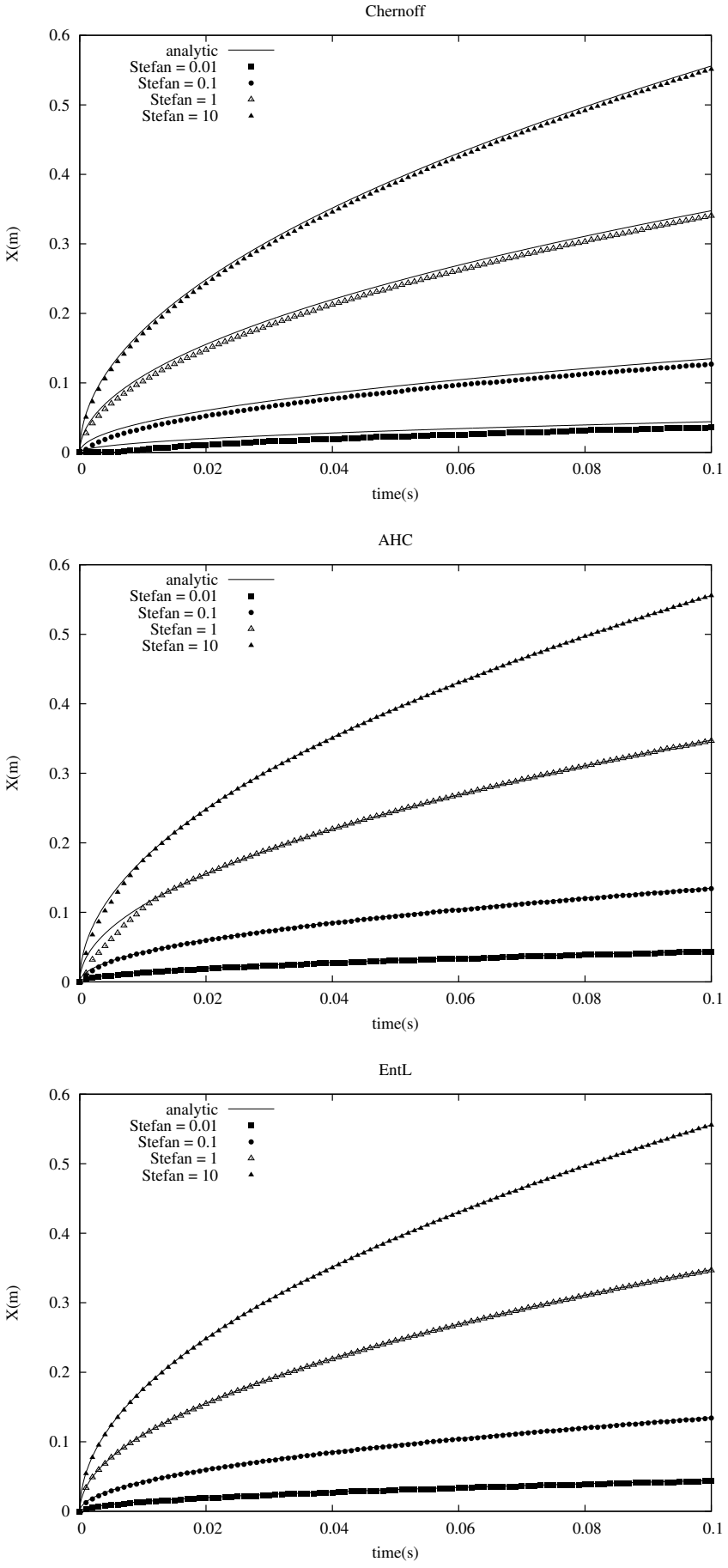

FIGURE 4.5: Numerical and analytical front position for different Stefan numbers.

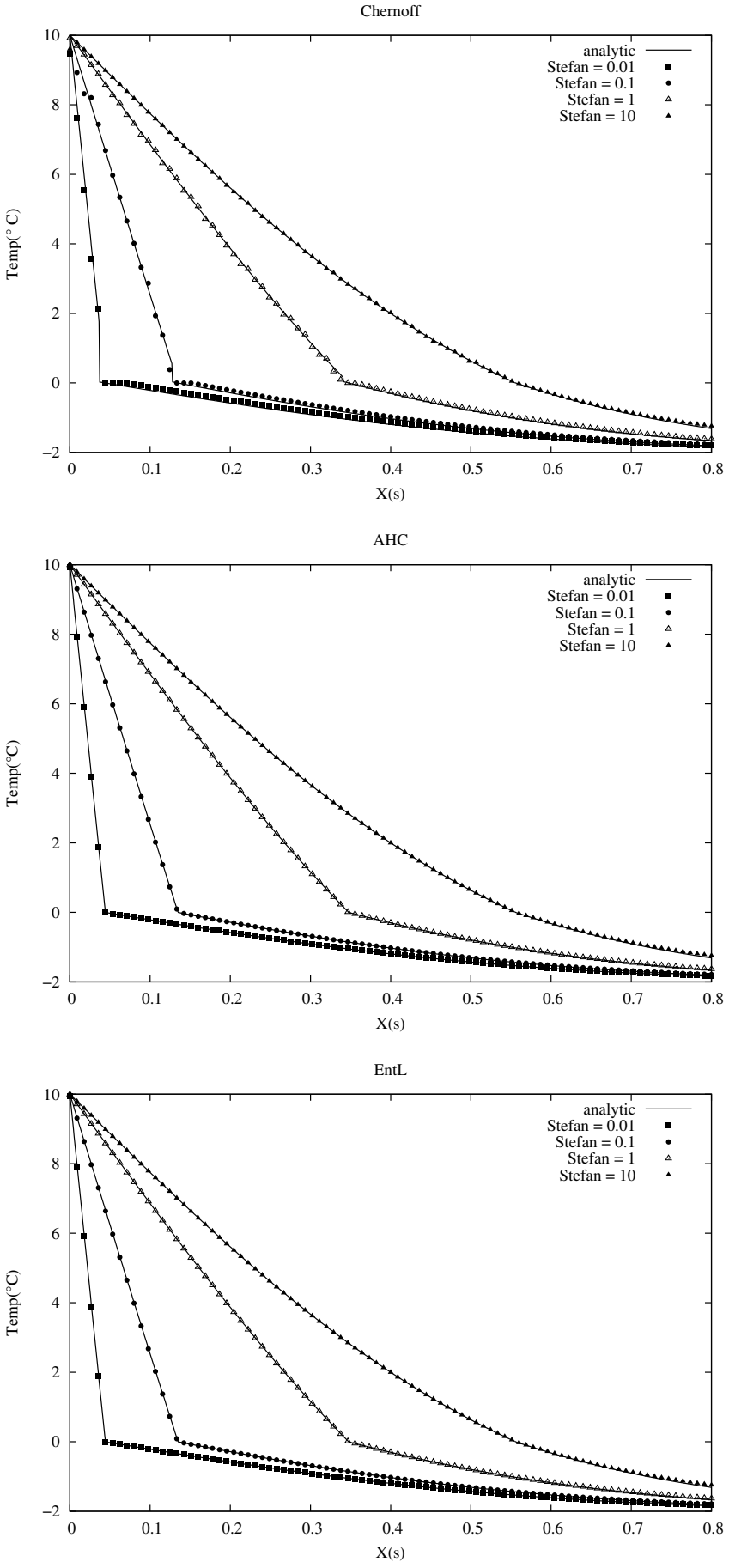

FIGURE 4.6: Numerical and analytical temperature fields for different Stefan numbers at $time = 0.1\ s$.

for all values of the Stefan number. These tests also show that the enthalpy linearization scheme is always more accurate then the other two schemes while giving very close results to the other two. This is due to the fact that in the enthalpy scheme an iteration loop is made within every time step which insures the accuracy of the approximated temperature field contrary to the other two schemes where this step is realized only once within a time step.

x(m)	$T_{analytic}$	Err_{EntL}	Err_{AHC}	$Err_{Chernoff}$	
0.0	10	0.0067073	0.00670613	0.052913	
0.1	-0.215548	0.00858772	0.0118513	0.455857	
0.2	-0.57919	0.00292618	0.0049285	0.158094	
0.3	-0.911256	0.00179826	0.0034904	0.0889761	**Stefan=0.01**
0.4	-1.19469	0.00155095	0.00300234	0.0575808	
0.5	-1.42899	0.00185119	0.00307765	0.0394154	
0.0	10	0.00223074	0.00223166	0.0411233	
0.1	2.50433	0.00970846	0.0109924	0.0864192	
0.2	-0.284548	0.0050985	0.00644933	0.257046	
0.3	-0.685477	0.00221486	0.00381217	0.0947196	**Stefan=0.1**
0.4	-1.02769	0.00186411	0.00339834	0.0538163	
0.5	-1.31057	0.00228494	0.00366858	0.0349053	
0.0	10	0.000939109	0.000938639	0.0081286	
0.1	6.84435	0.0015315	0.0013071	0.00112533	
0.2	3.86878	0.00280175	0.00209965	0.00945772	
0.3	1.15159	0.00890794	0.00600252	0.0432803	**Stefan=1**
0.4	-0.302119	0.002131	0.00549338	0.137269	
0.5	-0.796097	0.00399093	0.00411625	0.0451251	
0.0	10	0.000672708	0.000672543	0.0396607	
0.1	7.73951	0.00096517	0.000895403	0.0013454	
0.2	5.60801	0.00134746	0.00117978	0.00295057	
0.3	3.6616	0.00182748	0.00153182	0.00591753	**Stefan=10**
0.4	2.00024	0.00224507	0.00181242	0.00903803	
0.5	0.626918	0.000182191	0.000596814	0.0186937	

TABLE 4.4: Relative errors on the temperature for several Stefan numbers.

4.3.2 A two dimensional problem : freezing of a half-pipe

The implementation of the numerical schemes introduced in the previous section is independent of the dimension of the treated problem. In this section we consider the 2D-problem of the growth of a freeze-layer around a cooled half-pipe of radius $r = 1m$ seen in [94]. Initially the half-pipe is placed in a liquid at liquid temperature $T_L = 0.1°C$. At $t = 0s$ the temperature of the half-pipe is lowered to $T_S = -5°C$. The melting temperature of the liquid surrounding the half-pipe is $T_m = 0°C$. As in [94] all thermo-physical

properties are set to one. At $t > 0s$ an interface corresponding to the freezing point of the liquid begins to move from around the half-pipe and into the other end of the liquid where in one side of this interface the liquid has frozen and in the other side it is at a liquid temperature $T < T_L$. This problem is axi-symmetric and can be solved as a one dimensional problem in cylindrical polar coordinates (r, ϕ, z). The analytic front position is $X(t) = r + \xi\sqrt{t}$ where r is the radius of the half-pipe and ξ is solution of a transcendent equation of type (4.34). With the thermo-physical values set to one and the initial and boundary conditions given above we have $\xi = 2.05$.

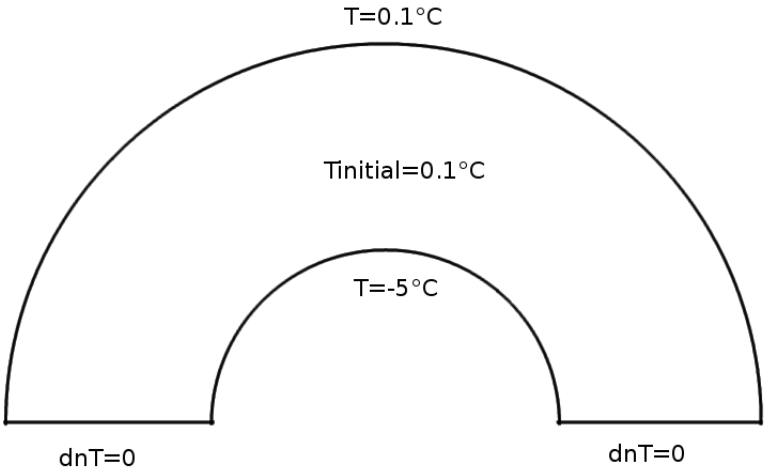

FIGURE 4.7: Transversal section of the half-pipe.

The results of the study conducted in the previous section using the 1D-problem allowed to select three numerical schemes which gave better approximation for the analytic solution compared to the estimation given by the fourth one. These three numerical schemes are the Chernoff scheme, the apparent heat capacity scheme and the enthalpy linearization scheme. The aim of this test is to determine which of these three schemes gives more accurate results in case of a 2D-problem.

The parameter representing the width of the phase change interval was taken $\epsilon = 10^{-3}$ since the goal of the simulation is to catch the analytic position of the solidification front. The time step $dt = 10^{-3}$ was chosen small enough in order to ensure that every node of the mesh undergoes the phase change. In order to enforce this, we have adapted the mesh

around the moving boundary at each time step using the adaptmesh function present in FreeFem++. This is made with respect to the variations of the Lagrange P1 interpolates of the liquid fraction, the temperature and the gradient of the temperature. An example of a mesh adapted around the solid-liquid interface is shown in Figure 4.8.

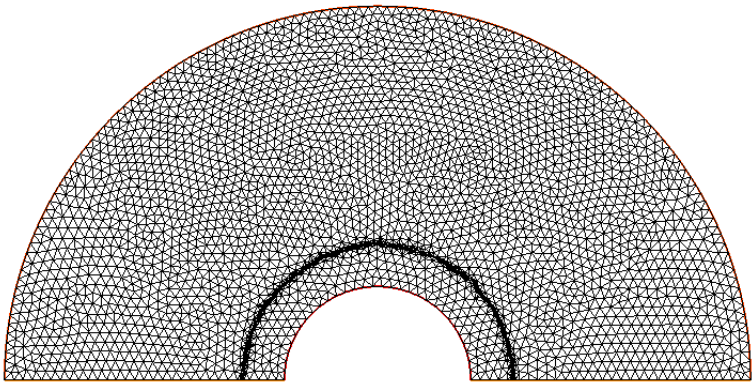

FIGURE 4.8: Example of a mesh where an adaptation is done around the position of the moving front.

The simulations are set to stop when the number of iterations of the time loop reaches 100 iterations. In figure 4.9 we plot for each of the numerical schemes the position of the numerical solidification front and the analytic front position both as a function of time. We also plot the position of the numerical solidification front using the x and y coordinates of the points located at the interface solid-liquid and we plot the analytic value as well.

As we can see on the left set of graphs all three numerical schemes allow to catch the interface at different times and it has been noticed that the precision of the interface position is greatly influenced by the mesh adaptation process specially for the Chernoff and apparent heat capacity schemes. This is less the case for the enthalpy linearization scheme because this schemes uses a linearization loop inside the time loop which allow to correct the approximation error that results from using an approximated value for the enthalpy as in Equation 4.12. For the right set of graphs we plot the numerical and analytical freezing front as functions of time. Here we notice a small difference between the analytic and the numerical freezing fronts, at the beginning of the solidification process, but this difference vanishes with time. This is specially the case for the apparent heat

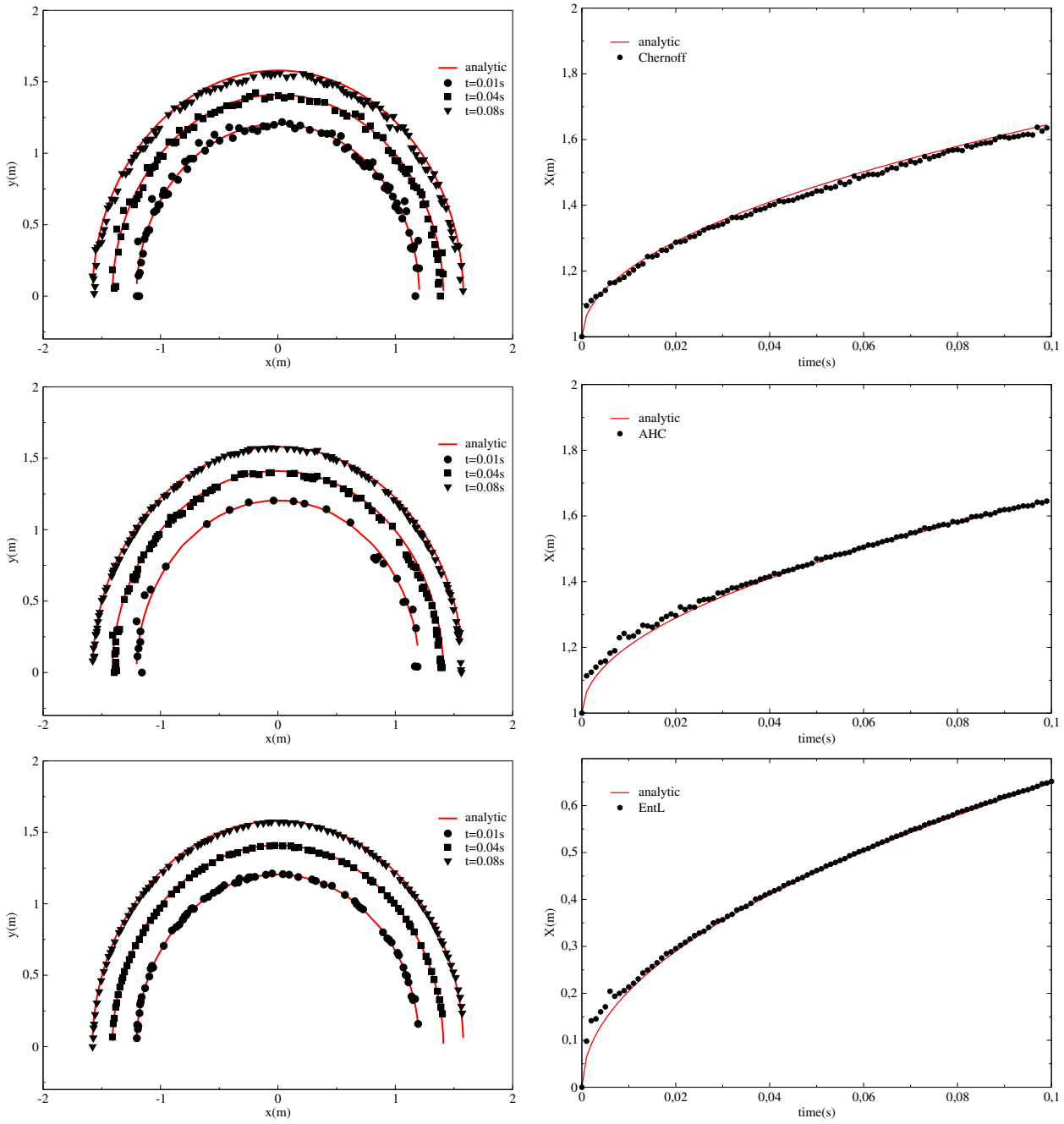

FIGURE 4.9: From top to bottom : analytic and numerical front positions for the Chernoff scheme, the apparent heat capacity and the enthalpy linearization.

capacity scheme and the enthalpy linearization scheme. This behaviour is due to the linearization process that becomes more accurate as the time iterations increases.

In order to compare the accuracy of the schemes we calculate two errors, the relative error between the analytic and numerical front position at the end of the simulation (Error1) and the mean of this error over time (Error2). The first error will allow us to determine which scheme is more accurate when the solution of the solidification problem approaches that of the steady state model and the second error will allow to determine the accuracy

of a scheme over the course of the simulation by accounting for the error at every time step.

$$Error1 = \frac{|Xnum_{end} - Xana_{end}|}{|Xana_{end}|}$$

$$Error2 = \frac{1}{N}\sum_{i=1}^{N}\frac{|Xnum_i - Xana_i|}{|Xana_i|}$$

In Table 4.5 we give the values of $Error1$ and $Error2$, as we can see the errors are of the same order for all three schemes and range from 10^{-3} to 10^{-4}. Looking closer we notice that, for $Error1$, the apparent heat capacity appears to be the most accurate scheme. On the other hand, when comparing the values of $Error2$, the enthalpy linearization scheme seems to be more accurate. We expected such results since for the apparent heat capacity and the Chernoff scheme, there is not a correction loop inside the time loop hence the reason why these schemes are expected to give an accurate solution only after several time iterations. However, for the enthalpy linearization scheme a correction loop is used at every time step to unsure the precise of the enthalpy and temperature approximations which explains the accuracy of this scheme over time.

schemes	AHC	Chernoff	EntL
Error1	2.7×10^{-4}	5.6×10^{-3}	5.3×10^{-3}
Error2	7.3×10^{-3}	8.3×10^{-3}	5.1×10^{-3}

TABLE 4.5: The relative error at the end of the simulation and the mean relative error over the time of the simulation.

Based on these results we can choose one numerical scheme depending on the problem that we are solving. For example if we are interested in the values of the temperature as the solution of the model near the solution of the steady state problem we can use either the apparent heat capacity or the Chenroff scheme. However if we are interested in the solution in the transient state the enthalpy linearization scheme would be a better choice.

4.3.3 A composite media with contact resistance

In this section we study a 2D heat conduction problem in a composite media consisting of a phase change material surrounded by a second material at a solid state modelled by Equation 4.1. The domain is the unity square and the PCM is filling a small square part that represents one quarter of the domain and the solid material is filling the rest

of the domain (see Figure 4.10). The PCM is suppose to melt at a constant temperature $T_m = 0°\ C$. At the initial state $t = 0\ s$ both materials are at a solid state at temperature $T = -10°C$, at $t > 0\ s$ the solid material is heated at $T = 20°\ C$ on the upper and right wall such that the melting process will begin from the sides along the solid material into the PCM. This experiment is inspired by an article (see [16]) where a similar problem is solved and the thermo-physical properties were taken identical to the ones given in this reference. For the PCM $\rho_S = 1\ kg/m^3$, $C_S = 2.510^6\ J/kg/K$, $\kappa_S = 1\ W/mK$ and $L = 210^4\ J/kg$ and for the solid material we have $\rho_G = 1\ kg/m^3$, $C_G = 10^6\ J/kg/K$ and $\kappa_S = 0.5\ W/mK$.

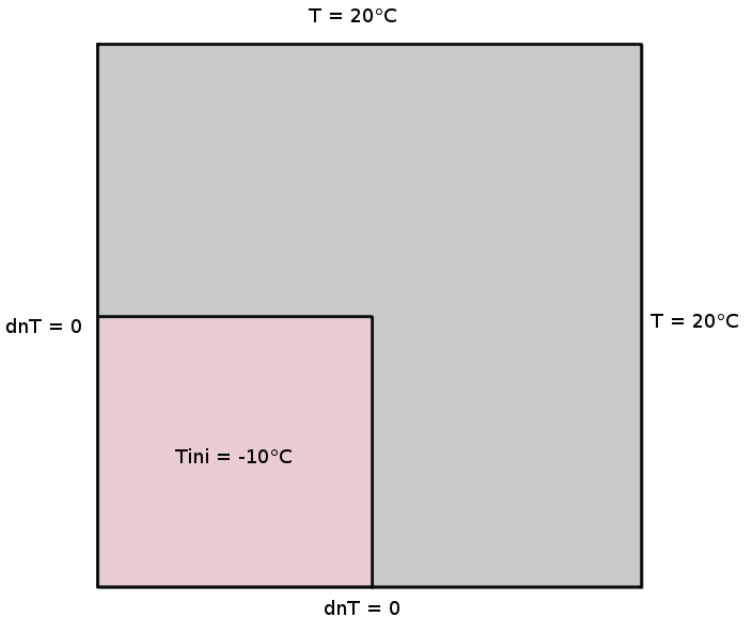

FIGURE 4.10: Initial and boundary conditions.

For this first test we have no contact resistance between both materials which means that the temperature is continuous between both domain which results in the normal components of the temperature gradient to be zero on this interface.

At first the non-linear in-stationary problem is solved on a very fine mesh with the implicit Euler Backward method for the time discretization and a Newton method for the nonlinear-part and the linear problem is solved using a hybrid finite element method presented in the chapter 2 where the temperature field is approached with Lagrange $P0$

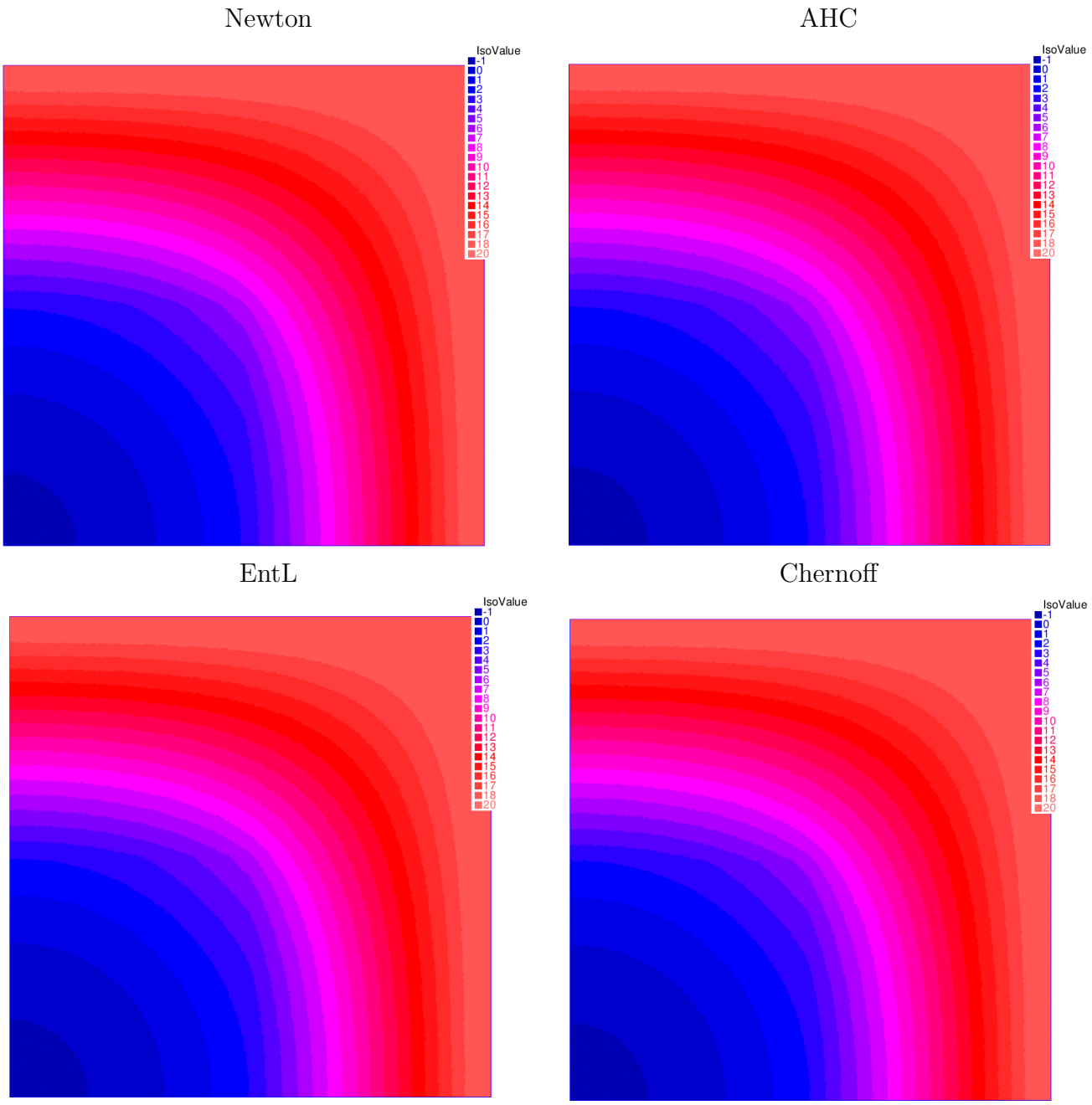

FIGURE 4.11: Temperature in the composite domain calculated for $R = 0$ at time $t_{end} = 2.7$ days.

elements and the temperature gradient is approached using Raviart-Thomas finite elements. Since there is no analytic solution to this problem, the temperature field calculated using this method will serve as a reference in order to test the accuracy of the numerical schemes.

In Table 4.5 we give the error in norm L_2 between the temperature field calculated using the Newton method and the temperature fields calculated using each one of the numerical

schemes. This show that for the unsteady state heat conduction problem in a composite without thermal contact resistance, the three numerical schemes allow to solve the problem with great precisions ($\sim 10^{-6}$). We can see as well that the apparent heat capacity and the enthalpy linearization give slightly more accurate results. This confirms the tendency shown by the tests exposed in the previous sections with a homogeneous PCM. In fact these two schemes give exactly the same error and the same solution (see Figure 4.11). This is the expected behaviour also mentioned in [94] and it is due to the fact that the first scheme could be seen as the second one without the inner loop within a time step used to correct the enthalpy and temperature predictions.

	AHC	EntL	Chernoff
Error	6.09×10^{-6}	6.06×10^{-6}	6.69×10^{-6}

TABLE 4.6: The relative error with no contact resistance..

Next we wanted to see if the value of the contact resistance could affect the accuracy of the numerical schemes. In order to investigate this we solved the above presented problem with various values for the contact resistance R. Figure 4.12 to 4.15 show the temperature filed calculated with Chernoff, the apparent heat capacity, the enthalpy linearization and to compare we also represent the temperature field calculated with the Newton method. As we can see the melting front moves slower for higher R. This is resulting from enforcing a contact resistance which introduces a discontinuity of the temperature at the interface separating both materials which delays the melting process in the PCM.
For every value of R we calculate the relative error in L_2–norm between the temperature fields given by Newton with the ones obtained with the other three schemes. These errors are given in Table 4.7. At first we notice that for all three numerical schemes the error decreases as R increases which is the expected behaviour. As we can see all three schemes give very accurate results with errors ranging from 10^{-5} for small values of R to 10^{-6} for the higher ones. And once more we can see that, while the apparent heat capacity and the enthalpy linearization give very close results, the latter is slightly more accurate thanks to the correction loop as explained previously.

R	$Error_{AHC}$	$Error_{EntL}$	$Error_{Chernoff}$
10^3	1.77292e-06	1.77292e-06	2.00331e-06
10^2	3.51713e-06	3.51713e-06	3.97345e-06
10	4.17422e-06	3.9721e-06	4.18825e-06
1	1.54117e-05	1.5297e-05	1.50057e-05
0.1	2.40938e-05	2.39782e-05	2.49798e-05
0.01	2.46214e-05	2.4503e-05	2.6241e-05
0.001	2.4697e-05	2.45699e-05	2.63888e-05

TABLE 4.7: Relative error on the temperature field in norm L_2 for different values of R.

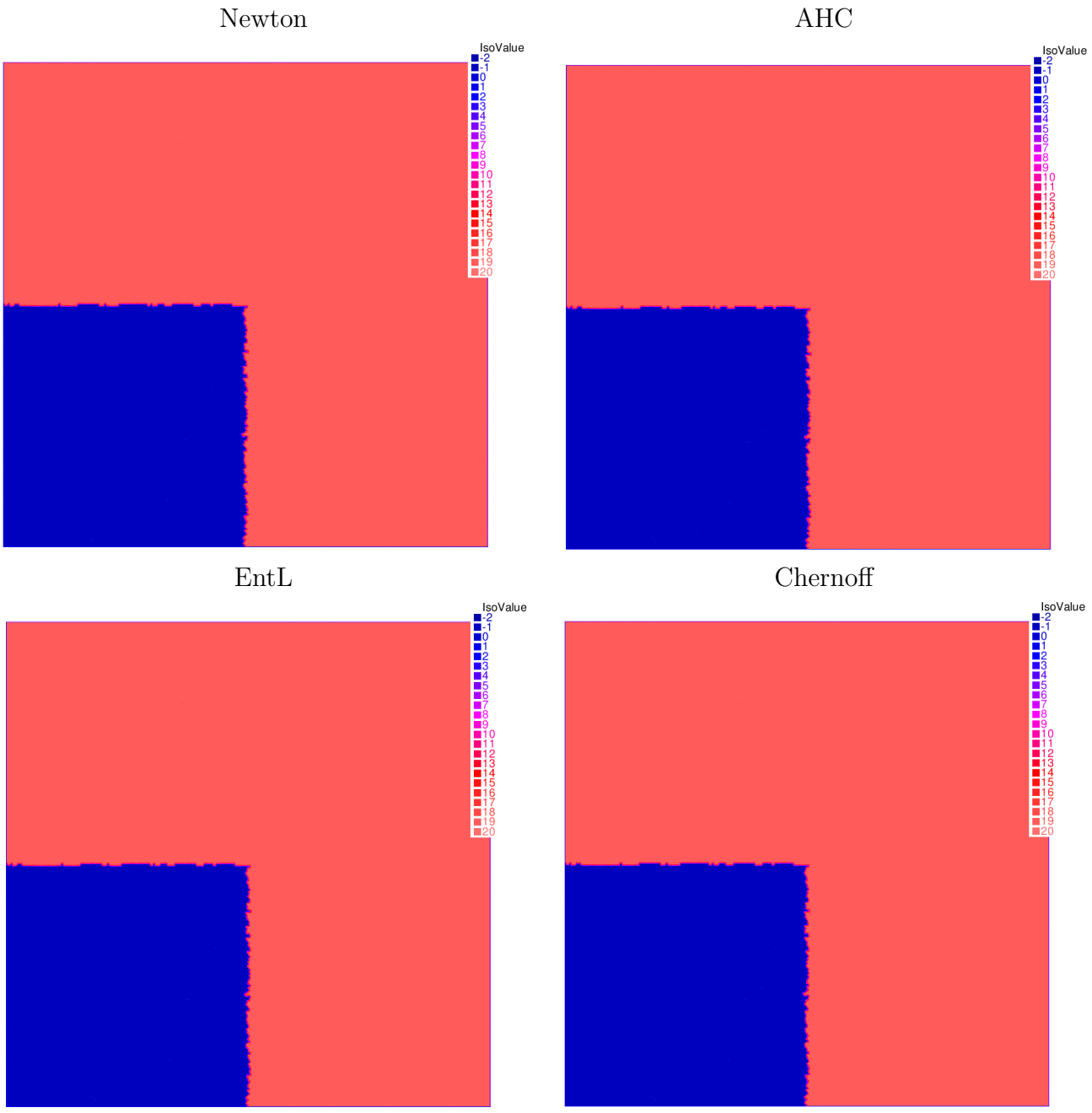

FIGURE 4.12: Temperature in the composite domain calculated for $R = 100$ at time $t_{end} = 2.7$ days.

4.4 Conclusions

In this chapter we have presented several numerical schemes used to solve the two phase Stefan problem. The accuracy of these schemes has been tested using two experiments where an analytic solution is given. Results of these two tests show that the apparent heat capacity scheme and the enthalpy linearization scheme are both slightly more accurate

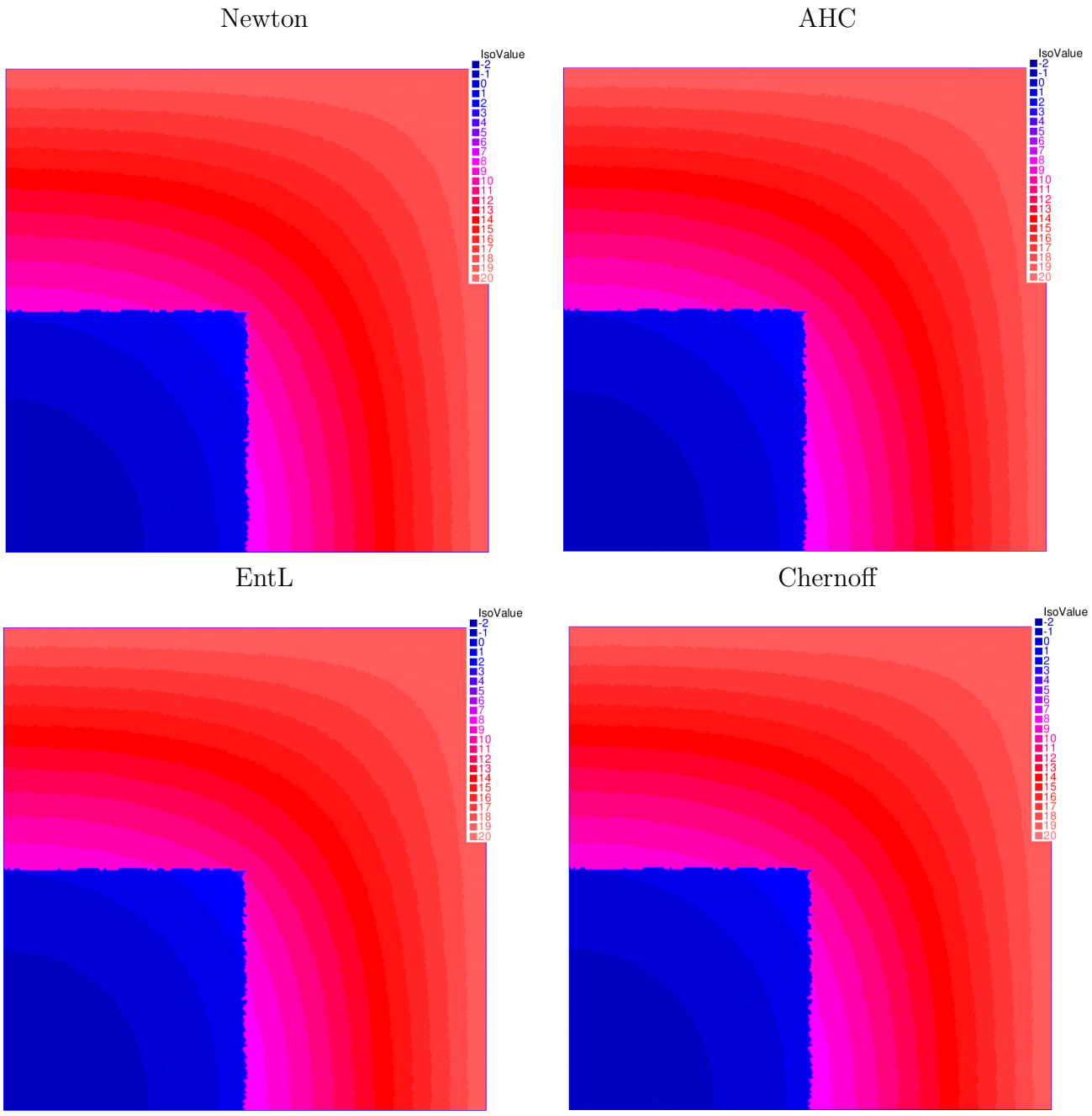

FIGURE 4.13: Temperature in the composite domain calculated for $R = 1$ at time $t_{end} = 2.7$ days.

than the Chernoff scheme but all three still give comparable results. They also show that after a given number of time iterations the apparent heat capacity is equivalent to the linearization scheme as expected. The last test consisted in solving the nonlinear phase change problem in a composite material with contact resistance. In this case there is no analytic solution hence the temperature field obtained with the Newton method is used as a reference solution in order to compare the numerical schemes. Different values of the contact resistance were used to see how the error behaves with regards to this parameter.

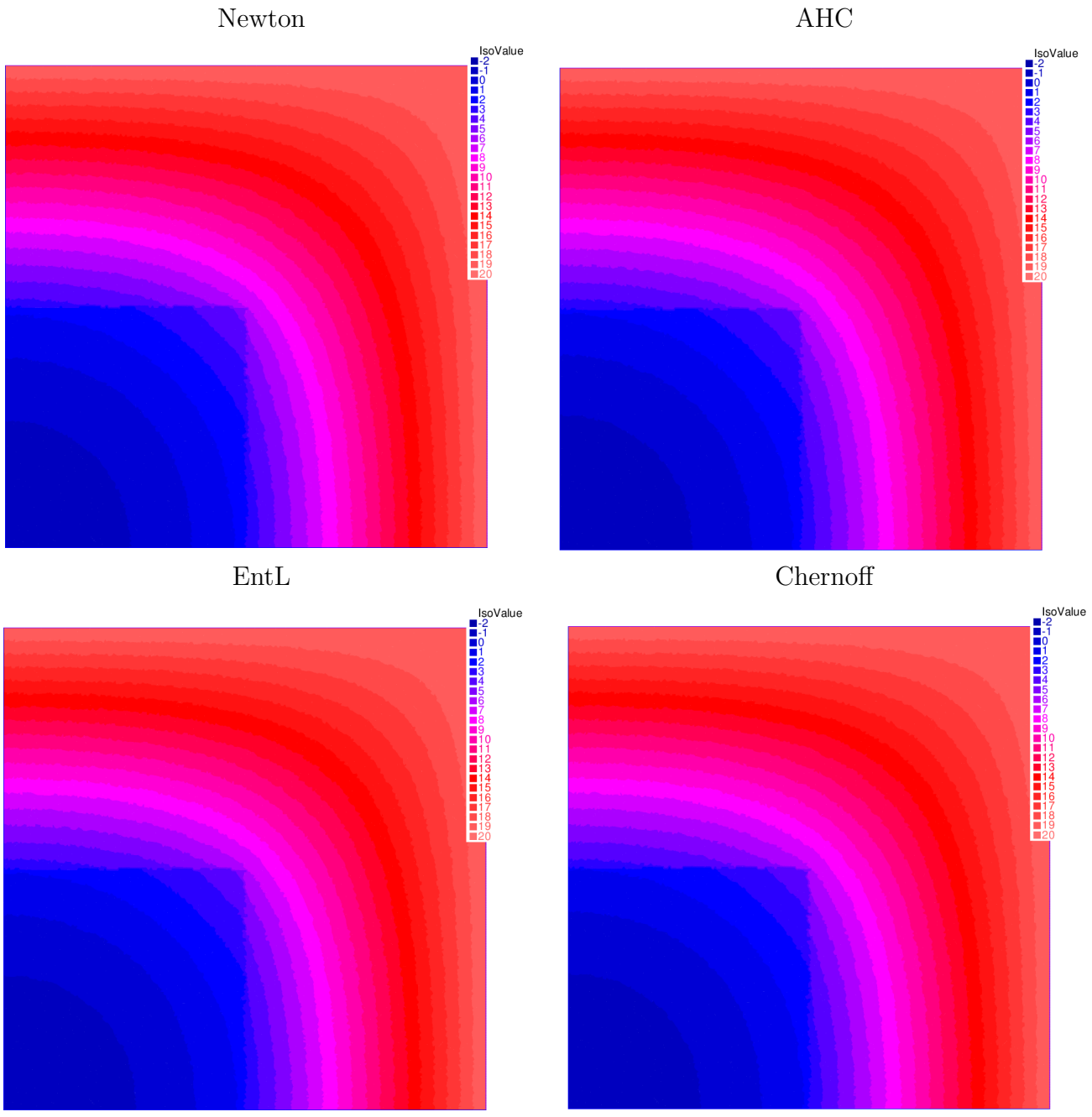

FIGURE 4.14: Temperature in the composite domain calculated for $R = 0.1$ at time $t_{end} = 2.7$ days.

Results show that all three schemes give very accurate and comparable results.

Based on theses three tests we conclude that the Chernoff scheme is the best choice for solving the heat conduction problem in a composite with complex geometry. The first reason is the proven accuracy of this scheme. In addition, this scheme could be implemented in a way that makes it faster than the other two. This is a consequence of replacing the derivative of the enthalpy with respect to the temperature with a coefficient

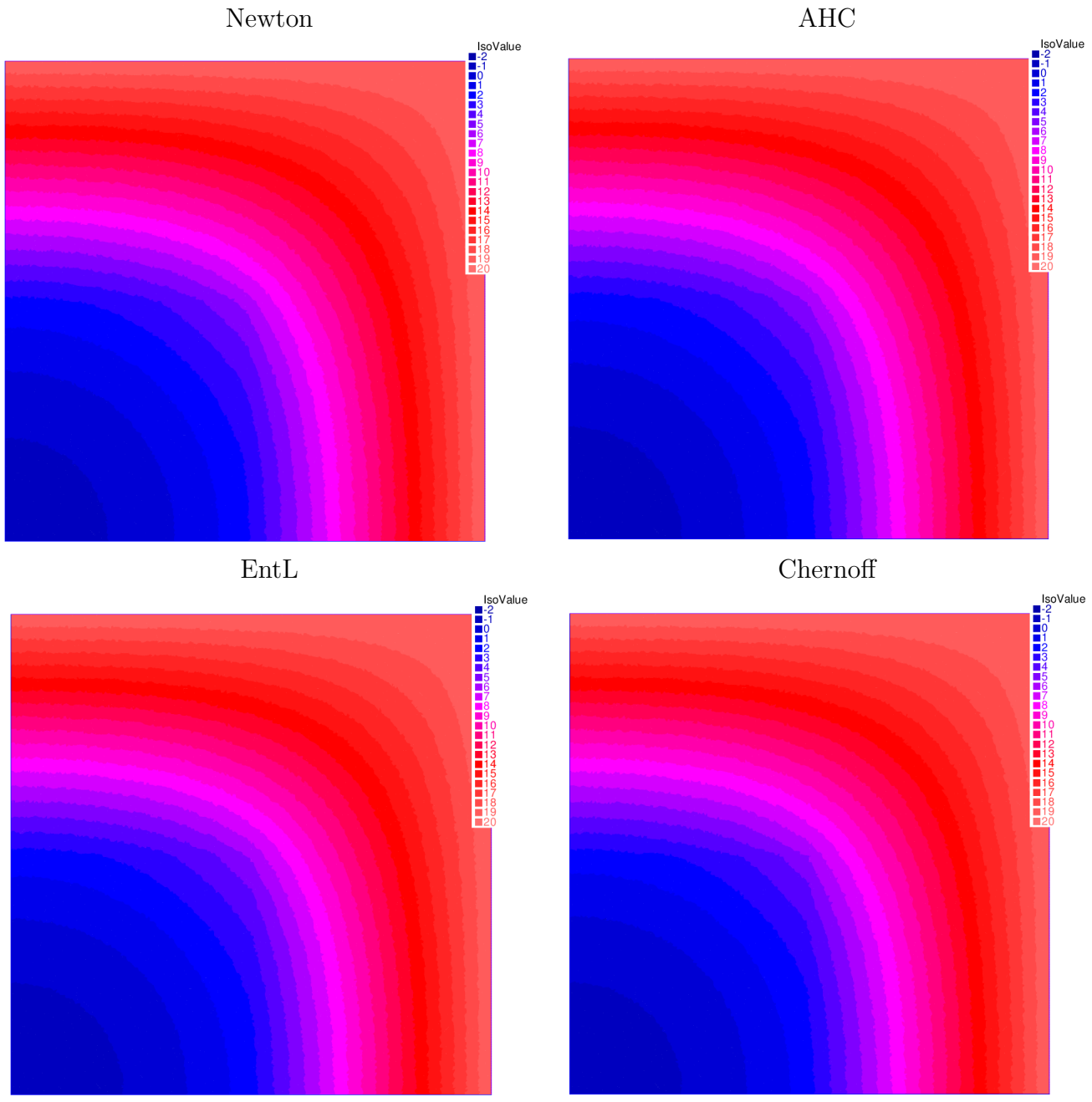

FIGURE 4.15: Temperature in the composite domain calculated for $R = 10^{-3}$ at time $t_{end} = 2.7$ days.

γ (see Equation 4.22) which consequently makes the matrix resulting from discretizing the linear problem not depending on time and hence can be defined outside the time loop.

Chapter 5

Asymptotic properties of composite materials

Understanding thermal exchanges within a composite material requires developing accurate models that allow to take into account all the physical phenomena not only at the macroscopic scale but also at the microscopic scale. As a result models that allow to achieve this aim are often complex and very hard to solve. There are some special cases, depending on the structure of the composite, where these models could be simplified. An example is when the composite material has some specific properties such a uniform pore distribution with uniform size. For this case, it could be proven that the model is simplified by solving a similar problem with a homogeneous material with physical properties equivalent to the properties of the composite material.

In this chapter we conduct some numerical simulations using two different composite materials, both used as part of a latent heat thermal energy storage system in a solar plant. These two composite structures are different in the size and shape of the pores. The results show that the composite material with more regular distribution of pores could be assimilated to a homogeneous media with equivalent thermo-physical properties. However this is not the case for the second composite material which has a less regular pore distribution. Another series of numerical simulations have been carried out to study the influence of thermal conductivity as well as the influence of the shape and size of the pores on the thermal behavior of the composites.

5.1 Introduction

In [18] several composite materials are presented. They are resulting from infiltrating pitch-based graphitic foams ($KFoam^{®}$) and coal-based graphite foams(CFoam) with a molten PCM (a binary mixture of hydroxides). All informations that might be needed for simulations, such as the thermal conductivity and the porosity, are given in this article. For this work we have chosen two of the composites presented in [18], the $KFoam^{®}$ $L1$ 250 and the $KFoam^{®}$ $D1$ infiltrated with a molten salt (see Figure 5.1). These two composites were chosen because they have dissimilar pore distributions and the size of their pores are very different. This will allow to highlight the impact of having a more or less uniform pore distribution.

The thermo-physical properties of both composite materials are given in 5.1 where κ is the thermal conductivity, ρ the density, C_p the specific heat and Δh_m is the latent heat of fusion of the PCM. Notice that the thermal conductivities of the foams and the effective thermal conductivities of both composite materials are not given in this table. Since we want to be able to compare results of simulations for both composite materials we need to have equal effective thermal conductivity values for both composites. As will be explained in section 5.2 this is possible to achieve thanks to the linear relation between the effective thermal conductivity of the composite and the thermal conductivity in the foam.

Parameter	**KL1_250**	**KD1**
porosity(%)	82	70
κ_{PCM} $(W/m/K)$	1	1
$C_{p_{PCM}}$ $(J/kg/K)$	4544	4544
$C_{p_{Foam}}$ $(J/kg/K)$	1402	1402
ρ_{PCM} $(J/kg/K)$	1634	1634
ρ_{Foam} $(J/kg/K)$	1318	1318
Δh_m (KJ/kg)	480	480

TABLE 5.1: Physical properties of the composite materials.

As explained in [18] 3D images of the infiltrated foams were made using thousands of 2D projections from different angles and using a projection algorithm. A binary file corresponding to a 3D image of a given sample is constructed using the number of pixels and by assigning 0 for the pixel in the foam and 1 for the pixel in the PCM. For our simulations we produced 2D rectangular cuts of images of the composites using these binary files. This is done by constructing a 2D structural mesh and defining a color function

that corresponds to the values given by the binary file assigned to the mesh nodes.

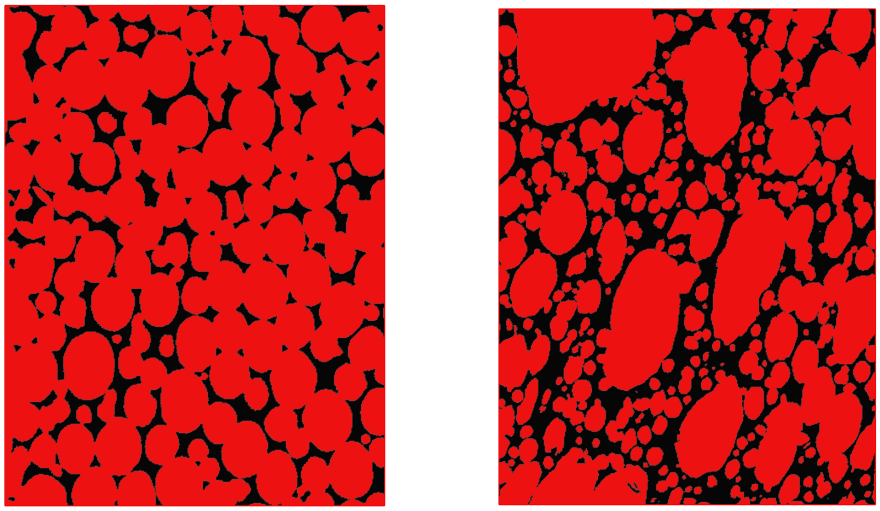

FIGURE 5.1: The composite structures used, $KL1\_250$ left and $KD1$ right.

Our first goal in this chapter is to determine whether one or both of theses composites could be assimilated to a homogeneous PCM. In order to investigate this we conduct two numerical simulations which consist in solving a heat conduction problem with phase change in a composite described by the following set of equations

$$\begin{cases} \partial_t H(T) - \operatorname{div}(\kappa \nabla T) = 0 & in\ \Omega_S \cup \Omega_G, \\ [\kappa \partial_n T] = 0 & on\ \gamma, \\ T = T_D & on\ \Gamma_D. \\ \kappa \partial_n T = 0 & on\ \Gamma_N. \end{cases} \tag{5.1}$$

without contact resistance and using the above 2D-images. Results for these composites are compared with results for a homogeneous PCM. This explained and discussed in the following section 5.2. Next, in section 5.3 we present results of simulations where we solve the above problem with several values of the thermal contact resistance. The goal here is to investigate the effect of having a thermal resistance on the temperature distribution within the composite.

Our next goal is to emphasize the effect that increasing the effective thermal conductivity has on the other thermal properties of the composite. For this we realized simulations

consisting in solving Equation 5.1 with five different values for the effective thermal conductivity. Results are presented and discussed in section 5.4.
At last we investigate how increasing the size of the pores of the composites or modifying their shapes effects their thermal behaviours. This is done by means of numerical dilatations using the binary files. In order to increase the size of the pores we realized two dilatations, with equal coefficients, in the $\boldsymbol{x}$-direction and in the $\boldsymbol{y}$-direction. As for modifying their shapes dilatations are done one direction at the time. For every new composite we conduct similar simulations as for the previous cases. Results are presented and discussed in sections 5.5 and 5.6.

5.2 Study of the composites and comparison with a homogeneous PCM

In this section we wish to compare the composites presented in 5.1 to a homogeneous PCM and to one an other. In order to justify such comparisons two conditions must be met. First we need to ensure that the storage capacity Q has the same value for both composites. Consider a 2D rectangular samples of two composite materials with dimensions $l_1 \times L_1$ and $l_2 \times L_2$ with porosities $\mathcal{E}_1$ and $\mathcal{E}_2$ and the same latent heat of fusion Δh_m. The thermal heat capacity of storage is given by

$$Q_1 = \mathcal{E}_1 l_1 L_1 \Delta h_m$$

for the first material and

$$Q_2 = \mathcal{E}_2 l_2 L_2 \Delta h_m$$

for the second material. Hence to have $Q_1 = Q_2$ with $l_1 = l_2$ we need to have $\mathcal{E}_1 L_1 = \mathcal{E}_2 L_2$ and since $\mathcal{E}_{KL1\_250} = 82\% > \mathcal{E}_{KD1} = 70\%$ we took $L_{KD1} > L_{KL1\_250}$ (see Figure5.2).

Second, the composites must have the same effective thermal conductivity. If κ_G is the thermal conductivity of the matrix and κ_S the thermal conductivity of the PCM, we know that there exists a linear relation between the effective thermal conductivity of the composite and the ratio $\frac{\kappa_G}{\kappa_S}$ (see [19]). In our case $\kappa_S = 1$ therefore we expect to have a linear relation between the effective thermal conductivity and κ_G. In order to explicit

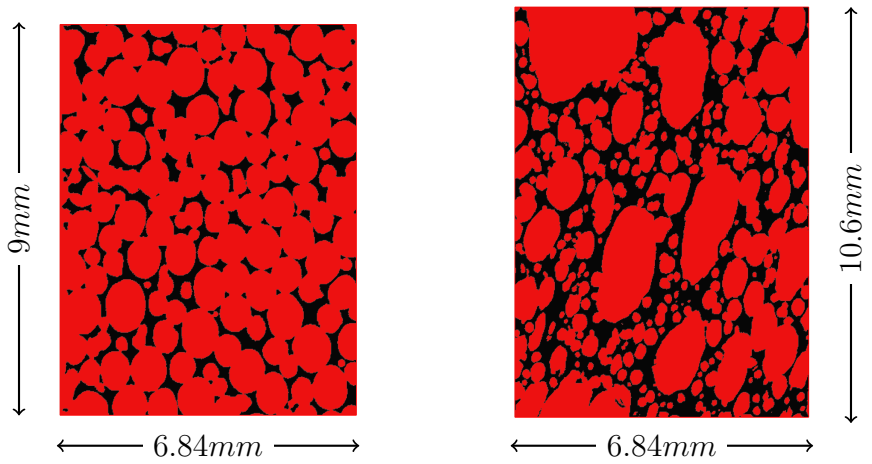

FIGURE 5.2: The composite structures used, $KL1\_250$ left and $KD1$ right.

this relation we conduct five numerical simulations for each composite, each simulation consists in solving the following steady state heat conduction problem in the composite

$$\begin{cases} \operatorname{div}(\kappa \nabla T) = 0 & in\ \Omega_S \cup \Omega_G, \\ [\kappa \partial_n T] = 0 & on\ \gamma, \\ T = T_D & on\ \Gamma_D, \\ \kappa \partial_n T = 0 & on\ \Gamma_N. \end{cases} \tag{5.2}$$

where T is the temperature, $\kappa = (\kappa_G, \kappa_S)$ is the thermal conductivity. Ω_G represents the foam and Ω_S the PCM. Γ_D designates the upper and lower walls and Γ_N the right and left walls.

On the top wall we have $T_D = 320°C$ and on the bottom wall we have $T_D = 310°C$. Every simulation corresponds to a different value of κ_{matrix}.

The effective thermal conductivity of the composite materials is calculated using the following equation (see [51])

$$\kappa_{\text{effective}} = \frac{L \int q dA}{\Delta T \int dA}$$

where q is the heat flux through the cross-section dA between the temperature difference ΔT on a distance L. Heat flow through the unit area of the surface with normal $\boldsymbol{n}$ is linked with the temperature gradient in the n-direction by Fourier's law as

$$q = -\kappa \frac{\partial T}{\partial \boldsymbol{n}}$$

Figure 5.3 shows the effective thermal conductivity as a function of κ_{matrix} for both composites. We can see that in order to have an effective thermal conductivity of $20W/m/K$ for both composites we need to set $\kappa_{matrix} = 958W/m/K$ for KL1_250 and $\kappa_{matrix} = 336W/m/K$ for KD1.

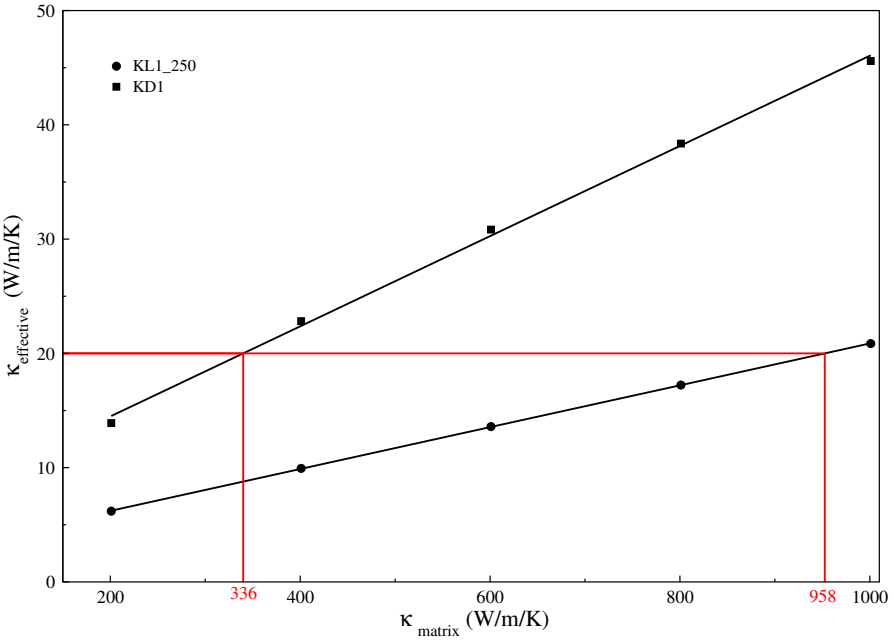

FIGURE 5.3: The effective thermal conductivity as a function of the thermal conductivity of the matrix.

5.2.1 Initial and boundary conditions

The initial and boundary conditions are chosen in order to have an evolution of the temperature in the $\boldsymbol{y}$-direction. The domain is initially at a temperature close to the melting temperature of the PCM $T_{initial} = 311.9°C$, at $t = 0s$ the temperature at the bottom wall $\boldsymbol{y} = 0$ is raised to $T_D = 322°C$. At all times during the simulations we have $\partial_n T = 0$ at the left wall, the right wall and the top wall. This is illustrated in Figure 5.4.

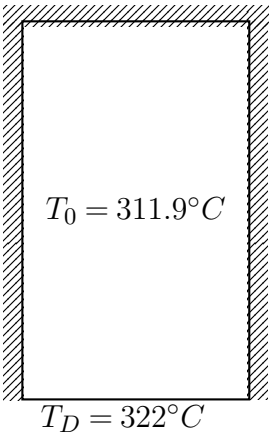

FIGURE 5.4: Temperature conditions for all simulations.

For comparison purposes we consider a 2D-sample of a PCM of the same size as the samples of the composites. Consider a composite material consisting of a matrix with pores filled with a second material. The porosity of this composite material is defined by

$$\epsilon = \frac{V_{pores}}{V_{Total}} \tag{5.3}$$

If ρ_G and ρ_S are respectively the density of the matrix and the density of the PMC then the density of the equivalent homogeneous material is given by

$$\rho = \epsilon\rho_S + (1-\epsilon)\rho_G. \tag{5.4}$$

The symbols C_{p_G} and C_{p_S} are respectively the specific heat capacity of the matrix and the specific heat capacity of the PCM, the specific heat capacity of the equivalent homogeneous material is given by

$$C_p = \epsilon C_{p_S} + (1-\epsilon)C_{p_G}. \tag{5.5}$$

We designate by L_{a_s} the latent heat of the PCM, so the latent heat of the equivalent homogeneous material is calculated as follows

$$L_a = \epsilon L_{aS}. \tag{5.6}$$

The non-linear heat conduction problem of a homogeneous phase change material filling a similar 2D-rectangular domain with similar initial and boundary conditions has an analytic solution of similarity type. Since the domain is initially at a temperature close to the melting temperature this problem is considered as one-phase Stefan problem since only the liquid phase is active as oppose to the two phase Stefan problem presented in the previous chapter where both the liquid and solid phase are actives. For this problem the temperature as a function of time and position is given by

$$T(y,t) = T_D + (T_m - T_D)\frac{erf(\frac{y}{2\sqrt{\alpha t}})}{erf(\xi)} \quad 0 < y \leq X(t), \tag{5.7}$$

where T_m is the melting temperature erf is the error function, $erfc$ is the complementary error function and $X(t)$ is the position of the melting front defined by

$$X(t) = 2\xi\sqrt{\alpha t}\ .$$

Here ξ is the solution of the following non-linear equation

$$\frac{Stefan}{erf(\xi)e^{\xi^2}} = \sqrt{\pi}\xi$$

with

$$Stefan = \frac{c(T_D - T_m)}{L_a}$$

is the Stefan number and c and L_a are the specific heat and the latent heat of fusion of the material. The heat flux at the surface $\boldsymbol{y} = 0$ is defined by

$$q(0,t) = -\frac{\kappa(T_m - T_D)}{erf(\xi)\sqrt{\pi\alpha t}}$$

With the dimensionless variables

$$x^* = \frac{x}{x_{max}},\ t^* = \frac{\alpha t}{x^2},\ T^* = \frac{T - T_D}{T_m - T_D},\ X^* = \frac{X}{x_{max}}\ and\ q^* = \frac{x_{max}q}{\kappa(T_m - T_D)}$$

we define the dimensionless temperature, front position and heat flux at $\boldsymbol{y} = 0$ as follows

$$T^*(x^*,t) = \frac{erf(\frac{x^*}{2\sqrt{t^*}})}{erf(\xi)},\ X^*(t) = 2\xi\sqrt{t^*},\ q^*(0,t) = -\frac{1}{\sqrt{\pi}erf(\xi)\sqrt{t^*}}$$

A similar study as the one that we present in this section has been done in the thesis by Vincent Morrison[61] where he compares the results of simulations with the same initial

and boundary conditions mentioned above to the ones given by a model for a composite domain with graphite foam and molten PCM. In this study it is shown that the thermal state evolution is similar with respect to the similarity variable $\mu = \frac{y}{2\sqrt{\alpha t}}$, the melting front position is proportional to the squared root of time and the heat flux at the boundary surface is proportional to the inverse of the squared root of time.
The simulations done in this chapter to test the homogenization of the composite structures are inspired by this work.

5.2.2 Results and discussions

Problem 5.1 is solved with both composites presented in chapter 2. The first order backward Euler method is used for time discretization along with the Chernoff scheme for the treatment of the non-linearity. The Raviart-Thomas finite element method presented in chapter 2 is used to solve the linear problem at each time step as explained in the previous chapter section 4.2. Simulations are stopped when all the PCM in the composite has melted. As explained previously the boundary conditions are chosen to obtain an evolution of the temperature in the $\boldsymbol{y}$-direction from bottom to top. Hence in order to compare both results from both simulations we calculate at every time step the mean temperature for every value of $\boldsymbol{y}$, the mean temperature in the carbon and the mean temperature in the PCM. The difference between the mean temperature in the graphite and the mean temperature in the PCM for each value of $\boldsymbol{y}$ and for different values of time is presented in Figure 5.5.

We can see that for the KL1_250 structure the difference between the mean temperature in the graphite and the mean temperature in the PCM decreases with time and with $\boldsymbol{y}$. This means that the temperature tends to a stable value that is the same in both the graphite and the PCM. However this is obviously not the case for the KD1 composite as we can see at the end of the simulation big differences are noticeable for the highest values of $\boldsymbol{y}$. This could be the consequence of the uneven distribution of pores with the biggest pores at the top of the cut as seen in Figure 5.2. A similar observation could be made when we look at Figure 5.6 where we plot the mean temperature in the graphite and the mean temperature of the PCM both as functions of the dimensionless $\boldsymbol{y}$ and for times ranging from $t = 0.05s$ to $t = 182s$ time at which all the PCM has melted. It is obvious that in the case of the composite based on the KL1_250 structure the mean temperature in the graphite and the mean temperature in the PCM seem to have very close values at $t = 182s$. This is not the case where the composite based on the KD1 structure is

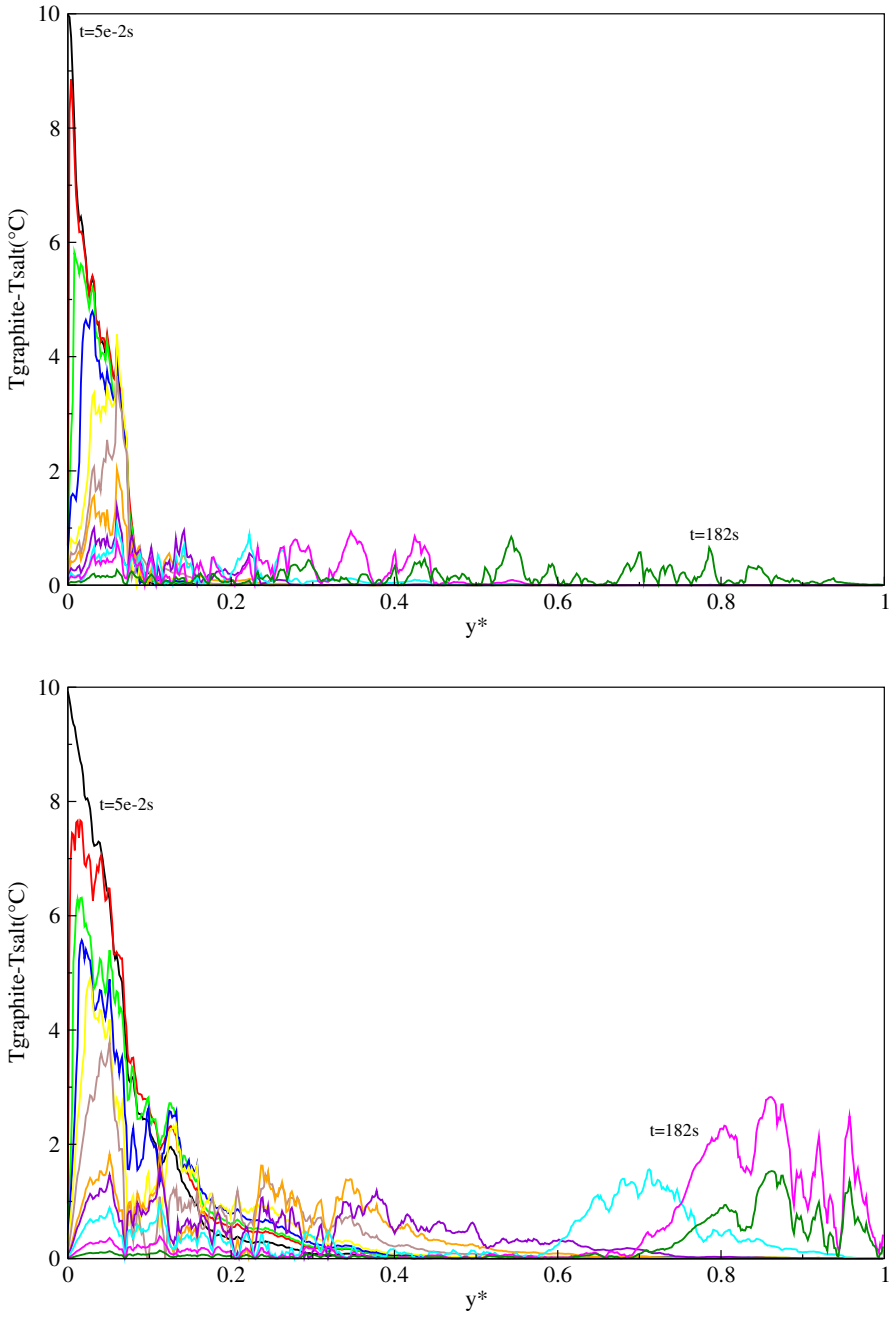

FIGURE 5.5: The difference between the mean temperature in the Graphite and the mean temperature in the Salt for KL1_250 (top) and KD1(bottom).

used. As we can see at $t = 182s$ there are obvious significant differences between the mean temperature in the graphite and the mean temperature in the salt specially for $\boldsymbol{y}$ close to $\boldsymbol{y}_{max}$.

Figure 5.7 shows the plot of the dimensionless mean temperature as a function of the similarity variable for the composite structure based on the KL1_250 on the left and on the right for KD1. As before the mean temperatures are plotted for times ranging

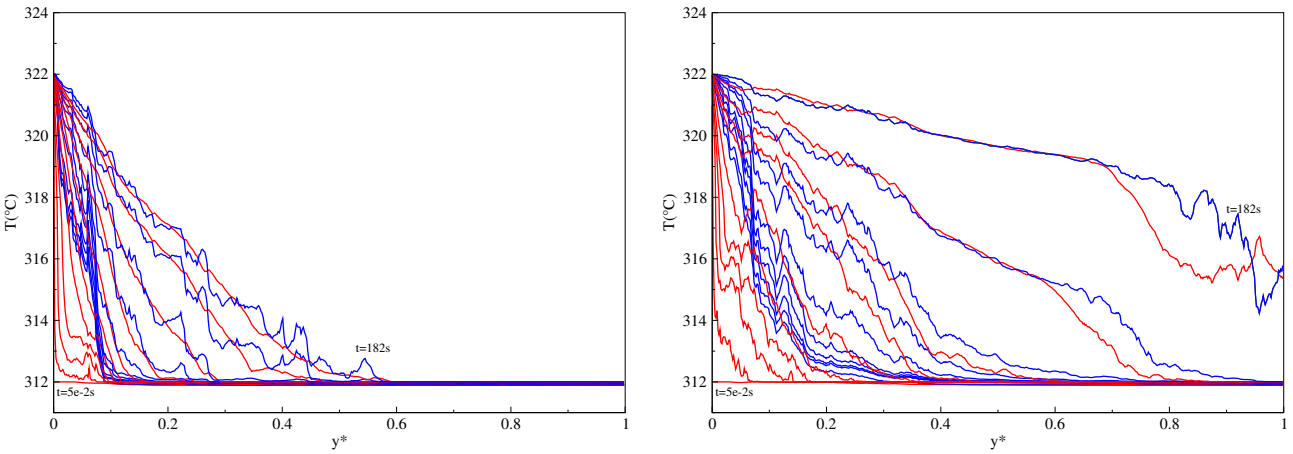

FIGURE 5.6: Mean temperature in the Graphite in blue and the mean temperature in the Salt in red as functions of y^* for KL1_250 (left) and KD1(right).

from $t = 0.05s$ to $t = 182s$ time at which all the PCM has melted. In addition we plot the dimensionless temperature calculated analytically in red for comparison. We can see that, for the KL1_250, with time the mean temperatures tends to a stable value close to the mean temperature given by the analytic solution for the homogeneous material. This is not the case for the KD1 where the mean temperature does not seem to tend to a stable value.

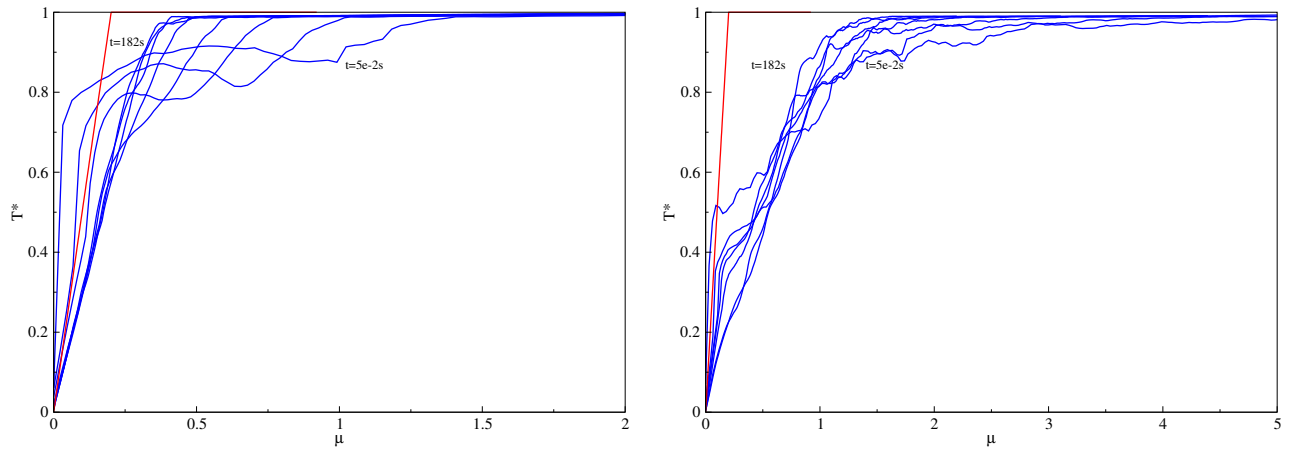

FIGURE 5.7: Mean dimensionless temperature as a function of the similarity variable for KL1_250 (left) and KD1(right).

The same observation is made when we look at Figure 5.8 where the mean dimensionless temperature is plotted for KL1_250 (left) and KD1 (right) as a function of the error function of the similarity variable for times that ranges from $0.05s$ to $182s$ as in the previous cases. In red is the mean dimensionless temperature for the homogeneous case calculated using the analytic expression (5.7).

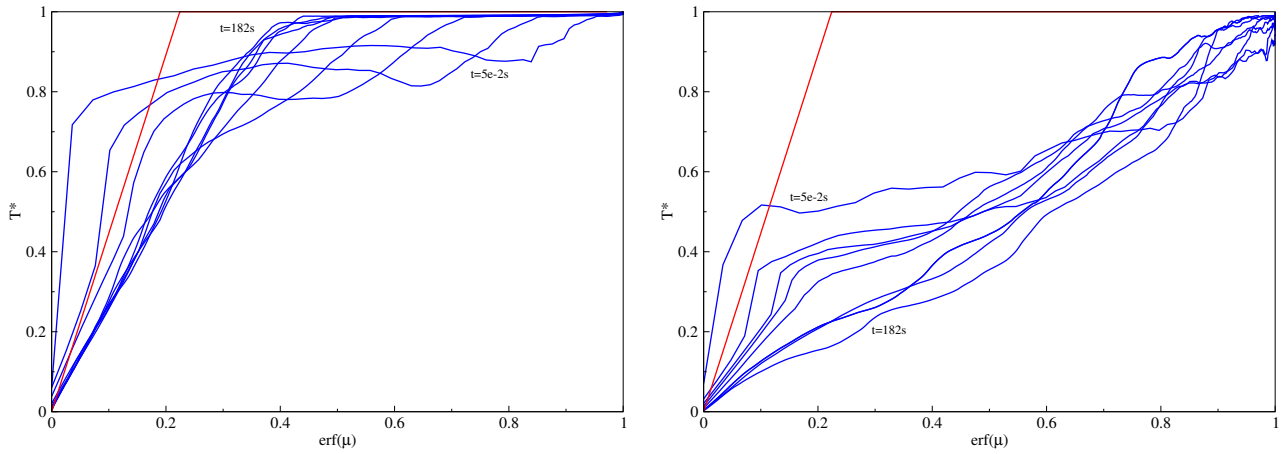

FIGURE 5.8: Mean dimensionless temperature as a function of $erf(\mu)$ for KL1_250 (left) and KD1(right).

At $t = 182s$ we plot the dimensionless mean temperature as a function of μ for KL1_250 and KD1 (left) and the dimensionless temperature as a function of the error function of the similarity variable (right) Figure 5.9 . The dimensionless mean analytic temperature is plotted in red. We can see that for both graphs the mean temperature for the KL1_250 composite gives results close to the analytic results with the homogeneous material. Whereas, in the case of the KD1, a large gap between the mean dimensionless temperature and the analytic temperature is observed on both graphs.

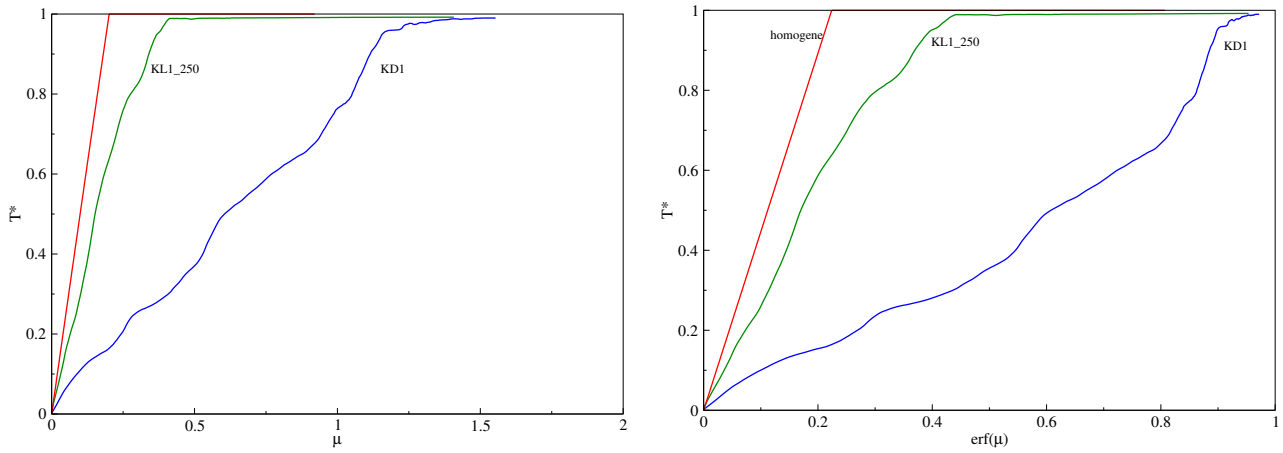

FIGURE 5.9: Mean dimensionless temperature at $t = 182s$ as a function of μ(left) and $erf(\mu)$(right) for KL1_250 in green, KD1 in blue and a homogeneous PCM in red.

Another comparison is made in Figure 5.10 where in the left graph we plotted the heat flux at the surface $\boldsymbol{y} = 0$, for both KL1_250 and KD1, as a function of the inverse of the square root of time as well as the analytic value of this flux for the homogeneous material. We can see that the heat flux for KL1_250 is closer to the analytic one. A similar

observation is made for the right graph where we plot the position of the melting front for KL1_250, for KD1 and for the homogeneous case given by the analytic expression all as functions of the square root of time. In this case also the position of the front for KL1_250 is closer to the position of the front for the homogeneous material.

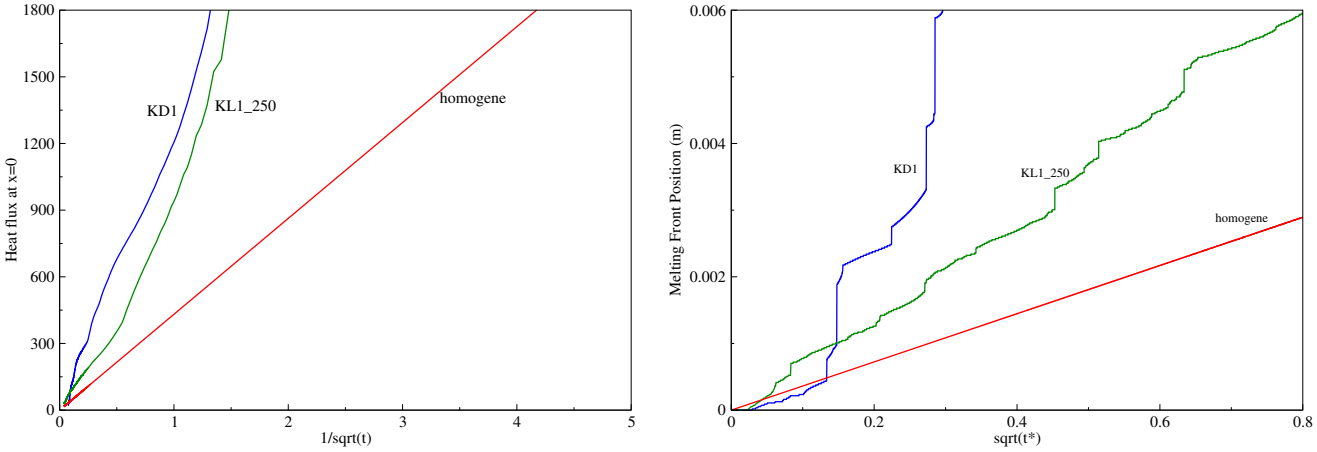

FIGURE 5.10: Heat flux at $\boldsymbol{y} = 0$ as a function of $\frac{1}{\sqrt{t}}$ and the melting front position as a function of $\sqrt{t^*}$ for KL1_250(red), KD1(green) and a homogeneous PCM(red).

Based on the numerical results presented in this section, we can say that from $time \geq 182s$ the composite material based on the KL1_250 structure could be assimilated to a homogeneous PCM with equivalent physical properties. This is not the case for the composite material based on the KD1 structure where all results show that there is a big gap between the temperature, the heat flux and the melting front of this material compared to the temperature, heat flux an melting temperature of a homogeneous PCM with equivalent physical properties. This could be explained by the fact that in the first case where the composite is based on the KL1_250, the pores all have similar size and shapes and have a uniform distribution. In the second case where the composite is based on the KD1, the pores have different shapes and sizes and do not present a uniform distribution. Hence the sample used in this simulation is not representative of the composite where a uniform distribution of the pores is visible.

5.3 Composite with contact resistance

The previously showed results are obtained by solving the phase change model in the composite material without contact resistance. However in more realistic cases the contact

resistance between the components of the composite is not zero. As explained in chapter 1 this one is due to the changes in the thermo-physical properties from one material to another as well as a result of heat flowing across the interface separating the different components of the composite material. In this section we consider the more complete model of heat conduction in a composite with phase change and with contact resistance presented in Chapter 1. The goal is mainly to see if considering a more complete model has an impact on the thermal behaviour of the composite over time.

5.3.1 Problem and samples

We recall the problem of heat conduction in a composite media with contact resistance

$$\Omega_G = \Omega \setminus \overline{\Omega}_S, \qquad \gamma = \partial\Omega_S. \tag{5.8}$$

The indices S and G call to mind salt and graphite. We consider also that the boundary $\partial\Omega$ is the disjoint union of two parts, Γ_D and Γ_N. In this geometry, the differential system we intend to deal with is the unsteady heat conduction problem with phase change. The unknown is the temperature T of the medium that satisfies therefore

$$\begin{cases} \partial_t H(T) - \operatorname{div}(\kappa \nabla T) = 0 & in\ \Omega_S \cup \Omega_G, \\ [\kappa \partial_n T] = 0 & on\ \gamma, \\ R(\kappa \partial_n (T|_{\Omega_S})) = [T] & on\ \gamma, \\ T = T_D & on\ \Gamma_D. \\ \kappa \partial_n T = 0 & on\ \Gamma_N. \end{cases} \tag{5.9}$$

Where $\boldsymbol{n}$ is the unit normal vector to $\partial\Omega$ exterior to Ω and also to γ exterior to Ω_S, $[\cdot]$ is the jump through γ, equal to the value on Ω_G minus the value on Ω_S. The temperature T, the conductivity κ, the density ρ and the specific heat capacity c are discontinuous through γ. The parameter R represents the thermal resistance at the interface γ introduced in section 1.2.3 and T_D is the external temperature.
The initial and boundary conditions are taken the same as in the previous sections. As previously, the problem is solved using first the Euler backward method for time discretization, a Chernoff scheme for the non-linearity in the Stefan problem for the PCM and finally a Raviart-Thomas finite element method is used to solve the linear problem. For the simulations presented in this section we used smaller samples than the ones used in

the previous sections. The advantage is to reduce the simulation time. This will also allow to see, in the case of the KL1_250, if taken a smaller sample effects the homogenization time obtained in section 5.2. The dimensions of the new samples are given in Figure 5.11.

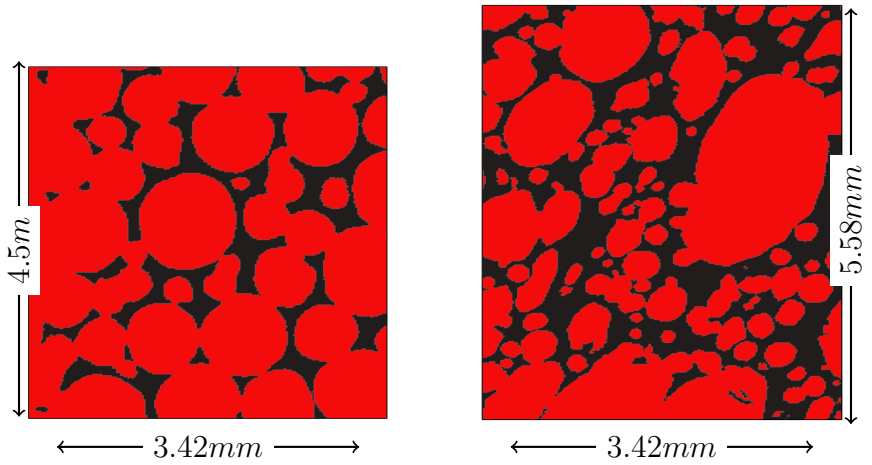

FIGURE 5.11: The samples used in this section, KL1_250 left and $KD1$ right.

5.3.2 Results and discussions

A first consequence of introducing a contact resistance condition at the interface between the PCM and the foam given in Equation 5.9 is to slow down the melting of the PCM since it introduces a discontinuity of the temperature at the interface. Looking at Table 5.2 where the melting time is given for several values of R, we can see that, as expected, the melting time increases with R. We can also see that for most values of R the time is much shorter in the case of the second sample $KD1$ because of the higher volume fraction of carbon present in this sample. This is not the case for $R = 0.1$ where the discontinuity at the interface is more significant than the high conductivity nature of the foam.

	$R = 0$	$R = 10^{-3}$	$R = 10^{-2}$	$R = 0.1$
KL1_250	$222s$	$566s$	$1148s$	$1567s$
$KD1$	$30.7s$	$53.2s$	$207s$	$1650s$

TABLE 5.2: Melting time of the PCM in seconds.

Another aspect that we wanted to investigate is how taking into account this contact resistance will affect the temperature's evolution in both materials and in the composite

as a hole. In order to understand this effect we began by showing in Figure 5.12 the difference between the mean temperature in the carbon foam and the mean temperature in the PCM for different values of the thermal contact resistance for the first sample KL1_250. We notice that this difference increases with the values of R. This gap is the largest for the higher values of y which corresponds to the top of the sample in Figure 5.11. The reason is the significant alignment of pores at this location. This results is more noticeable in the case of the second sample as can be seen in Figure 5.13. This is a consequence of the non-regular pore distribution and pore sizes compared to the first sample.

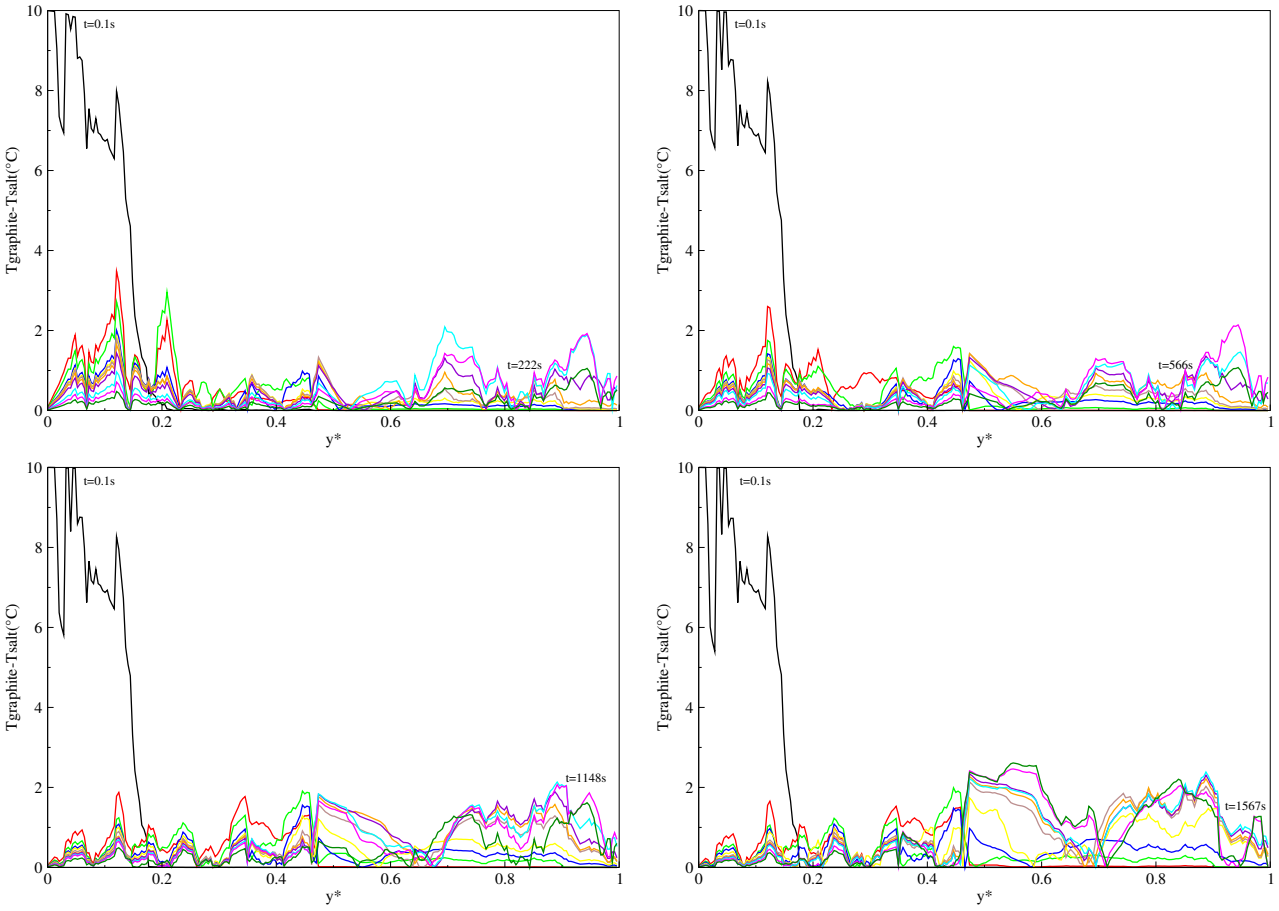

FIGURE 5.12: Difference between the mean temperature in the carbon foam and the mean temperature in the PCM as a function of y^* for KL1_250. In top left for $R = 0$, top right $R = 10^{-3}$, bottom left $R = 10^{-2}$ and in the bottom right $R = 0.1$.

In order to see more in depth the reasons for the gaps between the mean temperature in the foam and the mean temperature in the PCM we plot the mean temperature in the carbon foam in blue and the mean temperature in the PCM as functions of the dimensionless position in Figure 5.14–Figure 5.15 for different values of R. For both samples we observe that for $R = 0$ and $R = 10^{-3}$ both the temperature profiles in the foam and

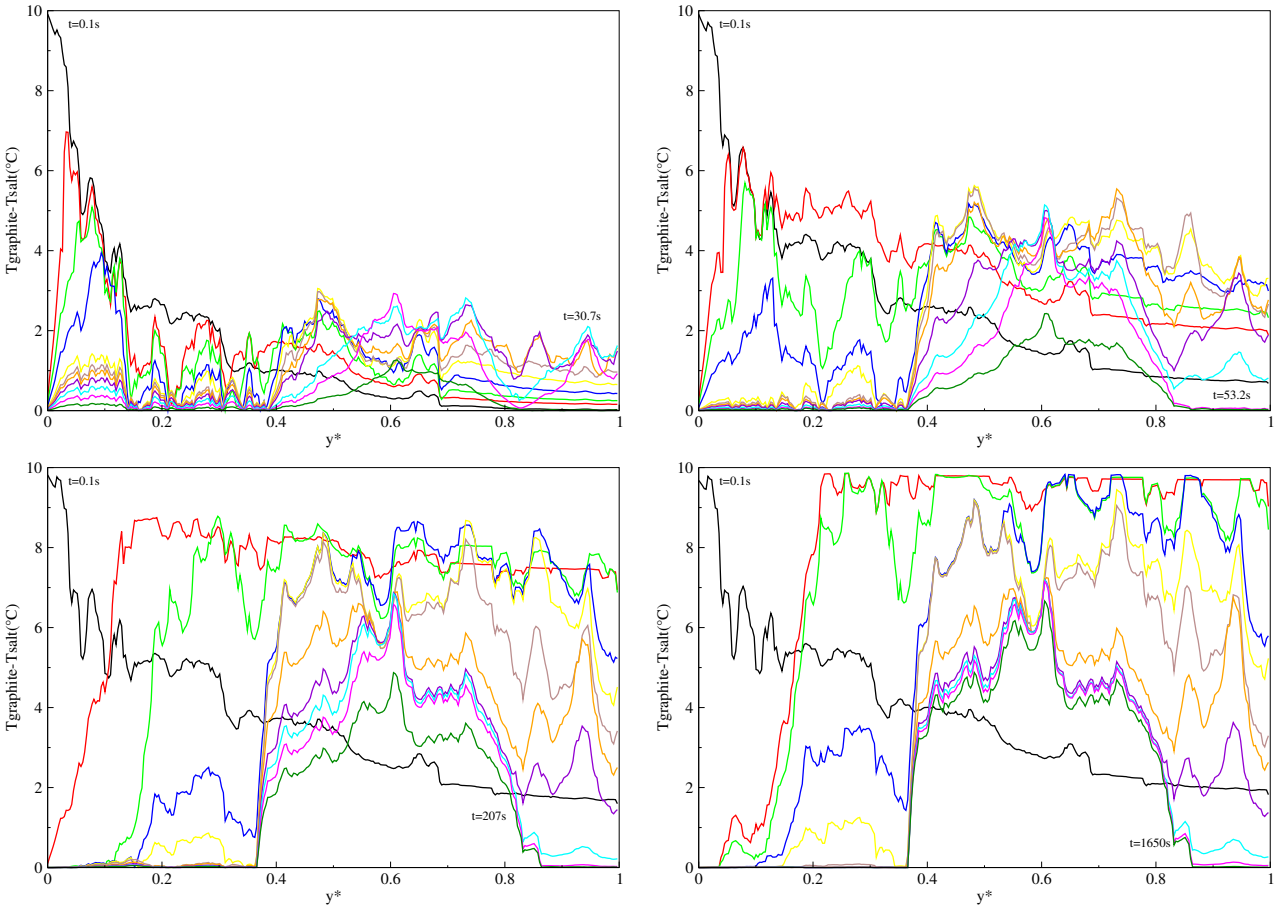

FIGURE 5.13: Difference between the mean temperature in the carbon foam and the mean temperature in the PCM as a function of y^* for $KD1$. In top left for $R = 0$, top right $R = 10^{-3}$, bottom left $R = 10^{-2}$ and in the bottom right $R = 0.1$.

in the PCM tends to have a similar value as the y increases. However for $R = 10^{-2}$ and $R = 10^{-3}$ a big difference could be seen between both temperature profiles specially for the higher values of y in the case of the second sample. These observations explain the previous ones. Consequently we can say that based on these first results adding a thermal contact resistance to the model introduces a discontinuity to the temperature field that results in having large differences between the temperature profiles in the PCM and in the foam.

Lastly we wanted to investigate the effect of adding a contact resistance on the ability of the composite to be assimilated to a homogeneous material with equivalent thermo-physical properties. These equivalent properties are determined using the thermo-physical properties of the composite as explained in section 5.2.1. For the first sample we plot in Figure 5.16, for different values of R ,the mean dimensionless temperature in the composite at different times of the simulation in blue and the analytic temperature obtained

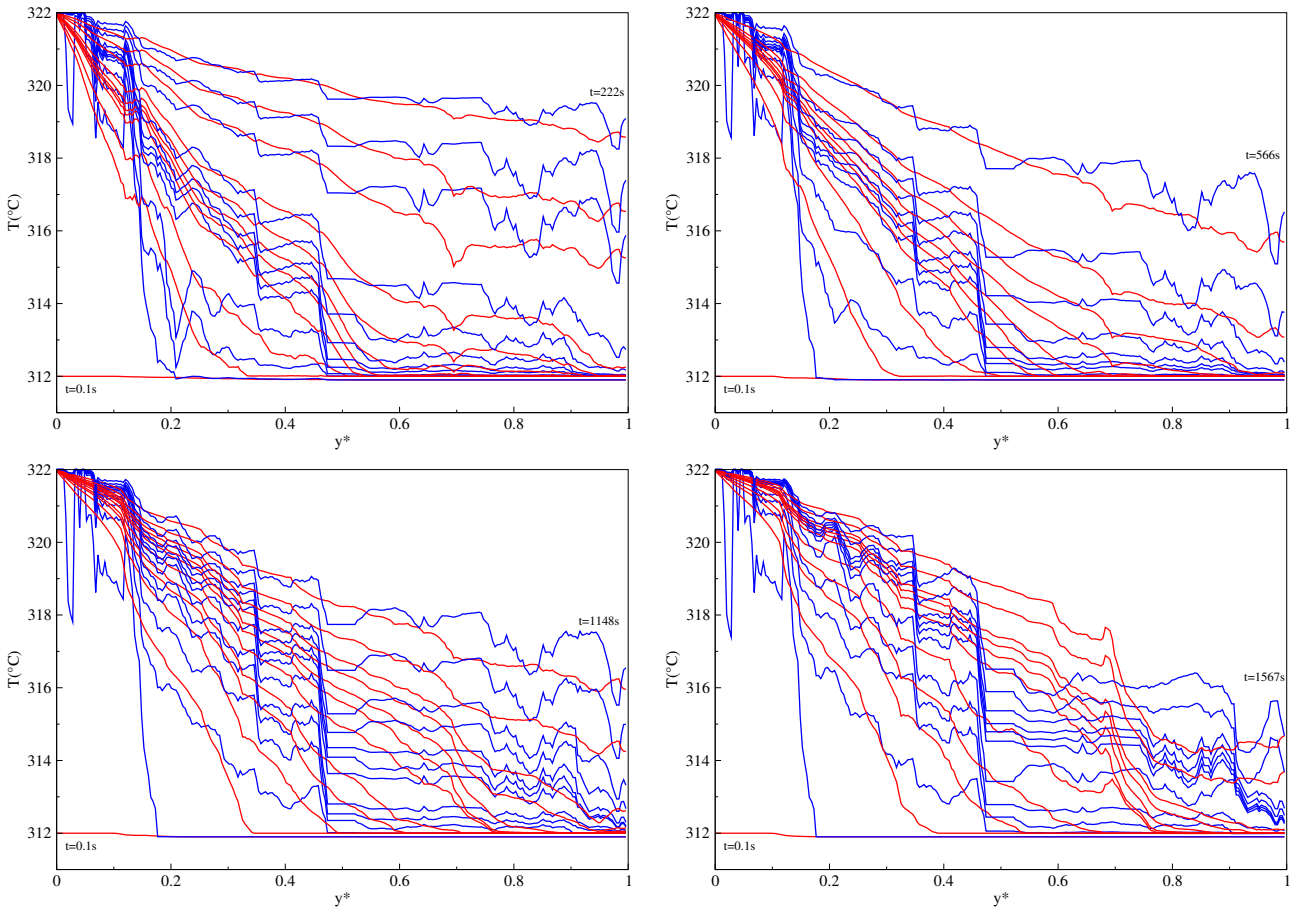

FIGURE 5.14: The mean temperature in the carbon foam in blue and the mean temperature in the PCM in red as functions of y^* for KL1_250. In top left for $R = 0$, top right $R = 10^{-3}$, bottom left $R = 10^{-2}$ and in the bottom right $R = 0.1$.

by solving the Stefan problem in case of a pure PCM in red. We notice that for $R = 0$ the temperature profiles tend to have the same bent as time goes. This is less the case for higher values of R since we can see that for $R = 0.1$ for example the mean temperature are closer with time but tend to have very different tendency. This means that as R increases the time from which we can compare the composite to a homogeneous PCM increases. This also shows that this time is necessarily higher than the time after which all the PCM in the composite has melted which is not the case for the composite with $R = 0$. This observations are more obvious in the case of the second sample as can be seen in Figure 5.16 where a similar plot shows that the gaps between the tendencies of the mean temperature are more and more noticeable as R increases.

In conclusion these results show that increasing the value of the thermal contact resistance leads to a thermal behaviour dissimilar to the expected thermal behaviour of a homogeneous PCM.

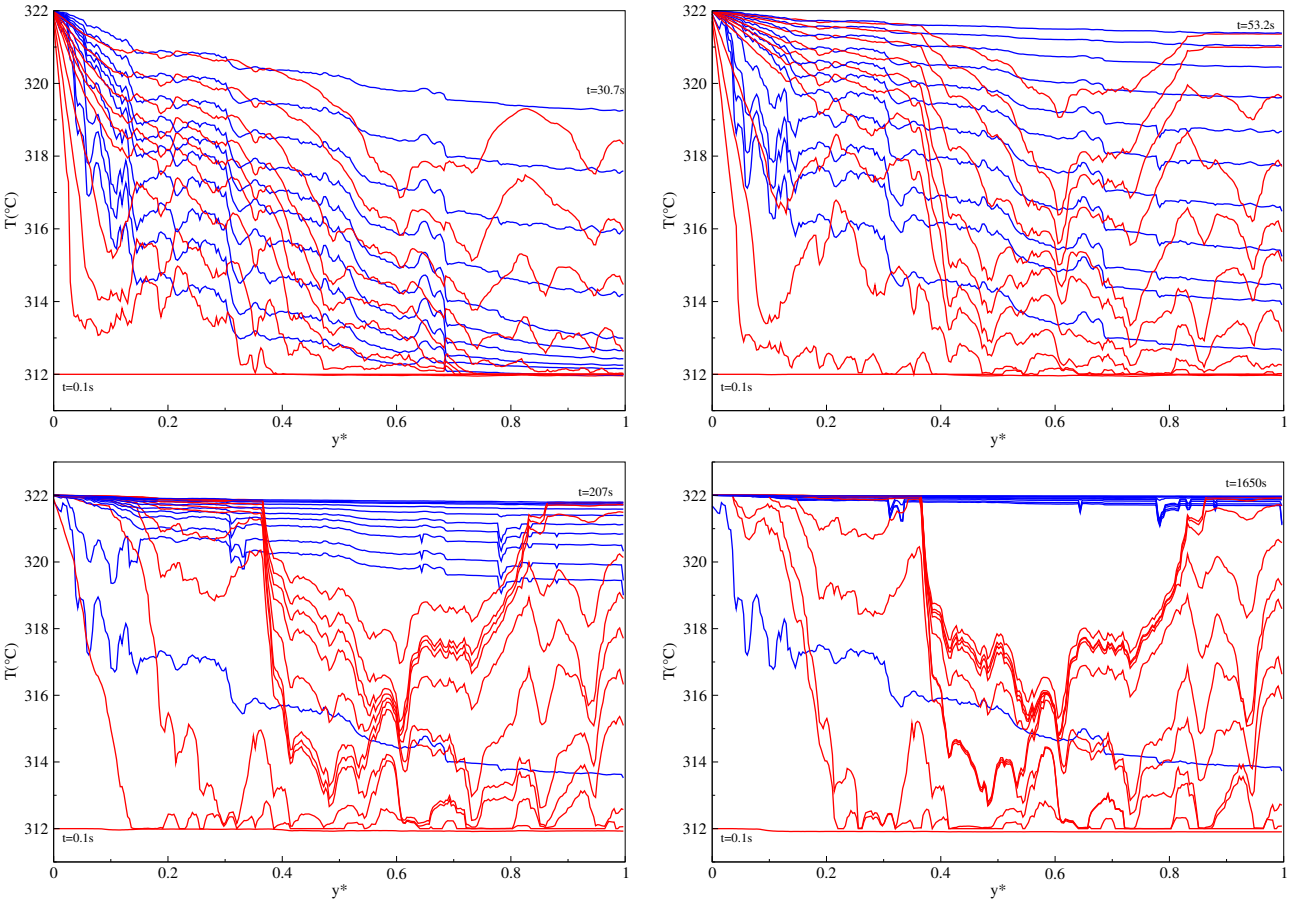

FIGURE 5.15: The mean temperature in the carbon foam in blue and the mean temperature in the PCM in red as functions of y^* for KD1. In top left for $R = 0$, top right $R = 10^{-3}$, bottom left $R = 10^{-2}$ and in the bottom right $R = 0.1$.

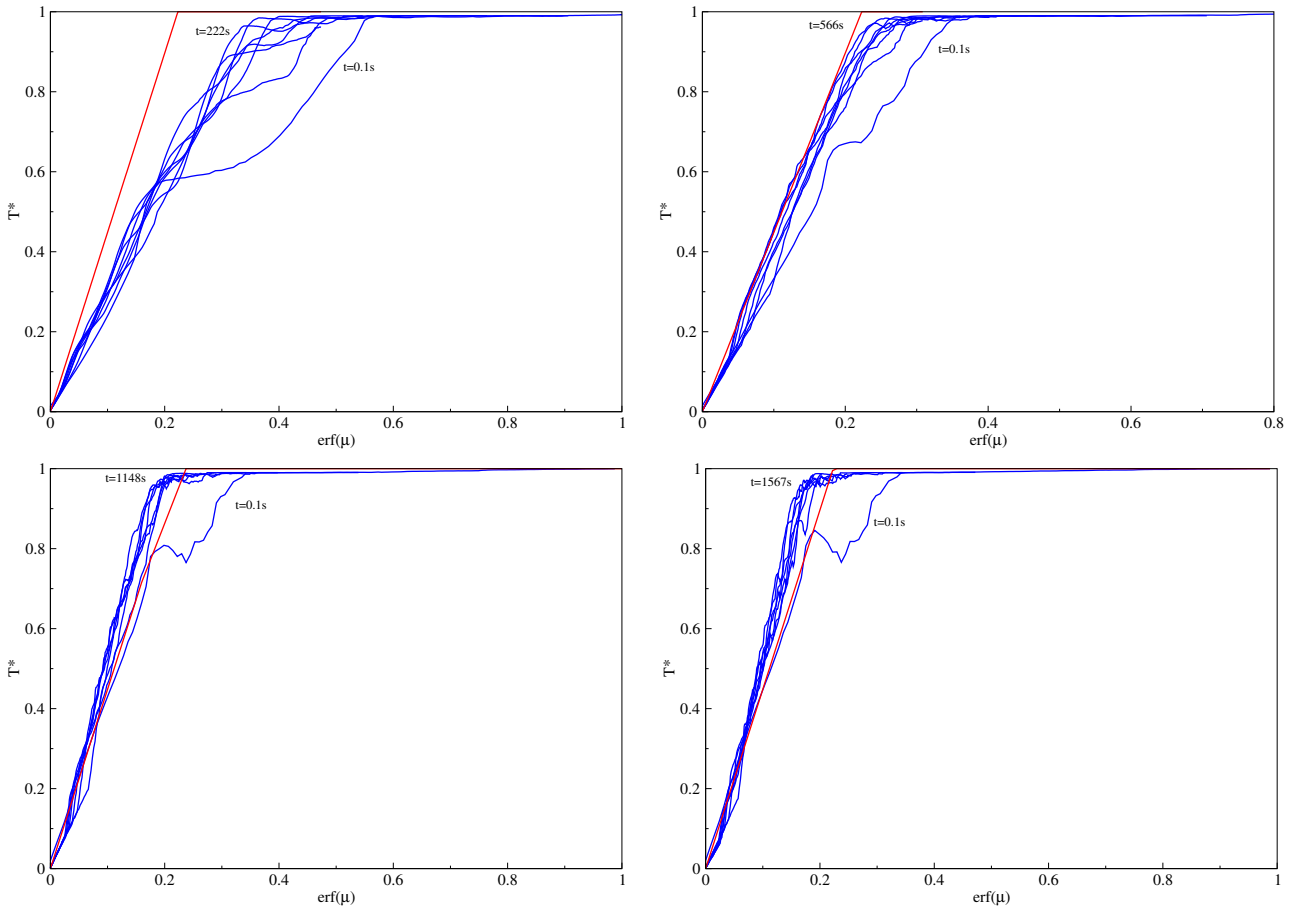

FIGURE 5.16: Mean dimensionless temperature in the composite as a function of $erf(\mu)$ for KL1_250 in blue and for a homogeneous material in red. In top left for $R = 0$, top right $R = 10^{-3}$, bottom left $R = 10^{-2}$ and in the bottom right $R = 0.1$.

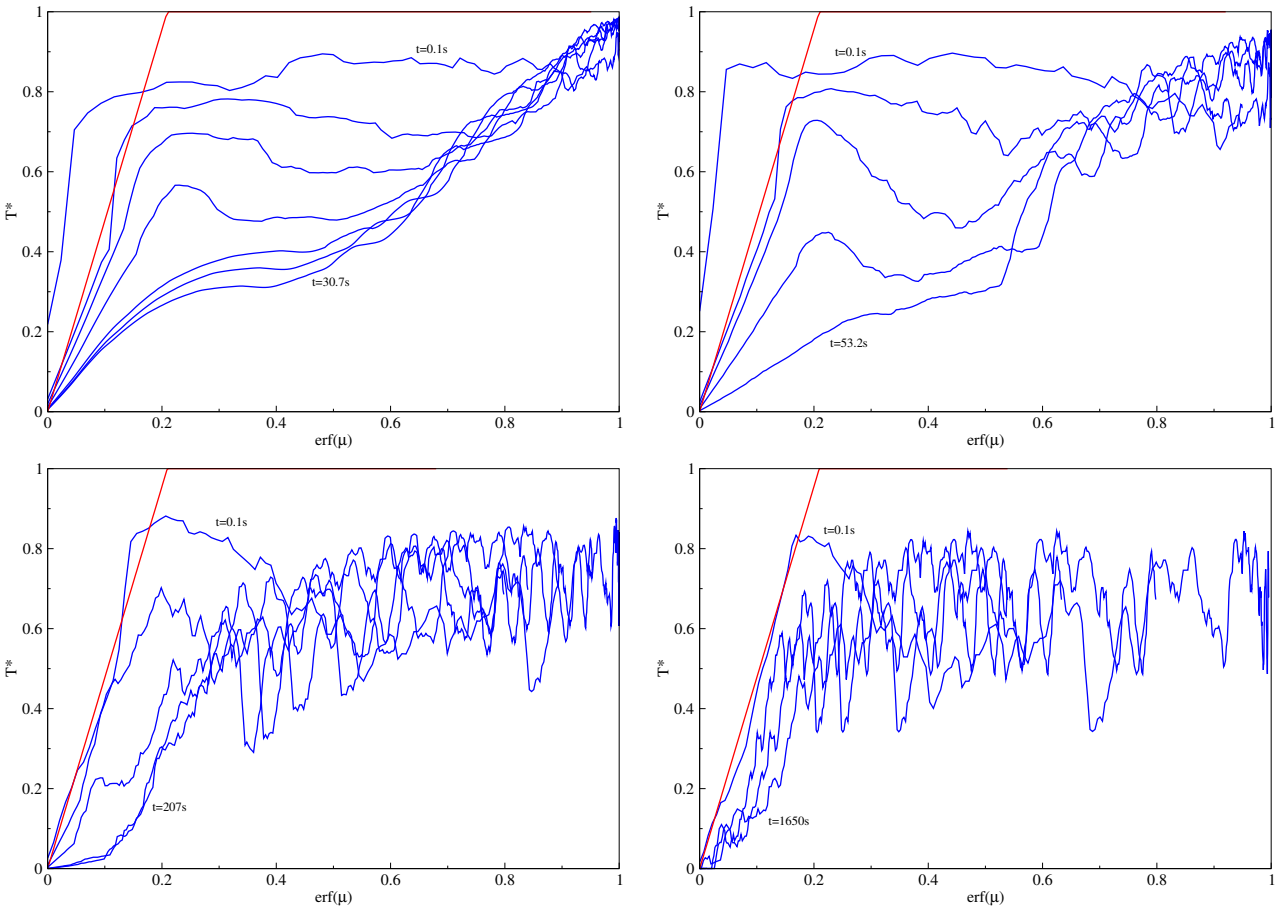

FIGURE 5.17: Mean dimensionless temperature in the composite as a function of $erf(\mu)$ for KD1 in blue and for a homogeneous material in red. In top left for $R = 0$, top right $R = 10^{-3}$, bottom left $R = 10^{-2}$ and in the bottom right $R = 0.1$.

5.4 Investigating the impact of changing the thermal conductivity on the thermal behaviours of the composites.

In this section we aim to understand the effect of the thermal conductivity on the thermo-physical properties such as the temperature distribution, the heat flux and the melting front position. In order to do this we conducted several simulations with both of the composite structures KL1_250 and KD1 with various effective thermal conductivities. We used Figure 5.1 in order to determine the value for the thermal conductivity of the foam corresponding to the desired value for the effective thermal conductivity as done in the previous section. The results shown here correspond to composites with values of the thermal conductivity presented in Table 5.3. We conducted simulations for every composite material KL1_250 and KD1 and for different values of the effective thermal conductivity given in Table 5.3.

$\kappa_{effective}$ $(W/m/K)$	κ_{Foam} KL1_250	κ_{Foam}KD1
10	410	125
20	958	336
30	1510	580
40	2060	848
50	2615	1128

TABLE 5.3: Values of the thermal conductivity.

The initial and boundary conditions are taken the same as in section 5.2 where the domain is initially at the melting temperature of the PCM i.e $312°C$ and at the start of the simulation the temperature of the bottom wall is suddenly brought to $320°C$ while at the left, right and top wall we have Neumann boundary conditions on the temperature $\partial_n T = 0$. As explained in section 5.2 the purpose of taking such boundary conditions is first to have an evolution of the temperature only in the $\boldsymbol{y}$-direction and the second purpose is that with a homogeneous material filling the 2D domain and with these initial and boundary conditions the heat conduction problem with phase change has a known analytic solution. This will allow to compare the results with the composite materials with the results in the case of a homogeneous material.

5.4.1 Results and discussion

We conduct four simulations for each of the composite materials KL1_250 and KD1. Every simulation corresponds to a value of the effective thermal conductivity. In each case we solve the non-linear heat conduction problem with a phase change problem in the PCM domain using the Raviart Finite element method for the linear part and a Chernoff scheme for the non-linear part. The simulations are stopped ones the stationary state has been reached which is supposed to happen when all PCM has melted.

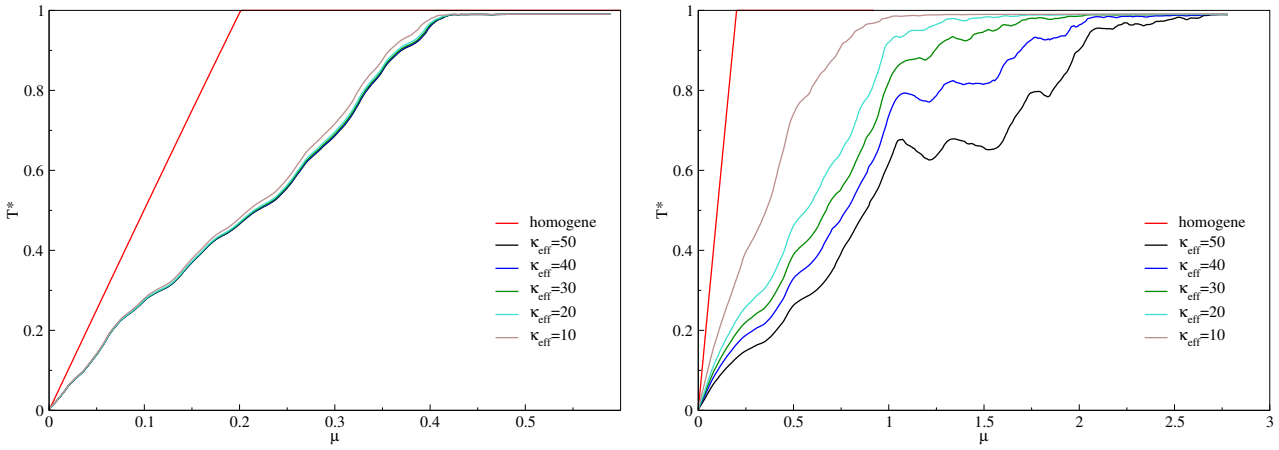

FIGURE 5.18: The mean dimensionless temperature as a function of the similarity variable for different values of the effective thermal conductivity for KL1_250 (left) and KD1(right).

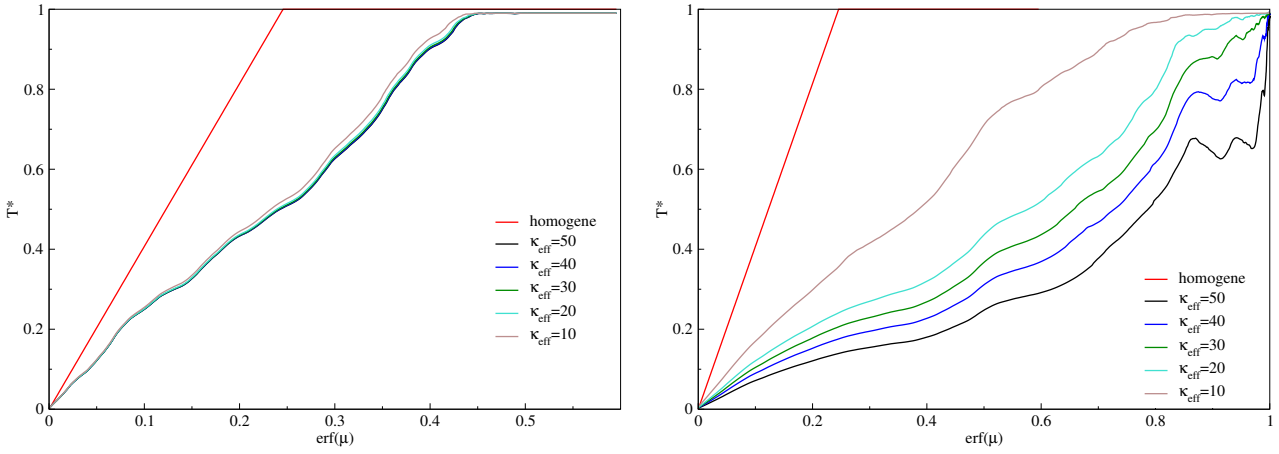

FIGURE 5.19: The mean dimensionless temperature as a function of $erf(\mu)$ for KL1_250 (left) and KD1(right).

In Figure 5.18 we plot the mean dimensionless temperature T^* as a function of the similarity variable for every value of the effective thermal conductivity given in Table 5.3 for

KL1_250 and for KD1. And in Figure 5.19 we plot T^* as a function of the error function of the similarity variable for KL1_250 and for KD1. As we can see in the case of KL1_250 the temperature remains almost the same for the different values of the effective thermal conductivity. Whereas in the case of KD1 we observe gaps between the profiles of the temperature that increase as the effective thermal conductivity increases.

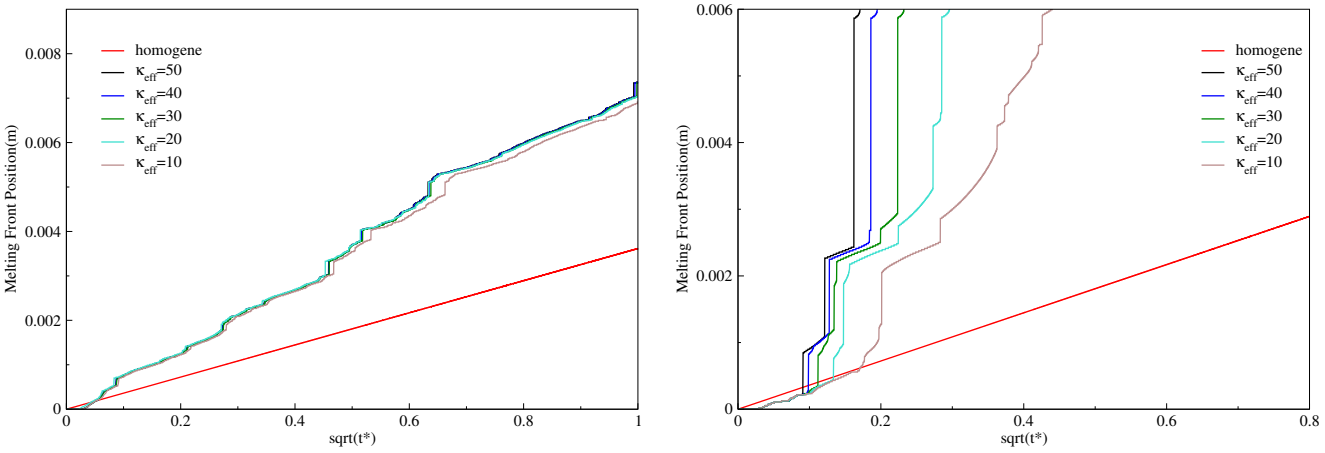

FIGURE 5.20: Evolution of the melting front position as a function of $\sqrt{t^*}$ for different values of the effective thermal conductivity for KL1_250 (left) and KD1(right).

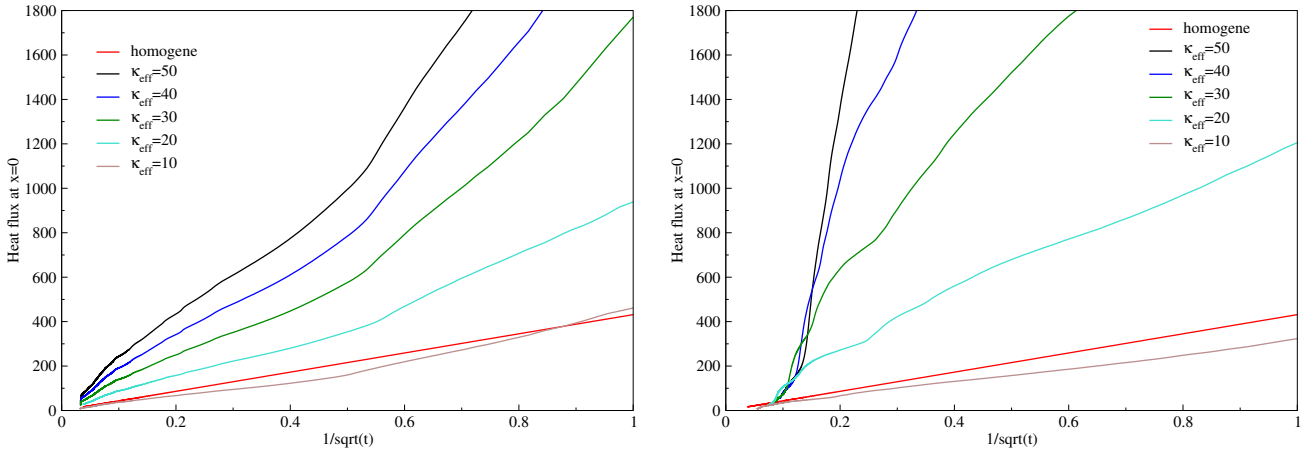

FIGURE 5.21: Evolution of the thermal heat flux at the surface $\boldsymbol{y} = 0$ as a function of $\frac{1}{\sqrt{t}}$ for different values of the effective thermal conductivity for KL1_250 (left) and KD1(right).

In Figure 5.20 we plot the evolution of the position of the melting front as a function of the square root of the dimensionless time for every value of the effective thermal conductivity given in Table 5.3. In the right graph is the plot for KL1_250 and in the right is the plot for the KD1. In this case also we can see that for the results in the case of KL1_250 there is not a big difference between melting fronts for different values of the effective thermal

conductivity. We observe however that for the melting fronts calculated for the KD1 case and for different values of the effective thermal conductivity gaps between the fronts are observed and show that the front is moving faster for higher values of the effective thermal conductivity. This is a logical behaviour since the PCM is supposed to melt faster when the foam has higher thermal conductivity because it allows to pass the heat faster to the PCM.

In Figure 5.21 we plot the evolution of the heat flux at the surface $\boldsymbol{y} = 0$ as a function of the inverse of the square root of time for every value of the effective thermal conductivity in Table 5.3, for KL1_250 in the left graph and for KD1 in the right graph. We can see that in the case of KL1_250 the values of the heat flux increases with the values of the effective thermal conductivity. In the case of KD1, the same behaviour is observed however we can see that in this case the differences in the heat flux values are more noticeable.

5.4.2 Conclusion

Based on the results presented above, increasing the effective thermal conductivity allow to increase the heat flux calculated at $\boldsymbol{y} = 0$ and there for accelerates the melting process. This is more noticeable in the case of the composite structure KL1_250 than in the case of the composite KD1 and there are few reasons to this. First is in the way the pores are distributed in the composites. In KL1_250 the pores are distributed in a uniform way covering most of the sample. Where in KD1 the distribution of the pores is less regular and there are more gaps in between pores. The second reason is the volume of the pores in both cases, for KL1_250 the volume of the pores represents 82% of the total volume of the sample where in KD1 their volume represents only 70% of the total volume of the sample. This means there is more carbon foam in the KD1 sample than in the KL1_250 sample which makes it logical that changing the values of the thermal conductivity of the carbon foam has more effect on the temperature distribution and other physical properties in the KD1 case.

5.5 Dilatation in both directions: study of the influence of the pores size

An interesting question that we try to answer in this section is whether changing the size of the pores of the carbon foam without changing their shape has an effect on either of the physical properties of the material such as the temperature distribution over time, position of the melting front, evolution of the heat flux over time etc. One way to investigate this numerically is to generate various composites based on the initial composite where the pores size increases in each one. This however must be done without changing the value of the porosity or else we are no longer working with the same composite material and the comparison no longer make sense. This is done by performing some numerical transformations using the color function that defines the initial composite structure shown in Figure 5.2. This consisted in doing dilatations in both directions with equal coefficients while keeping the same values of the porosity as the initial structure. To explain this, suppose $f(x, y)$ being the color function corresponding to one of the initial composite structures KL1_250 or KD1. The new color function for the new composite structure, corresponding to a dilatation of equal coefficient in the both directions, is defined by

$$f_{new}(x, y) = f(\alpha x, \alpha y)$$

where α is the dilatation coefficient. Different structures for different values of α are shown in Figure 5.22–Figure 5.26, as we can see the size of the pores increases as the value of dilatation coefficient α decreases. For each value of α, the thermal conductivity is given a value such that the effective thermal conductivity of the new composite structure is equal to 20 $W/m/K$ in order to compare the new composites with one another and the initial one. We performed numerical simulations, using the new composite structures, with initial and boundary conditions the same as used in the previous sections in order to have an evolution of the temperature in the $\boldsymbol{y}$-direction and also to have an analytic solution for the same heat conduction problem with the same boundary condition and where the 2D domain is filled with a homogeneous PCM. As in the previous section we used a Raviart-Thomas finite element method to solve the linear part of the model and a Chernoff scheme to solve the non-linear part. The simulations are stopped when all the PCM has melted and the temperature has reached a steady state.

FIGURE 5.22: KL1_250 initial domain(left) and KD1 initial domain (right).

FIGURE 5.23: KL1_250 (left) and KD1 (right) with dilatation coefficient $\alpha = 0.9$.

FIGURE 5.24: KL1_250 (left) and KD1 (right) with dilatation coefficient $\alpha = 0.8$.

FIGURE 5.25: KL1_250 (left) and KD1 (right) with dilatation coefficient $\alpha = 0.7$.

FIGURE 5.26: KL1_250 (left) and KD1 (right) with dilatation coefficient $\alpha = 0.6$.

5.5.1 Results for modified structures based on the KL1_250 composite

For every value of α we plot the mean dimensionless temperature for every value of $\boldsymbol{y}$ as a function of the similarity variable and as the a function of the error function of the similarity variable in Figure 5.27. We can see on both plots that as the value of α decreases which means that the size of the pores is increasing, the mean temperature has higher values which are closer to the value of the mean dimensionless temperature in the case of a homogeneous PCM.

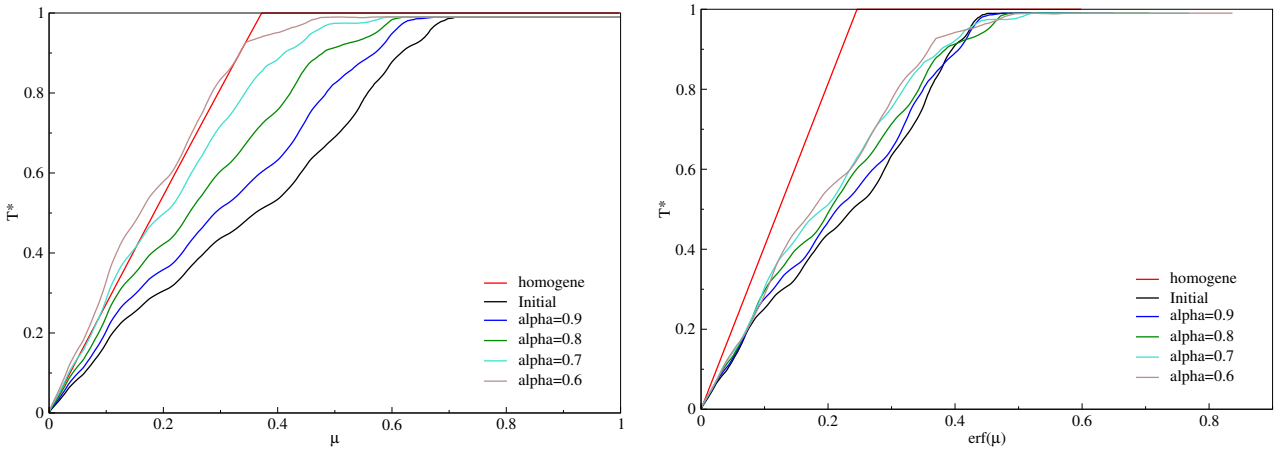

FIGURE 5.27: Mean dimensionless temperature at $t = t_{end}$ as a function of μ (left) and as a function of $erf(\mu)$ (right).

We also plot in Figure 5.28, for every value of α, the evolution of the heat flux $q(0,t)$ at the surface $\boldsymbol{y} = 0$ as a function of the inverse of the square root of time in the left side of the graph and the evolution of the melting front's position as a function of the square root of the dimensionless time in the right side. In each case we also plot the value of the

heat flux and of the front position for the initial case were $\alpha = 1$ and in the analytic case where we have a homogeneous PCM.

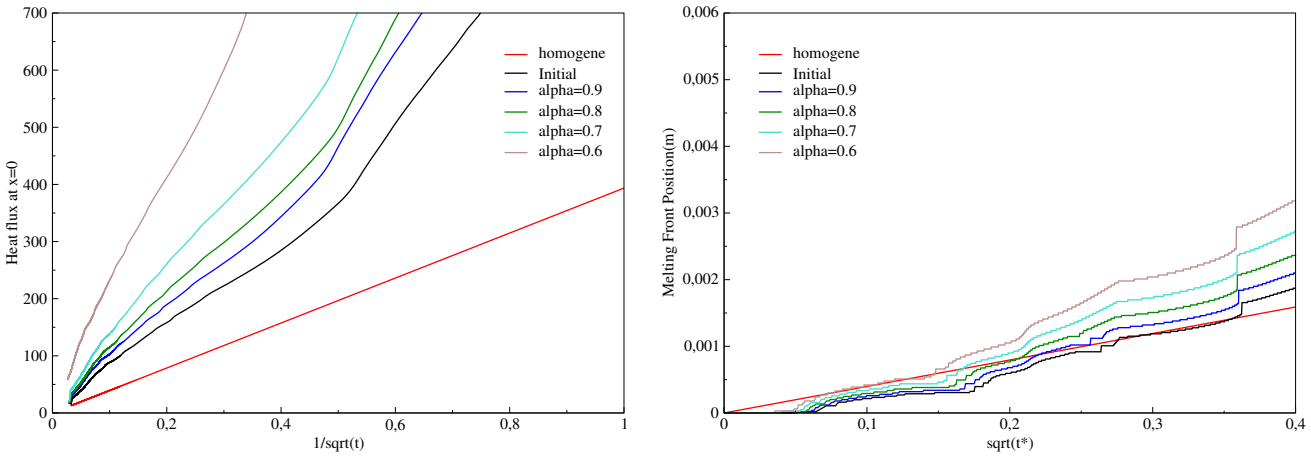

FIGURE 5.28: Evolution of the thermal heat flux at the surface $\boldsymbol{y} = 0$ for every value of α as a function of $\frac{1}{\sqrt{t}}$ (left) and the evolution of the melting front's position for every α as a function of $\sqrt{t*}$.

These graphs show that the heat flux increases as the pores size increases and we also notice that the melting front moves faster as the pores size increases. This means that for composite with pores bigger than the KL1_250 pores but with the same shape and distribution tend to allow for a faster heat conduction resulting in a PCM melting faster and thus accelerating the charging and discharging cycles.

5.5.2 Results for modified structures based on the KD1 composite

For every value of α we conduct simulations explained above with the corresponding new composite that is based on dilatation in both directions of the KD1 sample shown in Figure 5.1. At the end of simulations i.e. when temperature has reached a steady state we plot, for every α, the mean dimensionless temperature for every value of $\boldsymbol{y}$ as a function of the similarity variable and as the a function of the error function of the similarity variable in Figure 5.29. We can see in this case as well that as the value of α decreases, which means that the size of the pores is increasing, the mean dimensionless temperature has higher values which are closer to the value of the mean dimensionless temperature in the case of a homogeneous PCM. However, this is less noticeable than in the case of KL1_250 as shown in Figure 5.27.

We also plot in Figure 5.30, for every value of α, the evolution of the thermal heat flux $q(0,t)$ at the surface $\boldsymbol{y} = 0$ as a function of the inverse of the squre root of time in the left side of th graph and the evolution of the melting front's position as a function of the square root of the dimensionless time in the right side of the graph. In each case we also plot the value of the heat flux and of the front position for the initial case were $\alpha = 1$ and also for the analytic case where we have a homogeneous PCM. These graphs show that the heat flux increases with the size of the pores and the melting front moves faster as the pores size increases. This is the same observation as in the composite based on KL1_250. This shows once more that by enlarging the pores while keeping the same shape and distribution we allow for the composite material to conduct the heat faster and as a consequence to have faster charging and discharging cycles.

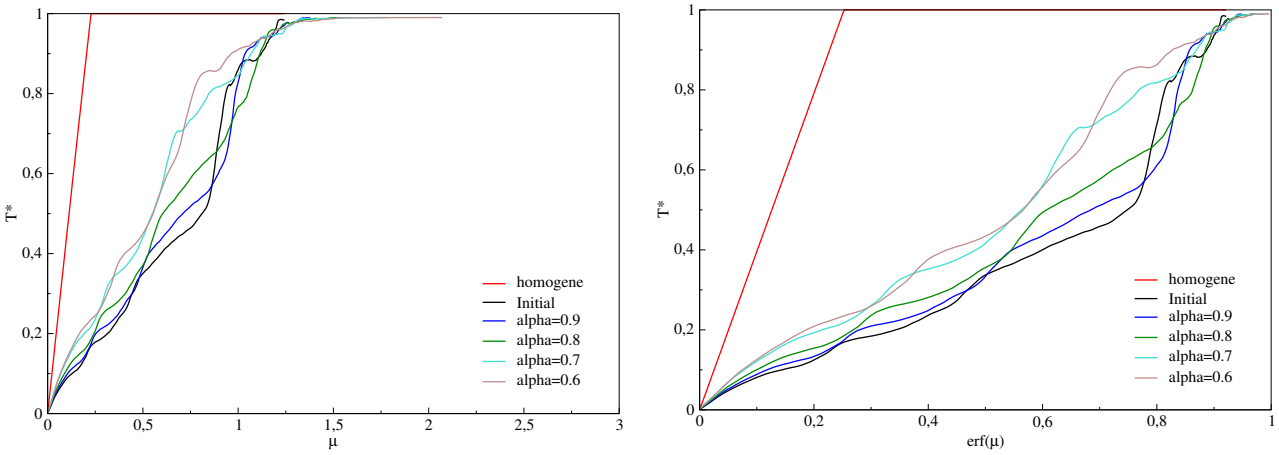

FIGURE 5.29: Mean dimensionless temperature at $t = t_{end}$ as a function of the similarity variable (left) and as a function of $erf(\mu)$ (right).

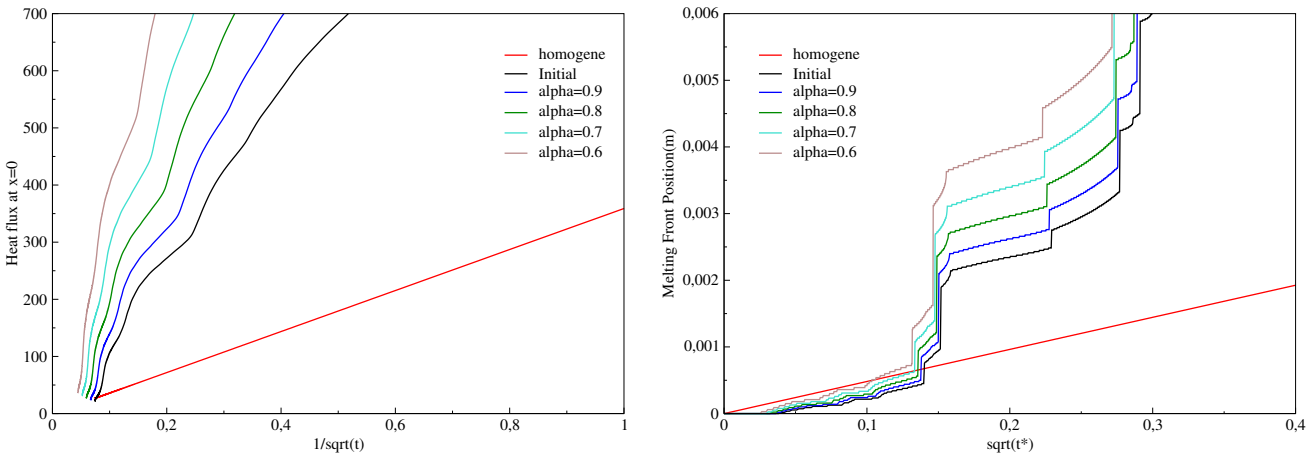

FIGURE 5.30: Evolution of the thermal heat flux at the surface $\boldsymbol{y} = 0$ for every value of α as a function of $\frac{1}{\sqrt{t}}$ (left) and the evolution of the melting front's position for every α as a function of $\sqrt{t*}$.

5.6 Dilatation in one direction: study of the influence of the pores shape

In order to optimize the micro-structure of the composite material we need to investigate what happens when the shape of the pores is modified in a certain way. This could provide some informations on how to change the micro-structure in order to optimize one particular parameter such as the thermal conductivity of the foam or in order to have a more homogenisable structure i.e a structure that could be assimilated to a homogeneous medium. In order to investigate this numerically we followed the same process as the one described in the previous section and we constructed various composites based on the initial composites KL1_250 and KD1 where in each one we change the pores shape by performing numerical dilatation on the initial composite structure while keeping a constant porosity. As previously explained we used the color function $f(x, y)$ associated to the initial composite structures shown in Figure 5.2 and constructed new color functions $f_{new}(x, y)$ corresponding to new composite structures by performing dilatations one-direction at a time with coefficients α in the $\boldsymbol{x}$-direction and β in the $\boldsymbol{y}$-direction such that

$$f_{new} = f(\alpha x, \beta y)$$

α and β are taken in $\{0.9, 0.8, 0.7, 0.6\}$. Following this procedure we have generated eight composite structures shown in Figure 5.31 to Figure 5.34.

For each new composite structure we perform simulations using the steady heat conduction model described by Equation 5.2 in order to explicitly determine the linear relation

relying the thermal conductivity of the carbon foam to the effective thermal conductivity of the composite as explained in section 5.2. Once this is done we determine a value for the thermal conductivity of the carbon foam such that the effective thermal conductivity of each of the new composite structures is equal to $20W/m/K$ in order to have comparable composites. In Figure 5.35 we plot for KL1_250 (left) and KD1(right), the values of the effective thermal conductivity of the carbon foam as a function of the dilatations coefficients. For KL1_250 we can see that by stretching the composite in the $\boldsymbol{y}$–direction we need to keep increasing the values of the thermal conductivity of the carbon foam in order to keep $\kappa_{eff} = 20W/m/K$. However, polling the composite in the $\boldsymbol{x}$–direction we need to keep decreasing its values. We can observe the opposite behaviour for the KD1 composite. This is due to the fact that in the first case the composite has more carbon in the $\boldsymbol{x}$–direction and by maximizing this surface we allow to minimize the value of the effective thermal conductivity of the composite. The opposite is true for KD1 where most of the carbon foam is in the $\boldsymbol{y}$–direction which is why maximizing this surface allow to minimize the value of the thermal conductivity of the foam to reach the value wished for.

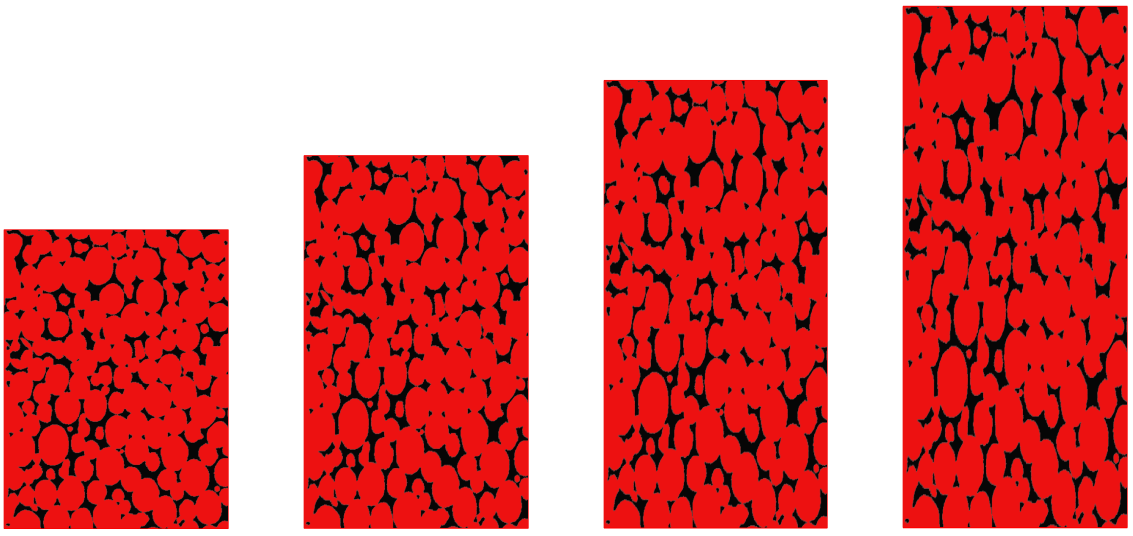

FIGURE 5.31: Composite materials based on KL1_250 with dilatations coefficient β in the $\boldsymbol{y}$-direction.

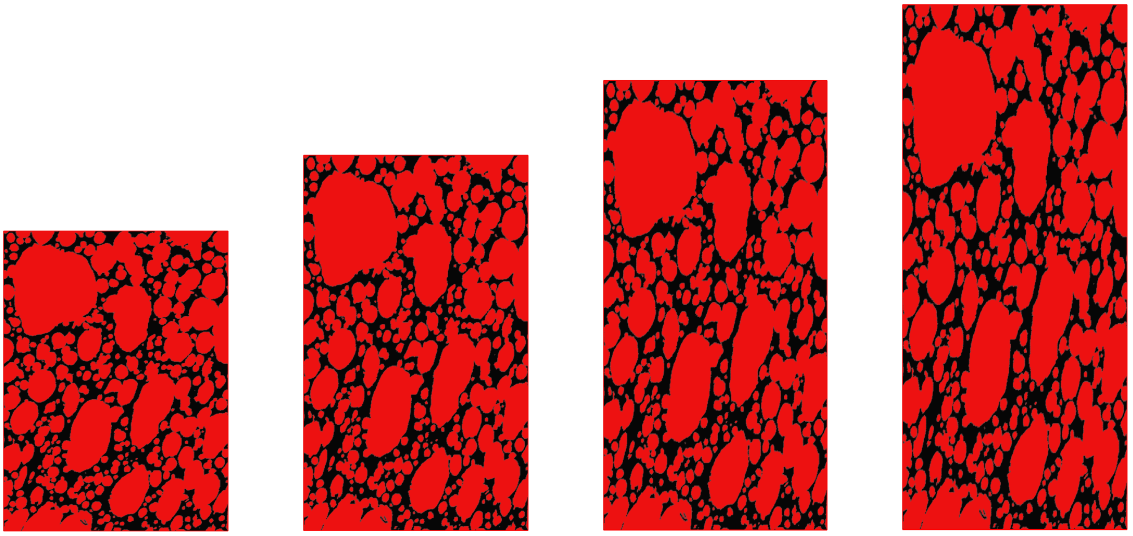

$\beta = 0.9$ $\beta = 0.8$ $\beta = 0.7$ $\beta = 0.6$

FIGURE 5.32: Composite materials based on KD1 with dilatations coefficient β in the $\boldsymbol{y}$-direction.

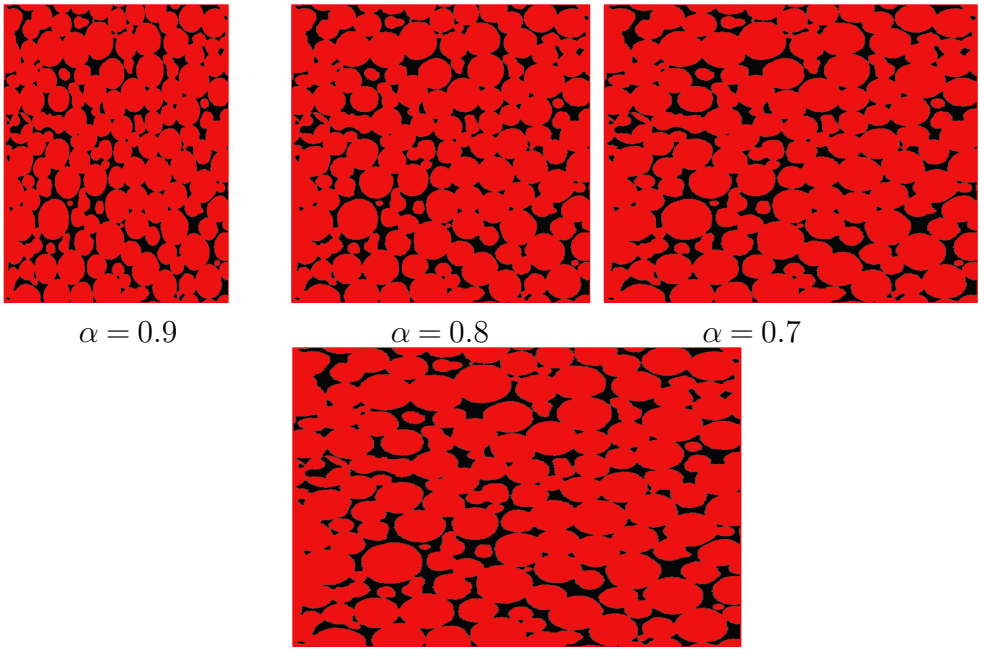

$\alpha = 0.9$ $\alpha = 0.8$ $\alpha = 0.7$

$\alpha = 0.6$

FIGURE 5.33: Composite materials based on KL1_250 with dilatations coefficient α in the $\boldsymbol{x}$-direction.

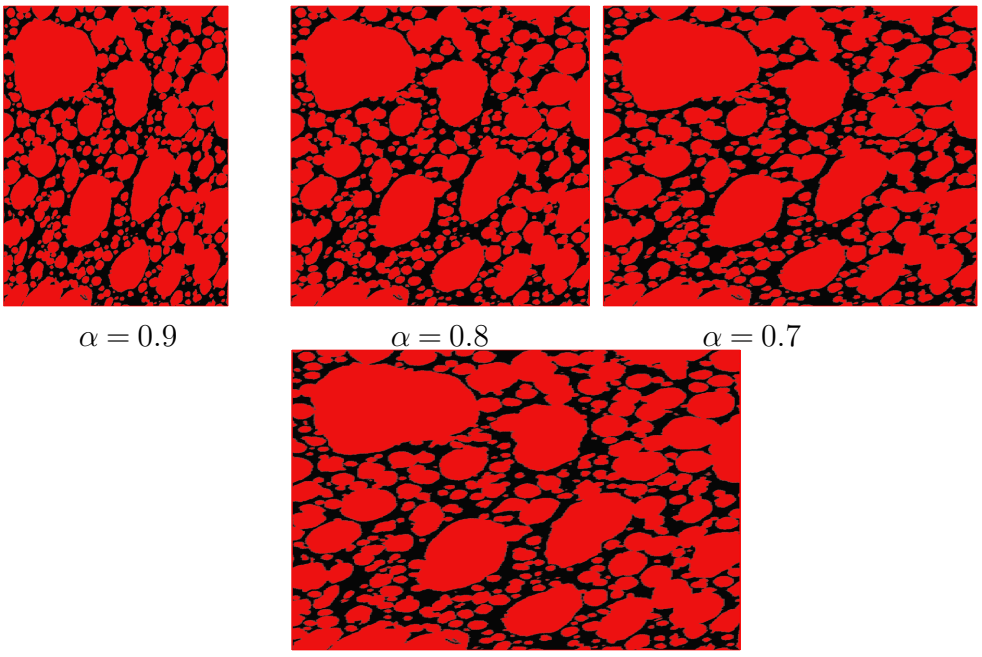

FIGURE 5.34: Composite materials based on KD1 with dilatations coefficient α in the $\boldsymbol{x}$-direction.

We performed numerical simulations, using the new composite structures, with initial and boundary conditions the same as the ones explained in section 5.2 where the domain is initially at a temperature close to the melting temperature of the PCM i.e $311.9°C$. All walls are adiabatic except the bottom one where a Dirichlet boundary condition ($T_D = 322°$) is enforced. For all composites we used the values given in Table 5.1. The simulations are set to stop when all PCM has melted.

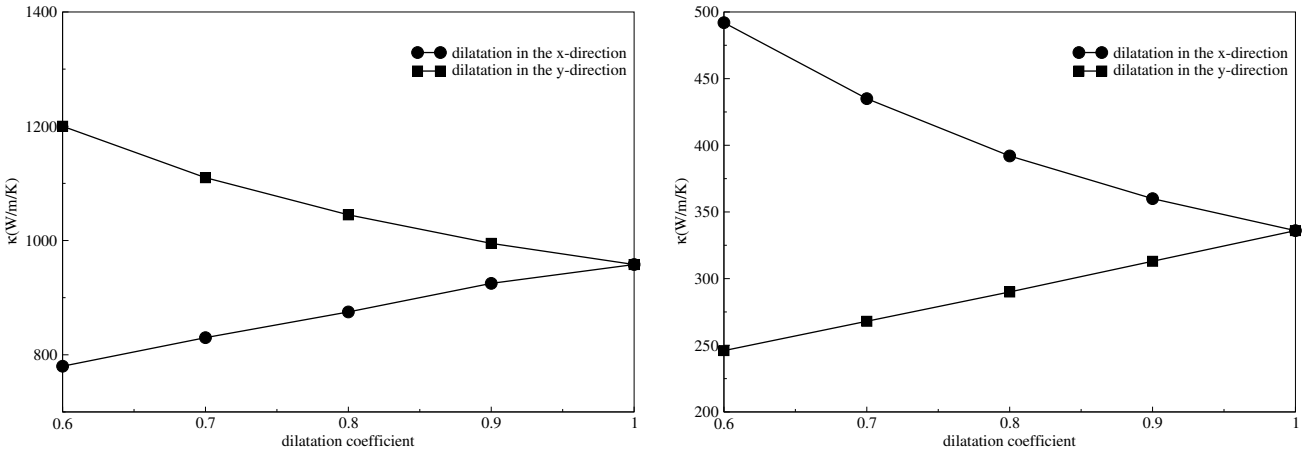

FIGURE 5.35: Thermal conductivity of the carbon foam for KL1_250(left) and KD1(right).

5.6.1 Results for modified structures based on the KL1_250 composite

In this section, we consider the eight composite structures constructed using KL1_250 and by performing dilations in the $\boldsymbol{x}$-direction with the dilatation coefficient $\alpha \in \{0.9, 0.8, 0.7, 0.6\}$ and in the $\boldsymbol{y}$-direction with the dilatation coefficient $\beta \in \{0.9, 0.8, 0.7, 0.6\}$. We suppose that at $t = t_{end}$ all the PCM has melted. We calculate the mean dimensionless temperature for every value of $\boldsymbol{y}$, this should give enough informations on the temperature distribution in the composite since the initial and boundary conditions are chosen such that the temperature's evolution is in the $\boldsymbol{y}$-direction. This is shown in Figure 5.36 where in the left is the plot corresponding to the dilation in the $\boldsymbol{y}$-direction and in the right is the plot corresponding to the dilation in the $\boldsymbol{x}$ - direction. In both plots are shown the results for the initial composite structure KL1_250 in black and for the homogeneous PCM in red. We observe that the dimensionless mean temperature for the composite structures generated by dilatations of α in the $\boldsymbol{x}$-direction tends to be closer to the value of the dimensionless mean temperature for the homogeneous PCM case. This is not the case for the composite structures generated by dilatations of β in the $\boldsymbol{y}$-direction where the dimensionless mean temperature is increasingly distant from the mean dimensionless temperature for the homogeneous PCM case as the value of β decreases.

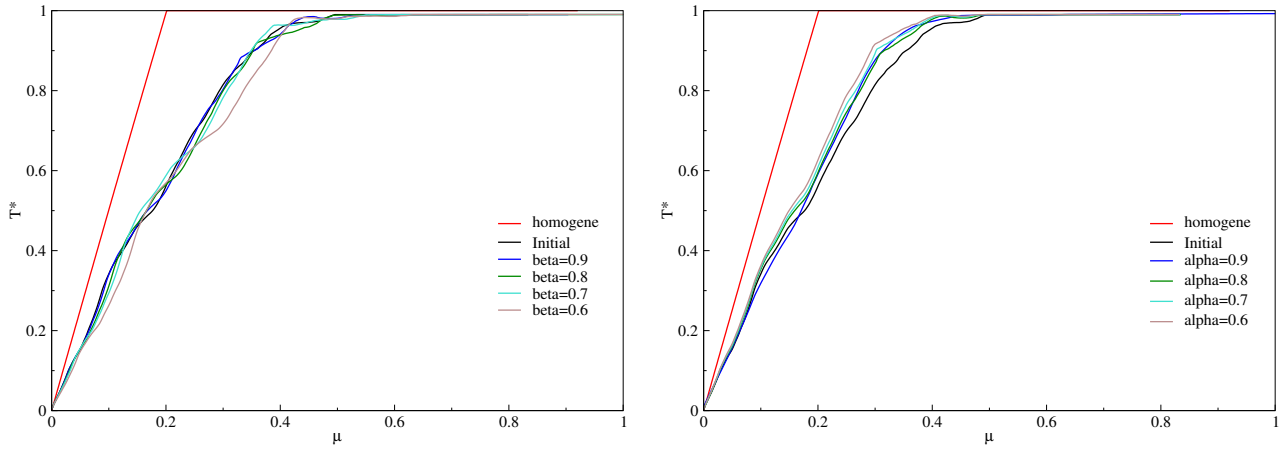

FIGURE 5.36: Mean dimensionless temperature at $t = t_{end}$ as a function of the similarity variable for various β (left) and various α (right) for KL1_250.

In Figure 5.37 we represent the mean dimensionless temperature calculated at $t = t_{end}$ as a function of the error function of the similarity variable. The curves on the left concerns the composite structures generated by dilatation of β in the $\boldsymbol{y}$-direction of the initial KL1_250 composite structure. Whereas in the right side we consider the composite

structures generated by dilatation of α in the $\boldsymbol{x}$-direction of the same initial structure. We can see in this case as well that the values of the mean dimensionless temperature tend to the mean dimensionless temperature for the case of a homogeneous PCM as α decreases. And as observed previously we see the opposite on the left graph where the values of the dimensionless temperature tend to move off from its value in the case of a homogeneous PCM as β decreases.

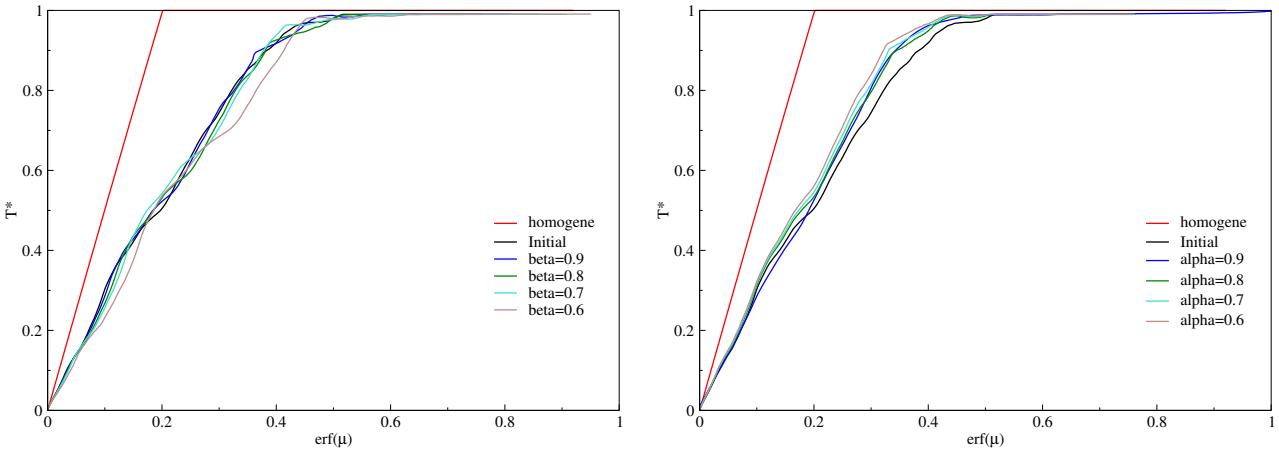

FIGURE 5.37: Mean dimensionless temperature at $t = t_{end}$ as a function of $erf(\mu)$ for various β (left) and various α (right) for KL1_250.

For all eight composite structures we calculate the heat flux at the surface $\boldsymbol{y} = 0$ and the melting front's position over time. In Figure 5.38 we plot in the left graph the heat flux as a function of the inverse of the square root of time for the four composite structures corresponding to $\beta = 0.9, 0.8,\ 0.7$ *and* 0.6 and in the right graph its values for the four composite structures corresponding to $\alpha = 0.9, 0.8,\ 0.7$ *and* 0.6. For comparison we plot in both graphs the heat flux for the initial composite structure KL1_250 in black and the heat flux for the case of a homogeneous PCM. In Figure 5.39 we plot in the left graph the melting front's position as a function of the square root of the dimensionless time for the composites corresponding to $\beta = 0.9, 0.8,\ 0.7$ *and* 0.6 and in the right graph the melting front's position for the four composites corresponding to $\alpha = 0.9, 0.8,\ 0.7$ *and* 0.6. We plot in both graphs the melting front's position for the initial composite KL1_250 in black in addition to the melting front's position in the case of a homogeneous PCM in red. We can see that the heat flux slightly increases with α. For the position of the melting front we can see that it moves faster for the composite based on dilatations in the $\boldsymbol{y}$-direction. While for composites based on dilations in the $\boldsymbol{x}$-direction the melting fronts remains almost unchanged. This means that by enlarging the pores in the $\boldsymbol{x}$-direction we

do not effect much of the characteristics of the initial composite. However when enlarging the pores in the $\boldsymbol{y}$-direction we see differences in the composites characteristics specially the heat flux calculated at the surface $\boldsymbol{y} = 0$ and the position of the melting front. This is due to the fact that, for all the tests realized in this section, we heat the composites by imposing a temperature gradient in the $\boldsymbol{y}$-direction.

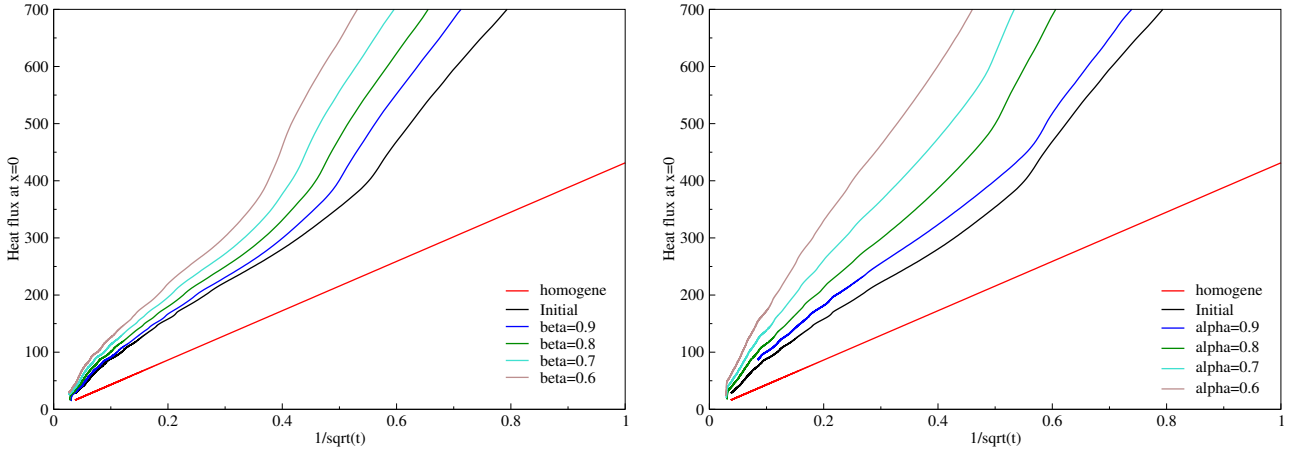

FIGURE 5.38: Evolution of the thermal heat flux at the surface $\boldsymbol{y} = 0$ as a function of $\frac{1}{\sqrt{t}}$ for various β (left) and various α (right).

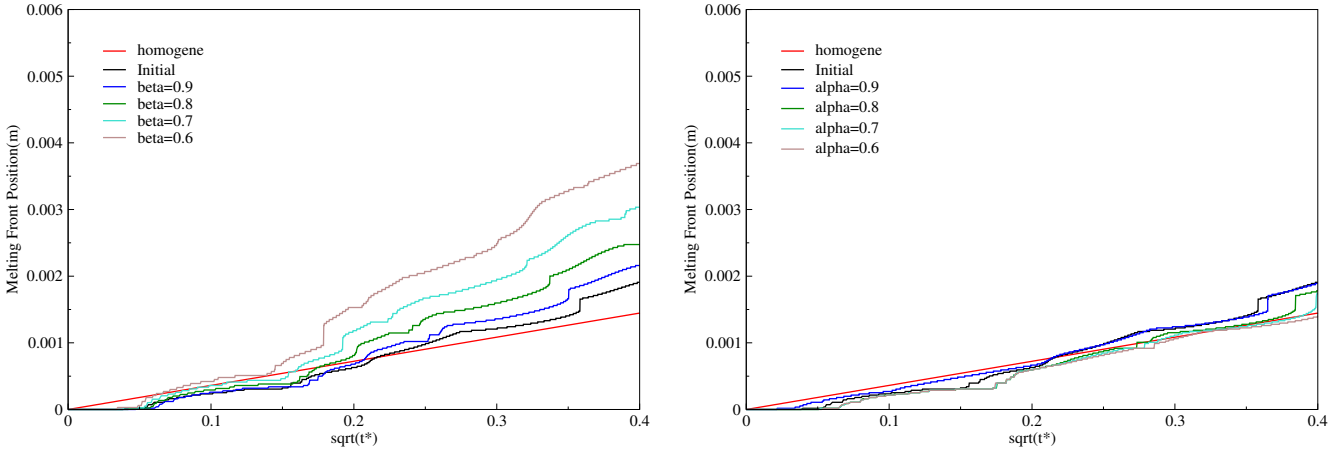

FIGURE 5.39: Evolution of the melting front's position as a function of $\sqrt{t^*}$ for various β (left) and various α (right).

5.6.2 Results for modified structures based on the KD1 composite

In this section simulations are carried out for KD1, as it is previously done for KL1_250 in the above paragraph. For this we consider the eight composite structures constructed

using the initial composite and by performing dilations in the $\boldsymbol{x}$-direction with dilatation coefficient $\alpha \in \{0.9, 0.8, 0.7, 0.6\}$ and in the $\boldsymbol{y}$-direction with dilatation coefficient $\beta \in \{0.9, 0.8, 0.7, 0.6\}$. Figure 5.40 shows the mean dimensionless temperature for these composites where in the left side, are the plots corresponding to dilation in the $\boldsymbol{y}$-direction and in the right are the plots corresponding to dilation in the $\boldsymbol{x}$–direction. In both cases we represent the mean dimensionless temperature for the initial composite as well as the temperature for the homogeneous PCM. As we can see, the values of the temperature tend to the value of the temperature of the homogeneous PCM as the pores are expanded in the $\boldsymbol{x}$–direction. This is not the case for the composite structures generated by dilatations of β in the $\boldsymbol{y}$-direction where the temperature has almost the same value for all composites.

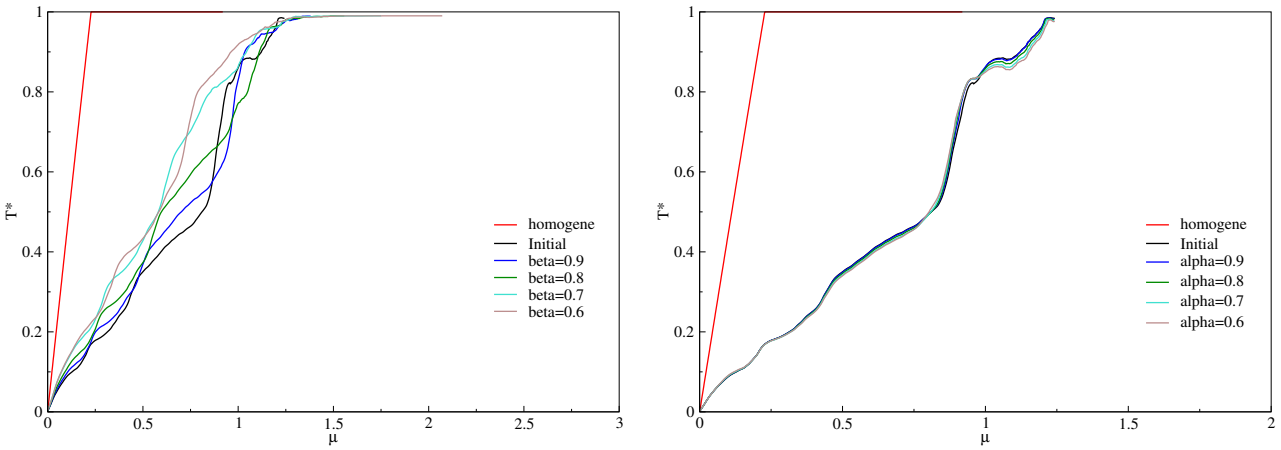

FIGURE 5.40: Mean dimensionless temperature at $t = t_{end}$ as a function of the similarity variable for KD1 for various β (left) and various α (right).

This leaning is confirmed when we represent, for the same structures, the mean dimensionless temperature as a function of the error function of the similarity variable (see Figure 5.41).

For the same composites we represent the melting front's position (see Figure 5.43) and the thermal heat flux (see Figure 5.42). We can see that the value of the heat flux and the melting front position both increases as the value of β decreases i.e as the pores are enlarged in the $\boldsymbol{y}$–direction. As for dilatations in the $\boldsymbol{x}$–direction, the melting front has more or less the same value for all composites while the values of the heat flux are slightly decreasing with α.

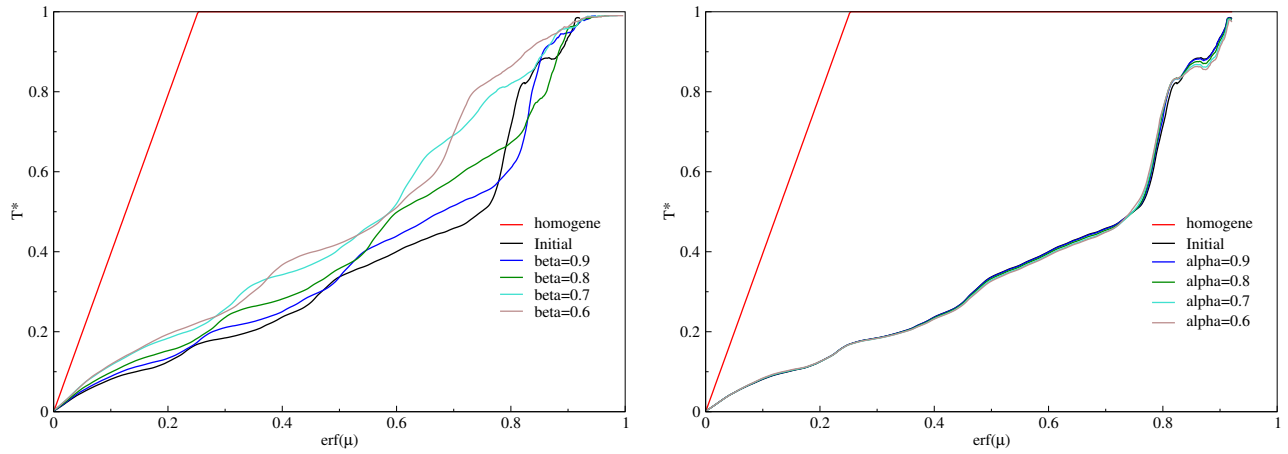

FIGURE 5.41: Mean dimensionless temperature at $t = t_{end}$ as a function of $erf(\mu)$ for KD1 for various β (left) and various α (right).

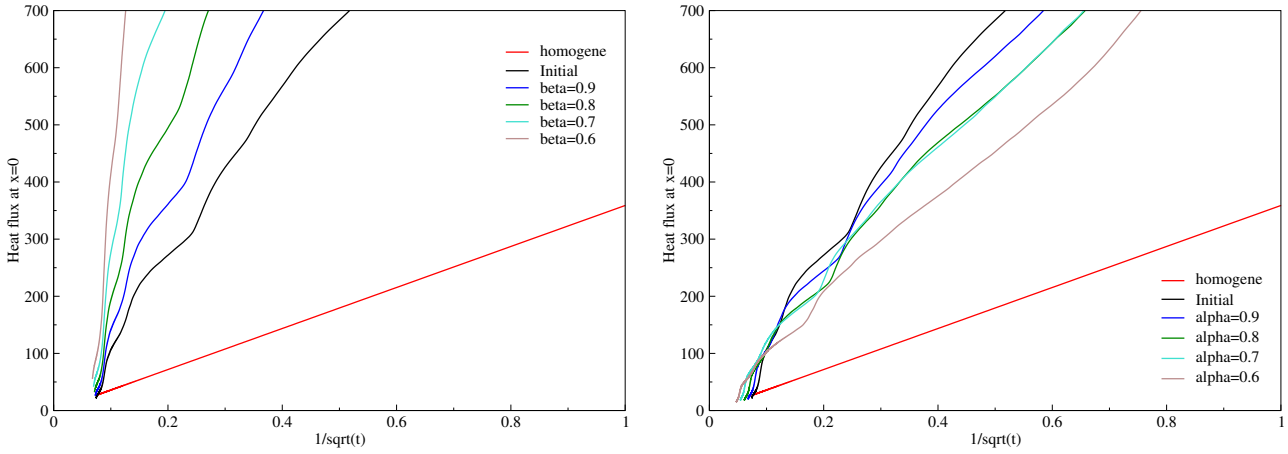

FIGURE 5.42: Evolution of the thermal heat flux at the surface $\boldsymbol{y} = 0$ as a function of $\frac{1}{\sqrt{t}}$ for KD1 for various β (left) and various α (right).

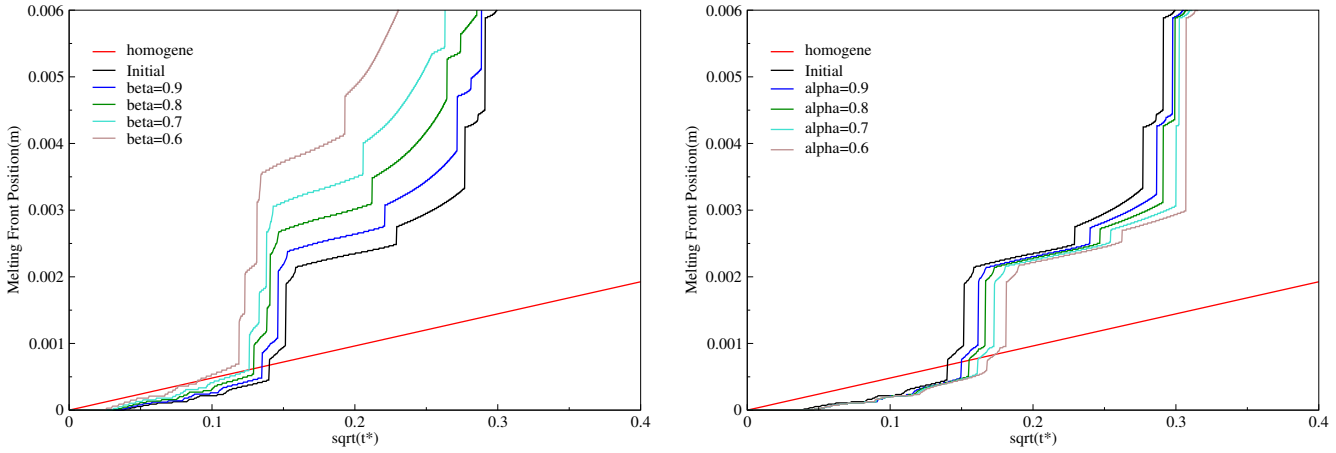

FIGURE 5.43: Evolution of the melting front's position as a function of $\sqrt{t^*}$ for KD1 for various β (left) and various α (right).

Overall the results of the study conducted in this section show that by enlarging the pores according to the direction where the composite material is sought we obtain composites that allow for faster conduction of heat and as a consequence shortens the melting time of the PCM.

5.7 Conclusion

In this chapter we have studied two composite materials, KL1_250 and KD1, resulting from infiltrating a carbon foam with a PCM. In section 5.2 we have conducted simulations which results showed that the first composite can be assimilated to homogeneous PCM with equivalent physical properties. This study show that this is not the case for the second composite. The aim of this is to reduce calculation times by solving a heat conduction model in a homogeneous domain instead of a composite domain. In section 5.3 we have studied the same composites by adding a thermal contact resistance to the heat conduction model. This showed that the thermal behaviour of both composites is increasingly distant from that of a homogeneous PCM. Another question that we answered in this chapter is how increasing the thermal conductivity of the carbon foam effects the thermal behaviour of the composites. In fact, we have shown in section 5.4 that it allowed to increase the thermal heat flux and accelerate the melting process. In section 5.5 we have investigated the influence of changing the pores size on the composite. For both composites we showed that enlarging the pores allowed to accelerate the melting process. Finally, in section 5.6, we studied the influence of the pores shapes on the thermal behaviour of the composites and have shown that by changing the pores shape in the direction following which the material is sought we were able to optimize the thermal conductivity of the foam and enhance the heat flux specially for KD1.

Chapter 6

Conclusions

6.1 Achievements

In this thesis we have studied the unsteady heat conduction problem in a composite media with contact resistance. Developing a robust numerical tool to solve this problem follows a meticulous process. At first we have focused in chapter 2 on the steady state problem for a composite with contact resistance. In this chapter we give two weak formulations to the problem, the classical variational formulation and the hybrid dual formulation. In both cases the existence and uniqueness of the solution is proven. The choice of the weak formulations results in two possible finite element methods to approach the solution. The Lagrange P1 finite element method for variational formulation and the Raviart-Thomas finite element method for the hybrid dual formulation. Theoretical results on the convergence rate of these two methods are given followed by numerical examples that confirm the theoretical predictions. This study showed that the Raviart-Thomas finite element method is a very fit method to solve the steady conduction problem in addition to being very easy to implement in available scientific computing codes. However, this is not the case for the Lagrange finite element method especially for complex geometries where the interface between the materials in the composite is defined with level-set type functions. Since in practice composite materials are mostly of complex structures, the Raviart-Thomas finite element method is chosen in the remaining of the thesis.
In addition to the non-linear nature of the unsteady state problem related to the change in phase occurring in one of the materials, another non-linearity related to the nature of the PCMs studied here is introduced. In fact, the PCMs considered in this work are pure materials where the change in phase is suppose to occur at a constant temperature. This

is described by a discontinuity in the liquid fraction function of the material which consequently introduces a jump in the enthalpy at the melting temperature. In chapter 3 we introduce a smoothing interval around the melting temperature to avoid any additional numerical difficulties related to this discontinuity. A theoretical and numerical study is conducted in this chapter in order to relate errors on the temperature and on the moving front's position to the width of the smoothing interval ε. This study showed that these errors decay as ε outside of the phase change interval and as $\sqrt{\varepsilon}$ inside of the interval.
After using a backward Euler method for time discretization, a second method is needed to accurately account for the non-linearity related to the phase change. Four of the most used methods for this purpose are exposed in chapter 4 : the update source method, the Chernoff scheme, the apparent heat capacity method and the enthalpy linearization scheme. A one dimensional problem of melting a PCM and where an analytical solution is given allowed to test the ability of the schemes to reproduce the results given in chapter 3 with regards to ε. The apparent heat capacity and the enthalpy linearization schemes were able to reproduce these results. While the Chernoff scheme did not allow to find similar results, it still gave very good results. This was not the case for the update source method. Other tests were conducted with a two dimensional freezing of a PCM and finally a test case with a composite material. For this last test an analytical solution is not available and a Newton method is used to give a reference solution. These tests show that the apparent heat capacity, the enthalpy linearization and the Chernoff scheme allow to solve very accurately the Stefan problem and gave in all test cases comparable results. Our goal is to develop a method to solve the unsteady heat conduction problem in a composite media with complex geometries and it is important to have accurate as well as fast methods. The choice was made to use the Chernoff scheme for the remaining of the thesis since, a side from being very accurate, this method is designed in a way that allow to define the matrix resulting from discretizing the problem outside the time loop and in addition using a direct solver of type LU for example enable to reduce greatly the calculation time.
In chapter 5 we studied two composite materials using 2D images of a carbon foam infiltrated with salt(PCM). For both composites, we solved the heat conduction problem using the backward Euler method for time discretization, the Chernoff method for the non-linearity and the Raviart-Thomas finite element method for the space discretization. At the end of the phase change process, the temperature fields and other thermal properties of both materials are compared to the values for a homogeneous PCM with equivalent thermo-physical properties. This allowed to prove that the composite with the more uniform pore distribution could be assimilated to a homogeneous PCM. Other tests

were conducted and allowed to show that modifying the micro-structure of the composite by changing the shape or the size of the pores allowed to optimize certain properties of the composite such as the thermal conductivity of the foam.

6.2 Future Work

The work presented here can be extended in several directions. For instance, a similar study as the one conducted in chapter 2 can be realized for the heat conduction problem in the composite where an error estimation on the solution of the problem in the composite with respect to the mesh size as well as the width of the smoothing interval can be provided. Indeed it is interesting to quantify the errors made for the approximations of the moving boundary's position inside the PCM or for the temperature field in the PCM and in the composite. This could be useful for validating numerical schemes as the ones presented in chapter 4. Since for a composite material there is not an analytic solution available, a Newton method can be used to provide a reference solution in order to validate the theoretical findings with numerical results.
On the other hand, a study similar to the one conducted in chapter 5 can be realized using the heat conduction model with contact resistance. We can try to understand how changing the size of the pores or their shapes is influencing the thermal behaviour of the studied composite materials. At last, one can envision optimizing the performance of the composites by changing the porosity of the composites by means of adding or removing pores.
Finally, the problem studied in this thesis assumes the heat to be exchanged only by conduction which could be limiting if the application require a more complete model. One can envision completing the model by adding a Boussinesq approximation to account for the convective motion in the liquid phase of the PCM. The finite elements methods along with the numerical schemes presented on this work can very well be adapted to solve this problem.

Bibliography

[1] M. Abramowitz and I. A. Stegun, *Handbook of Mathematical Functions*, Dover, New York, fifth ed., 1964.

[2] R. A. Adams and J. J. F. Fournier, *Sobolev spaces*, vol. 140 of Pure and Applied Mathematics (Amsterdam), Elsevier/Academic Press, Amsterdam, second ed., 2003.

[3] V. Alexiades, *Mathematical Modeling Of Melting And Freezing Processes*, Taylor & Francis, 1992.

[4] V. Alexiades and A. Solomon, *A. Mathematical Modeling of Melting and Freezing Processes.*, Hemisphere Publishing Corporation, 1993.

[5] M. R. S. Ammi and O. Mul, *Error estimates for the chernoff scheme to approximate a nonlocal parabolic problem*, (2007).

[6] R. Ankri and T. Zebbiche, *Résolution d'un problème de changement de phase en présence de la convection naturelle par la méthode enthalpique: Application au gallium*, Revue des Energies Renouvelables CISM'08 Oum El Bouaghi, (2008), pp. 25–36.

[7] D. N. Arnold, F. Brezzi, B. Cockburn, and L. D. Marini, *Unified analysis of discontinuous galerkin methods for elliptic problems*, SIAM J. Numer. Anal., 39 (2001), pp. 1749–1779.

[8] V. I. Arnold, *Ordinary Differential Equations*, Springer, Berlin, 1997.

[9] D. Atthey, *A finite difference scheme for melting problems*, IMA Journal of Applied Mathematics, 13 (1974), pp. 353–366.

[10] F. Ben Belgacem, C. Bernardi, F. Jelassi, and M. Mint Brahim, *Finite element methods for the temperature in composite media with contact resistance*, J. Sci. Comput, (2015).

[11] Bernard and Jean-MarieEmmanuel, *Density results in sobolev spaces whose elements vanish on a part of the boundary*, Chinese Annals of Mathematics, Series B, 32 (2011), pp. 823–846.

[12] C. Bernardi, Y. Maday, and A. Patera, *A new nonconforming approach to domain decomposition: the mortar element method*, Collège de France Seminar, (1990).

[13] C. Bernardi, Y. Maday, and F. Rapetti, *Discrétisations variationnelles de problèmes aux limites elliptiques*, Mathématiques et Applications, Springer, 2004.

[14] S. Brenner and R. Scott, *The Mathematical Theory of Finite Element Methods*, Texts in Applied Mathematics, Springer, 2008.

[15] F. Brezzi and M. Fortin, *Mixed and hybrid finite elements methods*, Springer series in computational mathematics, Springer-Verlag, 1991.

[16] J. H. Brusche, A. Segal, C. Vuik, and H. Urbach, *A comparison of an ethalpy and a temperature method for melting problems on composite domains*, European Conference on Computational Fluid Dynamics, The Netherlands, (2006).

[17] J. R. Cannon, D. B. Henry, and D. B. Kotlow, *Continuous differentiability of the free boundary for weak solutions of the stefan problem*, Bull. Amer. Math. Soc., 80 (1974), pp. 45–48.

[18] V. Canseco, Y. Anguy, J. J. Roa, and E. Palomo, *Structural and mechanical characterization of graphite foam/phase change material composites*, Carbon, 74 (2014), pp. 266–281.

[19] C. Cao, A. Yu, Q.-H. Qin, et al., *Evaluation of effective thermal conductivity of fiber-reinforced composites*, International Journal of Architecture, Engineering and Construction, 1 (2012), pp. 14–29.

[20] H. Carslaw and J. Jaeger, *Conduction of Heat in Solids*, Oxford science publications, Clarendon Press, 1986.

[21] H. S. Carslaw and J. C. Jaeger, *Conduction of Heat in Solids*, Clarendon Press, Oxford, 1959.

[22] R. M. Christensen, *Mechanics of composite materials*, Courier Corporation, 2012.

[23] P. Ciarlet, *The Finite Element Method for Elliptic Problems*, Studies in Mathematics and its Applications, Elsevier Science, 1978.

[24] D. Cleland, A. Cleland, R. Earle, and S. Byrne, *Prediction of rates of freezing, thawing or cooling in solids or arbitrary shape using the finite element method*, International journal of refrigeration, 7 (1984), pp. 6–13.

[25] G. Comini, S. Del Guidice, R. Lewis, and O. Zienkiewicz, *Finite element solution of non-linear heat conduction problems with special reference to phase change*, International Journal for Numerical Methods in Engineering, 8 (1974), pp. 613–624.

[26] R. Courant et al., *Variational methods for the solution of problems of equilibrium and vibrations*, Bull. Amer. Math. Soc, 49 (1943), pp. 1–23.

[27] J. Crank, *Free and Moving Boundary Problems*, Oxford science publications, Clarendon Press, 1987.

[28] J. Douglas, Jr. and T. M. Gallie, Jr., *On the numerical integration of a parabolic differential equation subject to a moving boundary condition*, Duke Math. J., 22 (1955), pp. 557–571.

[29] P. W. Egolf and H. Manz, *Theory and modeling of phase change materials with and without mushy regions*, International Journal of Heat and Mass Transfer, 37 (1994), pp. 347–366.

[30] I. Ekeland and R. Témam, *Convex Analysis and Variational Problems*, Classics in Applied Mathematics, Society for Industrial and Applied Mathematics, 1999.

[31] M. Farhloul and M. Fortin, *Review and complements on mixed-hybrid finite element methods for fluid flows*, Journal of Computational and Applied Mathematics, 140 (2002), pp. 301 – 313. Int. Congress on Computational and Applied Mathematics 2000.

[32] L. Fletcher, *Conduction in solids—imperfect metal-to-metal contacts: Thermal contact resistance, section 502.5*, Heat Transfer and Fluid Mechanics Data Books, Genium Publishing Company, Schenectady, New York, (1991).

[33] A. Friedman, *The stefan problem in several space variables*, Transactions of the American Mathematical Society, (1968), pp. 51–87.

[34] H. Garg, S. Mullick, and V. K., *Solar Thermal Energy Storage*, Clarendon Press, Oxford, 1959.

[35] V. Girault and P. Raviart, *Finite element methods for Navier-Stokes equations: theory and algorithms*, Springer series in computational mathematics, Springer-Verlag, 1986.

[36] D. Goswami, F. Kreith, and J. Kreider, *Principles of Solar Engineering, Second Edition*, Taylor & Francis, 2000.

[37] P. Grisvard, *Boundary value problems in non-smooth domains*, no. 19 in Lecture notes, University of Maryland, Dept. of Mathematics, 1980.

[38] ——, *Elliptic problems in nonsmooth domains*, Monographs and studies in mathematics, Pitman Advanced Pub. Program, 1985.

[39] C. Grossmann and A. Noack, *Smoothing and rothe's method for stefan problems in enthalpy form*, Journal of Computational and Applied Mathematics, 138 (2002), pp. 2917–2924.

[40] S. Gupta, *The Classical Stefan Problem: basic concepts, modelling and analysis*, vol. 2 of North-Holland Series in Applied Mathematics and Mechanics, Amsterdam ; London : Elsevier, 2003.

[41] F. Hecht, *FREEFEM++, A FINITE ELEMENT PDE SOLVER.*

[42] F. Hecht, *New development in freefem++*, J. Numer. Math., 20 (2012), pp. 251–265.

[43] F. Hecht, O. Pironneau, and K. Ohtsuka, *FreeFem++ Manual.*

[44] H. Hu and A. S. A., *Mathematical modelling of solidification and melting: a review*, Modelling and Simulation in Materials Science and Engineering, 4 (1996), pp. 371–396.

[45] H. Hu and S. A. Argyropoulos, *Mathematical modelling of solidification and melting: a review*, Modelling and Simulation in Materials Science and Engineering, 4 (1996), p. 371.

[46] S. Idelsohn, M. Storti, and L. Crivelli, *Numerical methods in phase-change problems*, Archives of Computational Methods in Engineering, 1 (1994), pp. 49–74.

[47] S. R. Idelsohn, M. A. Storti, and L. A. Crivelli, *Numerical methods in phase-change problems*, Archives of Computational Methods in Engineering, 1 (1994), pp. 49–74.

[48] F. Jelassi, M. Azaïez, and E. Palomo Del Barrio, *A substructuring method for phase change modelling in hybrid media*, Computers and Fluids, 88 (2013), pp. 81–92.

[49] D. S. Jerison and C. E. Kenig, *The neumann problem on lipschitz domains*, Bull. Amer. Math. Soc. (N.S.), 4 (1981), pp. 203–207.

[50] J. W. Jerome and M. E. Rose, *Error estimates for the multidimensional two-phase stefan problem*, Math. Comp., 39 (1982), pp. 377–414.

[51] H. Jopek and T. Strek, *Optimization of the effective thermal conductivity of a composite*, INTECH Open Access Publisher, 2011.

[52] A. L. Kalamkarov, I. V. Andrianov, V. V. Danishevsâ, et al., *Asymptotic homogenization of composite materials and structures*, Applied Mechanics Reviews, 62 (2009), p. 030802.

[53] A. L. Kalamkarov and K. S. Challagulla, *Effective properties of composite materials, reinforced structures and smart composites: Asymptotic homogenization approach*, in Effective Properties of Heterogeneous Materials, Springer, 2013, pp. 283–363.

[54] D. A. Knoll, D. B. Kothe, and B. Lally, *A new nonlinear solution method for phase change problems*, Numerical Heat Transfer: Part B: Fundamentals, 35 (1999), pp. 439–459.

[55] E. Lemmon, *Multidimensional integral phase change approximations for finite element conduction codes*, Numerical methods in heat transfer.(A 82-28551 13-34) Chichester, Sussex, England and New York, Wiley-Interscience, 1981„ (1981), pp. 201–213.

[56] J. Lions and E. Magenes, *Problèmes aux limites non homogènes et applications ...*, Problèmes aux limites non homogènes et applications, Dunod, 1968.

[57] J. Lopez, Z. Acem, and E. P. Del Barrio, *Kno 3/nano 3–graphite materials for thermal energy storage at high temperature: Part ii.–phase transition properties*, Applied Thermal Engineering, 30 (2010), pp. 1586–1593.

[58] A. Mejdi, F. Jelassi, M. M. Brahim, and J. Shen, *Two phases stefan problem with smoothed enthalpy*, Communications in Mathematical Sciences, (2016).

[59] K. Morgan, R. Lewis, and O. Zienkiewicz, *An improved algrorithm for heat conduction problems with phase change*, International Journal for Numerical Methods in Engineering, 12 (1978), pp. 1191–1195.

[60] K. Morgan, R. W. Lewis, and O. C. Zienkiewicz, *An improved algorithm for heat conduction problems with phase change*, International Journal for Numerical Methods in Engineering, vol. 12 (1978), pp. 1191–1195.

[61] V. Morisson, *Heat transfer modelling within graphite/salt composites: from the pore scale equations to the energy storage system*, PhD thesis, Bordeaux 1, 2008.

[62] M. Muhieddine, E. Canot, and R. March, *Various Approaches for Solving Problems in Heat Conduction with Phase Change*, International Journal on Finite Volumes, (2009), p. 19.

[63] ——, *Various approaches for solving problems in heat conduction with phase change*, International Journal on Finite Volumes, (2009), p. 19.

[64] F. J. Murray and K. S. Miller, *Theorems for Ordinary Differential Equations*, Reprinted, Original Edition published by New York University Press 1954, 1976.

[65] B. Nedjar, *An enthalpy-based finite element method for nonlinear heat problems involving phase change*, Computers and Structures, (2002), pp. 9–21.

[66] R. H. Nochetto, *Error estimates for two-phase stefan problems in several space variables, i: Linear boundary conditions*, Calcolo, 22 (1985), pp. 457–499.

[67] R. H. Nochetto and C. Verdi, *The combined use of a nonlinear chernoff formula with a regularization procedure for two-phase stefan problems*, (1987).

[68] O. Oleinik, *A method of solution of the general stefan problem*, in Sov. Math. Dokl, vol. 1, 1960, pp. 1350–1354.

[69] S. Pendyala, *Macroencapsulation of phase change materials for thermal energy storage*, (2012).

[70] Q. Pham, *Comparison of general-purpose finite-element methods for the stefan problem*, Numerical Heat Transfer, 27 (1995), pp. 417–435.

[71] Q. Pham, *Comparison of general-purpose finite element methods for the stefan problem*, Numerical Heat Transfer Part B - Fundamentals, (1995), pp. 417–435.

[72] Q. T. Pham, *A fast, unconditionally stable finite-difference scheme for heat conduction with phase change*, Int. J. Heat Mass Transfer, 28 (1985), pp. 2079–2084.

[73] ——, *The use of lumped capacitance in the finite element solution of heat conduction problems with phase change*, Int. J. Heat Mass Transfer, 29 (1986), pp. 285–291.

[74] K. Pietrak and T. S. Wisniewski, *A review of models for effective thermal conductivity of composite materials*, Journal of Power Technologies, (2015), pp. 14–24.

[75] D. A. D. Pietro, M. Vohralik, and S. Yousef, *Adaptative regularization, linearization, and discretization and a posteriori error control for the two-phase stefan problem*, Mathematics of Computation, (2014).

[76] G. Prakash and H. Garg, *Solar Energy: Fundamentals and Applications*, Tata McGraw-Hill Publishing Company, 2000.

[77] P.-A. Raviart and J.-M. Thomas, *A mixed finite element method for 2-nd order elliptic problems*, in Mathematical aspects of finite element methods, vol. 606, Springer, 1977, pp. 292–315.

[78] J. E. Roberts and J.-M. Thomas, *Mixed and hybrid methods*, Handbook of numerical analysis, 2 (1991), pp. 523–639.

[79] W. D. Rolph and K.-J. Bathe, *An efficient algorithm for analysis of nonlinear heat transfer with phase changes*, International Journal for Numerical Methods in Engineering, 18 (1982), pp. 119–134.

[80] J. Roose and O. Storrer, *Modelization of phase changes by fictitious-heat flow*, International journal for numerical methods in engineering, 20 (1984), pp. 217–225.

[81] L. I. Rubenstein, *The Stefan problem*, American Mathematical Society, Providence, R.I., 1971. Translated from the Russian by A. D. Solomon, Translations of Mathematical Monographs, Vol. 27.

[82] L. I. Rubinstein, *The Stefan problem*, vol. 27, Translations of Mathematical Monographs. Amer. Math. Soc, 1971.

[83] W. Rudin, *Principles of Mathematical Analysis*, McGraw-Hill, New York, third ed., 1976.

[84] Y. SAFA, *Simulation numérique des phénomènes thermiques et magnéthohydrodynamiques dans une cellule de HALL-HEROULT*, PhD thesis, École polytechnique fédérale de Lausanne, 2005.

[85] Scilab Enterprises, *Scilab: Free and Open Source software for numerical computation*, Scilab Enterprises, Orsay, France, 2012.

[86] A. Sharma, V. Tyagi, C. Chen, and D. Buddhi, *Review on thermal energy storage with phase change materials and applications*, Renewable and Sustainable Energy Reviews, 13 (2009), pp. 318–345.

[87] A. Sieminski, *International energy outlook*, (2014).

[88] A. Solomon, *A note on the stefan number in slab melting and solidification*, Letters in Heat and Mass Transfer, 8 (1981), pp. 229–235.

[89] E. Süli, *Lecture notes on finite element methods for partial differential equations*, Mathematical Institute, University of Oxford, (2012).

[90] E. T. Swartz and R. O. Pohl, *Thermal boundary resistance*, Rev. Mod. Phys., 61 (1989), pp. 605–668.

[91] D. Tarzia, *Explicit and Approximated Solutions for Heat and Mass Transfer Problems with a Moving Interface*, INTECH Open Access Publisher, 2011.

[92] D. A. Tarzia, *A bibliography on moving free-boundary problems for the heat diffusion equation. the stefan and related problems (with 5869 references)*, MAT-Serie A, 2 (www.austral.edu.ar/MAT-SerieA/2), (2000), pp. 1–297.

[93] V. R. Voller, *Implicit finite-difference solutions of the enthalpy formulation of stefan problems*, IMA Journal of Numerical Analys, (1985), pp. 201–214.

[94] ——, *An overview of numerical methods for solving phase change problems*, Advances in Numerical Heat Transfer, (1996), pp. 341–375.

[95] H. M. Weber and R. B., *Die Paruellen Differentialgleichungen der Mathematischen Physik*, vol. 2, Friedrich Vieweg, 1912.

[96] W. Zhao, *Characterization of encapsulated phase change materials for thermal energy storage*, (2013).

[97] M. Zlámal, *On the finite element method*, Numerische Mathematik, 12 (1968), pp. 394–409.